Transparent Conducting Oxides and Other Functional Thin Films Grown via Aerosol Assisted Chemical Vapour Deposition

Donglei Zhao

A thesis presented for the degree of

Doctor of Philosophy

Supervised by

Principal Supervisor: Professor Claire J. Carmalt

Subsidiary Supervisor: Professor Christopher Blackman

Department of Chemistry

Mathematical and Physics Sciences Faculty

University College London

September 2022

Declaration

I, Donglei Zhao, confirm that the work presented in this thesis is my own. Where information has been derived from other sources (publications, websites and database), I confirm that this has been indicated in the thesis.

Abstract

This thesis describes the preparation and characterisation of different functional thin films, with the main focus being transparent conducting oxide (TCO) thin films including both n-type and p-type, but also other functional thin films (such as catalytic thin films used in the oxygen evolution reaction (OER)) grown via aerosol assisted chemical vapour deposition (AACVD). The main aim to this work was to discover and investigate more suitable functional thin films (TCOs and catalytic materials) via the film preparation method, AACVD.

The synthetic route of all the functional thin films used in this thesis is AACVD, which is one specialized form of CVD that is cost effective and easily scalable, operating at ambient pressure.

In this thesis, Mo-, P- and B-doped zinc oxide (ZnO) thin films have been investigated as n-type TCOs, with all films showing low resistivities of 2.6×10^{-3} $\Omega.cm$, 6.0×10^{-3} $\Omega.cm$ and 5.10×10^{-3} $\Omega.cm$, respectively. The optical properties also reached over 75% as transmittance in the visible area for all doped thin films.

Boron phosphide (BP) thin films were synthesized and investigated as a p-type TCO, although the results indicated that BP may not be an ideal p-type material and further doping investigations were not investigated.

P-doped molybdenum disulfide (MoS_2) thin films have been considered as potential catalytic materials in the OER area. The MoS_2 thin films with 1 mol.% P doping displayed superior catalytic performance of OER process with lowest overpotential at 319 mV for 10 mA cm^{-2} as current density and 173 mV for 10 mA mg^{-1} as current density, respectively, in 1M KOH medium. Moreover, the mass activity was also high at 1000 A g^{-1} with small overpotential at 450 mV, which suggested the doping method could improve the properties of thin films through AACVD.

Impact Statement

This PhD project focuses on preparing and characterizing different functional thin films using the aerosol assisted chemical vapour deposition (AACVD) method. The impact and highlights of this thesis are listed below:

(1) ZnO based thin films with different dopants (Mo, P and B) were synthesized in order to combine good optical and electrical properties at the same time. These films can be considered as potential alternative transparent conducting oxide (TCO) materials for the current widely used tin doped indium oxide (ITO) materials.

(2) The transition metal sulfide based material, P-doped MoS_2, was developed for oxygen evolution reaction (OER) in alkaline medium, which has excellent catalytic performance for water splitting.

(3) Preparation of catalytic thin films from the convenient and inexpensive AACVD route,suggests many other transition metals based thin films with significant catalytic properties could be grown using AACVD to further reduce the cost of the electrocatalysts for renewable energy (hydrogen) production.

Acknowledgement

Firstly, I would like to express my deepest gratitude to my principal supervisor, Professor Claire J. Carmalt, for the kindly and continual support and guidance during the last four years.

Secondly, a huge thanks to Dr. Sanjayan Sathasivam, who trained me in experimental skills for the first few months and provided many useful ideas and advice for the whole project.

I am also very grateful to my subsidiary supervisor, Professor Chris Blackman, for the kindly help of the first year report/viva and upgrade report/viva.

I would like to thank all my collaborators during my PhD study, including Professor Ivan P. Parkin, Dr. Sanjayan Sathasivam, Dr. Jianwei Li, Dr. Siyu Zhao, Dr. Guanjie He, Mingyue Wang and Yeshu Tan.

A big thanks to all the people who helped me a lot for the characterisations, including Dr. Steve Firth, Dr. Martin Vickers, Dr. Kersti Karu, Dr Tom Gregory, Dr. Sanjayan Sathasivam, Dr. Joanna Borowiec and Mingyue Wang.

I would also like to thank each person in the Carmalt/Parkin research group, who created an excellent and helpful research environment.

I am very grateful for the funding from the UCL Dean's Prize and China Scholarship Council (CSC) (UCL-CSC project).

Finally, I would like to thank my parents for all the love and support during my PhD project.

UCL Research Paper Declaration Form: referencing the doctoral candidate's own published work(s)

Please use this form to declare if parts of your thesis are already available in another format, e.g. if data, text, or figures:

have been uploaded to a preprint server;
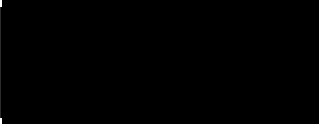
are in submission to a peer-reviewed publication;

have been published in a peer-reviewed publication, e.g. journal, textbook.

This form should be completed as many times as necessary. For instance, if you have seven thesis chapters, two of which containing material that has already been published, you would complete this form twice.

For a research manuscript that has already been published (if not yet published, please skip to section 2):		
Where was the work published? (e.g. journal name)	ACS Applied Electronic Materials	
Who published the work? (e.g. Elsevier/Oxford University Press):	2019 American Chemical Society	
When was the work published?	18/12/2019	
Was the work subject to academic peer review?	Yes	
Have you retained the copyright for the work?	No	
[If no, please seek permission from the relevant publisher and check the box next to the below statement]: ☒ *I acknowledge permission of the publisher named under 1b to include in this thesis portions of the publication named as included in 1a.*		
For a research manuscript prepared for publication but that has not yet been published (if already published, please skip to section 3):		
Has the manuscript been uploaded to a preprint server? (e.g. medRxiv):	Please select.	If yes, which server? Click or tap here to enter text.
Where is the work intended to be published? (e.g. names of journals that you are planning to submit to)	Click or tap here to enter text.	
List the manuscript's authors in the intended authorship order:	Click or tap here to enter text.	
Stage of publication	Please select.	
For multi-authored work, please give a statement of contribution covering all authors (if single-author, please skip to section 4):		
This work is completed by Sanjayan Sathasivam, Jianwei Li, Claire J. Carmalt and myself. The main part of the work including thin film deposition, most of the characterization and analysis were carried out by myself. SS and CC provided many useful ideas, advice and supervision of the research. SS carried out the XPS analysis and the unit cell parameters were calculated by JL.		
In which chapter(s) of your thesis can this material be found?		

Chapter 3			
e-Signatures confirming that the information above is accurate (this form should be co-signed by the supervisor/ senior author unless this is not appropriate, e.g. if the paper was a single-author work):			
Candidate:	Donglei Zhao	**Date:**	26/07/2022
Supervisor/ Senior Author (where appropriate)**:**	██████████████	**Date:**	18/08/2022

UCL Research Paper Declaration Form: referencing the doctoral candidate's own published work(s)

Please use this form to declare if parts of your thesis are already available in another format, e.g. if data, text, or figures:

have been uploaded to a preprint server;

are in submission to a peer-reviewed publication;

have been published in a peer-reviewed publication, e.g. journal, textbook.

This form should be completed as many times as necessary. For instance, if you have seven thesis chapters, two of which containing material that has already been published, you would complete this form twice.

For a research manuscript that has already been published (if not yet published, please skip to section 2):	
Where was the work published? (e.g. journal name)	RSC Advances
Who published the work? (e.g. Elsevier/Oxford University Press):	The Royal Society of Chemistry 2020
When was the work published?	17/09/2020
Was the work subject to academic peer review?	Yes
Have you retained the copyright for the work?	No
[If no, please seek permission from the relevant publisher and check the box next to the below statement]:	
☒ *I acknowledge permission of the publisher named under 1b to include in this thesis portions of the publication named as included in 1a.*	

For a research manuscript prepared for publication but that has not yet been published (if already published, please skip to section 3):		
Has the manuscript been uploaded to a preprint server? (e.g. medRxiv):	Please select.	If yes, which server? Click or tap here to enter text.
Where is the work intended to be published? (e.g. names of journals that you are planning to submit to)	Click or tap here to enter text.	
List the manuscript's authors in the intended authorship order:	Click or tap here to enter text.	
Stage of publication	Please select.	

For multi-authored work, please give a statement of contribution covering all authors (if single-author, please skip to section 4):
This work is completed by Jianwei Li, Sanjayan Sathasivam, Claire J. Carmalt and myself. The main part of the work such as thin film deposition, characterizations and analysis were carried out by myself. SS and CC provided many useful ideas, advice and supervision of the project. SS carried out the XPS analysis and JL provided ideas and calculated the unit cell parameters.

In which chapter(s) of your thesis can this material be found?

Chapter 4			
e-Signatures confirming that the information above is accurate (this form should be co-signed by the supervisor/ senior author unless this is not appropriate, e.g. if the paper was a single-author work):			
Candidate:	Donglei Zhao	**Date:**	26/07/2022
Supervisor/ Senior Author (where appropriate)**:**	████████████	**Date:**	18/08/2022

UCL Research Paper Declaration Form: referencing the doctoral candidate's own published work(s)

Please use this form to declare if parts of your thesis are already available in another format, e.g. if data, text, or figures:

have been uploaded to a preprint server;

are in submission to a peer-reviewed publication;

have been published in a peer-reviewed publication, e.g. journal, textbook.

This form should be completed as many times as necessary. For instance, if you have seven thesis chapters, two of which containing material that has already been published, you would complete this form twice.

For a research manuscript that has already been published (if not yet published, please skip to section 2)**:**	
Where was the work published? (e.g. journal name)	RSC Advances
Who published the work? (e.g. Elsevier/Oxford University Press):	The Royal Society of Chemistry 2022
When was the work published?	11/11/2022
Was the work subject to academic peer review?	Yes
Have you retained the copyright for the work?	No
[If no, please seek permission from the relevant publisher and check the box next to the below statement]:	
☒ *I acknowledge permission of the publisher named under 1b to include in this thesis portions of the publication named as included in 1a.*	

For a research manuscript prepared for publication but that has not yet been published (if already published, please skip to section 3)**:**		
Has the manuscript been uploaded to a preprint server? (e.g. medRxiv):	Please select.	**If yes, which server?** Click or tap here to enter text.
Where is the work intended to be published? (e.g. names of journals that you are planning to submit to)	Click or tap here to enter text.	
List the manuscript's authors in the intended authorship order:	Click or tap here to enter text.	
Stage of publication	Please select.	

For multi-authored work, please give a statement of contribution covering all authors (if single-author, please skip to section 4)**:**
This work is completed by Sanjayan Sathasivam, Mingyue Wang, Claire J. Carmalt and myself. The main part of the work including thin film deposition, characterizations and analysis were carried out by myself. SS and CC provided many useful ideas, advice and supervision. MW calculated the unit cell parameters.

In which chapter(s) of your thesis can this material be found?

Chapter 5			
e-Signatures confirming that the information above is accurate (this form should be co-signed by the supervisor/ senior author unless this is not appropriate, e.g. if the paper was a single-author work):			
Candidate:	Donglei Zhao	**Date:**	17/01/2023
Supervisor/ Senior Author (where appropriate)**:**	██████████████	**Date:**	18/01/2023

UCL Research Paper Declaration Form: referencing the doctoral candidate's own published work(s)

Please use this form to declare if parts of your thesis are already available in another format, e.g. if data, text, or figures:

have been uploaded to a preprint server;

are in submission to a peer-reviewed publication;

have been published in a peer-reviewed publication, e.g. journal, textbook.

This form should be completed as many times as necessary. For instance, if you have seven thesis chapters, two of which containing material that has already been published, you would complete this form twice.

For a research manuscript that has already been published (if not yet published, please skip to section 2)**:**		
Where was the work published? (e.g. journal name)	Click or tap here to enter text.	
Who published the work? (e.g. Elsevier/Oxford University Press):	Click or tap here to enter text.	
When was the work published?	Click or tap to enter a date.	
Was the work subject to academic peer review?	Please select.	
Have you retained the copyright for the work?	Please select.	
[If no, please seek permission from the relevant publisher and check the box next to the below statement]:		
☐	*I acknowledge permission of the publisher named under 1b to include in this thesis portions of the publication named as included in 1a.*	
For a research manuscript prepared for publication but that has not yet been published (if already published, please skip to section 3)**:**		
Has the manuscript been uploaded to a preprint server? (e.g. medRxiv):	No	**If yes, which server?** Click or tap here to enter text.
Where is the work intended to be published? (e.g. names of journals that you are planning to submit to)		
List the manuscript's authors in the intended authorship order:	Donglei Zhao, Jianwei Li, Siyu Zhao, Sanjayan Sathasivam, Yeshu Tan, Guanjie He, Ivan P. Parkin and Claire J. Carmalt	
Stage of publication	Not yet submitted	
For multi-authored work, please give a statement of contribution covering all authors (if single-author, please skip to section 4)**:**		
This work is completed by Jianwei Li, Siyu Zhao, Sanjayan Sathasivam, Yeshu Tan, Guanjie He, Ivan P. Parkin, Claire J. Carmalt and myself. The main part of the work thin film depositions, characterizations and analysis were carried out by myself. JL, SZ and CC provided many useful ideas, advice and discussions during the whole process; CC and SS supervised the work. YT offered		

his help and kind advice for the electrochemical characterizations, GH and IPP have given many useful advice and discussions for the submitted manuscript.

In which chapter(s) of your thesis can this material be found?

Chapter 7

e-Signatures confirming that the information above is accurate (this form should be co-signed by the supervisor/ senior author unless this is not appropriate, e.g. if the paper was a single-author work):

Candidate:	Donglei Zhao	**Date:**	27/07/2022
Supervisor/ Senior Author (where appropriate)**:**		**Date:**	18/08/2022

Abbreviation

AACVD   Aerosol assisted chemical vapour deposition

ALD   Atomic layer deposition

AO   Atomic orbital

APCVD   Atmospheric pressure chemical vapour deposition

ASAP   Atmospheric solids analysis probe

AZO   Aluminium doped zinc oxide

BGN   Band gap narrowing

BM   Burstein-Moss

CBM   Conduction band minimum

CE   Counter electrode

CV   Cyclic voltammetry

CVD   Chemical vapour deposition

CPS   Counts per second

ECSA   Electrochemical surface area

EDS   Energy dispersive X-ray spectroscopy

EIS   Electrochemical impedance spectroscopy

FTO   Fluorine doped tin oxide

FWHM   Full width at half maximum

FZO   Fluorine doped zinc oxide

GZO   Gallium doped zinc oxide

HER   Hydrogen evolution reaction

HESI   Heated electrospray ionisation

IPA   Isopropyl alcohol

ITO   Tin doped indium oxide

IZO   Indium doped zinc oxide

LCD   Liquid crystal display

LED   Light emitting diode

LPCVD   Low pressure chemical vapour deposition

LSV   Linear sweep voltammetry

MO   Molecular orbital

NF   Nickel foam

NIR   Near infrared

OER   Oxygen evolution reaction

ORR   Oxygen reduction reaction

PLD   Pulsed laser deposition

PVD   Physical vapour deposition

RDE   Rotating disk electrode

RE   Reference electrode

RHE   Reversible hydrogen electrode

SEM   Scanning electron microscopy

TCO   Transparent conducting oxide

THF   Tetrahydrofuran

TM   Transition metal

TMP   Transition metal phosphides

TMS   Transition metal sulfides

UV   Ultraviolet

VBM   Valence band maximum

XPS   X-ray photoelectron spectroscopy

XRD   X-ray difraction

Table of Contents

List of Figures

List of Tables

Chapter 1 Introduction

1.1 General introduction

This thesis describes functional thin films, namely transparent conducting oxides (TCOs) and catalyst for thin films for oxygen evolution reaction (OER), prepared though aerosol assisted chemical vapour deposition (AACVD). TCO materials are unique semiconductors that combine both low resistivity and high transmittance simultaneously. The catalytic films used in the OER are electrocatalysts used for the water splitting to generate green renewable energy in the form of hydrogen.

AACVD is a specilised form of CVD used to grow thin films. It utilizes aerosol droplets to transfer precursors into the vapor phase and is the deposition technique used in this work. AACVD has several advantages, over traditional CVD, including easily control of morphology, stoichiometry, film thickness, ambient pressure process, simple operation and low cost. In this project, AACVD has been used to prepare several functional thin films, including Mo-, P- and B-doped ZnO thin films as n-type TCOs, BP thin film as a p-type TCO and P-doped MoS_2 thin films as an electrocatalyst for OER.

TCO materials have two conductivity types, which are known as n-type and p-type. In the current market, tin doped indium oxide (ITO) and fluorine doped tin oxides (FTO) are the most widely used n-type TCO materials resulting from their outstanding electrical (~ 10^{-4} Ω.cm) and optical (> 80%) properties.[1–6] ITO dominates as the electrode of choice for the electronic devices such as solar cells and liquid crystal displays.[7] However, there are issues related to indium that make ITO expensive.[8,9] Indium's concentration in the earth's crust is low at 0.052 ppm (copper for example is ~27 ppm) but the supply issues arise from the limited knowledge of current and future indium as well as the fact indium is a 'by-products metal' during zinc production – leading to price fluctuations.[7] FTO is not prone to such problems as tin is more abundant than indium and is not a 'by-products metal'. However FTO suffers from intrinsic conductivity limitations therefore alternative TCO systems to both ITO and FTO need to be investigated.[9]

Zinc oxide (ZnO) has been considered as one prospective alternative n-type TCO thin

film and there have been many investigations on this material due to advantages such as abundant source, low cost, low toxicity and relatively wide band gap. Undoped ZnO is an intrinsic n-type conductor with relatively high resistivity, and hence doping cations into ZnO crystals is a common and useful method to reduce the resistivity to ~ 10^{-3} - 10^{-4} Ω.cm level, achieved due to increased free electrons from the cation dopants leading to higher bulk concentration.

P-type TCO materials are also useful in many areas, such as transparent diodes, photovoltaic, photocatalytic, solar cell and p-n heterojunctions. Boron phosphide (BP) thin films have relatively high chemical and physical stability, including high melting point and decomposition temperature with a narrow band gap. Both n-type and p-type BP thin films have been reported previously, which suggests BP can be used widely in the p-n heterojunctions area.

Water splitting can be divided into two half-reactions, hydrogen evolution reaction (HER) and oxygen evolution reaction (OER). The OER is the main efficiency limiting process for water splitting and therefore has drawn a lot of research attention to overcome the bottle neck. The current widely used catalysts are noble metal oxides, such as RuO_x and IrO_x, and therefore alternative materials are required to reduce the cost. Transition metal sulfides, including molybdenum sulfide (MoS_2) based thin films is considered an emerging alternative OER electrocatalysts.[10]

To establish the background for the research in this thesis, this chapter will introduce and discuss the functional materials of relevance here, such as both n-type and p-type TCO materials and electrocatalysts for HER and OER. In Chapter 2, film preparation routes including the main film synthetic route in this investigation, AACVD, as well as some general characterization techniques will be discussed. Following on from Chapter 2, several chapters to display and discuss the results of all of the research projects that have been completed during the PhD study period will be described.

1.2 Transparent conducting oxide (TCO) materials

1.2.1 Introduction

Transparent conducting oxides (TCOs) are metal oxide thin films that have attracted much attention and are an important component in many widely used devices in recent years, such as solar cells, touchscreens, screen displays, LCD panels and OLEDs, shown in Figure 1.1. [2,3,11,12] They have both low metal-like electrical resistivity ($< 10^{-3}$ Ω.cm) and high transmittance ($> 80\%$) in the visible area (~ 400 - 700 nm).

The first TCO thin film reported was cadmium oxide (CdO), which was grown via thermally oxidizing a vacuum sputtering method by Badeker in 1907.[3,6] However, TCO materials were not widely used for a long time based on the high toxicity of CdO films.[3,6] During World War II, antimony (Sb) doped tin oxide (SnO_2) thin films started to be used as TCO materials on aircraft windshields on a large scale.[6] Since 1957, TCO materials have developed significantly and are seen everywhere in our daily life through industrial production.[3] The most important TCO material in the past 60 years on the market is Sn doped In_2O_3 (usually known as ITO), which has taken $\sim$ 90% of the current display market.[6]

To understand how TCOs are able to function it is important to understand some key concepts such as band theory and the Drude model.

Figure 1.1: The application of TCOs in a) solar cells, b) flat panel displays, c) OLED touchscreens.

1.2.2 Band theory

Band theory is a theoretical model that explains the electrical and optical properties of solids such as semiconductors. Since electrons in an isolated atom are found in atomic orbitals at discrete energy levels, the electrons in a molecule that is made of atoms occupy molecular orbitals of discreet energy. In a solid, where the number of atoms tends towards infinity the number of overlapping orbitals towards infinity. As the number of energy levels increases the separation between them decreases and tends towards zero such that a continuum of energy levels is formed called bands.
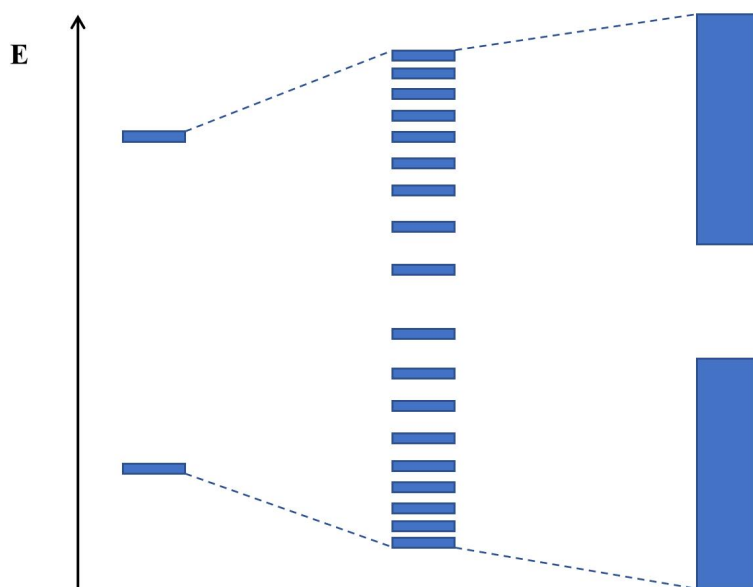
Figure 1.2 : Schematic of molecular orbitals forming bands with increasing atomic orbitals.

The highest occupied band is called the valence band and the lowest unoccupied band is called the conduction band. The energy separation between the highest occupied molecular orbital (HOMO) i.e. the top of the VB and the lowest unoccupied molecular orbital (LUMO) i.e the bottom of the CB is called the band gap (E_g). The energy of the highest occupied energy level at absolute zero is known as the Fermi level, E_F. For conductors such as metals, E_F and the CBM is usually lower in energy than the VB maxima. This means that electrons can become readily thermally excited

from the VB to the CB as there is E_g resulting in low resistivity. For insulators such as Al_2O_3, there is a relatively large band gap E_g between the VB maxima and the CB minima such that the probability of finding electrons in the CB is very low and thus resistivity is high. The E_g for insulators is so large that they do not show good electric conductivity even under extreme conditions.

Semiconductors have electrical properties between that of a conductor and an insulator. The E_g for semiconductors is wider than conductors but narrower than insulators. In normal cases (i.e intrinsic), semiconductors cannot show sufficient electrical conductivity, since minimal excitation across the band gap occurs at room temperature. However, a semiconductor can obtain low resistivity under some conditions, for example when heated or irritated with photos with energy above the band gap energy. A semiconductor can also more easily exhibit conductivity at room temperature when doped either intrinsically (e.g oxygen vacancies) or extrinsically (substitutionally through donor atoms). Furthermore, the band gap of a semiconductor also has significant influence on the optical performance including transmittance and colour. The larger the band gap, the more photons of the electromagnetic spectrum that can be transmitted through the material. In order to combine the properties of high optical transmittance and high electrical conductivity to obtain TCOs, a semiconductor needs to have a sufficiently large band gap and be doped to increase the electron concentration in the conduction band.

1.2.3 Semiconductor

There are two types of degenerately doped semiconductors based on two types of doping regimes. These are classified as n-type and p-type semiconductors. There are two strategies to achieving n-type or p-type conductivity – 1) by using extrinsic dopants i.e introduction of impurities into the host material or 2) by intrinsic means such as oxygen vacancies or metal interstitials. Since route 2 is not viable for practical applications of TCOs, only route 1 will be discussed in detail.

Doping impurities into the crystal lattice is the main method to modify semiconductor materials for improved electrical and optical properties. The role of the dopants is to increase the bulk carrier concentrations leading to lower resistivities of the modified semiconductors. The types of doping can be divided into substitutional doping (substituting for ions of the semiconductor) and interstitial doping (dopants atom occupies a normally unoccupied site in the semiconductor crystal structure), which is shown in Figure 1.3.

(a)   (b)
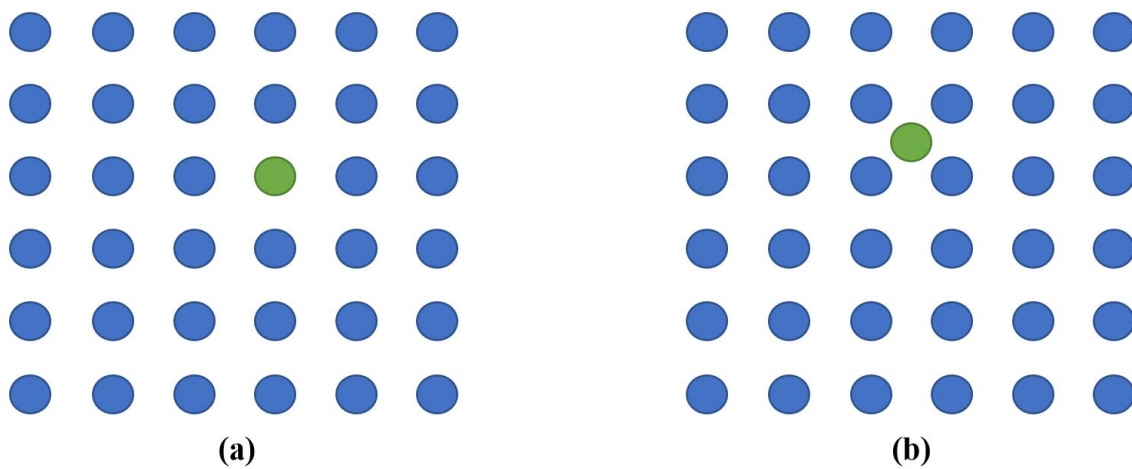
Figure 1.3: Schematic indication for the (a) substitutional doping and (b) interstitial doping.

For undoped semiconductors, known as intrinsic semiconductors (i-type semiconductors), the electrical properties including carrier concentration and mobility are only dependent on the semiconductor itself. This type of semiconductor has a E_g determined by the original distance of the VBM and the CBM, which often cannot obtain satisfactory electric conductivity at room temperature.

For n-type semiconductors, the key charge carriers are negative electrons and the dopant atoms have relatively higher valence states than the bulk atoms to offer at least one electron to the conduction band.[11] The increased number of free electrons from doping can form discrete energy levels called donor levels, which are very close to the CBM. The distance of the energy gap between the donor level and the CBM tends to be much lower than between the CBM and VBM and hence electrons can be easily excited. The n-type semiconductors usually have much higher bulk concentrations

after doping relatively high valence dopants into the base n-type materials.

For p-type semiconductors, the key charge carriers are positive holes and most dopant atoms in them have relatively lower valence states than the bulk atoms, which can cause an electronic defect to form an acceptor level resulting from the introduction of unoccupied energy level higher than the valence band.[11] Similarly, the acceptor level is very close to the VBM and the new energy gap between the acceptor level and the VBM is also much lower than between the CBM and VBM, resulting in more easily exciting electrons. As the dopants concentrations are quite low in the semiconductors, both the donor levels in n-type materials and acceptor levels in p-type systems cannot be considered as bands and usually are known as inter-band atomic states that allow for the hopping of charge.
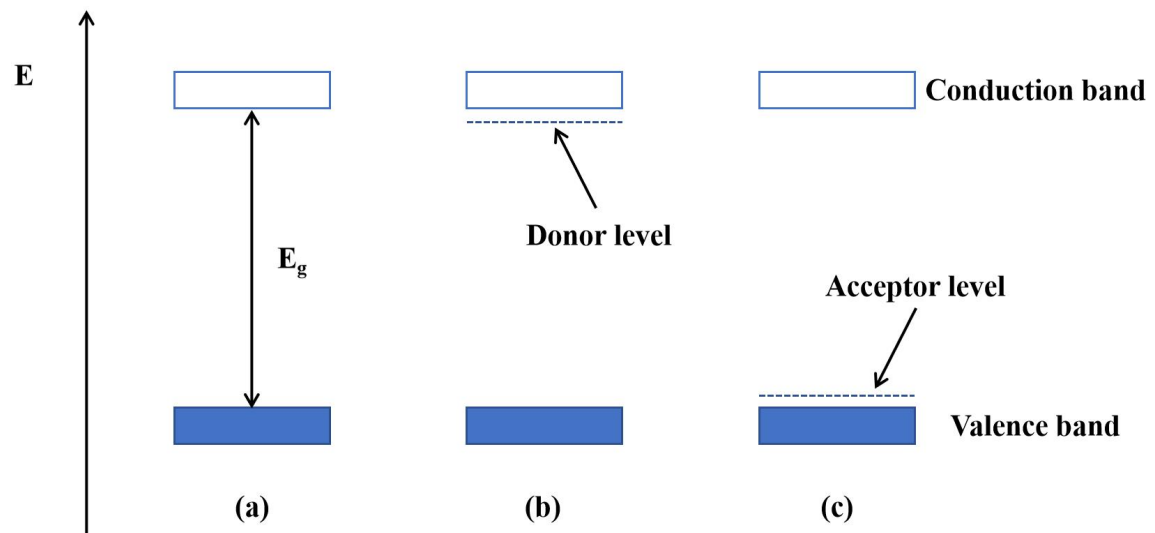
Figure 1.4: Band gap illustration for the (a) undoped semiconductors, (b) n-type semiconductors and (c) p-type semiconductors.

In general, both n-type and p-type semiconductors using different types of dopants can reduce the excitation energy for free electrons from the VB to the CB based on the formation of donor levels (n-type) or acceptor levels (p-type). These are much lower than the original E_g causing low resistivities for the doped semiconductors at room temperature, as displayed in Figure 1.4.

The conductivity of charge carriers in semiconductors follows the Drude model - a classical model of electrical conductivity of electrons in metals. In the Drude model,

the movement of electrons in a solid is considered in classical mechanics terms, ignoring quantum mechanical properties. Electrons are scattered randomly by lattice ions and these collisions result in loss of momentum and a finite mean free path.

The conductivity is proportional to the concentration of the carriers (e.g. electrons) and their velocity.

As the resistivity (ρ) can be known as:

$$\rho = \frac{1}{\sigma} = ne\mu \qquad (1.01)$$

Where:

σ is conductivity

n is bulk concentration,

μ is carrier mobility

e is charge on electron

the higher n and μ values the lower the resistivity. The addition of suitable donor dopants into semiconductors leads to the increase in bulk concentration therefore resulting in lower resistivity. In these circumstances, doping has become one of the most important methods to combine both optical and electrical properties through adjusting the actual band gaps of semiconductors and form transparent conducting oxides (TCO) materials widely used in the optoelectronic areas.

In addition, doping also can influence the optical properties of semiconductors based on the Burstein–Moss (BM) effect and band gap narrowing (BGN) effect. The Burstein–Moss (BM) effect, shown in Figure 1.5, leads to band gap widening on the basis of the blocking of low-energy transitions resulting from the Fermi exclusion principle.[13,14]

On the contrary, due to the correlated motion of the charge carriers and their scattering against ionized impurities, the modification of electronic states happens in the crystal causing many-body effects resulting in band gap renormalization (band

gap narrowing effect).[13,14]

The Burstein–Moss effect is competitive with the band gap narrowing effect, which has the main influence of the optical band gap of doped semiconductors.[13,14]
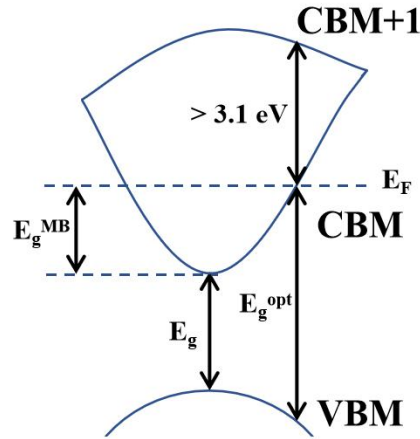
Figure 1.5: Diagram of the Moss–Burstein effect causing band gap widening, where E_g is energy gap between the VBM and the CBM, E_g^{MB} is the energy shift resulting from the Moss–Burstein effect, E_g^{opt} is the smallest optical band gap for the optical transitions from the VB to the CB and EF is the Fermi level.

1.2.4 n-type TCO materials

For n-type TCO materials, the most widely investigated and commercially used thin films are based on indium oxide (In_2O_3), tin oxide (SnO_2) and zinc oxide (ZnO).

The crystal structure of pure In_2O_3 is cubic, as shown in Figure 1.6,[15] where there are two inequivalent In^{3+}. In both cases the In^{3+} are bound to six O^{2-} to form distorted corner and edge sharing octahedra. However, in one case the corner sharing octahedral tilt angle ranges from 54-55° and the bond distances range from 2.14-2.23 Å whereas in the second case the tilt angle of the corner sharing octahedral is 54° and the bond distances are 2.19 Å, Sn doped In_2O_3 (ITO) is formed by the substitution of In^{3+} by Sn^{4+} in the tetrahedral interstitials through the doping method. After doping,

ITO retains the cubic bixbyite structure with some unit cell expansion resulting from the larger ionic radius of Sn^{2+} (0.93 Å) compared with that of In^{3+} (0.79 Å).

The dopant Sn can increase the bulk electron concentration to reduce resistivity as well as cause an upward shift of the Fermi level leading to an increase of the optical band gap from ~ 3.75 eV to ~ 4.2 eV at room temperature.[16] This leads to a wider optical window and improved optical properties resulting from the Burstein-Moss effect.[5]

For the theoretical mechanism regarding the excellent electrical properties of ITO materials, there are three s-like impurity bands that can be found after one Sn atom is doped into the In_2O_3 lattice via substitutional doping, one of the bands contains the Fermi level like metal and has overlap with the conduction band[3,17,18] resulting in quite low resistivities. In addition, impurity phases including SnO, SnO_2 and Sn_2O_4 may be formed when the Sn content increases, which results in a lower band gap at ~ 4.1 eV leading to lower optical transmittance.[19] Thus, the Sn dopants should be controlled very carefully, for example, to produce ITO films on a large scale, sintered ceramic In_2O_3 with ~3-10 wt% SnO_2 dopant concentration is a common ratio used.[4]

The oxygen partial pressure also has a significant effect on the electrical properties of ITO thin films based on the formation of doubly charged oxygen vacancies besides the normal Sn^{4+} substitution. Competition can be seen between the substituting Sn^{4+} and neutral oxides, which suggests that not all Sn dopants contribute additional free electrons without reaching the solubility limit.[4,20] Both amorphous ITO (a-ITO) and crystalline ITO (c-ITO) have been used in the display area, and prepared via RF or DC magnetron sputter deposition methods at ~ 250 - 350 °C .[4]
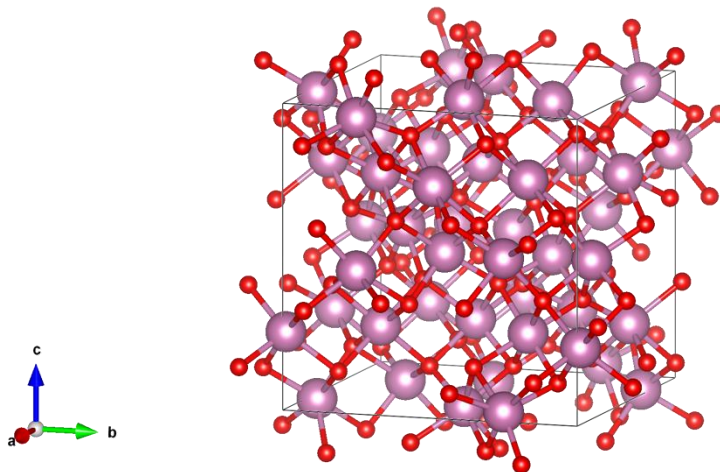
Figure 1.6: Crystal structure of In_2O_3 (ICSD #14387).

Fluorine doped tin oxide (FTO) is a widely used TCO material. Pure tin oxide (SnO_2) can adopt the tetragonal rutile structure with Sn^{4+} bonded to six equivalent O^{2-} atoms to form corner and edge sharing SnO_6 octahedra, shown in Figure 1.7.[21] The corner sharing octahedra have a tilt angle of 51°. There are two bond lengths of two 2.06 Å and four 2.07 Å. O^{2-} found in trigonal planar coordination with three Sn^{4+} atoms that are all equivalent.

The lattice size of FTO is a little smaller than that of pure SnO_2 resulting from the smaller ionic radius of F^- (1.17 Å) than O^{2-} (1.22 Å). Similar to ITO materials the optical properties improve due to the band gap of FTO increasing significantly from about 3.6 eV to 4.2 eV at room temperature, as a result of the Burstein-Moss effect.[5] For SnO_2 based materials, the Sn interstitials can fill in the conduction band besides oxygen vacancy and form defect structures of SnO_2, leading to n-type TCO materials with shallow donor levels.[4,22,23]

FTO thin films can be produced through spray pyrolysis deposition from organometallic precursors or chlorides on a large scale with relatively low cost for both original materials and production process, which are used as coatings in efficient windows in many constructions.[4] The best electrical properties of FTO films are displayed at $\sim 6 \times 10^{-4}$ Ω.cm resistivity, $5 - 8 \times 10^{20}$ cm^{-3} bulk concentration and 20 cm^2 V^{-1} s carrier mobility, respectively.[4]
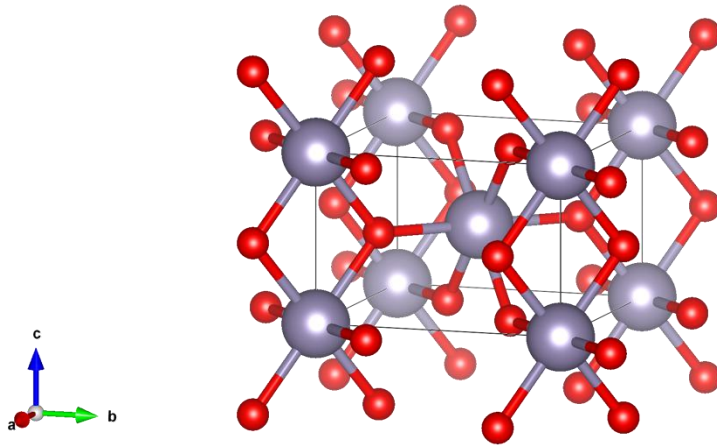
Figure 1.7: Crystal structure of SnO$_2$ (ICSD #9163).

With the development of the optoelectronic market, the demand for TCO materials is increasing. However, the most commonly used TCO materials, namely ITO thin films, which makes up >90% of the display area,[24] may suffer from a shortage of materials in future years due to the relatively low reserves of In and Sn in the earth.[3] Based on this, the cost of the In source has increased rapidly, for example some reports have indicated that there was a ~10× increase in the price of In in recent years.[3] Thus, the potential of the widely used In based TCO materials may be limited and alternative TCO materials with lost cost need to be investigated. In the recent years, zinc oxide (ZnO) based n-type TCOs thin films have attracted much attention due to advantages including being non-toxic and relatively low cost compared to the most widely used TCOs materials mentioned before, such as ITO thin films.

ZnO can adopt a hexagonal wurtzite crystal structure shown in Figure 1.8.[25] Corner sharing ZnO$_4$ tetrahedra are formed when Zn^{2+} is bonded to four equivalent O^{2-}. There are three shorter bond lengths of 1.97 Å and one longer bond of 1.97 Å. The O^{2-} are also in tetrahedral geometry in the form of corner sharing OZn$_4$.[3] ZnO is stable under H$_2$ plasma i.e it will not get reduced by H$_2$ like some other metal oxides such as SnO$_2$. This is because H$_2$ can reduce the oxides of less electropositive metals such as Sn but not the oxides of more electropositive metals such as Zn. H$_2$ plasma is used in the production of thin film Si Solar cells. ZnO is an appropriate TCO for thin film Si solar

cells as ZnO can withstand H_2 plasma treatment that is necessary for the solar absorber layer fabrication.[3,26] ZnO also has a relatively wide band gap at ~ 3.37 eV (via the spectroscopic elliposometry)[27] or ~ 3.27 eV (via the Tauc method from the UV-visible spectroscopy data),[28–34] which suggests ZnO has good optical transmittance to be used as n-type TCO materials.
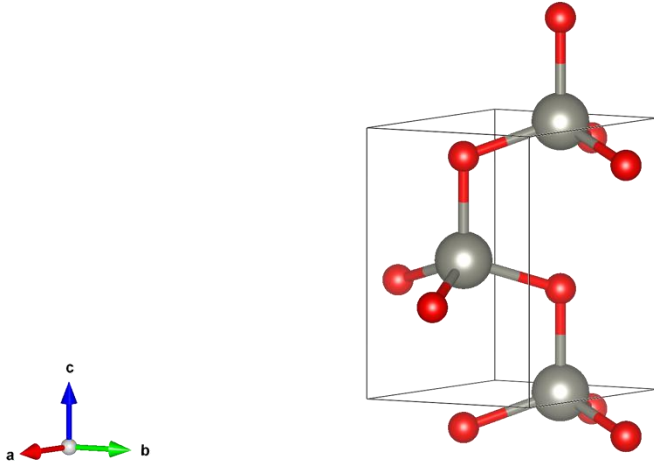
Figure 1.8: Crystal structure of ZnO (ICSD #26170).

ZnO is considered an intrinsic n-type TCO material. There have been some investigations regarding intrinsic n-type conductivity. Initially some studies reported that oxygen vacancies may cause donor defects,[35–37] with oxygen vacancies as a deep donor without many free carriers resulting from the large ionization energy.[38,39] However, adventitious hydrogen or carbon acting as shallow donors is considered as a source of intrinsic n-type conductivity of ZnO thin films.[3,34,39,40] For the nominally undoped ZnO, the resistivity is too high to be applied in electronic devices. Extrinsic donor dopants are often required to decrease the resistivity to the ~ 10^{-3} Ω.cm threshold necessary for practical application.

Based on the substituting hydrogen donor model,[16] doping elements from Groups 3 and 13 (such as Sc^{3+}, Y^{3+}, La^{3+}, B^{3+}, Al^{3+}, Ga^{3+} and In^{3+}), results in allowed levels lying close to the conduction band (EC) edge and the valence band (EV) edge[16]. There have also been several investigations reported for the Groups 4 and 14 dopants such as Ti, Zr, Hf, Si, Ge and Sn and high oxidation state dopants (Mo, P, W) and anions

dopants (Cl, F).

The cation dopants have a higher valence than Zn^{2+}, which can offer more free electrons to improve bulk concentrations leading to relatively lower resistivities. For cation doping, the resistivities likely tend to decrease initially and then increase again when the solubility limit of the dopants elements has been reached.[41,42] Moreover, the crystal parameters including cell volume will change after doping based on the different ionic radii between dopants ions and Zn^{2+} or O^{2-} ions.

For example, Al a typical dopant used to reduce resistivities of ZnO thin films from different Zn source and synthetic routes. The ZnO:Al thin films grown from zinc acetate dihydrate ($[Zn(OAc)_2 \cdot 2H_2O]$) via sol-gel method,[43] zinc acetylacetonate ($[Zn(acac)_2]$) via AACVD[44] and [ZnO] powder via RF magnetron sputtering[45] have been reported and exhibited good electrical and optical properties at 7.08×10^{-3} Ω.cm (T > 80% in visible area), 5×10^{-3} Ω.cm (T > 80% in visible area) and 5.6×10^{-4} Ω.cm (T ~ 80% in visible area), respectively.

In comparison to cation doping, anion doping of ZnO materials has been much less studied. Most reports used F as the anion dopant,[46–50] which were introduced into ZnO thin films to obtain more free electrons. The F atom dopants will replace O atoms since they have similar ionic radii. The element Cl is another possible anion dopant for the ZnO based thin films. From the $[Zn(OAc)_2 \cdot 2H_2O]$ precursor and AACVD technology, ZnO:Cl thin films have been investigated to reach 4.28×10^{-2} Ω.cm[51] and $2.72 \pm 0.04 \times 10^{-3}$ Ω.cm[52] as resistivities with visible transmittance at > 80% and ~ 82%, respectively.

According to some investigations, doping ZnO thin films with more than one kind of dopant also may result in enhanced electrical properties, which has been called co-doping. The co-dopants can be divided into cation/cation and cation/anion. For example, Al/Ga,[53] Al/In[53] and Ga/In[53] were used as cation/anion co-dopants in ZnO thin films with improved properties, while Al/F,[54] Ga/F[55] and In/F[56] were also used as cation/anion co-dopants to further improve the performance of the TCO materials. For the cation/cation type, the solubility limit of the total dopants is higher than the solubility limit of each cation. For the cation/anion type, the cation and anion can

replace Zn^{2+} and O^{2-}, respectively, which is predicted to produce more free electrons than that of only one dopant resulting in higher bulk concentrations and lower resistivities.

There are a few reports of p-type ZnO based materials, which results from the low thermodynamic stability of p-type ZnO and that p-type ZnO thin films will transform to the n-type ones within only a few days.[57]

Generally, ZnO based thin films can be considered as one of the most promising alternative n-type TCO materials as replacements for the current commonly used n-type ITO and FTO based TCO materials, which could have significant commercial applications in the optoelectronic devices areas.[58]

1.2.5 p-type TCOs materials

Since the first p-type TCO thin film was reported in 1993,[6,59] p-type TCO materials have started to play an important role in TCO materials and can be widely used in many areas, such as transparent diodes with rectifying behavior.[60,61] In combination with n-type TCO thin films to form p-n heterojunctions, they are used in a range of key applications such as for photovoltaic, photocatalytic, solar water splitting and p-n heterojunctions diodes.[6,61] However, in contrast to n-type TCO materials, p-type TCO materials have been limited to be produced and applied in large scale based on several significant challenges.[6,62,63] For example, it is hard to produce shallow acceptors and large hole effective masses resulting from the relatively high electronegativity and small radius of the oxygen atoms,[6] which may lead to the intrinsic electronic structure of metal oxides formed through the localized O 2p orbitals.[6,64,65] Furthermore, the positive holes after doping will be located on these oxygen atoms, which may not migrate within the crystal lattice under an applied electric field.[61]

Formation of extended valence band structures to induce the co-valency in the metal oxygen bonding may be considered as one possible solution, which has been known as chemical modulation of the valence band (CMVB), and was first investigated in

1997.[6,61,65] The CMVB method works based on the hybridization of O $2p^6$ orbitals and Cu $3d^{10}$ orbitals.[6,65] Due to the energy levels of O $2p^6$ and Cu $3d^{10}$ being similar, covalent bonding between these two orbitals can be formed which causes relatively high dispersion at the top of valence band leading to a decrease of localization of positive holes. Moreover, the $3d^{10}$ orbitals of Cu are closed shell, which helps maintain transparency through avoiding the opaque colour from the d-d excitation. According to this method, a series of Cu^+ based materials have been prepared and reported, such as $CuCrO_x$,[66,67] $CuAlO_2$,[65,68] $CuInO_2$,[69] $CuScO_2$[70] and $SrCu_2O_2$.[71]

There are also some p-type TCOs thin films that do not contain Cu^+ based materials. For example, Cr_2O_3:Ni thin film deposited using pulsed laser deposition (PLD) was shown to have a conductivity of 28 $S.cm^{-1}$ and used as a TCO thin film[72] while $La_{2/3}Sr_{1/3}VO_3$ thin film from molecular beam epitaxy had a conductivity of 54 $S.cm^{-1}$ for use as TCO electrodes.[73]

Thus, although some p-type TCO thin films have been prepared in the laboratory,[74] there are still many challenges that have limited the applications of p-type TCO materials on the large scale, and it is necessary to investigate more functional p-type TCO materials.

1.2.6 p-n heterojunctions

Potential materials for the electronics and optoelectronics areas include p-n heterojunctions formed through both n-type and p-type TCO materials, which contain different types of functional materials and have a heterojunction interface resulting in multifunctional properties with high performance.[75]

There are several typical structures for p-n heterojunctions, such as bilayer, cross-stacked, multi-segmented, core–shell, and branched structures.[75] The p–n heterojunction TCO materials have some advantages including low cost, simple and low energy consumption process, light weight and abundant original resources.[75–79]

For example, heterojunction diodes can be known as one important application for

heterojunctions. The p-n heterojunctions with Mg-doped ZnO as the n-type layer and Si as the p-type layer grown via atmospheric pressure chemical vapour deposition (APCVD) have been studied and with diode parameters at 1.43 - 2.92 as ideality factor (η) used as heterojunction diodes.[80] Moreover, there are some other heterojunction applications such as solar cells, photocatalysis and photodetectors. The heterojunctions formed by $SrTiO_3$:Nb (n-type) and NiO:Li (p-type) through PLD route were reported to be used as photocatalysis and photodetectors with 4.3 as ideality factor and 2×10^3 as rectification ratio.[81]

Although some p-n heterojunctions have been applied in the optoelectronic areas, there are still many challenges for the controllable production in large scale.[75]

1.3 Electrocatalyst materials

1.3.1 Renewable energy

Fossil fuel is considered as the main energy source in current society, which offers ~85% of electrical energy.[82] However, fossil fuel is a non-renewable energy and cannot meet the increasing energy demands in the future. For example, the reserves of coal, oil and natural gas, which are known as the most widely used fossil fuels, may only be available for ~ 150 - 400 years, ~ 40 - 80 years and ~ 60 - 160 years, respectively.[83] Thus, fossil fuel does not have a satisfactory prospect to meet with rapid development and requires ample alternative renewable energy sources to be developed.

In addition, the traditional fossil fuel produces a large amount of greenhouse gases, such as carbon dioxide (CO_2) during the burning process, which may be one important cause of the increasing temperature in recent years and has significant influence on the global environment. In order to the avoid the devastating effect on ecosystems resulting from the high temperature environment, the consumption of fossil fuel needs to be continuously decreased and replaced by green energy sources.

1.3.2 Hydrogen energy from water splitting

1.3.2.1 General introduction

There are several kinds of green renewable energy sources that have attracted much attention recently, such as solar, wind and hydrogen energy. Electrocatalytic water splitting is a prospective strategy for the production of renewable hydrogen energy, which in turn could reduce the contradiction between the energy crisis and environmental pollution.[84–90] The process of water splitting exhibited in Figure 1.9 is made up of two half-reactions, namely the hydrogen evolution reaction (HER) and the oxygen evolution reaction (OER).[84,90–92] Due to the OER being a four-electron

transfer reaction while the HER is only a two-electron transfer reaction, the OER is the main speed-limiting process, which can reduce the efficiency of water splitting and requires suitable electrocatalysts to accelerate the process.[84,90,93]
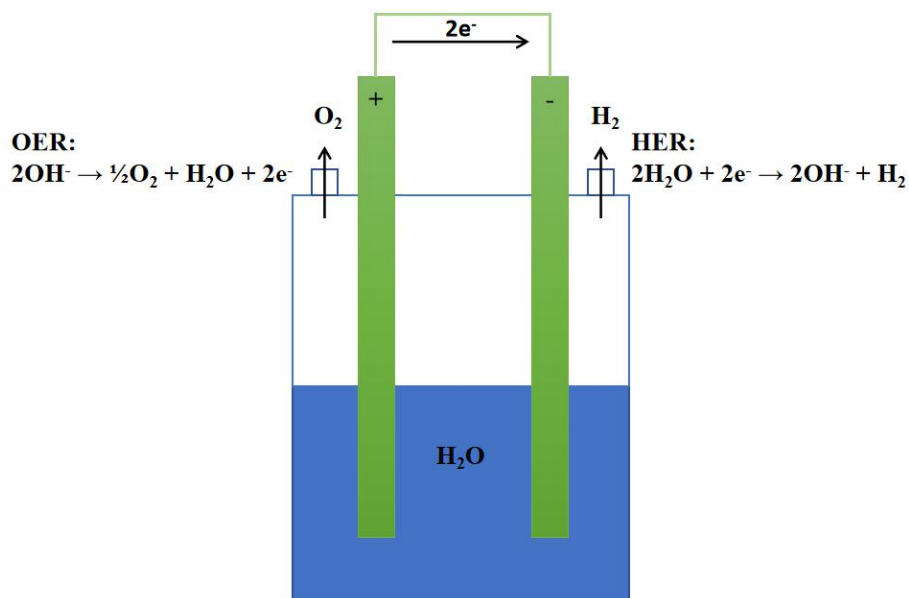
Figure 1.9: The schematic representation for the electrocatalytic water splitting.

1.3.2.2 OER in alkaline medium

The thin films prepared in this project (Chapter 7) are only used to accelerate OER in alkaline medium. Therefore, the introduction will also focus on the mechanism of OER in alkaline medium.

For the hall cell equations of HER and OER in alkaline media:

HER: $2H_2O + 2e^- \rightarrow 2OH^- + H_2$ (1.02)

OER: $4OH^- \rightarrow O_2 + 2H_2O + 4e^-$ (1.03)

Overall: $2H_2O \rightarrow 2H_2 + O_2$'   (1.04)
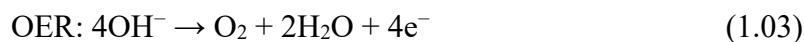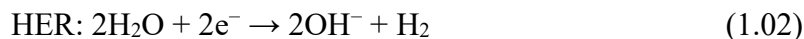
As mentioned above, OER is the half reaction of water splitting with four-electron transfer and the mechanism of OER in alkaline environment can be divided into five steps.

Step 1 is to absorb OH species and generate MOH species (M is metal, provides active sites for catalysis):

$M + OH^- \rightarrow MOH + e^-$ (1.05)

The active sites of the catalytic materials can obtain oxygen species to produce MO

from the reaction between MOH and OH⁻ species, as shown in **Step 2**:

$$MOH + OH^- \rightarrow MO + H_2O + e^- \tag{1.06}$$

Then, **Step 3** produces O_2 based the combination of the MO species:

$$2MO \rightarrow 2M + O_2 \tag{1.07}$$

At the same time as Step 3, **Step 4** produces MOOH as an intermediate from MO and OH⁻:

$$MO + OH^- \rightarrow MOOH + e^- \tag{1.08}$$

Finally, oxygen can be formed from MOOH in **Step 5**:

$$MOOH + OH^- \rightarrow M + O_2 + H_2O + e^- \tag{1.09}$$

1.3.3 Electrocatalyst for OER

Noble metal oxides, including RuO_2 and IrO_2, are well known OER catalysts with rutile structure that display excellent activities. One of the key attributes for achieving high OER results is high surface area-to-mass ratios of the electrocatalyst that minimise the overpotential.[94,95] However, the commercial applications of these catalysts on the large scale have been limited due to their high price, scarcity and low stability.[89,96] Hence, it is necessary to find alternative materials with specific advantages such as low cost, long time stability and high catalytic performance. There have been many reports describing non-precious electrocatalysts for OER, including transition metal oxides,[97–99] sulfides,[100] phosphides,[101] nitrides,[102] hydroxides[103] and carbon-based materials.[104]

For example, (Mo, Fe)P_2O_7 on Ni foam (NF) was investigated as an efficient electrocatalyst, which was known as the derivatives of high catalytic Prussian blue analogues (PBAs) material, with relatively low overpotential of 290 mV at high current density at 600 mA cm⁻² in alkaline medium.[105]

Moreover, transition metal based catalytic materials have attracted many attention due to advantages, such as low cost, easily modified electronic structures and relatively high catalytic properties. The functional thin film with OER catalytic activity

prepared through AACVD in this project is a transition metal sulfide based material and belongs to the transition metal based materials.

1.4 Project Aims

The main aim of this thesis is the exploration of strategies to enhance the functional properties of thin film materials, namely TCOs based on ZnO and OER electrodes based on MoS_2. The strategy employed involves the study of extrinsic dopants to improve the optoelectronic properties of ZnO TCOs and the electrochemical properties of MoS_2. All materials have been synthesized using the AACVD approach which is industrially and commercially relevant.

1.5 References

(1)   Dixon, S. C.; Scanlon, D. O.; Carmalt, C. J.; Parkin, I. P. N-Type Doped Transparent Conducting Binary Oxides: An Overview. *J. Mater. Chem. C* **2016**, *4* (29), 6946–6961. https://doi.org/10.1039/c6tc01881e.

(2)   Minami, T. Transparent Conducting Oxide Semiconductors for Transparent Electrodes. *Semicond. Sci. Technol.* **2005**, *20* (4). https://doi.org/10.1088/0268-1242/20/4/004.

(3)   Mallick, A.; Basak, D. Revisiting the Electrical and Optical Transmission Properties of Co-Doped ZnO Thin Films as n-Type TCOs. *Prog. Mater. Sci.* **2018**, *96*, 86–110. https://doi.org/10.1016/j.pmatsci.2018.03.004.

(4)   Delahoy, A. E.; Guo, S. Transparent Conducting Oxides for Photovoltaics. *Handb. Photovolt. Sci. Eng.* **2011**, *32* (MARCH 2007), 716–796. https://doi.org/10.1002/9780470974704.ch17.

(5)   Chopra, K. L.; Major, S.; Pandya, D. K. Transparent Conductors—A Status Review. *Thin Solid Films* **1983**, *102* (1), 1–46. https://doi.org/https://doi.org/10.1016/0040-6090(83)90256-0.

(6)   Zhang, K. H. L.; Xi, K.; Blamire, M. G.; Egdell, R. G. P-Type Transparent Conducting Oxides. *J. Phys. Condens. Matter* **2016**, *28* (38). https://doi.org/10.1088/0953-8984/28/38/383002.

(7)   Werner, T. T.; Mudd, G. M.; Jowitt, S. M. Indium: Key Issues in Assessing Mineral Resources and Long-Term Supply from Recycling. *Inst. Min. Metall. Trans. Sect. B Appl. earth Sci.* **2015**, *124* (4), 213–226. https://doi.org/10.1179/1743275815Y.0000000007.

(8)   Zepf, V. *Materials Critical to the Energy Industry : An Introduction / Volker Zepf ... [et Al.].*, 2nd ed.; BP: London, 2014.

(9)   Swallow, J. E. N.; Williamson, B. A. D.; Whittles, T. J.; Birkett, M.; Featherstone, T. J.; Peng, N.; Abbott, A.; Farnworth, M.; Cheetham, K. J.; Warren, P.; Scanlon, D. O.; Dhanak, V. R.; Veal, T. D. Self-Compensation in

Transparent Conducting F-Doped SnO$_2$. *Adv. Funct. Mater.* **2018**, *28* (4), 1–10. https://doi.org/10.1002/adfm.201701900.

(10)   Kasap, S. O. (Safa O.; Capper, P. *Springer Handbook of Electronic and Photonic Materials / Safa Kasap and Peter Capper (Eds.)*; Springer: New York, 2006.

(11)   Dixon, S. C.; Scanlon, D. O.; Carmalt, C. J.; Parkin, I. P. N-Type Doped Transparent Conducting Binary Oxides: An Overview. *J. Mater. Chem. C* **2016**, *4* (29), 6946–6961. https://doi.org/10.1039/c6tc01881e.

(12)   Godinho, K. G.; Carey, J. J.; Morgan, B. J.; Scanlon, D. O.; Watson, G. W. Understanding Conductivity in SrCu$_2$O$_2$: Stability, Geometry and Electronic Structure of Intrinsic Defects from First Principles. *J. Mater. Chem.* **2010**, *20* (6), 1086–1096. https://doi.org/10.1039/b921061j.

(13)   Moss, T. S. The Interpretation of the Properties of Indium Antimonide. *Proc. Phys. Soc. Sect. B* **1954**, *67* (10), 775–782. https://doi.org/10.1088/0370-1301/67/10/306.

(14)   Burstein, E. Anomalous Optical Absorption Limit in InSb. *Phys. Rev.* **1954**, *93* (3), 632–633. https://doi.org/10.1103/PhysRev.93.632.

(15)   Marezio, M. Refinement of the Crystal Structure of In$_2$O$_3$ at Two Wavelengths. *Acta Crystallogr.* **1966**, *20* (6), 723–728. https://doi.org/10.1107/S0365110X66001749.

(16)   Yu, P. Y. *Fundamentals of Semiconductors : Physics and Materials Properties / Peter Y. Yu, Manuel Cardona.*, 3rd, rev. ed.; Cardona, M., Ed.; Berlin : Berlin , 2001.

(17)   Sberveglieri, G.; Groppelli, S.; Coccoli, G. Radio Frequency Magnetron Sputtering Growth and Characterization of Indium-Tin Oxide (ITO) Thin Films for NO$_2$ Gas Sensors. *Sensors and actuators* **1988**, *15* (3), 235–242. https://doi.org/10.1016/0250-6874(88)87013-6.

(18)   Ito, N.; Sato, Y.; Song, P. K.; Kaijio, A.; Inoue, K.; Shigesato, Y. Electrical and Optical Properties of Amorphous Indium Zinc Oxide Films. *Thin Solid Films* **2006**, *496* (1), 99–103. https://doi.org/10.1016/j.tsf.2005.08.257.

(19)   Kim, H.; Gilmore, C. M.; Piqué, A.; Horwitz, J. S.; Mattoussi, H.; Murata, H.;

        Kafafi, Z. H.; Chrisey, D. B. Electrical, Optical, and Structural Properties of

        Indium–Tin–Oxide Thin Films for Organic Light-Emitting Devices. *J. Appl.*

        Phys. **1999**, *86* (11), 6451–6461. https://doi.org/10.1063/1.371708.

(20)   Frank, G.; Köstlin, H. Electrical Properties and Defect Model of Tin-Doped

        Indium Oxide Layers. *Appl. Phys. A Solids Surfaces* **1982**, *27* (4), 197–206.

        https://doi.org/10.1007/BF00619080.

(21)   Baur, W. H.; Khan, A. A. Rutile-Type Compounds. IV. SiO_2, GeO_2 and a

        Comparison with Other Rutile-Type Structures. *Acta Crystallogr. Sect. B* **1971**,

        27 (11), 2133–2139. https://doi.org/10.1107/S0567740871005466.

(22)   Kılıç, Ç.; Zunger, A. Origins of Coexistence of Conductivity and Transparency

        in SnO_2. *Phys. Rev. Lett.* **2002**, *88* (9), 955011–955014.

        https://doi.org/10.1103/PhysRevLett.88.095501.

(23)   Leng, D.; Wu, L.; Jiang, H.; Zhao, Y.; Zhang, J.; Li, W.; Feng, L. Preparation

        and Properties of SnO_2 Film Deposited by Magnetron Sputtering. *Int. J.*

        Photoenergy **2012**, *2012*. https://doi.org/10.1155/2012/235971.

(24)   Minami, T. Present Status of Transparent Conducting Oxide Thin-Film

        Development for Indium-Tin-Oxide (ITO) Substitutes. *Thin Solid Films* **2008**,

        516 (17), 5822–5828. https://doi.org/10.1016/j.tsf.2007.10.063.

(25)   Abrahams, S. C.; Bernstein, J. L. Remeasurement of the Structure of

        Hexagonal ZnO. *Acta Crystallogr. Sect. B* **1969**, *25* (7), 1233–1236.

        https://doi.org/10.1107/S0567740869003876.

(26)   Hu, J.; Gordon, R. G. Textured Aluminum-Doped Zinc Oxide Thin Films from

        Atmospheric Pressure Chemical-Vapor Deposition. *J. Appl. Phys.* **1992**, *71* (2),

        880–890. https://doi.org/10.1063/1.351309.

(27)   Washington, P.; Ong, H.; Dai, J.; Chang, R. Determination of the Optical

        Constants of Zinc Oxide Thin Films by Spectroscopic Ellipsometry. *Appl. Phys.*

        Lett. **1998**, *72*, 3261–3263. https://doi.org/10.1063/1.121617.

(28)   Segev, D.; Janotti, A.; Van de Walle, C. G. Self-Consistent Band-Gap

        Corrections in Density Functional Theory Using Modified Pseudopotentials.

Phys. Rev. B. Condens. Matter Mater. Phys. **2007**, *75* (3). https://doi.org/10.1103/PhysRevB.75.035201.

(29) Kang, D.; Lee, D.; Choi, K.-S. Electrochemical Synthesis of Highly Oriented, Transparent, and Pinhole-Free ZnO and Al-Doped ZnO Films and Their Use in Heterojunction Solar Cells. *Langmuir* **2016**, *32* (41), 10459.

(30) Bauermann, L. P.; Gerstel, P.; Bill, J.; Walheim, S.; Huang, C.; Pfeifer, J.; Schimmel, T. Templated Self-Assembly of ZnO Films on Monolayer Patterns with Nanoscale Resolution. *Langmuir* **2010**, *26* (6), 3774.

(31) Yumak, A.; Turgut, G.; Kamoun, O.; Ozisik, H.; Deligoz, E.; Petkova, P.; Mimouni, R.; Boubaker, K.; Amlouk, M.; Goumri-Said, S. Stability and Morphology-Dependence of Sc^{3+} Ions Incorporation and Substitution Kinetics within ZnO Host Lattice. *Mater. Sci. Semicond. Process.* **2015**, *39*, 103–111.

(32) Lin, S.-S.; Huang, J.-L.; Šajgalik, P. The Properties of Ti-Doped ZnO Films Deposited by Simultaneous RF and DC Magnetron Sputtering. *Surf. Coat. Technol.* **2005**, *191* (2), 286–292.

(33) Jain, A.; Sagar, P.; Mehra, R. M. Band Gap Widening and Narrowing in Moderately and Heavily Doped N-ZnO Films. *Solid. State. Electron.* **2006**, *50* (7–8), 1420–1424.

(34) Mccluskey, M. D.; Jokela, S. J. Defects in ZnO. *J. Appl. Phys.* **2009**, *106* (7). https://doi.org/10.1063/1.3216464.

(35) Vidya, R.; Ravindran, P.; Fjellvåg, H.; Svensson, B. G.; Monakhov, E.; Ganchenkova, M.; Nieminen, R. M. Energetics of Intrinsic Defects and Their Complexes in ZnO Investigated by Density Functional Calculations. *Phys. Rev. B - Condens. Matter Mater. Phys.* **2011**, *83* (4), 1–12. https://doi.org/10.1103/PhysRevB.83.045206.

(36) Zhang, S. B.; Wei, S. H.; Zunger, A. Intrinsic N-Type versus p-Type Doping Asymmetry and the Defect Physics of ZnO. *Phys. Rev. B - Condens. Matter Mater. Phys.* **2001**, *63* (7), 1–7. https://doi.org/10.1103/PhysRevB.63.075205.

(37) Oba, F.; Togo, A.; Tanaka, I.; Paier, J.; Kresse, G. Defect Energetics in ZnO: A Hybrid Hartree-Fock Density Functional Study. *Phys. Rev. B - Condens.*

Matter Mater. Phys. **2008**, *77* (24), 3–8.
https://doi.org/10.1103/PhysRevB.77.245202.

(38)   Janotti, A.; Van De Walle, C. G. Oxygen Vacancies in ZnO. *Appl. Phys. Lett.*
2005, *87* (12), 1–3. https://doi.org/10.1063/1.2053360.

(39)   Janotti, A.; Van De Walle, C. G. Native Point Defects in ZnO. *Phys. Rev. B -
Condens. Matter Mater. Phys.* **2007**, *76* (16), 1–22.
https://doi.org/10.1103/PhysRevB.76.165202.

(40)   Van De Walle, C. G. Hydrogen as a Cause of Doping in Zinc Oxide. *Phys. Rev.
Lett.* **2000**, *85* (5), 1012–1015. https://doi.org/10.1103/PhysRevLett.85.1012.

(41)   Miki-Yoshida, M.; Paraguay-Delgado, F.; Estrada-López, W.; Andrade, E.
Structure and Morphology of High Quality Indium-Doped ZnO Films Obtained
by Spray Pyrolysis. *Thin Solid Films* **2000**, *376* (1–2), 99–109.
https://doi.org/10.1016/S0040-6090(00)01408-5.

(42)   Shinde, S. S.; Shinde, P. S.; Pawar, S. M.; Moholkar, A. V.; Bhosale, C. H.;
Rajpure, K. Y. Physical Properties of Transparent and Conducting Sprayed
Fluorine Doped Zinc Oxide Thin Films. *Solid State Sci.* **2008**, *10* (9), 1209–
1214. https://doi.org/10.1016/j.solidstatesciences.2007.11.031.

(43)   Lin, K. moh; Tsai, P. Growth Mechanism and Characterization of ZnO: Al
Multi-Layered Thin Films by Sol-Gel Technique. *Thin Solid Films* **2007**, *515*
(24 SPEC. ISS.), 8601–8604. https://doi.org/10.1016/j.tsf.2007.04.012.

(44)   Potter, D. B.; Bhachu, D. S.; Powell, M. J.; Darr, J. A.; Parkin, I. P.; Carmalt, C.
J. Al-, Ga-, and In-Doped ZnO Thin Films via Aerosol Assisted CVD for Use
as Transparent Conducting Oxides. *Phys. Status Solidi Appl. Mater. Sci.* **2016**,
213 (5), 1346–1352. https://doi.org/10.1002/pssa.201532996.

(45)   Spadoni, A.; Addonizio, M. L. Effect of the RF Sputtering Power on
Microstructural, Optical and Electrical Properties of Al Doped ZnO Thin Films.
Thin Solid Films **2015**, *589*, 514–520. https://doi.org/10.1016/j.tsf.2015.06.035.

(46)   Tsai, Y. Z.; Wang, N. F.; Tsai, C. L. Fluorine-Doped ZnO Transparent
Conducting Thin Films Prepared by Radio Frequency Magnetron Sputtering.
Thin Solid Films **2010**, *518* (17), 4955–4959.

https://doi.org/10.1016/j.tsf.2010.03.086.

(47) Nam, G. M.; Kwon, M. S. F-Doped ZnO by Sol-Gel Spin-Coating as a Transparent Conducting Thin Film. *Electron. Mater. Lett.* **2011**, *7* (2), 127–131. https://doi.org/10.1007/s13391-011-0607-8.

(48) Ratheesh Kumar, P. M.; Sudha Kartha, C.; Vijayakumar, K. P.; Singh, F.; Avasthi, D. K. Effect of Fluorine Doping on Structural, Electrical and Optical Properties of ZnO Thin Films. *Mater. Sci. Eng. B Solid-State Mater. Adv. Technol.* **2005**, *117* (3), 307–312. https://doi.org/10.1016/j.mseb.2004.12.040.

(49) Cao, L.; Zhu, L.; Jiang, J.; Zhao, R.; Ye, Z.; Zhao, B. Highly Transparent and Conducting Fluorine-Doped ZnO Thin Films Prepared by Pulsed Laser Deposition. *Sol. Energy Mater. Sol. Cells* **2011**, *95* (3), 894–898. https://doi.org/10.1016/j.solmat.2010.11.012.

(50) Yoon, H. S.; Lee, K. S.; Lee, T. S.; Cheong, B.; Choi, D. K.; Kim, D. H.; Kim, W. M. Properties of Fluorine Doped ZnO Thin Films Deposited by Magnetron Sputtering. *Sol. Energy Mater. Sol. Cells* **2008**, *92* (11), 1366–1372. https://doi.org/10.1016/j.solmat.2008.05.010.

(51) Jiamprasertboon, A.; Powell, M. J.; Dixon, S. C.; Quesada-Cabrera, R.; Alotaibi, A. M.; Lu, Y.; Zhuang, A.; Sathasivam, S.; Siritanon, T.; Parkin, I. P.; Carmalt, C. J. Photocatalytic and Electrically Conductive Transparent Cl-Doped ZnO Thin Films: Via Aerosol-Assisted Chemical Vapour Deposition. *J. Mater. Chem. A* **2018**, *6* (26), 12682–12692. https://doi.org/10.1039/c8ta01420e.

(52) Jiamprasertboon, A.; Dixon, S. C.; Sathasivam, S.; Powell, M. J.; Lu, Y.; Siritanon, T.; Carmalt, C. J. Low-Cost One-Step Fabrication of Highly Conductive ZnO:Cl Transparent Thin Films with Tunable Photocatalytic Properties via Aerosol-Assisted Chemical Vapor Deposition. *ACS Appl. Electron. Mater.* **2019**, *1* (8), 1408–1417. https://doi.org/10.1021/acsaelm.9b00190.

(53) Potter, D. B.; Powell, M. J.; Parkin, I. P.; Carmalt, C. J. Aluminium/Gallium, Indium/Gallium, and Aluminium/Indium Co-Doped ZnO Thin Films Deposited:

Via Aerosol Assisted CVD. *J. Mater. Chem. C* **2018**, *6* (3), 588–597. https://doi.org/10.1039/c7tc04003b.

(54) Ponja, S. D.; Sathasivam, S.; Parkin, I. P.; Carmalt, C. J. Transparent Conductive Aluminium and Fluorine Co-Doped Zinc Oxide Films Viaaerosol Assisted Chemical Vapour Deposition. *RSC Adv.* **2014**, *4* (91), 49723–49728. https://doi.org/10.1039/c4ra09997d.

(55) Shi, Q.; Zhou, K.; Dai, M.; Lin, S.; Hou, H.; Wei, C.; Hu, F. Structural and Opto-Electric Properties of Ga and F Codoped ZnO Thin Films on PC Substrates. *Vacuum* **2013**, *94*, 81–83. https://doi.org/10.1016/j.vacuum.2013.01.008.

(56) Vimalkumar, T. V; Poornima, N.; Jinesh, K. B.; Kartha, C. S.; Vijayakumar, K. P. On Single Doping and Co-Doping of Spray Pyrolysed ZnO Films: Structural, Electrical and Optical Characterisation. *Appl. Surf. Sci.* **2011**, *257* (20), 8334–8340. https://doi.org/10.1016/j.apsusc.2011.03.118.

(57) Morko, ̇ Hadis.; Ȯzgȕr, U. *Zinc Oxide Fundamentals, Materials and Device Technology / Hadis Morko ̇and Ümit Ȯzgȕr.*; Wiley-VCH: Weinheim, 2009.

(58) Janotti, A.; Van De Walle, C. G. Fundamentals of Zinc Oxide as a Semiconductor. *Reports Prog. Phys.* **2009**, *72* (12). https://doi.org/10.1088/0034-4885/72/12/126501.

(59) Sato, H.; Minami, T.; Takata, S.; Yamada, T. Transparent Conducting P-Type NiO Thin Films Prepared by Magnetron Sputtering. *Thin Solid Films* **1993**, *236* (1–2), 27–31. https://doi.org/10.1016/0040-6090(93)90636-4.

(60) Kudo, A.; Yanagi, H.; Ueda, K.; Hosono, H.; Kawazoe, H.; Yano, Y. Fabrication of Transparent p–n Heterojunction Thin Film Diodes Based Entirely on Oxide Semiconductors. *Appl. Phys. Lett.* **1999**, *75* (18), 2851–2853. https://doi.org/10.1063/1.125171.

(61) Kawazoe, H.; Yanagi, H.; Ueda, K.; Hosono, H. Transparent P-Type Conducting Oxides: Design and Fabrication of p-n Heterojunctions. *MRS Bull.* **2000**, *25* (8), 28–36. https://doi.org/10.1557/mrs2000.148.

(62) Ellmer, K. Past Achievements and Future Challenges in the Development of

Optically Transparent Electrodes. *Nat. Photonics* **2012**, *6* (12), 809.

(63)   Ohta, H.; Hosono, H. Transparent Oxide Optoelectronics. *Mater. Today* **2004**, *7* (6), 42–51.

(64)   Hautier, G.; Miglio, A.; Ceder, G.; Rignanese, G. M.; Gonze, X. Identification and Design Principles of Low Hole Effective Mass P-Type Transparent Conducting Oxides. *Nat. Commun.* **2013**, *4*, 1–7. https://doi.org/10.1038/ncomms3292.

(65)   Kawazoe, H.; Yasukawa, M.; Hyodo, H.; Kurita, M.; Yanagi, H.; Hosono, H. P-Type Electrical Conduction in Transparent Thin Films of $CuAlO_2$. *Nature* **1997**, *389* (6654), 939.

(66)   Majee, M. K.; Bhobe, P. A.; Deshpande, U. P.; Nigam, A. K. Local Crystal Structure and Physical Properties Change of p -Type Transparent Conducting Oxide: $CuCrO_2$ upon Ti-Substitution. *J. Appl. Phys.* **2017**, *122* (22). https://doi.org/10.1063/1.5003965.

(67)   Wang, J.; Daunis, T. B.; Cheng, L.; Zhang, B.; Kim, J.; Hsu, J. W. P. Combustion Synthesis of P-Type Transparent Conducting $CuCrO_{2+x}$ and $Cu:CrO_x$ Thin Films at 180 °c. *ACS Appl. Mater. Interfaces* **2018**, *10* (4), 3732–3738. https://doi.org/10.1021/acsami.7b13680.

(68)   Yanagi, H.; Inoue, S. I.; Ueda, K.; Kawazoe, H.; Hosono, H.; Hamada, N. Electronic Structure and Optoelectronic Properties of Transparent P-Type Conducting $CuAlO_2$. *J. Appl. Phys.* **2000**, *88* (7), 4159–4163. https://doi.org/10.1063/1.1308103.

(69)   Yanagi, H.; Hase, T.; Ibuki, S.; Ueda, K.; Hosono, H. Bipolarity in Electrical Conduction of Transparent Oxide Semiconductor $CuInO_2$ with Delafossite Structure. *Appl. Phys. Lett.* **2001**, *78* (11), 1583–1585. https://doi.org/10.1063/1.1355673.

(70)   Chuai, Y. H.; Bai, Y.; Zheng, C. T.; Liu, C. Y.; Wang, X.; Yue, D. Chemical Modulation of Valence Band and Photoelectric Properties of Epitaxial P-Type Infrared Transparent Conducting $CuScO_2$ Thin Films. *Mater. Res. Express* **2019**, *6* (12). https://doi.org/10.1088/2053-1591/ab78c8.

(71)   Kudo, A.; Yanagi, H.; Hosono, H.; Kawazoe, H. SrCu$_2$O$_2$: A p-Type Conductive Oxide with Wide Band Gap. *Appl. Phys. Lett.* **1998**, *73* (2), 220–222. https://doi.org/10.1063/1.121761.

(72)   Zhang, K. H. L.; Du, Y.; Papadogianni, A.; Bierwagen, O.; Sallis, S.; Piper, L. F. J.; Bowden, M. E.; Shutthanandan, V.; Sushko, P. V.; Chambers, S. A. Perovskite Sr-Doped LaCrO$_3$ as a New p-Type Transparent Conducting Oxide. *Adv. Mater.* **2015**, *27* (35), 5191–5195. https://doi.org/10.1002/adma.201501959.

(73)   Arca, E.; Kehoe, A. B.; Veal, T. D.; Shmeliov, A.; Scanlon, D. O.; Downing, C.; Daly, D.; Mullarkey, D.; Shvets, I. V.; Nicolosi, V.; Watson, G. W. Valence Band Modification of Cr$_2$O$_3$ by Ni-Doping: Creating a High Figure of Merit p-Type TCO. *J. Mater. Chem. C* **2017**, *5* (47), 12610–12618. https://doi.org/10.1039/c7tc03545d.

(74)   Wildsmith, T.; Hill, M. S.; Johnson, A. L.; Kingsley, A. J.; Molloy, K. C. Exclusive Formation of SnO by Low Temperature Single-Source AACVD. *Chem. Commun.* **2013**, *49* (78), 8773–8775. https://doi.org/10.1039/c3cc45676e.

(75)   Li, Q.; Ding, S.; Zhu, W.; Feng, L.; Dong, H.; Hu, W. Recent Advances in One-Dimensional Organic p-n Heterojunctions for Optoelectronic Device Applications. *J. Mater. Chem. C* **2016**, *4* (40), 9388–9398. https://doi.org/10.1039/c6tc03280j.

(76)   Hu, W.; Bai, F.; Bjornholm, T.; Fu, H.; Gong, X.; Zhan, X. *Organic Optoelectronics*, 1. Aufl.; Weinheim: Wiley-VCH: Weinheim, 2012.

(77)   Dong, H.; Zhu, H.; Meng, Q.; Gong, X.; Hu, W. Organic Photoresponse Materials and Devices. *Chem. Soc. Rev.* **2012**, *41* (5), 1754–1808. https://doi.org/10.1039/c1cs15205j.

(78)   Dong, H.; Wang, C.; Hu, W. ChemInform Abstract: High Performance Organic Semiconductors for Field-Effect Transistors. *ChemInform* **2010**, *41* (46). https://doi.org/https://doi.org/10.1002/chin.201046270.

(79)   Wang, C.; Dong, H.; Hu, W.; Liu, Y.; Zhu, D. Semiconducting π-Conjugated

Systems in Field-Effect Transistors: A Material Odyssey of Organic Electronics. *Chem. Rev.* **2012**, *112* (4), 2208–2267. https://doi.org/10.1021/cr100380z.

(80) Chen, L.; Yang, J.; Klaus, S.; Lee, L. J.; Woods-Robinson, R.; Ma, J.; Lum, Y.; Cooper, J. K.; Toma, F. M.; Wang, L. W.; Sharp, I. D.; Bell, A. T.; Ager, J. W. P-Type Transparent Conducting Oxide/n-Type Semiconductor Heterojunctions for Efficient and Stable Solar Water Oxidation. *J. Am. Chem. Soc.* **2015**, *137* (30), 9595–9603. https://doi.org/10.1021/jacs.5b03536.

(81) Zhang, K. H. L.; Wu, R.; Tang, F.; Li, W.; Oropeza, F. E.; Qiao, L.; Lazarov, V. K.; Du, Y.; Payne, D. J.; Macmanus-Driscoll, J. L.; Blamire, M. G. Electronic Structure and Band Alignment at the NiO and SrTiO$_3$ P-n Heterojunctions. *ACS Appl. Mater. Interfaces* **2017**, *9* (31), 26549–26555. https://doi.org/10.1021/acsami.7b06025.

(82) I. E. Agency, "Key World Energy Statistics," 2017.

(83) Krol, R. van de; Grätzel, M. *Photoelectrochemical Hydrogen Production*, 1. Aufl.; Electronic materials. Science & technology; Springer-Verlag: New York, NY, 2011; Vol. 102.

(84) Zhao, S.; Yang, M.; Tan, Y.; Brett, D. J. L.; He, G.; Parkin, I. P. Facile Room-Temperature Synthesis of Cobalt Sulphide for Efficient Oxygen Evolution Reaction. *Multifunct. Mater.* **2021**, *4* (2). https://doi.org/10.1088/2399-7532/abfeb8.

(85) Huang, N.; Yan, S.; Zhang, M.; Ding, Y.; Yang, L.; Sun, P.; Sun, X. A MoS$_2$-Co$_9$S$_8$-NC Heterostructure as an Efficient Bifunctional Electrocatalyst towards Hydrogen and Oxygen Evolution Reaction. *Electrochim. Acta* **2019**, *327*. https://doi.org/10.1016/j.electacta.2019.134942.

(86) She, Z. W.; Kibsgaard, J.; Dickens, C. F.; Chorkendorff, I.; Nørskov, J. K.; Jaramillo, T. F. Combining Theory and Experiment in Electrocatalysis: Insights into Materials Design. *Sci. (American Assoc. Adv. Sci.* **2017**, *355* (6321). https://doi.org/10.1126/science.aad4998.

(87) Zhou, Z.; Pei, Z.; Wei, L.; Zhao, S.; Jian, X.; Chen, Y. Electrocatalytic

Hydrogen Evolution under Neutral PH Conditions: Current Understandings, Recent Advances, and Future Prospects. *Energy Environ. Sci.* **2020**, *13* (1), 3185–3326.

(88)   Anantharaj, S.; Ede, S. R.; Sakthikumar, K.; Karthick, K.; Mishra, S.; Kundu, S. Recent Trends and Perspectives in Electrochemical Water Splitting with an Emphasis on Sulfide, Selenide, and Phosphide Catalysts of Fe, Co, and Ni: A Review. *ACS Catal.* **2016**, *6* (12), 8069–8097. https://doi.org/10.1021/acscatal.6b02479.

(89)   Singh, A.; Yadav, R.; Kociok-Köhn, G.; Trivedi, M.; Azad, U. P.; Singh, A. K.; Kumar, A. Syntheses of Nickel Sulfides from 1,2-Bis(Diphenylphosphino)Ethane Nickel(II)Dithiolates and Their Application in the Oxygen Evolution Reaction. *Int. J. Hydrogen Energy* **2018**, *43* (12), 5985–5995. https://doi.org/10.1016/j.ijhydene.2018.02.043.

(90)   Li, B.; Li, Z.; He, F.; Pang, Q.; Shen, P. One-Pot Preparation of Ni_3S_2@3-D Graphene Free-Standing Electrode by Simple Q-CVD Method for Efficient Oxygen Evolution Reaction. *Int. J. Hydrogen Energy* **2019**, *44* (59), 30806–30819. https://doi.org/10.1016/j.ijhydene.2019.09.246.

(91)   Gao, Z.; Qi, J.; Chen, M.; Zhang, W.; Cao, R. An Electrodeposited NiSe for Electrocatalytic Hydrogen and Oxygen Evolution Reactions in Alkaline Solution. *Electrochim. Acta* **2017**, *224*, 412–418. https://doi.org/10.1016/j.electacta.2016.12.070.

(92)   Bandal, H. A.; Jadhav, A. R.; Tamboli, A. H.; Kim, H. Bimetallic Iron Cobalt Oxide Self-Supported on Ni-Foam: An Efficient Bifunctional Electrocatalyst for Oxygen and Hydrogen Evolution Reaction. *Electrochim. Acta* **2017**, *249*, 253–262. https://doi.org/10.1016/j.electacta.2017.07.178.

(93)   Suen, N.-T.; Hung, S.-F.; Quan, Q.; Zhang, N.; Xu, Y.-J.; Chen, H. M. Electrocatalysis for the Oxygen Evolution Reaction: Recent Development and Future Perspectives. *Chem. Soc. Rev.* **2017**, *46* (2), 337–365. https://doi.org/10.1039/c6cs00328a.

(94)   Escudero-Escribano, M.; Pedersen, A. F.; Paoli, E. A.; Frydendal, R.; Friebel,

D.; Malacrida, P.; Rossmeisl, J.; Stephens, I. E. L.; Chorkendorff, I. Importance of Surface IrO$_x$ in Stabilizing RuO$_2$ for Oxygen Evolution. *J. Phys. Chem. B* **2018**, *122* (2), 947–955. https://doi.org/10.1021/acs.jpcb.7b07047.

(95) Lee, Y.; Suntivich, J.; May, K. J.; Perry, E. E.; Shao-Horn, Y. Synthesis and Activities of Rutile IrO$_2$ and RuO$_2$ Nanoparticles for Oxygen Evolution in Acid and Alkaline Solutions. *J. Phys. Chem. Lett.* **2012**, *3* (3), 399–404. https://doi.org/10.1021/jz2016507.

(96) Marshall, A. T.; Haverkamp, R. G. Electrocatalytic Activity of IrO$_2$-RuO$_2$ Supported on Sb-Doped SnO$_2$ Nanoparticles. *Electrochim. Acta* **2010**, *55* (6), 1978–1984. https://doi.org/10.1016/j.electacta.2009.11.018.

(97) Chu, H.; Zhang, D.; Jin, B.; Yang, M. Impact of Morphology on the Oxygen Evolution Reaction of 3D Hollow Cobalt-Molybdenum Nitride. *Appl. Catal. B Environ.* **2019**, *255* (May). https://doi.org/10.1016/j.apcatb.2019.117744.

(98) Garcia, A. C.; Touzalin, T.; Nieuwland, C.; Perini, N.; Koper, M. T. M. Enhancement of Oxygen Evolution Activity of Nickel Oxyhydroxide by Electrolyte Alkali Cations. *Angew. Chem. - Int. Ed.* **2019**, *58* (37), 12999–13003. https://doi.org/10.1002/anie.201905501.

(99) Prasad, D.; Patil, K. N.; Sandhya, N.; Chaitra, C. R.; Bhanushali, J. T.; Samal, A. K.; Keri, R. S.; Jadhav, A. H.; Nagaraja, B. M. Highly Efficient Hydrogen Production by Hydrolysis of NaBH4 Using Eminently Competent Recyclable Fe$_2$O$_3$ Decorated Oxidized MWCNTs Robust Catalyst. *Appl. Surf. Sci.* **2019**, *489* (January), 538–551. https://doi.org/10.1016/j.apsusc.2019.06.041.

(100) Li, H.; Shao, Y.; Su, Y.; Gao, Y.; Wang, X. Vapor-Phase Atomic Layer Deposition of Nickel Sulfide and Its Application for Efficient Oxygen-Evolution Electrocatalysis. *Chem. Mater.* **2016**, *28* (4), 1155–1164. https://doi.org/10.1021/acs.chemmater.5b04645.

(101) Zhang, H.; Zhou, W.; Dong, J.; Lu, X. F.; Lou, X. W. (David). Intramolecular Electronic Coupling in Porous Iron Cobalt (Oxy)Phosphide Nanoboxes Enhances the Electrocatalytic Activity for Oxygen Evolution. *Energy Environ. Sci.* **2019**, *12* (11), 3348–3355. https://doi.org/10.1039/c9ee02787d.

(102) Chen, J.; Cui, P.; Zhao, G.; Rui, K.; Lao, M.; Chen, Y.; Zheng, X.; Jiang, Y.; Pan, H.; Dou, S. X.; Sun, W. Low-Coordinate Iridium Oxide Confined on Graphitic Carbon Nitride for Highly Efficient Oxygen Evolution. *Angew. Chem. - Int. Ed.* **2019**, *58* (36), 12540–12544. https://doi.org/10.1002/anie.201907017.

(103) Chen, L.; Zang, J.; Liu, X.; Zhang, Y.; Jia, S.; Tian, P.; Wang, Y. A Self-Supporting Graphene Supported Cobalt Hydroxide for Enhanced Oxygen Evolution Catalysis. *Electrochim. Acta* **2018**, *281*, 386–393. https://doi.org/10.1016/j.electacta.2018.05.193.

(104) Xu, Y.; Kraft, M.; Xu, R. Metal-Free Carbonaceous Electrocatalysts and Photocatalysts for Water Splitting. *Chem. Soc. Rev.* **2016**, *45* (11), 339–352. https://doi.org/10.1039/c5cs00729a.

(105) Wang, J.; Huang, J.; Zhao, S.; Parkin, I. P.; Tian, Z.; Lai, F.; Liu, T.; He, G. Mo/Fe Bimetallic Pyrophosphates Derived from Prussian Blue Analogues for Rapid Electrocatalytic Oxygen Evolution. *Green Energy Environ.* **2022**. https://doi.org/10.1016/j.gee.2022.02.014.

Chapter 2 Film Deposition and Characterisation Methods

2.1 Synthesis Techniques

2.1.1 Chemical vapour deposition (CVD)

The synthesis, processing and film deposition methods have a significant influence on the total cost and properties of the thin films.[1] In addition, the morphological properties of the thin films depend on the method of film deposition and can influence the resulting properties significantly.[2] There are many methods which can be used to form different thin films, such as chemical vapour deposition (CVD), sol–gel, spin coating, physical vapour deposition (PVD) and atomic layer deposition (ALD).[3] CVD is a quite common route to prepare thin films and the method has some significant advantages over other techniques including limited pre-reaction, low reaction temperature, precursors with stability of air, moisture and relatively low toxicity.[3] The key steps in the CVD process include (1) the production of a volatile precursor (e.g. $TiCl_4$ and WCl_6), (2) transport of the precursors to the substrate and (3) chemical reactions/decomposition to produce the desired coating on the substrate. Atmospheric pressure chemical vapour deposition (APCVD) is a traditional CVD method shown in Figure 2.1,[4] where the main requirement is that there is a suitable vapour pressure of precursor to make sure the thin films can be prepared successfully. Due to this condition, the range of precursors available are limited and hence the deposition of a chosen thin film may not be easily achievable. Moreover, precursors used in APCVD often have some hazards including corrosivity, pyrophoricity, flammability, explosivity and environmental toxicity.[5]
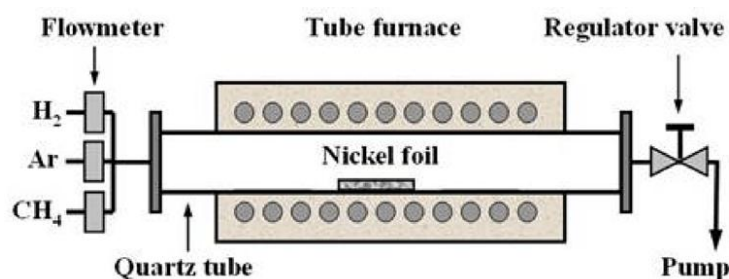
Figure 2.1: The schematic from former literature of the APCVD apparatus.[4]

In recent years, a specialized form of CVD, known as aerosol assisted (AA)CVD, has been considered as a promising research hotspot for functional thin film preparation.[3]

AACVD uses soluble precursors instead of vaporizing volatile precursors used in APCVD, which can offer a larger range of precursors to be chosen to avoid some of the hazards indicated above.[5–7] The AACVD reactor utilized in this project is shown in Figure 2.2 as a previously reported schematic[7] and Figure 2.3 as a photo of the actual equipment during a deposition process. In comparison with other synthetic technologies, there are also some other benefits of AACVD, including easy control over stoichiometry, film thickness and surface morphology,[1,8] and that it is a relatively simple process that operates at ambient pressure resulting in low cost.[1,3,8] Moreover, although there are several challenges of using AACVD in large scale for industrial applications, such as sizes and distribution of aerosol droplets, losses during the long distance transmission, evaporation of the solvent in the delivery process and complicated reactions during depositions due to the solvent, the feasibility of industrial production via AACVD have been proved through modeling [9] Filho et al, have shown through full process modelling that it is possible to adapt current thin film coating production lines that use APCVD to an AACVD system. [9]

AACVD, like traditional CVD is a non-equilibrium process, which is controlled by both thermodynamic and kinetic factors. Due to chemical reactions taking place during the deposition process, whether the reaction can take place will be determined through the thermodynamics, which is evaluated by the overall change of Gibb's free energy (ΔG, $\Delta G < 0$ represents the reactions tend to happen) related to reaction temperature and pressure. The substrate is heated to obtain negative ΔG resulting in the feasibility of chemical reactions during the deposition process as the AACVD is under atmospheric pressure. However, even when thermodynamically feasibility has been reached, thin film growth may not be observed if the kinetic barrier is not overcome. In addition, besides the kinetics controlling the growth rate, the high temperature also has significant effect on the increasing etching of thin films and rapid homogenous side reactions in gas phase leading to the decrease of growth rate, which suggests the deposition temperature is supposed to just above the temperature for the negative ΔG to meet both thermodynamic and kinetic benefit.

A schematic of the AACVD reactor used for projects in this thesis is show in Figure 2.2. The aerosol mist is generated from the precursor solution using a piezoelectronic device. The size of the aerosol droplets is dependent on the frequency at which the piezoelectric component vibrates. The aerosol mist is carried into the reactor using a carrier gas (typically N_2 or compressed air) through a brass baffle to obtain a laminar flow over the substrates. The reactor encompasses a carbon block with a cartridge heater upon which the glass substrates are positioned. The temperature of the substrate is monitored using a Type-K thermocouple. Depositions are carried out heating the horizontal bed reactor to the required temperature and allowing the gas stream to pass over the glass substrate.

The overall mechanism of the AACVD process, which is displayed in Figure 2.4.[6,10] **Step 1** is the generation of aerosols (precursor mist) from the precursors dissolved in solvent created using the ultrasonic humidifier (nebulizer). Then, the aerosols are transported to the AACVD reactor by carrier gas, e.g. Ar, N_2, as **Step 2**. When the aerosols reach the substrate, the solvent tends to be evaporated based on the high temperature leaving the vaporised precursors in the gaseous state, which is **Step 3**. Finally, **Step 4** involves the gaseous vaporised precursors depositing onto the substrate and the desired material is grown as a thin film.[6,10] Moreover, according to the process of film growth for AACVD, many factors, such as precursors, solvent, deposition temperature and substrate, have an effect on the microstructure and surface morphology of the thin films.[6,10]

In addition, AACVD has been used to fabricate many thin films with excellent functional properties based on the outstanding advantages mentioned above, such as Sc-doped ZnO,[5] Si-doped ZnO,[1] Mo-doped SnO_2,[11] Nb_2O_5,[2] Cr-doped MoS_2,[12] Re-doped MoS_2,[13] $CuInS_2$ based films,[14] superhydrophobic polytetrafluoroethylene (PTFE) films,[15] ambient-air-stable methylammonium lead iodide (MAPI) perovskite thin films,[16] tungsten oxide nanoneedles thin film functionalized with gold nanoparticles (NPs),[17] CdS based film,[18] CdSe and CdSSe thin films.[19] Therefore, this project will focus on the preparation of functional thin films through AACVD.
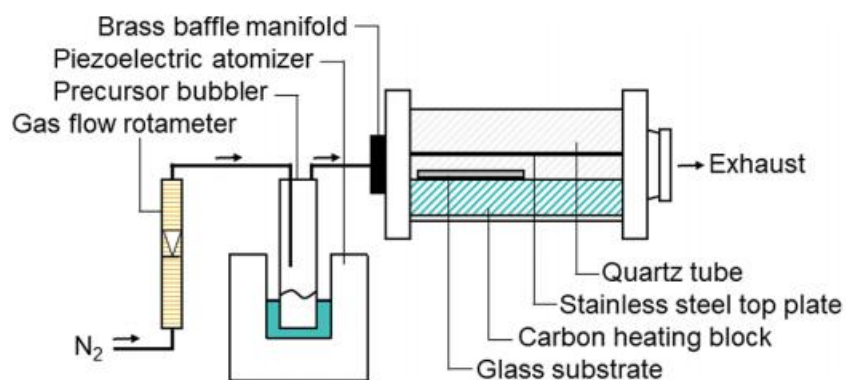
Figure 2.2: The schematic from former literature of the AACVD apparatus used for the synthesis of the thin films discussed in this report.[7]
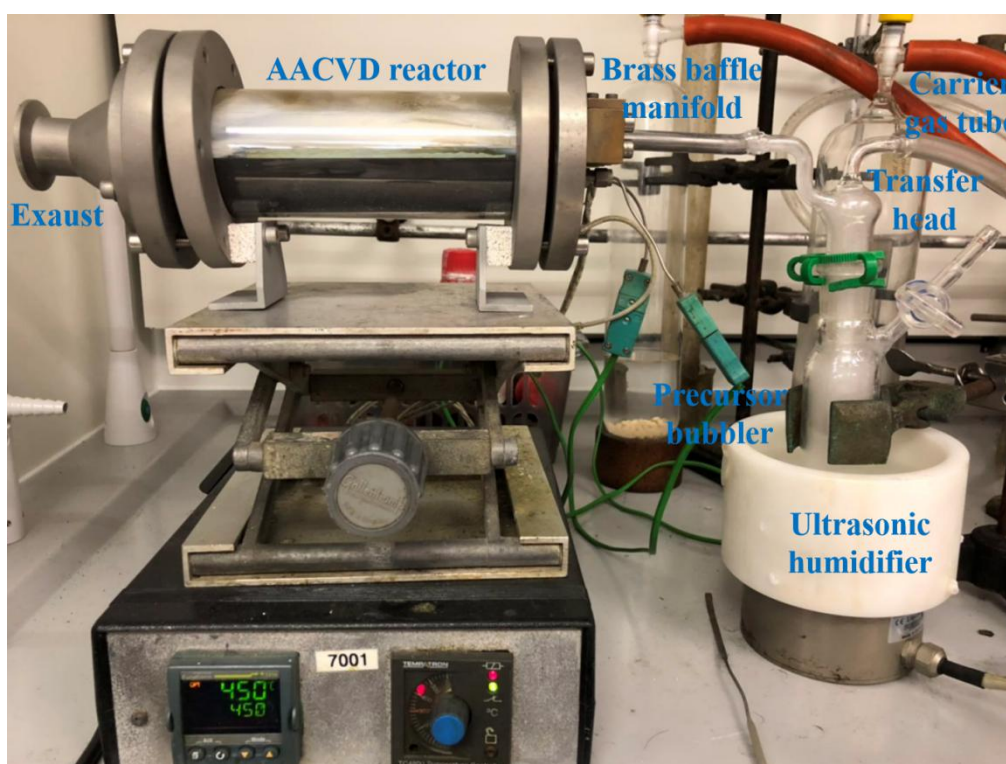
Figure 2.3: The schematic photo of the AACVD apparatus used for the synthesis of the thin films discussed in this report.
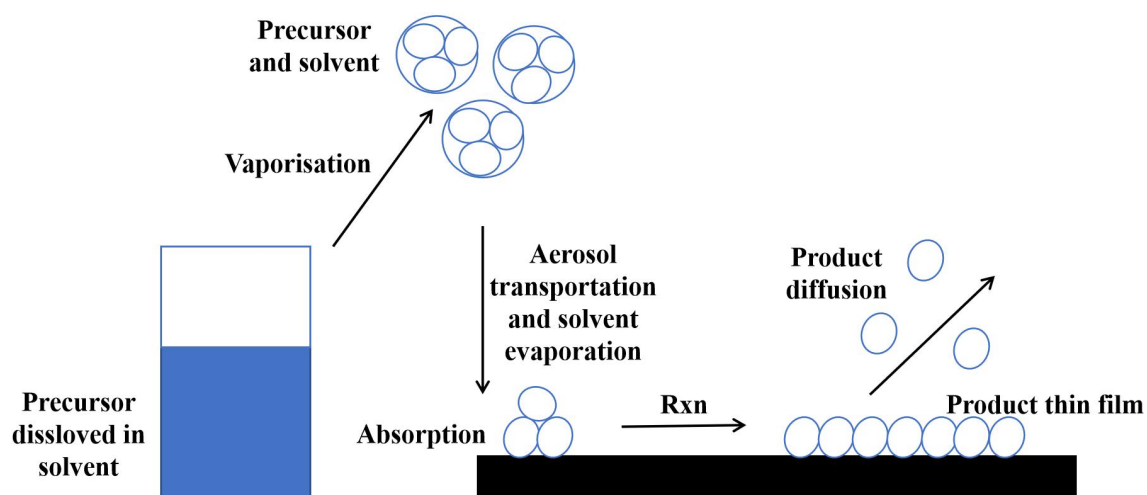
Figure 2.4: The schematic for the mechanism of the general AACVD process.

2.1.2 Other Synthesis Techniques

Although this investigation is focused on the CVD route, there are also some other widely used film synthesis routes, such as PLD, ALD and magnetron sputtering coatings.

PLD is another widely used method to prepare thin films, which vaporizes the surface of a solid target through high-energy laser pulses and the vapour then condenses on the substrate to form thin films.[20] The PLD method can control film stoichiometry for multi-element thin films easily and a high surface diffusion, based on the laser material removal mechanism.[20] The conditions that influences PLD include pulse energy of laser, material type of target, distance between target and substrate, pressure and gas of chamber.

Many thin films also can be grown through ALD, which is a special variant of CVD. This synthesis technology has significant benefits to prepare thin films on complicated 3D structures with uniformity thickness and perfect conformality with atomic level control resulting from a self-limiting growth mechanism.[21] According to this advantage, ALD can be used widely in the microelectronics areas.[21]

Sol–gel method is one kind of wet chemical technology that can prepare thin films with unique properties. This method has good control at the molecular level for both compositions and structures of thin films.[22] The general process of the sol–gel method

includes precursor hydrolysis, colloidal sol formation, sol–gel transition frozen as gel network, wet gel drying and crystalline phases formed by heat treatment.[22] The simple preparation process with low cost and high purity products are the advantages of the sol–gel method, which has also attracted many attention recently.

Thin films with thickness in the micrometers and nanometers scales can be grown through the spin coating method, such as some photosensitive organic thin films. The process of this method involves the dispense, spin up and out flow of the fluid with evaporation as the drying method.[23] Spin coating has been widely used in many electronic areas, for example, integrated circuits fabrications.[23]

Sputtering coatings including dc reactive magnetron sputtering and RF magnetron sputtering,[24,25] and can be considered as a type of physical vapor deposition route for thin film synthesis. The synthesis method uses energetic ionic species to sputter the solid target resulting from the magnetically enhanced glow discharge.[24] Sputtering coatings can yield different types of thin films, such as ceramics and metals on the different types of substrates under relatively low pressures with fast deposition. This method can also form strongly adhesive thin films on substrates with complex geometries.[26]

2.2 Characterization Techniques

2.2.1 X-ray Diffraction (XRD)

XRD can determine the phase identification and crystal structure of the synthesized thin films. X-ray diffraction occurs in the crystal based on the similar scales between the characteristic wavelength of X-ray and the distances of contiguous atoms. The Bragg equation shows the periodic changes of the wavelength of the incident X rays with interplanar distance and the incident angle:

Bragg Equation:

$$n\lambda = 2d\sin\theta \tag{2.01}$$

where n is a positive integer, λ is the wavelength of the incident X-ray, d is the interplanar distance and θ is the incident angle.

According to this equation, it can be determined if the distribution of atoms in a crystal is also periodic, which means the peaks of diffraction wave in the diffraction pattern correspond to the characteristic atom. Thus, the arrangement of atoms can be found in the crystal. In this project, the composition and the preferred orientation of the synthesised thin films are of interest.

Furthermore, crystallite sizes can also be determined from the XRD through the Scherrer equation:

$$D = \frac{k\lambda}{\beta\cos\theta} \tag{2.02}$$

where D is the crystallite size, k is the Scherrer constant (which is usually used as 0.9), λ is the wavelength of the incident X-rays, β is the full width at half maximum (FWHM) and θ is the Bragg diffraction angle, in radians.[5,27]

2.2.2 X-ray Photoelectron Spectroscopy (XPS)

The composition and oxidation states of elements on the surface of a material can be measured using X-ray photoelectron spectroscopy (XPS). According to the

photoelectric effect, the electrons on the surface will be ejected when the surface atoms are irradiated by X-rays. The kinetic energy of the emitted electrons are measured to determine the electron binding energy through the equation:

$$KE = h\nu - BE \tag{2.03}$$

where KE is the kinetic energy, hν is the photon energy and BE is the binding energy. Then, according to the characteristic binding energy, the species and oxidation states of the surface elements will be defined. Compared to the peak area of the characteristic binding energy, the proportion of each element can be determined. However, due to the low mean free path electrons, XPS only can provide analysis less than 10 nm below surface and cannot determine the chemical environment of the material in depth. Hard X-ray Photoelectron Spectroscopy (HAXPES) offers more insight into the depth of the sample by the use of higher energy X-rays to penetrate deeper into the sample allowing for electrons to be ejected with high kinetic energy.

2.2.3 Scanning Electron Microscopy (SEM)

Scanning electron microscopy (SEM) provides images of the surface of the specific sample to determine its surface characterization and morphology.

A high-energy electron beam is used in SEM, which can scan over the sample surface as small probe. The electrons and photons that are emitted and are then detected.[28] There are both elastic and inelastic collisions between electrons and sample. The elastic collisions cause backscattering without energy transfer while the inelastic collisions have kinetic energy transfer and generate low-energy secondary electrons, which can be tested through a detector. Moreover, the morphology of samples can be determined based on the number of secondary electrons.

High resolution is possible for SEM, whose spatial resolution is better than 100 nm in compositional mode and 10 nm in topographic mode.[29]
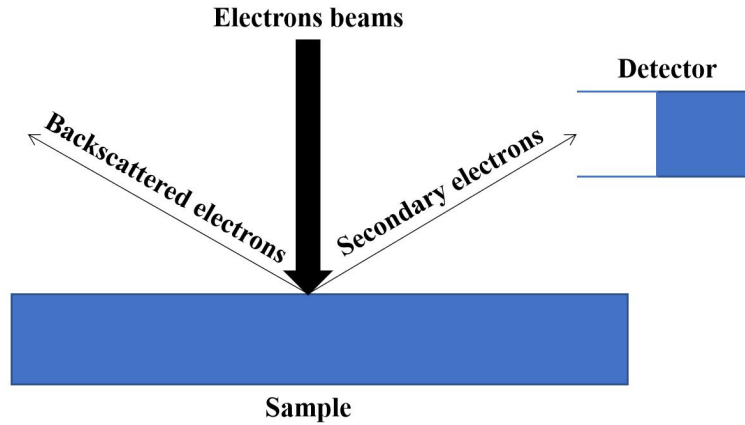
Figure 2.5: Schematic of scanning electron microscopy.

2.2.4 Energy Dispersive X-ray Spectroscopy (EDS)

Energy dispersive X-ray spectroscopy (EDS) can be used to analyze the composition of solid surfaces through the difference of photon characteristic energies of the X-rays of different elements shown in Figure 2.6.[30] The solid surface is irradiated by a focused X-ray beam or a high energy beam of charged particles resulting in generating X-ray emission, which has distinct characteristics on the basis of unique electronic structure of different atoms. The detector then receives the fingerprint spectrum, which can be used to determine the species and relative content of elements by comparing to the reference spectrum caused by the unique atomic structure of each element which gives a specific unique position of its peak on the spectrum.[31,32]

Hence, the composition of an individual point can be defined through the fingerprint spectrum while the lateral distribution of the individual point can be determined through the imaged area that has been mapped out. Furthermore, some samples that are bulk, in the deposits, in isolated areas or on some special particles can also be determined through EDS analysis. The EDS analysis may be used to compare with some other techniques, such as SEM, TEM, STEM, XPS and FTIR.[31,32]
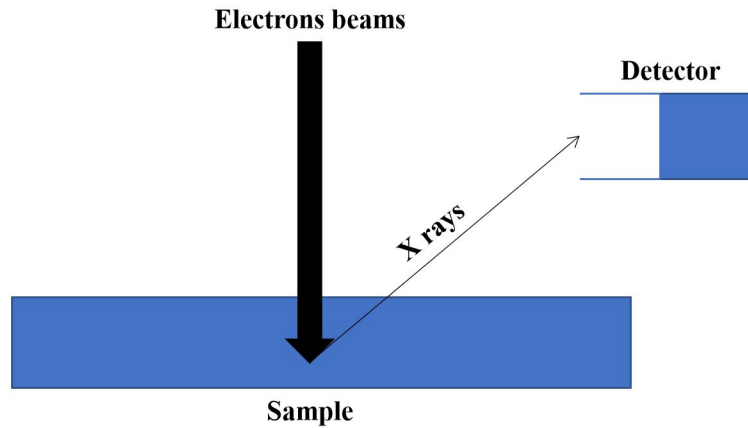
Figure 2.6: Schematic of energy dispersive X-ray spectroscopy.

2.2.5 Raman Spectroscopy

Raman spectroscopy has good ability to determine the local crystallinity of materials and exhibit a lot of information of materials within several seconds, such as crystal structure type, crystal orientation strain or stress present and concentration of dopants. The information from Raman spectroscopy is collected from Raman scattering (inelastically scattering) to determine the vibrational modes of one specific material. Reflection, absorption or scattering can be found when light exposures to one material and Rayleigh scattering (elastic scattering) was the more common without energy variation. Thus, the inelastically scattering causing energy change shown in Figure 2.7 can be monitored and analyzed, which is considered as one characteristic change determined through the vibrational state of one specific material. The transition energies can be plotted as spectrum to identify one material from the molecular fingerprint.
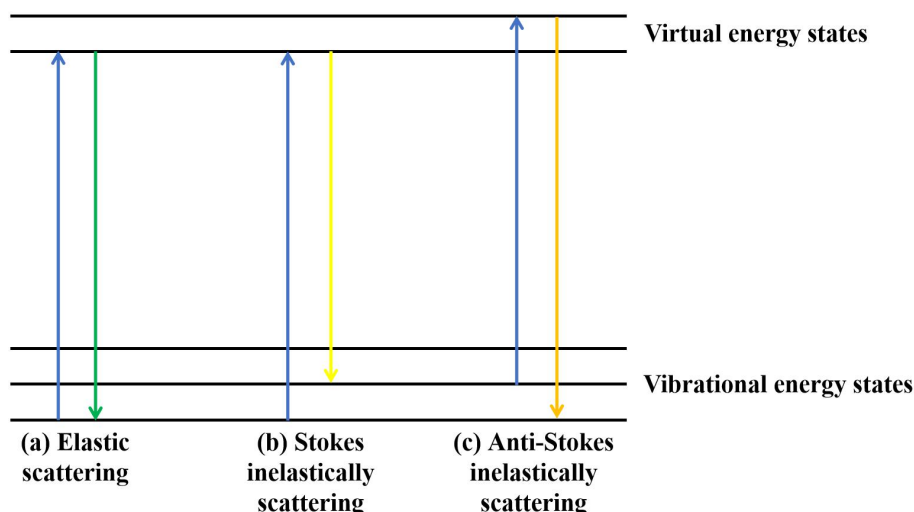
Figure 2.7: Schematic vibrational energy level diagram for elastically (Rayleigh) scattering and inelastically (Raman) scattering.

2.2.6 Mass spectrometry (MS)

Mass spectrometry (MS) measures the mass-to-charge ratio (m/z) of ionised molecules controlled by the electric and magnetic fields, which is often used to identify the compositions of relatively large separable molecules.

The sample is bombarded by an ion beam that produces fragments of the sample molecule with/without charges. The charged fragments can be divided and determined based on the different mass-to-charge ratio of different fragments through the electric or magnetic field. The compositions of molecules in sample can be inferred via the known mass pieces and characteristic fragments. Moreover, there are many types of mass spectrometers and the atmospheric solids analysis probe (ASAP) and heated electrospray ionisation (HESI) were used here for ion generation while the Q Exactive Plus mass spectrometer was used to detected and analysed the m/z ratio of related fragments.

2.2.7 Fourier transform infrared spectroscopy (FT-IR)

Fourier-transform infrared spectroscopy (FT-IR) can collect and analyze the infrared spectrum of absorption or emission of one material, which is usually to be used to determine the characteristic structures or functional groups of the compositions for specific materials.

The FT-IR launches a beam with different frequencies of light at the same time and the frequencies absorbed by the test material will then be determined. This process will repeat based on different kinds of frequencies and evaluate the absorption from different wavelengths. Finally, the FT-IR spectrum can be obtained after Fourier transform of the light absorptions for each wavelength.

2.2.8 Hall Effect Measurement

Hall effect measurement can be used to determine the bulk concentration, carrier mobility and resistivity in semiconductors based on the Hall effect.

For Hall effect shown in Figure 2.8, the electron will under one Lorentz force when this electron goes pass one magnetic field applied perpendicular to the direction of the current. Thus, the electrons will move to the top of the sample while the horizontal motions keeping. The negative and positive charges will appear at the top and bottom of the sample due to the deflecting of electrons causing the potential difference between the two sides of the sample, which is known as Hall voltage (VH).[33]

Moreover, the Hall coefficient, R_H, is defined as:

$$R_H = \frac{E_y}{j_x B_z} \tag{2.04}$$

Where E_y is the electric field in the y direction resulting from the Hall voltage, j_x is the electric current density per unit of cross section in the x direction and B_z is the applied magnetic field in the z direction.

In this measurement, a series Hall voltage with or without external magnetic field will be measured in order to determine the sheet carrier density (nS) through the equation:

$$n_S = \frac{IB}{q|VH|} \tag{2.05}$$

where I is electrical current, B is magnetic field and q is elementary charge (1.602×10^{-19} C).

Then, according to the sample thickness (d), the bulk density and resistivity can also be determined according to the equations:

$$n = \frac{n_S}{d} \tag{2.06}$$

and

$$r = R_S d \tag{2.07}$$

where R_S is sheet resistance that can be known by this measurement technique.

In addition, the type of semiconductor (n-type or p-type) can be determined by the sign of the Hall voltage. Usually, the sign of carrier concentration (n) is used to determine the type of semiconductor instead of the Hall voltage, which is also related to the carrier mobility (μ) and the resistivity (ρ), $R_H = \mu\rho$. The negative bulk concentration represents n-type semiconductor while positive represents p-type one.[33]
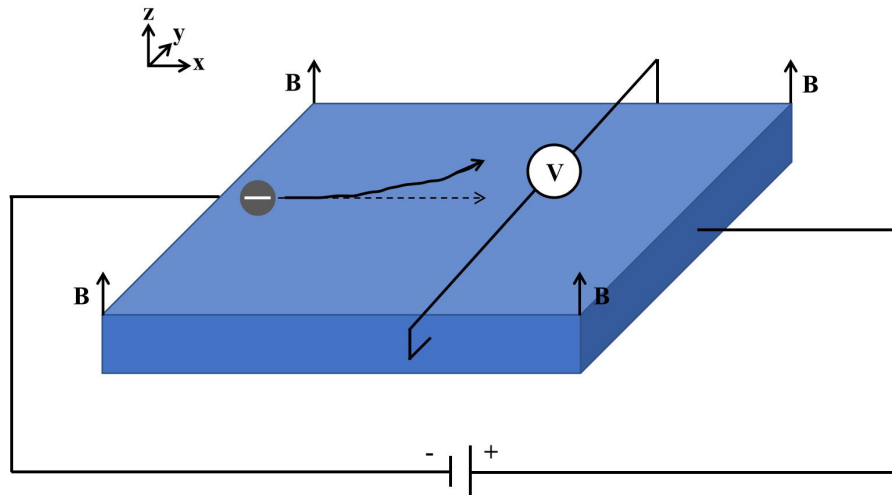
Figure 2.8: Schematic indication for one electron undergo Hall effect.

2.2.9 Ultraviolet-visible (UV-vis) spectra

The transmittance and optical band gap of TCO films can be determined through UV-vis spectroscopic measurements. The UV-vis spectroscopy will determine the ratio ($\frac{I}{I_0}$) of the intensity of light initially and passing through the sample, which is known as transmittance, %T. The transmittance (T) and reflection (R) is given automatically by the UV-vis spectrometer utilised in this work. The absorbance (A) can be determined through the equation:

$$\%A = 2 - \log(\%T) \tag{2.08}$$

Next, the absorption coefficient, α can be known via equation:

$$\alpha\left(cm^{-1}\right) = \frac{\ln(10) \times A}{1(cm)} \tag{2.09}$$

Finally, a direct band gap can be calculated via the Tauc plot from the hν vs. $(\alpha \times h\nu)^2$ using Origin.

2.3 References

(1)   Potter, D. B.; Powell, M. J.; Darr, J. A.; Parkin, I. P.; Carmalt, C. J. Transparent Conducting Oxide Thin Films of Si-Doped ZnO Prepared by Aerosol Assisted CVD. *RSC Adv.* **2017**, *7* (18), 10806–10814. https://doi.org/10.1039/c6ra27748a.

(2)   Sathasivam, S.; Williamson, B. A. D.; Althabaiti, S. A.; Obaid, A. Y.; Basahel, S. N.; Mokhtar, M.; Scanlon, D. O.; Carmalt, C. J.; Parkin, I. P. Chemical Vapor Deposition Synthesis and Optical Properties of Nb_2O_5 Thin Films with Hybrid Functional Theoretical Insight into the Band Structure and Band Gaps. *ACS Appl. Mater. Interfaces* **2017**, *9* (21), 18031–18038. https://doi.org/10.1021/acsami.7b00907.

(3)   Knapp, C. E.; Carmalt, C. J.; Knapp, C. E. Chem Soc Rev Solution Based CVD of Main Group Materials. **2016**, 1036–1064. https://doi.org/10.1039/c5cs00651a.

(4)   Zhu, D.; Liu, Y.; Yuan, L.; Liu, Y.; Li, X.; Yi, L.; Wei, H.; Yao, K. Controllable Synthesis of Large-Area Free-Standing Amorphous Carbon Films and Their Potential Application in Supercapacitors. *RSC Adv.* **2014**, *4* (109), 63734–63740. https://doi.org/10.1039/c4ra11378k.

(5)   Dixon, S. C.; Sathasivam, S.; Williamson, B. A. D.; Scanlon, D. O.; Carmalt, C. J.; Parkin, I. P. Transparent Conducting N-Type ZnO:Sc-Synthesis, Optoelectronic Properties and Theoretical Insight. *J. Mater. Chem. C* **2017**, *5* (30), 7585–7597. https://doi.org/10.1039/c7tc02389h.

(6)   Marchand, P.; Hassan, I. A.; Parkin, I. P.; Carmalt, C. J.; Marchand, P. Materials Fabrication. **2013**, 9406–9422. https://doi.org/10.1039/c3dt50607j.

(7)   Dixon, S. C.; Manzi, J. A.; Powell, M. J.; Carmalt, C. J.; Parkin, I. P. Re Fl Ective Silver Thin Film Electrodes from Commercial Silver (I) Tri Fl Ate via Aerosol-Assisted Chemical Vapor Deposition. **2018**, No. I. https://doi.org/10.1021/acsanm.8b00949.

(8)   Hou, B. X.; Choy, K. Processing and Applications of Aerosol- Assisted Chemical Vapor Deposition. **2006**, 583–596. https://doi.org/10.1002/cvde.200600033.

(9)   Filho, P. I. O.; Carmalt, C. J.; Angeli, P.; Fraga, E. S. Mathematical Modeling for the Design and Scale-Up of a Large Industrial Aerosol-Assisted Chemical Vapor Deposition Process under Uncertainty. *Ind. Eng. Chem. Res.* **2020**, *59* (3), 1249–1260. https://doi.org/10.1021/acs.iecr.9b05869.

(10)   Knapp, C. E.; Carmalt, C. J. Solution Based CVD of Main Group Materials. *Chem. Soc. Rev.* **2016**, *45* (4), 1036–1064. https://doi.org/10.1039/c5cs00651a.

(11)   Ma, T.; Nikiel, M.; Thomas, A. G.; Missous, M.; Lewis, D. J. A Novel and Potentially Scalable CVD-Based Route towards SnO_2:Mo Thin Films as Transparent Conducting Oxides. *J. Mater. Sci.* **2021**, *56* (28), 15921–15936. https://doi.org/10.1007/s10853-021-06269-3.

(12)   Lewis, D. J.; Tedstone, A. A.; Zhong, X. L.; Lewis, E. A.; Rooney, A.; Savjani, N.; Brent, J. R.; Haigh, S. J.; Burke, M. G.; Muryn, C. A.; Raftery, J. M.; Warrens, C.; West, K.; Gaemers, S.; O'Brien, P. Thin Films of Molybdenum Disulfide Doped with Chromium by Aerosol-Assisted Chemical Vapor Deposition (AACVD). *Chem. Mater.* **2015**, *27* (4), 1367–1374. https://doi.org/10.1021/cm504532w.

(13)   Al-Dulaimi, N.; Lewis, E. A.; Savjani, N.; McNaughter, P. D.; Haigh, S. J.; Malik, M. A.; Lewis, D. J.; O'Brien, P. The Influence of Precursor on Rhenium Incorporation into Re-Doped MoS_2 ($Mo_{1-x}Re_xS_2$) Thin Films by Aerosol-Assisted Chemical Vapour Deposition (AACVD). *J. Mater. Chem. C* **2017**, *5* (35), 9044–9052. https://doi.org/10.1039/c7tc01903c.

(14)   Ming, S. K.; Taylor, R. A.; O'Brien, P.; McNaughter, P. D.; Lewis, D. J. Tunable Structural, Morphological and Optical Properties of Undoped, Mn, Ni and Ag-Doped $CuInS_2$ Thin Films Prepared by AACVD. *Mater. Sci. Semicond. Process.* **2022**, *137* (May 2021). https://doi.org/10.1016/j.mssp.2021.106224.

(15)   Zhuang, A.; Liao, R.; Dixon, S. C.; Lu, Y.; Sathasivam, S.; Parkin, P.; Carmalt, C. J. RSC Advances Step Aerosol Assisted Chemical Vapor Deposition †. *RSC*

Adv. **2017**, *7*, 29275–29283. https://doi.org/10.1039/C7RA04116K.

(16)   Ke, C. R.; Lewis, D. J.; Walton, A. S.; Chen, Q.; Spencer, B. F.; Mokhtar, M.
         Z.; Compean-Gonzalez, C. L.; O'Brien, P.; Thomas, A. G.; Flavell, W. R. Air-
         Stable Methylammonium Lead Iodide Perovskite Thin Films Fabricated via
         Aerosol-Assisted Chemical Vapor Deposition from a Pseudohalide Pb(SCN)$_2$
         Precursor. *ACS Appl. Energy Mater.* **2019**, *2* (8), 6012–6022.
         https://doi.org/10.1021/acsaem.9b01124.

(17)   Vallejos, S.; Umek, P.; Stoycheva, T.; Annanouch, F.; Llobet, E.; Correig, X.;
         De Marco, P.; Bittencourt, C.; Blackman, C. Single-Step Deposition of Au- and
         Pt-Nanoparticle-Functionalized Tungsten Oxide Nanoneedles Synthesized via
         Aerosol-Assisted CVD, and Used for Fabrication of Selective Gas Microsensor
         Arrays. *Adv. Funct. Mater.* **2013**, *23* (10), 1313–1322.
         https://doi.org/10.1002/adfm.201201871.

(18)   Buckingham, M. A.; Norton, K.; McNaughter, P. D.; Whitehead, G.; Vitorica-
         Yrezabal, I.; Alam, F.; Laws, K.; Lewis, D. J. Investigating the Effect of Steric
         Hindrance within CdS Single-Source Precursors on the Material Properties of
         AACVD and Spin-Coat-Deposited CdS Thin Films. *Inorg. Chem.* **2022**, *61*
         (21), 8206–8216. https://doi.org/10.1021/acs.inorgchem.2c00616.

(19)   Kevin, P.; Alghamdi, Y. G.; Lewis, D. J.; Azad, M. Materials Science in
         Semiconductor Processing Morphology and Band Gap Controlled AACVD of
         CdSe and CdS$_x$Se$_{1-x}$ Thin Fi Lms Using Novel Single Source Precursors : Bis
         (Diethyldithio / Diselenocarbamato) Cadmium (II). *Mater. Sci. Semicond.
         Process.* **2015**, *40,* 848–854. https://doi.org/10.1016/j.mssp.2015.07.076.

(20)   Liu, Z. 4.09 - Laser Applied Coatings. In *Shreir's Corrosion*; Cottis, B.,
         Graham, M., Lindsay, R., Lyon, S., Richardson, T., Scantlebury, D., Stott, H.,
         Eds.; Elsevier: Oxford, 2010; pp 2622–2635.
         https://doi.org/https://doi.org/10.1016/B978-044452787-5.00141-4.

(21)   Leskelä, M.; Niinistö, J.; Ritala, M. 4.05 - Atomic Layer Deposition. In
         Comprehensive Materials Processing; Hashmi, S., Batalha, G. F., Van Tyne, C.
         J., Yilbas, B., Eds.; Elsevier: Oxford, 2014; pp 101–123.

https://doi.org/https://doi.org/10.1016/B978-0-08-096532-1.00401-5.

(22) Guo, X.; Zhang, Q.; Ding, X.; Shen, Q.; Wu, C.; Zhang, L.; Yang, H. Synthesis and Application of Several Sol–Gel-Derived Materials via Sol–Gel Process Combining with Other Technologies: A Review. *J. Sol-Gel Sci. Technol.* **2016**, *79* (2), 328–358. https://doi.org/10.1007/s10971-015-3935-6.

(23) Sahu, N.; Parija, B.; Panigrahi, S. Fundamental Understanding and Modeling of Spin Coating Process: A Review. *Indian J. Phys.* **2009**, *83* (4), 493–502. https://doi.org/10.1007/s12648-009-0009-z.

(24) Cao, Z. 8 - Thin Film Growth for Thermally Unstable Noble-Metal Nitrides by Reactive Magnetron Sputtering. In *Thin Film Growth*; Cao, Z., Ed.; Woodhead Publishing Series in Electronic and Optical Materials; Woodhead Publishing, 2011; pp 185–210. https://doi.org/https://doi.org/10.1533/9780857093295.2.185.

(25) Wasa, K.; Matsushima, T. 9 - Micro-Fabrication by Sputtering. In *Handbook of Sputtering Technology (Second Edition)*; Wasa, K., Kanno, I., Kotera, H., Eds.; William Andrew Publishing: Oxford, 2012; pp 597–622. https://doi.org/https://doi.org/10.1016/B978-1-4377-3483-6.00009-7.

(26) Juhasz, J. A.; Best, S. M. 6 - Surface Modification of Biomaterials by Calcium Phosphate Deposition. In *Surface Modification of Biomaterials*; Williams, R., Ed.; Woodhead Publishing Series in Biomaterials; Woodhead Publishing, 2011; pp 143–169. https://doi.org/https://doi.org/10.1533/9780857090768.1.143.

(27) Potter, D. B.; Powell, M. J.; Parkin, I. P.; Carmalt, C. J. Aluminium/Gallium, Indium/Gallium, and Aluminium/Indium Co-Doped ZnO Thin Films Deposited: Via Aerosol Assisted CVD. *J. Mater. Chem. C* **2018**, *6* (3), 588–597. https://doi.org/10.1039/c7tc04003b.

(28) Rajeshkumar, S.; Bharath, L. V; Geetha, R. Chapter 17 - Broad Spectrum Antibacterial Silver Nanoparticle Green Synthesis: Characterization, and Mechanism of Action. In *Micro and Nano Technologies*; Shukla, A. K., Iravani Characterization and Applications of Nanoparticles, S. B. T.-G. S., Eds.; Elsevier, 2019; pp 429–444. https://doi.org/https://doi.org/10.1016/B978-0-08-

102579-6.00018-6.

(29)   Reed, S. J. B. *Electron Microprobe Analysis and Scanning Electron Microscopy in Geology*; Cambridge: Cambridge University Press: Cambridge, 2005; Vol. 9780521848. https://doi.org/10.1017/CBO9780511610561.

(30)   Baillot, R.; Deshayes, Y. 2 - Tools and Analysis Methods of Encapsulated LEDs; Baillot, R., Deshayes, Y. B. T.-R. I. of L. E. D. D. for P. L. A., Eds.; Elsevier, 2017; pp 43–106. https://doi.org/https://doi.org/10.1016/B978-1-78548-149-9.50002-X.

(31)   Mehrban, N.; Bowen, J. 5 - Monitoring Biomineralization of Biomaterials in Vivo; Narayan, R. J. B. T.-M. and E. of B. and their P. I. V., Ed.; Woodhead Publishing, 2017; pp 81–110. https://doi.org/https://doi.org/10.1016/B978-0-08-100603-0.00005-5.

(32)   Ismail, A. F.; Khulbe, K. C.; Matsuura, T. Chapter 3 - RO Membrane Characterization; Ismail, A. F., Khulbe, K. C., Matsuura, T. B. T.-R. O., Eds.; Elsevier, 2019; pp 57–90. https://doi.org/https://doi.org/10.1016/B978-0-12-811468-1.00003-7.

(33)   F76 Standard Test Methods for Measuring Resistivity and Hall Coefficient and Determining Hall Mobility in Single-Crystal Semiconductors. 2016. https://doi.org/10.1520/F0076-08R16E01.

Chapter 3 n-Type transparent and conductive Mo-doped ZnO thin films via aerosol assisted chemical vapor deposition

This chapter is adapted from work published in *ACS Appl. Electron. Mater.*: "*Transparent and Conductive Molybdenum-Doped ZnO Thin Films via Chemical Vapor Deposition*" [*ACS Appl. Electron. Mater.* 2020, **2**, 120-125; copyright 2019 American Chemical Society. DOI:10.1021/acsaelm.9b00647]. This work was completed by SS, JL, CC and myself. The main part of the work including thin film deposition, most of the characterization and analysis were carried out by myself. SS and CC provided many useful ideas, advice and supervision of the research. SS carried out the XPS analysis and the unit cell parameters were calculated by JL.
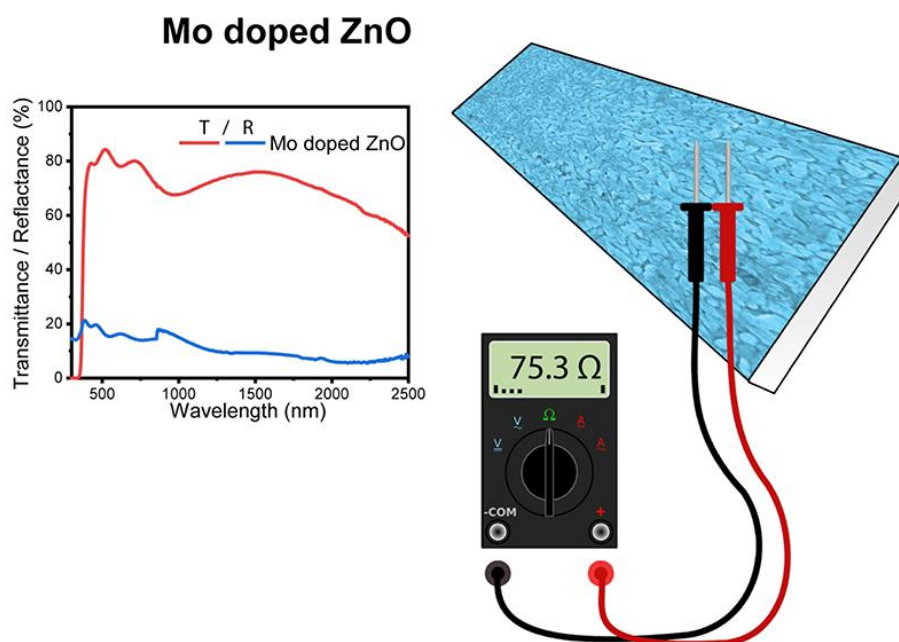
Representative image shows the excellent optical and electrical properties of the Mo-doped ZnO thin films.

3.1 General introduction

3.1.1 Background

ZnO is a non-toxic and relatively inexpensive semiconductor compared to the widely used and expensive In_2O_3. ZnO has a sufficiently wide band gap of 3.37 eV and shows intrinsic n-type conductivity, thought to originate from adventitious hydrogen.[1,2] Despite this the conductivity of nominally undoped ZnO is often too low (the resistivity is too high) for application in the electronic device area. To reduce the resistivity to 10^{-3} Ω.cm or below, extrinsic donor dopants are necessary. Al^{3+} and Ga^{3+} are widely used, as both are shallow donor dopants, i.e. the energy difference between the donor level and the CBM is sufficiently low that thermal ionization can occur at room temperature. Both Al^{3+} and Ga^{3+} are one electron donors when they replace Zn^{2+} in the ZnO lattice.[3] However, because of the small ionic radius of Al^{3+} (0.39 Å), ZnO:Al can suffer from poor stability.[3,4] Another donor dopant that is also often used is Ga^{3+} which has a larger ionic radius of 0.47 Å and shows better stability while donating one electron for conductivity.[3,4]

In the recent years, a strategy to further enhance the conductivity of ZnO by using even higher valence donor dopants (e.g. W, Nb and Mo) that can contribute more than one electron for conduction have been employed.[5–7] Molybdenum (Mo) is stable in the 4+ or 6+ oxidation states and thus when substitutionally doped on Zn sites, is able to contribute two or four electrons, respectively, into the conduction band of ZnO to enhance electrical conductivity. Moreover, the ionic radius of Zn^{2+}, Mo^{4+} and Mo^{6+} are 0.6 Å, 0.65 Å and 0.41 Å, respectively. Hence, Mo^{4+} or Mo^{6+} should be able to substitute for Zn^{2+} readily.[5,8] Other factors that have to be considered for suitability of the dopant in the host system is the preferred coordination geometry of the dopant compared to the host. In an ideal situation, both atoms would have the same preferred coordination number. In the case of ZnO, Zn is in a tetrahedral geometry bound to four oxygen atoms. Mo in MoO_2 is in an octahedral geometry bound to six oxygen atoms. However, although this may increase the formation energy necessary for Mo to

dope on Zn sites in ZnO and donate electrons for conductivity it does not stop it from occurring. Previous studies on Sc doped ZnO have show that Sc can successfully increase the conductivity of ZnO by occupying Zn sites, despite Sc preferring to be in in a octahedral geometry.[9] Comparing with typical dopants for ZnO thin films, Al will substitute for Zn in ZnO when ZnO is doped with Al. Two of the three electrons in the valence orbitals of Al (3s and 3p) are shared with the oxygen (forming Zn-O bonds) whilst the remaining valence electron of Al is loosely bound and occupies states close to the conduction band minimum of ZnO. At room temperature, the extra electron is excited to the conduction band and is free to move. This process increases the carrier concentration and thus increases the conductivity.[10] Similarly, Mo, B and P (the dopants studied for this thesis) are all shallow donors in ZnO in that the states that the extra valence electrons occupy are very close to the conduction band minima of ZnO such that thermal excitation can readily occur.[5,8,19–21,11–18]

Previous studies for Mo-doped ZnO have shown promising resistivities in the 10^{-3} and 10^{-4} Ω.cm range.[5,8,22,23] However, these films have, in most cases, been grown by ultra-high vacuum PVD techniques.[5,8,22] For example, ZnO:Mo thin films that were prepared via DC reactive magnetron sputtering and RF magnetron sputtering have quite low resistivities at 7.9×10^{-4} Ω.cm[5] and 9.2×10^{-4} Ω.cm,[8] respectively. To date, no Mo-doped ZnO films have been synthesized via CVD.

Phosphorus (P) is an interesting dopant candidate for ZnO as its multivalent nature existing in the III-, III+ and V+ states, technically allows it to be an n-type and/or p-type dopant via P^{3+}/P^{5+} on Zn^{2+} sites or P^{3-} on O^{2-} sites, respectively. Along with p-type conductivity, previous studies have shown an enhancement in electron density and n-type conductivity originating through the formation of P_{Zn} defects and P^{3+}, P^{5+} or P^{3-} related complexes.[24–28]

Boron (B) can also be considered as one prospective dopant to reduce the resistivities of ZnO based materials. Although B dopant only has +3 oxidation state and cannot offer as many electrons as some high valance dopants including $Mo^{6+/4+}$ and P^{5+} mentioned before, boron has abundant reserves with low cost and there have been

some investigations that reported good optical and electrical properties of B-doped ZnO thin films from some other synthesis technologies.[20,21]

In this chapter (Chapter 3), the growth of Mo-doped ZnO films on glass substrates through AACVD, a specialized form of CVD that is cost effective and easily scalable, operating at ambient pressure, has been investigated and discussed.[29,30]

In the Chapter 4, the effect of P doping on the material and optoelectronic properties of ZnO is investigated. The films were grown using AACVD to determine the suitability of P as a dopant for real world TCO applications and to study whether p or n type conductivity is achieved.[31]

In the Chapter 5, a series of B-doped ZnO (ZnO:B) thin films from two different solvents have been prepared and compared through AACVD technology. As the B dopant source is quite miscible in THF solvent but has relatively low miscibility in MeOH solvent, while the solubilities of the Zn precursor in these solvents is opposite, both the solvents THF and MeOH were chosen and used to prepare ZnO thin films via AACVD with different initial concentrations of B dopants

3.1.2 Project abstract

In this project, the molybdenum (Mo) doped ZnO thin films *via* the AACVD route were first synthesized and characterized. Thin films were grown using diethyl zinc, molybdenum hexacarbonyl, toluene and methanol. All films had a visible light transmittance of ~ 80% and electrical resistivity in the 10^{-3} Ω.cm region with the lowest resistivity of 2.6×10^{-3} Ω.cm observed for 0.6 at.% Mo-doped film. X-ray photoelectron spectroscopy (XPS) of the surface species and X-ray diffraction (XRD) based calculations of the ZnO unit cell parameters suggest that Mo is present in the 4+ oxidation state, thus contributing two electrons for electrical conduction for every Zn^{2+} ion replaced in the lattice.

3.2 Experiment methods

3.2.1 Film synthesis

Depositions were carried out under an N_2 (BOC Ltd., 99.99% purity) flow. Diethyl zinc [$ZnEt_2$] (15 wt.%) in toluene (99%), molybdenum hexacarbonyl ([$Mo(CO)_6$] (99%)) and methanol (99%) were purchased from Sigma. The [$ZnEt_2$] is pyrophoric and was handled under an inert atmosphere. The methanol was freshly dried over magnesium and stored over sieves prior to use while [$ZnEt_2$] and [$Mo(CO)_6$] were used as received. Toluene was purchased from Alfa Aesar and stored under alumina columns and dried through Anhydrous Engineering equipment. The glass substrates are float glass from Pilkington NSG. Glass substrates were cleaned using detergent, water and isopropanol then dried in a 70 °C oven.

[$ZnEt_2$] (0.5 g, 4.05 mmol) in toluene (20 mL) was placed in a glass bubbler. In a separate bubbler, [$Mo(CO)_6$] (X mol.% based on Zn, X = 0 - 4) was dissolved in methanol (20 mL). Both bubblers were connected to the CVD reactor by a Y piece. The solutions were atomised through a piezoelectric device (Johnson Matthey liquifog®). The aerosol mists were delivered to the AACVD reaction chamber via a Y piece and a water-cooled baffle to avoid blockage resulting from reactions taking place in the normal baffle at high temperature and passed over the heated substrate (float glass with a SiO_2 barrier layer) using N_2 carrier gas at 0.6 L min^{-1} x 2.[32] Depositions were carried out at 450 °C and lasted until the precursor solution was fully used. After the deposition the substrates were cooled under a flow of N_2. The glass substrate was not removed until the graphite block was cooled to below 50 °C. The films on the substrates were handled and stored in air.

3.2.2 Film characterisation

Scotch tape test was performed to test adhesion using previous literature methods.[33] A modified Bruker-Axs D8 diffractometer with parallel beam optics and a PSD LynxEye silicon strip detector was used for the X-ray diffraction (XRD), in which the

range measured range was 10 - 65° 2θ with a monochromated Cu K$_\alpha$ source operated at 40 kV with 30 mA emission current with 0.5° as incident beam angle and 0.05° at 1 s/step as step frequency. The surface elemental composition was investigated via X-ray photoelectron spectroscopy (XPS) by a Thermo Scientific K-alpha photoelectron spectrometer using monochromatic Al$_{k\alpha}$ radiation. Higher resolution scans were recorded for the principal peaks of molybdenum (3d) for Chapter 3, P (2p) for Chapter 4, boron (B 2s) for Chapter 5, zinc (2p), oxygen (1s) and carbon (1s) for all three chapters at a pass energy of 50 eV, and the data was dealt by CasaXPS software with calibration by adjusting the binding energy of adventitious carbon at 284.5 eV. The surface morphologies were evaluated through a JEOL JSM-6301F Field Emission Scanning Electron Microscopy (SEM) with 5 keV as accelerating voltage (samples were coated with gold to avoid charging). The Filmetrics F20 thin-film analyzer were used to measure the thickness of thin films. A Perkin Elmer Fourier transform Lambda 950 spectrometer was used to scan from 2500 nm to 300 nm to measure the optical properties of all films. The electrical properties including bulk concentration (n), carrier mobility (μ) and resistivity (ρ) were analyzed via Hall effect measurements based on the van Der Pauw method with a permanent magnet (0.58 T) and a constant current (1 mA, 1μA).

3.3 Results and Discussion

In the investigation of Mo-doped ZnO thin films, many different experiments were initially attempted. This included using the Zn source [Zn(OAc)$_2$·2H$_2$O] initially in combination with Mo(CO)$_6$. The deposited films were screened initially using the characterization techniques of XRD, XPS, SEM and Hall effect measurement. XRD showed formation of the wurtzite ZnO phase without any visible signs for any crystalline secondary phases existing. XPS results confirmed the presence of both Mo^{6+} and Mo^{4+} on the surface of samples. The Mo^{6+} is believed to be from surface oxidation of Mo in the samples whereas Mo^{4+} is likely from substitutional Mo^{4+} in the ZnO lattice. However, the lowest resistivity measured for this series of Mo:ZnO films formed from [Zn(OAc)$_2$·2H$_2$O] was only 5.7×10^{-2} Ω.cm at 6.1 at.% of Mo. Since, this is too high for practical applications more detailed characterizations and further depositions using [Zn(OAc)$_2$·2H$_2$O] as the Zn precursor were not continued. Instead, [ZnEt$_2$] was chosen as the Zn source as reports in the literature indicated that this precursor results in a lower baseline ZnO resistivity presumably resulting from adventitious hydrogen doping.[1,2,32]

Nominally undoped and Mo-doped ZnO films were grown on glass substrates from the two-pot AACVD reaction of [Mo(CO)$_6$] in methanol and [ZnEt$_2$] in toluene at 450 °C under N$_2$ flow and the scheme of the chemical reactions for the formation of undoped and Mo-doped ZnO thin films are shown in Equations (1) and (2).[30] All films were well adhered to the substrate and passed the Scotch tape test.[34] The bulk Mo concentration in the films was determined through energy dispersive X-ray spectroscopy (EDS) to be 0, 0.3, 0.4, 0.6, 1.0 and 1.6 at.%, as shown in Table 3.1 as well as the film thickness determined through side on SEM measurement.

$$\text{ZnEt}_2 + \text{MeOH} \xrightarrow[\text{dry toluene}]{450\,°C,\,N_2} \text{ZnO} \qquad \text{(1)}$$

$$\text{ZnEt}_2 + \text{MeOH} + \text{Mo(CO)}_6 \xrightarrow[\text{dry toluene}]{450\,°C,\,N_2} \text{Mo}:\text{ZnO} \qquad \text{(2)}$$
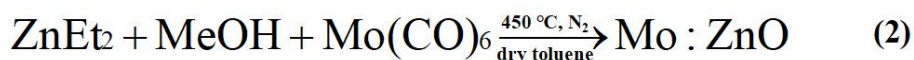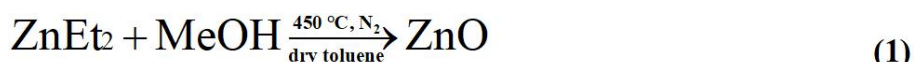
Table 3.1: The results of bulk concentrations of Mo (at.%) on the ZnO films via EDS analysis.

Initial Mo concentration / mol.%	Mo concentration / at.%	Film thickness / nm
0	0	350
0.5	0.3(4)	560
1.0	0.4(0)	250
2.0	0.6(7)	429
3.0	1.0(0)	386
4.0	1.6(7)	789

Figure 3.1(a) shows the X-ray diffraction patterns for the pure and Mo-doped ZnO thin films. Bragg reflections were found at 31.8, 34.4, 36.3, 47.5, 56.6 and 63.0°, and these match the standard ZnO pattern and represent the (100), (002), (101), (102),(110) and (103) planes of the wurtzite phase of ZnO. The slight shift between Mo doped ZnO thin films and undoped films may be due to the change of unit cell volume after the larger Mo^{4+} (0.65 Å > Zn^{2+} (0.60 Å)) ions were doped into the ZnO thin films. No secondary oxide phases for zinc and/or molybdenum were visible. An estimation of the crystallite size via the Scherrer equation showed that Mo doping had no significant effect.[35] The specific data of the crystallite size is shown in Table 3.3 and discussed below in combination with the analysis of the X-ray photoelectron spectroscopy (XPS) results.[30]
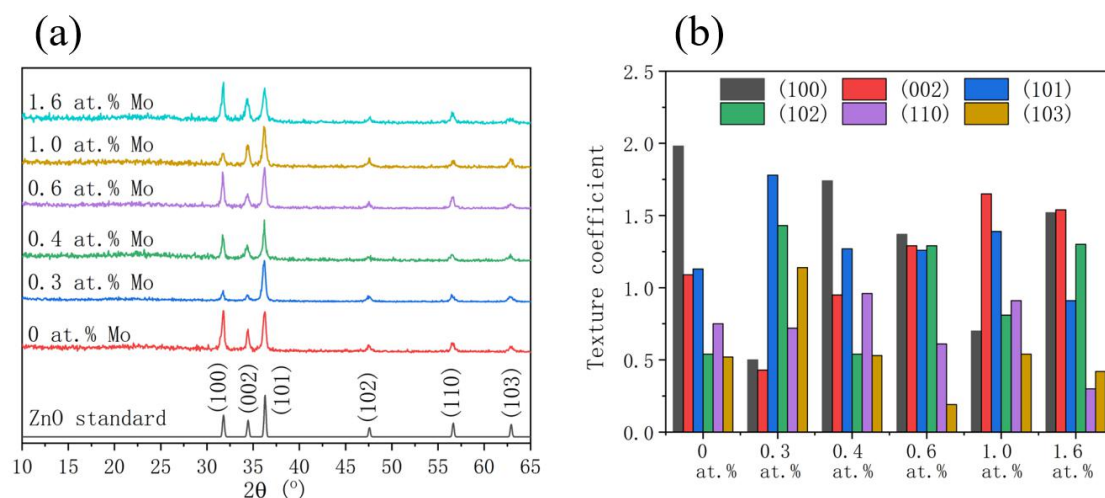
Figure 3.1: (a) XRD patterns describing the standard, pure and Mo-doped ZnO films prepared at 450 °C to be in the wurzite phase of ZnO. No secondary phases were visible. (b) Results of the texture coefficient calculation. A TC value of above 1 declares preference in that direction.

Typical of AACVD grown thin films, in comparison with the standard pattern, all the films studied here showed degrees of preferred orientation in various crystallographic directions. The preferred orientation was quantified by determining the texture coefficient (TC) for each plane with the results shown in Figure 3.1(b), where TC values above one indicates a preference for that plane and a TC value below one is a lack of preference.

The texture coefficient (TC) is given by:[36,37]

$$TC = \frac{(I_{(hkl)coat}/I_{(hkl)standard})}{(\frac{1}{n})[\sum_{1}^{n}(I_{(hkl)coat}/I_{(hkl)standard})]} \tag{3.01}$$

Where $I_{(hkl)coat}$ is the diffraction intensities of the (hkl) reflection planes for the textured coating surface, $I_{(hkl)standard}$ is the standard diffraction intensities of the untextured reference surface from the JCPDS card and n is the number of the reflections during the whole measurement.

The pure ZnO film prefers to grow on the (100) plane and illustrates a lack of growth in the (102), (110) and (103) planes. Again, this is likely a result of substrate influence based on the substrate-induced strain leading to different matching degrees between the film and the substrate, which can have significant effect on the grain boundary density and crystallite size.[38] With Mo doping, in most cases, the (100) and (101) planes are preferred, with the (002) plane also preferred but only at the higher doping levels of 0.6, 1.0 and 1.6 at.%. This is atypical of previous reports of Mo-doped ZnO (ZnO:Mo) thin films and cation (Al, Ga, W, Sc and Mg) doped ZnO in general, which all show only a strong preference for the (002) plane.[5,8,9,15,22,23,39–42] This is expected as the (002) plane has the lowest surface energy in the ZnO crystal. Furthermore, it was found that there was a significant decrease of the maximum peak intensities when the concentration of Mo dopants was relatively high (1.0 and 1.6 at.%), which demonstrates the disorder in the crystal structures leading to an increase of the resistivities of the thin films.[30,43]

The scanning electron microscopy (SEM) images of the ZnO and ZnO:Mo thin films can be seen in Figure 3.2. The nominally pure film illustrates a morphology consisting of platelet like features of varying sizes randomly orientated. The morphology of ZnO films is dependent on a range of factors including substrate, substrate temperature, carrier gas, precursor and oxidant source. ZnO films grown on glass from [ZnEt$_2$] through AACVD often have platelet like features such as the ones seen here. Upon the introduction of Mo, the ZnO films appear to become flatter with the morphology composed of globular grains of various dimensions that were parallel to the substrate. This is supported by the XRD results where preferred orientation was observed in various crystallographic directions for the ZnO:Mo films. This demonstrates that crystal growth was taking place evenly as opposed to in one particular plane, for example, the (002) which often grows perpendicular to the substrate leading to a more textured morphology.[30]
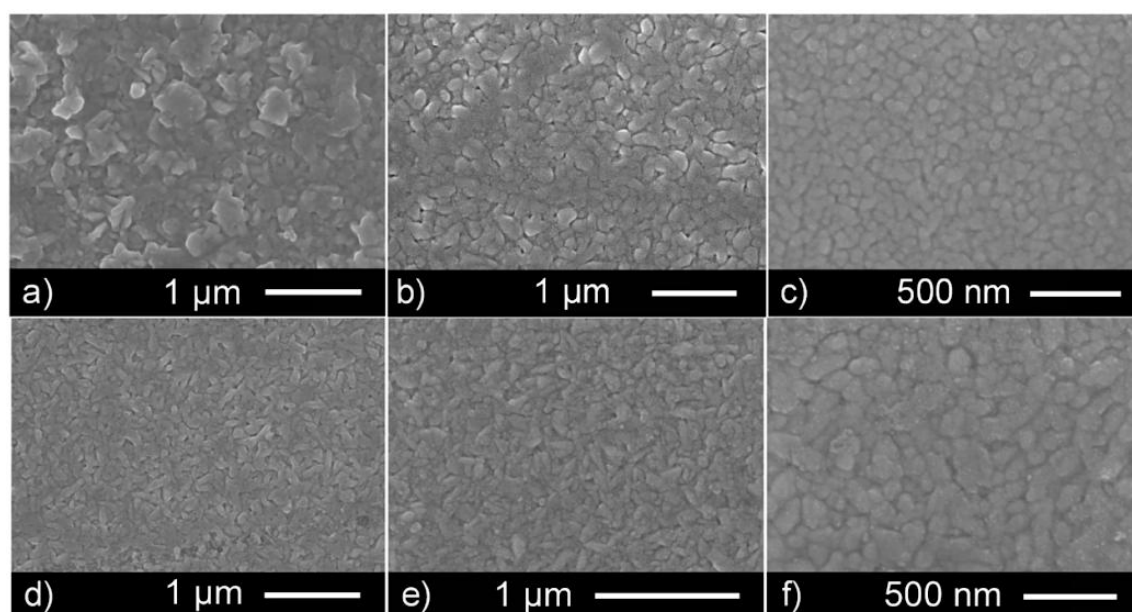
Figure 3.2: SEM images for the morphology of the a) pure and b) 0.3, c) 0.4, d) 0.6, e) 1.0 and f) 1.6 at.% Mo-doped ZnO films prepared via AACVD.

The X-ray photoemission spectroscopy (XPS) results for the deposited thin films can be found in Figure 3.3 and Table 3.2. As expected the oxidation state of Zn in all cases was 2+, with a binding energy of 1022.1 eV observed for 2p$_{3/2}$, which corresponds well with literature results for ZnO (Figure 3.3(a)).[44] For the Mo doped

samples the $Zn_{3/2}$ peak position generally shifts to slightly lower values between 1021.5-1021.8 eV (Figure 3.3 (a)), which also corresponds to Zn^{2+} well.[44] Figure 3.3(b) illustrates the high resolution scans in the Mo 3d region, which were carried out for all thin films. For dopant concentrations between 0.3 and 0.6 at.%, only a small bump with a low signal to noise ratio was observed and thus peak fitting to determine oxidation state was not practical (Figure 3.3(b)). For the 1.0 and 1.6 at.% Mo films, peak fitting of the asymmetric Mo 3d peaks was carried out using a pair of doublets. The primary $3d_{5/2}$ peak for both films was centered at 232.2 eV, matching Mo^{6+} with the secondary $3d_{5/2}$ peak situated at 230.4 eV and corresponding to Mo^{4+}.[45]
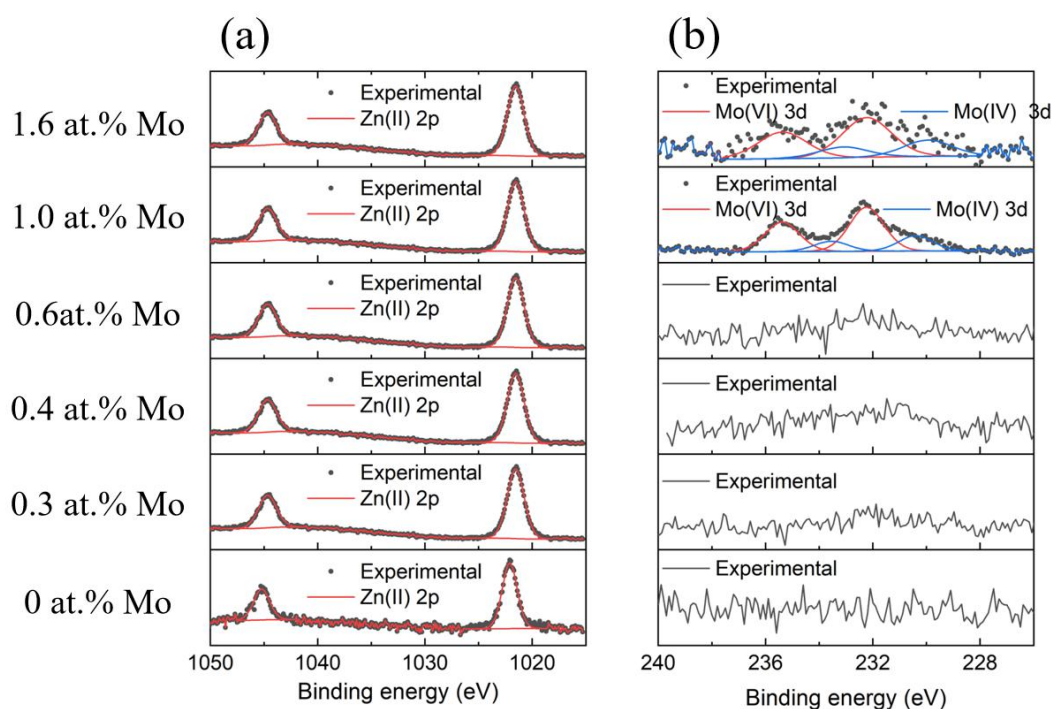
Figure 3.3: Core level XPS test showing the oxidation states of the (a) Zn and (b) Mo on the surface of the pure and Mo doped ZnO films.

The Mo^{6+} observed on the surface of both the 1.0 and 1.6 at.% doped films most probably results from surface oxidation and has been previously reported for Mo-doped metal oxides.[46] Without bulk analytical techniques such as hard XPS (HAXPES), it is difficult to confirm the oxidation state of the Mo within the bulk, however the detection of Mo^{4+} on the surface despite surface oxidation and the ionic radius of Zn^{2+} (0.6 Å) being more closely matched to that of Mo^{4+} (0.65 Å) than that

of Mo^{6+} (0.41 Å), suggests that Mo^{4+} is likely the principle form in the bulk. This suggests that the oxidation state of the majority of the Mo in the films is +4 while some Mo on the surface of ZnO films has been oxidized to +6. This is confirmed by the unit cell parameters calculations that displayed upon doping an expansion of the ZnO lattice as opposed to a contraction.

Table 3.2: The positions of Mo 3d from XPS analysis for the ZnO:Mo thin films prepared at 450 ⁰C through AACVD

Dopants Mo concentrations (at.%)	Positions of Mo 3d from XPS analysis (eV)	
	$3d_{3/2}$	$3d_{5/2}$
0	-	-
0.3	-	-
0.4	-	-
0.6	-	
1.0	235.2	232.1
1.6	235.2	232.1

The unit cell parameters of pure and doped films were determined by the modeling of the XRD patterns using JADE software (Table 3.3). The parameters *a* and *c* and the volume for the nominally undoped ZnO were calculated to be 3.2522(2), 5.2103(3) Å and 47.724(0)Å³, respectively. These values are slightly larger than the standard values (3.243, 5.195 Å and 47.3162 Å³) for wurtzite ZnO, primarily due to substrate induced stain on the CVD grown thin films.[38,47] Upon doping with Mo, the unit cell expands linearly (intercept = 47.724(1) Å³, slope = 0.16(3) with dopant concentration (Figure 3.4). This also suggests that substitutional doping is indeed taking place with Mo replacing Zn as opposed to only MoO_x phase formation.

Table 3.3: The unit cell parameters for the pure and Mo doped ZnO films grown through AACVD

Mo concentration /	Unit cell parameters

at.%	a / Å	c / Å	Volume / Å^3
0	3.2522(2)	5.2103(3)	47.724(0)
0.3	3.252(2)	5.21(3)	47.72(2)
0.4	3.254(2)	5.212(6)	47.80(1)
0.6	3.256(2)	5.211(5)	47.85(3)
1.0	3.257(2)	5.205(2)	47.82(5)
1.6	3.257(3)	5.212(6)	47.88(20)
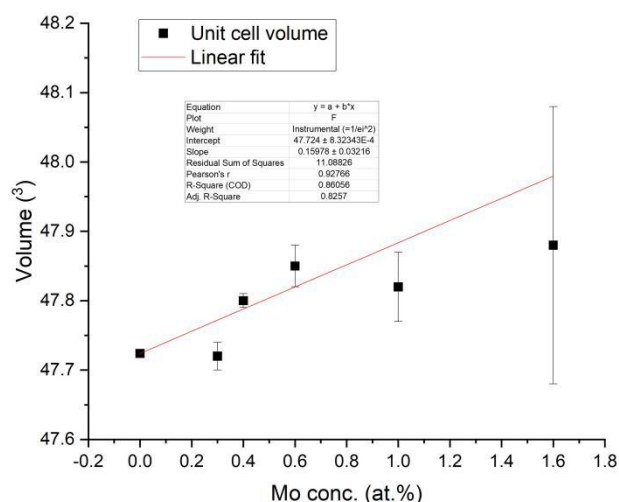
Figure 3.4: Graph showing the liner relationship between the Mo concentration in the AACVD ZnO films and the ZnO unit cell volume.

Figure 3.5 illustrates the bulk concentration, carrier mobility and resistivity of the ZnO and Mo-doped ZnO films determined from the Hall measurements. Hall measurements confirmed that electrons were the majority carrier for the Mo:ZnO thus making the films n-type TCOs. The nominally undoped sample has a bulk concentration of 1.31×10^{20} cm^{-3} and a mobility of 16.19 cm^2 V^{-1} s^{-1} leading to a resistivity of 3.7×10^{-3} Ω.cm. The bulk concentration is high for an undoped ZnO sample but not atypical of ZnO films grown using [ZnEt$_2$].[32] Though not fully understood, the high intrinsic conductivity is attributed to adventitious hydrogen.[1,2,32] Upon incorporation of Mo into the lattice, there is a slight drop in the bulk concentration to 1.01×10^{20} cm^{-3} (presumably due to possible self-compensating

mechanisms resulting from the acceptor defects which has contrary effect with dopants),[48] a drop in the carrier mobility and thus an increase in the resistivity to 4.9×10^{-3} Ω.cm. The lowest resistivity of 2.6×10^{-3} Ω.cm was measured for the 0.6 at.% Mo concentration arising primarily from a high bulk concentration of 2.4×10^{20} cm^{-3} as two donor electrons are released for conduction for every Zn^{2+} substituted with Mo^{4+}. At higher concentrations of Mo (1.0 and 1.6 at.%) the bulk concentration decreases (1.2×10^{20} and 0.6×10^{20} cm^{-3}, respectively) due to self-compensation mechanisms that are known to exist at high levels of higher valance cation doping in ZnO. In addition, due to the solubility limits of transition metals doping in the ZnO usually being low, with most around 1%,[49] at this concentration (Mo at.%), the solubility limits of the Mo-doping in ZnO films may have been reached, which means doping more Mo cannot contribute more to the electrical properties of the thin films. This led to an increase in resistivity to 4.6 and 8.2×10^{-3} Ω.cm. Briefly, the self-compensating mechanism always exists and keeps enhancing as Mo isdoped in ZnO films leading to the increase of resistivities.[48] When the other competitive mechanism to reduce resistivities, namely doping Mo into ZnO lattices resulting in the increase of bulk concentration, cannot have a greater influence on the ZnO thin films, the resistivity may show an rising trend. This results in the resistivity of the Mo-doped ZnO films decreasing if this mechanism is above the self-compensating mechanism. In addition, the carrier mobility of the ZnO:Mo films with lowest resistivity (0.6 at.%) was 10.2 cm^2 V^{-1} s^{-1}, which is above the highest carrier mobility data of Sc-doped ZnO (7.5 cm cm^2 V^{-1} s^{-1}),[9] Al-doped ZnO (9.0 cm cm^2 V^{-1} s^{-1}),[43] Ga-doped ZnO (10.1 cm cm^2 V^{-1} s^{-1})[43] and In-doped ZnO (5.1 cm cm^2 V^{-1} s^{-1})[43] synthesized via AACVD. This may be the result of the Zn source that was used in this study ($ZnEt_2$ dissolved in toluene), which may have more free-living hydrogen compared with other commonly used Zn source such as zinc acetate dihydrate ($[Zn(OAc)_2 \cdot 2H_2O]$) and zinc acetylacetonate ($[Zn(acac)_2]$).[1,2,32] The high level of carrier mobility can also lead to relatively low resistivity.
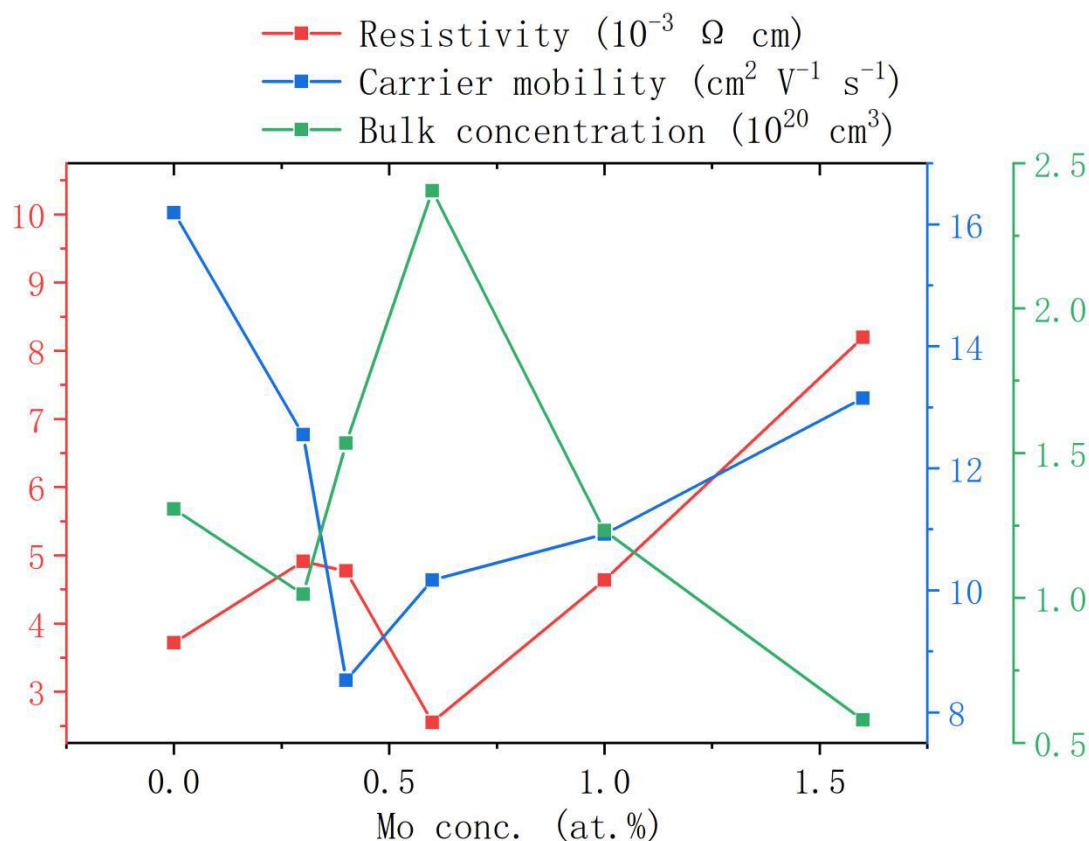
Figure 3.5: The electrical properties of the undoped and Mo-doped ZnO films derived from Hall measurements showing the trend in bulk concentration, carrier mobility and resistivity.

The electrical properties reported in the literature for ZnO:Mo films grown through PVD techniques including reactive magnetron sputtering and radio frequency magnetron sputtering shown in Table 3.4 are lower compared to the AACVD results in this project. Xiu *et al* reported a resistivity that is relatively low at 9.2×10^{-4} Ω.cm for RF magnetron grown films on glass substrates.[8] Another low resistivity of 7.9×10^{-4} Ω.cm was achieved by Wu *et al* for reactive magnetron sputtered films.[5] Such low resistivities were obtained and result from high carrier mobilities of 30.0 and 27.3 V^{-1} s^{-1}, which were nearly three times larger than what was seen for the films in this study. However, the synthetic route used here is AACVD, which is much more convenient with relatively lower cost comparing to some other synthetic technology,[50] and the resistivity of 2.6×10^{-3} Ω.cm for the 0.6 at.% Mo doped ZnO film in this study is the lowest resistivity recorded for a ZnO:Mo film synthesized via a CVD route. Moreover, comparing with some other doped ZnO films with the same synthetic method (AACVD) as ZnO:Mo film in this study, the ZnO:Mo film showed

relatively low resistivity of 2.6×10^{-3} Ω.cm, while the lowest resistivity of Al-doped ZnO, Ga-doped ZnO and In-doped ZnO were 0.5×10^{-2} Ω.cm,[43] 1.3×10^{-2} Ω.cm[43] and 1.7×10^{-2} Ω.cm,[43] respectively. Mo^{4+} can offer two extra free electrons while Al^{3+}, Ga^{3+} and In^{3+} only can offer one extra free electron, which further enhances the electron density resulting in the better electronic properties. Comparison with doped ZnO thin films prepared from the same Zn source, diethylzinc, some former results are shown in Table 3.5, the electrical properties are also at similar excellent level to be considered as one potential TCOs materials.

Table 3.4: Comparison with some other Mo doped ZnO thin films from different synthetic routes

Zn precursor	Dopant(s)	Dopant conc.	ρ ($\times$ 10^{-3} Ω.cm)	n ($\times$ 10^{20} cm^{-3})	μ (cm^2 V^{-1} s^{-1})	Ref
ZnO	Mo	RF magnetron sputtering	0.92	2.3	30	(8)[8]
pure metal zinc	Mo	reactive magnetron sputtering	0.79	3.1	27.3	(5)[5]
diethylzinc	Mo	AACVD	2.6	2.4	10.2	This project[30]

Table 3.5: Comparison with some other doped ZnO thin films through AACVD from the same Zn precursor

Zn precursor	Dopant(s)	Dopant conc.	ρ ($\times$ 10^{-3} Ω.cm)	n ($\times$ 10^{20} cm^{-3})	μ (cm^2 V^{-1} s^{-1})	Ref
diethylzinc	Ga	AACVD	0.79	4.23	18.7	(51)[51]
diethylzinc	Ga	AACVD	0.47	8.99	14.7	(52)[52]
diethylzinc	Al/F	AACVD	1.85	3.47	9.7	(53)[53]
diethylzinc	B	LP-MOCVD	1.05	-	-	(54)[54]
diethylzinc	P	ALD	3	1.3	8.4	(18)[18]
diethylzinc	Mo	AACVD	2.6	2.4	10.2	This project[30]

Figure 3.6 displays the ultraviolet-visible (UV-vis) spectra for the films on glass substrates from 300 to 2500 nm. The average transmittance of visible light (400 - 700 nm) for all films was ca. 80% and comparable to the PVD and spray pyrolysis grown films reported in literature.[5,8,23] Generally, the transmittance in the near infrared region reduces with rising bulk concentration. The reflectance of the films was on average ≥20% across all wavelengths and again comparable to literature findings.[5,8,23] The optical band gap was determined using the Tauc method shown in Figure 3.7. Both the pure and the doped films illustrated a band gap between 3.3 - 3.4 eV, matching to the expected value of 3.37 eV shown in the Table 3.6.
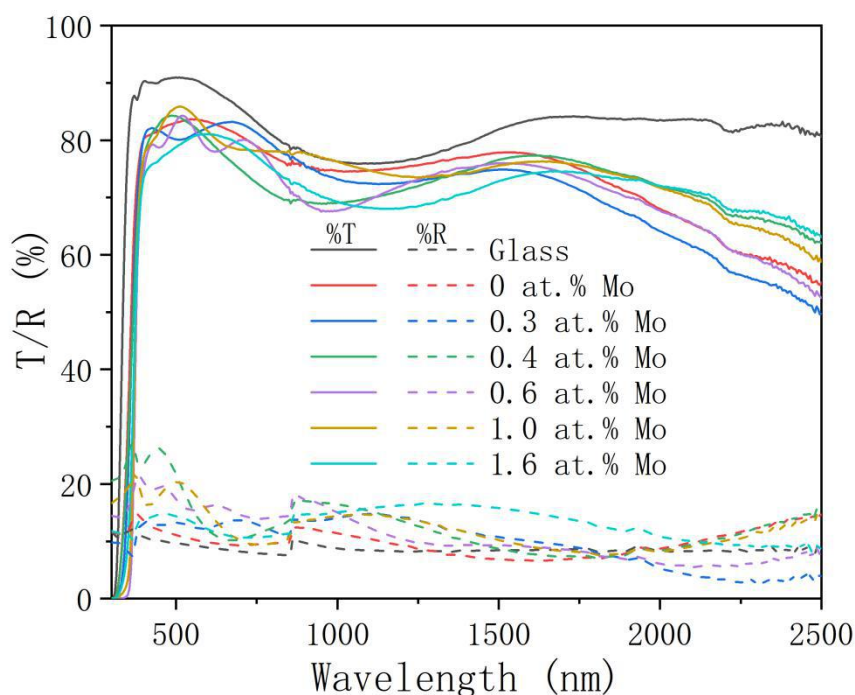
Figure 3.6: The optical data for the pure and Mo-doped ZnO films on glass substrates demonstrating the UV/vis spectra.
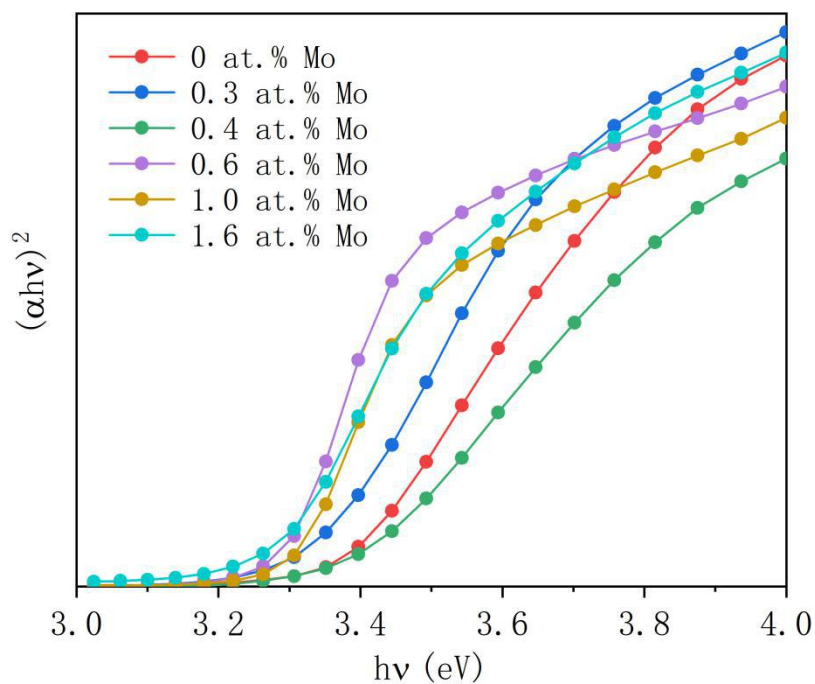
Figure 3.7: The Tauc plot for the pure and Mo-doped ZnO films on glass substrates calculating from the UV/vis data.

Table 3.6: Band gaps (E_g) of ZnO films with different Mo at.% calculated from UV-vis data

Mo atomic%	Standard	0	0.3	0.4	0.6	1.0	1.6
Band gaps (E_g) / eV	3.37	3.4	3.3	3.4	3.3	3.3	3.3

3.4 Conclusion

In this project, polycrystalline ZnO and Mo-doped ZnO thin films were grown on glass substrates using AACVD. XRD analysis showed all films to have no visible phase separation, with the unit cell parameters calculated to show an expansion in the ZnO lattice with Mo incorporation. This suggests that Mo^{4+}, with the larger ionic radius compared to Zn^{2+}, was the primary dopant instead of Mo^{6+}. XPS analysis of the surface illustrated both Mo^{4+} and Mo^{6+} (possibly due to surface oxidation) were present. Hall effect measurements displayed all films had low resistivity with the 0.6 at.% ZnO:Mo film having the minimum resistivity of 2.6×10^{-3} Ω.cm owing to a relatively high bulk concentration of 2.4×10^{20} cm^{-3}. This is the lowest resistivity reported for a ZnO:Mo film on glass deposited from a CVD route and the only reported instance of electrically conductive ZnO:Mo thin films having been grown via AACVD, which has been considered as a prospective synthetic technology.[30]

3.5 References

(1)   Mccluskey, M. D.; Jokela, S. J. Defects in ZnO. *J. Appl. Phys.* **2009**, *106* (7). https://doi.org/10.1063/1.3216464.

(2)   Janotti, A.; Van De Walle, C. G. Native Point Defects in ZnO. *Phys. Rev. B - Condens. Matter Mater. Phys.* **2007**, *76* (16), 1–22. https://doi.org/10.1103/PhysRevB.76.165202.

(3)   Ellmer, K.; Bikowski, A. Intrinsic and Extrinsic Doping of Zno and Zno Alloys. *J. Phys. D. Appl. Phys.* **2016**, *49* (41), 413002.

(4)   Sanger, A.; Kang, S. B.; Jeong, M. H.; Kim, C. U.; Baik, J. M.; Choi, K. J. All-Transparent NO_2 Gas Sensors Based on Freestanding Al-Doped ZnO Nanofibers. *ACS Appl. Electron. Mater.* **2019**, *1* (7), 1261–1268. https://doi.org/10.1021/acsaelm.9b00210.

(5)   Wu, C.; Shen, J.; Ma, J.; Wang, S.; Zhang, Z.; Yang, X. Electrical and Optical Properties of Molybdenum-Doped ZnO Transparent Conductive Thin Films Prepared by Dc Reactive Magnetron Sputtering. *Semicond. Sci. Technol.* **2009**, *24* (12). https://doi.org/10.1088/0268-1242/24/12/125012.

(6)   Can, M. M.; Fırat, T.; Shah, S. I. Journal of Magnetism and Magnetic Materials Magnetoelectrical Properties of W Doped ZnO Thin Films. *J. Magn. Magn. Mater.* **2012**, *324* (23), 4054–4060. https://doi.org/10.1016/j.jmmm.2012.07.014.

(7)   Shao, J.; Dong, W.; Li, D.; Tao, R.; Deng, Z.; Wang, T.; Meng, G.; Zhou, S.; Fang, X. Metal-Semiconductor Transition in Nb-Doped ZnO Thin Films Prepared by Pulsed Laser Deposition. *Thin Solid Films* **2010**, *518* (18), 5288–5291. https://doi.org/10.1016/j.tsf.2010.04.068.

(8)   Xiu, X.; Pang, Z.; Lv, M.; Dai, Y.; Ye, L.; Han, S. Transparent Conducting Molybdenum-Doped Zinc Oxide Films Deposited by RF Magnetron Sputtering. *Appl. Surf. Sci.* **2007**, *253* (6), 3345–3348. https://doi.org/10.1016/j.apsusc.2006.07.024.

(9)   Dixon, S. C.; Sathasivam, S.; Williamson, B. A. D.; Scanlon, D. O.; Carmalt, C. J.; Parkin, I. P. Transparent Conducting N-Type ZnO:Sc-Synthesis, Optoelectronic Properties and Theoretical Insight. *J. Mater. Chem. C* **2017**, *5* (30), 7585–7597. https://doi.org/10.1039/c7tc02389h.

(10)   Janotti, A.; Van de Walle, C. G. Fundamentals of Zinc Oxide as a Semiconductor. *Reports Prog. Phys.* **2009**, *72* (12), 126501-126501 (29). https://doi.org/10.1088/0034-4885/72/12/126501.

(11)   Dixon, S. C.; Scanlon, D. O.; Carmalt, C. J.; Parkin, I. P. N-Type Doped Transparent Conducting Binary Oxides: An Overview. *J. Mater. Chem. C* **2016**, *4* (29), 6946–6961. https://doi.org/10.1039/c6tc01881e.

(12)   Minami, T. Transparent Conducting Oxide Semiconductors for Transparent Electrodes. *Semicond. Sci. Technol.* **2005**, *20* (4). https://doi.org/10.1088/0268-1242/20/4/004.

(13)   Mallick, A.; Basak, D. Revisiting the Electrical and Optical Transmission Properties of Co-Doped ZnO Thin Films as n-Type TCOs. *Prog. Mater. Sci.* **2018**, *96*, 86–110. https://doi.org/10.1016/j.pmatsci.2018.03.004.

(14)   Delahoy, A. E.; Guo, S. Transparent Conducting Oxides for Photovoltaics. *Handb. Photovolt. Sci. Eng.* **2011**, *32* (MARCH 2007), 716–796. https://doi.org/10.1002/9780470974704.ch17.

(15)   Chopra, K. L.; Major, S.; Pandya, D. K. Transparent Conductors—A Status Review. *Thin Solid Films* **1983**, *102* (1), 1–46. https://doi.org/https://doi.org/10.1016/0040-6090(83)90256-0.

(16)   Zhang, K. H. L.; Xi, K.; Blamire, M. G.; Egdell, R. G. P-Type Transparent Conducting Oxides. *J. Phys. Condens. Matter* **2016**, *28* (38). https://doi.org/10.1088/0953-8984/28/38/383002.

(17)   Li, Y.; Liu, Z.; Ren, J. Properties of Phosphorus-Doped Zinc Oxide Films Grown by Pulsed Laser Deposition. *J. Vac. Sci. Technol. A Vacuum, Surfaces, Film.* **2011**, *29* (3), 03A109. https://doi.org/10.1116/1.3554838.

(18)   Yuan, H.; Luo, B.; Campbell, S. A.; Gladfelter, W. L. Atomic Layer Deposition of P-Type Phosphorus-Doped Zinc Oxide Films Using Diethylzinc,

Ozone and Trimethylphosphite. *Electrochem. Solid-State Lett.* **2011**, *14* (5), 181–183. https://doi.org/10.1149/1.3537326.

(19) Kim, Y. Y.; Han, W. S.; Cho, H. K. Determination of Electrical Types in the P-Doped ZnO Thin Films by the Control of Ambient Gas Flow. *Appl. Surf. Sci.* **2010**, *256* (14), 4438–4441. https://doi.org/10.1016/j.apsusc.2010.01.035.

(20) Wong, L. H.; Lai, Y. S. Characterization of Boron-Doped ZnO Thin Films Prepared by Magnetron Sputtering with (100-x)ZnO-XB2O3 Ceramic Targets. *Thin Solid Films* **2015**, *583* (1), 205–211. https://doi.org/10.1016/j.tsf.2015.04.003.

(21) Pawar, B. N.; Cai, G.; Ham, D.; Mane, R. S.; Ganesh, T.; Ghule, A.; Sharma, R.; Jadhava, K. D.; Han, S. H. Preparation of Transparent and Conducting Boron-Doped ZnO Electrode for Its Application in Dye-Sensitized Solar Cells. *Sol. Energy Mater. Sol. Cells* **2009**, *93* (4), 524–527. https://doi.org/10.1016/j.solmat.2008.12.010.

(22) Yu, C.; Yang, K.; Shu, Q.; Yu, J. C.; Cao, F.; Li, X.; Zhou, X. Preparation, Characterization and Photocatalytic Performance of Mo-Doped ZnO Photocatalysts. *Sci. China Chem.* **2012**, *55* (9), 1802–1810. https://doi.org/10.1007/s11426-012-4721-8.

(23) Boukhachem, A.; Ouni, B.; Karyaoui, M.; Madani, A.; Chtourou, R.; Amlouk, M. Structural, Opto-Thermal and Electrical Properties of ZnO:Mo Sprayed Thin Films. *Mater. Sci. Semicond. Process.* **2012**, *15* (3), 282–292. https://doi.org/10.1016/j.mssp.2012.02.014.

(24) Doggett, B.; Chakrabarti, S.; O'haire, R.; Meaney, A.; Mcglynn, E.; Henry, M. O.; Mosnier, J. P. Electrical Characterisation of Phosphorus-Doped ZnO Thin Films Grown by Pulsed Laser Deposition. *Superlattices Microstruct.* **2007**, *42* (1–6), 74–78.

(25) Vaithianathan, V.; Lee, B.-T.; Kim, S. S. Pulsed-Laser-Deposited p -Type ZnO Films with Phosphorus Doping. *J. Appl. Phys.* **2005**, *98* (4).

(26) Chen, Z. Q.; Kawasuso, A.; Xu, Y.; Naramoto, H.; Yuan, X. L.; Sekiguchi, T.; Suzuki, R.; Ohdaira, T. Production and Recovery of Defects in Phosphorus-

Implanted ZnO. *J. Appl. Phys.* **2005**, *97* (1).

(27)   Heo, Y. W.; Ip, K.; Park, S. J.; Pearton, S. J.; Norton, D. P. Shallow Donor Formation in Phosphorus-Doped ZnO Thin Films. *Appl. Phys. A* **2004**, *78* (1), 53–57.

(28)   Heo, Y. W.; Park, S. J.; Ip, K.; Pearton, S. J.; Norton, D. P. Transport Properties of Phosphorus-Doped ZnO Thin Films. *Appl. Phys. Lett.* **2003**, *83* (6), 1128–1130.

(29)   Marchand, P.; Hassan, I. A.; Parkin, I. P.; Carmalt, C. J.; Marchand, P. Materials Fabrication. **2013**, 9406–9422. https://doi.org/10.1039/c3dt50607j.

(30)   Zhao, D.; Sathasivam, S.; Li, J.; Carmalt, C. J. Transparent and Conductive Molybdenum-Doped ZnO Thin Films via Chemical Vapor Deposition. *ACS Appl. Electron. Mater.* **2020**, *2* (1), 120–125. https://doi.org/10.1021/acsaelm.9b00647.

(31)   Zhao, D.; Li, J.; Sathasivam, S.; Carmalt, C. J. N-Type Conducting P Doped ZnO Thin Films via Chemical Vapor Deposition. *RSC Adv.* **2020**, *10* (57), 34527–34533. https://doi.org/10.1039/d0ra05667g.

(32)   Bhachu, D. S.; Sankar, G.; Parkin, I. P. Aerosol Assisted Chemical Vapor Deposition of Transparent Conductive Zinc Oxide Films. *Chem. Mater.* **2012**, *24* (24), 4704–4710. https://doi.org/10.1021/cm302913b.

(33)   Mittal, K. L. Adhesion Measurement of Thin Films. *Electrocompon. Sci. Technol.* **1976**, *3* (1), 21–42. https://doi.org/10.1155/apec.3.21.

(34)   System, M. H. V; Assurance, P.; Corporation, I. B. M. ADHESION MEASUREMENT OF THIN FILMS. **1976**, *3* (C), 21–42.

(35)   Qazi, S. J. S.; Rennie, A. R.; Cockcroft, J. K.; Vickers, M. Use of Wide-Angle X-Ray Diffraction to Measure Shape and Size of Dispersed Colloidal Particles. *J. Colloid Interface Sci.* **2009**, *338* (1), 105–110. https://doi.org/10.1016/j.jcis.2009.06.006.

(36)   Peng, B.; Xu, Y. X.; Du, J. W.; Chen, L.; Kim, K. H.; Wang, Q. Influence of Preliminary Metal-Ion Etching on the Topography and Mechanical Behavior of TiAlN Coatings on Cemented Carbides. *Surf. Coatings Technol.* **2022**, *432*

(January). https://doi.org/10.1016/j.surfcoat.2021.128040.

(37)   Elmkhah, H.; Zhang, T. F.; Abdollah-zadeh, A.; Kim, K. H.; Mahboubi, F. Surface Characteristics for the Ti-Al-N Coatings Deposited by High Power Impulse Magnetron Sputtering Technique at the Different Bias Voltages. *J. Alloys Compd.* **2016**, *688*, 820–827. https://doi.org/10.1016/j.jallcom.2016.07.013.

(38)   You, A.; Be, M. A. Y.; In, I. Effect of Substrate-Induced Strain on the Structural , Electrical , and Optical Properties of Polycrystalline Thin Films. **2005**, *2689* (2004). https://doi.org/10.1063/1.1769598.

(39)   You, A.; Be, M. A. Y.; In, I. Blueshift of near Band Edge Emission in Mg Doped ZnO Thin Films and Aging. **2005**, *4772* (December 2003). https://doi.org/10.1063/1.1690091.

(40)   Nunes, P.; Fortunato, E.; Tonello, P.; Braz Fernandes, F.; Vilarinho, P.; Martins, R. Effect of Different Dopant Elements on the Properties of ZnO Thin Films. *Vacuum* **2002**, *64* (3–4), 281–285. https://doi.org/10.1016/S0042-207X(01)00322-0.

(41)   Materials, S. Preparation and Characterization of Transparent Conducting ZnO : W Films by DC Magnetron Sputtering Preparation and Characterization of Transparent Conducting ZnO : W Films by DC Magnetron Sputtering. **2011**. https://doi.org/10.1088/1674-4926/32/4/043002.

(42)   Nishino, J.; Ohshio, S. Preparation of Aluminum-Doped Zinc Oxide Films. **1992**, No. 19, 1–4.

(43)   Potter, D. B.; Bhachu, D. S.; Powell, M. J.; Darr, J. A.; Parkin, I. P.; Carmalt, C. J. Al-, Ga-, and In-Doped ZnO Thin Films via Aerosol Assisted CVD for Use as Transparent Conducting Oxides. *Phys. Status Solidi Appl. Mater. Sci.* **2016**, *213* (5), 1346–1352. https://doi.org/10.1002/pssa.201532996.

(44)   Hung-Chun Lai, H.; Basheer, T.; Kuznetsov, V. L.; Egdell, R. G.; Jacobs, R. M. J.; Pepper, M.; Edwards, P. P. Dopant-Induced Bandgap Shift in Al-Doped ZnO Thin Films Prepared by Spray Pyrolysis. *J. Appl. Phys.* **2012**, *112* (8). https://doi.org/10.1063/1.4759208.

(45)   Choi, J. G.; Thompson, L. T. XPS Study of As-Prepared and Reduced Molybdenum Oxides. *Appl. Surf. Sci.* **1996**, *93* (2), 143–149. https://doi.org/10.1016/0169-4332(95)00317-7.

(46)   Bhachu, D. S.; Scanlon, D. O.; Sankar, G.; Veal, T. D.; Egdell, R. G.; Cibin, G.; Dent, A. J.; Knapp, C. E.; Carmalt, C. J.; Parkin, I. P. Origin of High Mobility in Molybdenum-Doped Indium Oxide. *Chem. Mater.* **2015**, *27* (8), 2788–2796. https://doi.org/10.1021/cm503896h.

(47)   Division, M.; Heights, L. The Wurtzite Z Parameter for Beryllium Oxide and Zinc Oxide. **1968**, No. Ii, 2254–2256. https://doi.org/10.1107/S0567740869005528.

(48)   Sno, F.; Swallow, J. E. N.; Williamson, B. A. D.; Whittles, T. J.; Birkett, M.; Featherstone, T. J.; Peng, N.; Abbott, A.; Farnworth, M.; Cheetham, K. J.; Warren, P.; Scanlon, D. O.; Dhanak, V. R.; Veal, T. D. Self-Compensation in Transparent Conducting. **2018**, *1701900*, 1–10. https://doi.org/10.1002/adfm.201701900.

(49)   Soumahoro, I.; Colis, S.; Schmerber, G.; Leuvrey, C.; Barre, S.; Ulhaq-Bouillet, C.; Muller, D.; Abd-Lefdil, M.; Hassanain, N.; Petersen, J.; Berrada, A.; Slaoui, A.; Dinia, A. Structural, Optical, Spectroscopic and Electrical Properties of Mo-Doped ZnO Thin Films Grown by Radio Frequency Magnetron Sputtering. *Thin Solid Films* **2014**, *566*, 61–69. https://doi.org/10.1016/j.tsf.2014.07.017.

(50)   Knapp, C. E.; Carmalt, C. J.; Knapp, C. E. Chem Soc Rev Solution Based CVD of Main Group Materials. **2016**, 1036–1064. https://doi.org/10.1039/c5cs00651a.

(51)   Ponja, S. D.; Sathasivam, S.; Parkin, I. P.; Carmalt, C. J. Highly Conductive and Transparent Gallium Doped Zinc Oxide Thin Films via Chemical Vapor Deposition. *Sci. Rep.* **2020**, *10* (1), 1–7. https://doi.org/10.1038/s41598-020-57532-7.

(52)   Sanchez-Perez, C.; Dixon, S. C.; Darr, J. A.; Parkin, I. P.; Carmalt, C. J. Aerosol-Assisted Route to Low-E Transparent Conductive Gallium-Doped Zinc Oxide Coatings from Pre-Organized and Halogen-Free Precursor. *Chem.*

Sci. **2020**, *11* (19), 4980–4990. https://doi.org/10.1039/d0sc00502a.

(53)   Ponja, S. D.; Sathasivam, S.; Parkin, I. P.; Carmalt, C. J. Transparent Conductive Aluminium and Fluorine Co-Doped Zinc Oxide Films via Aerosol Assisted Chemical Vapour Deposition. *RSC Adv.* **2014**, *4* (91), 49723–49728. https://doi.org/10.1039/c4ra09997d.

(54)   Chen, X. L.; Lin, Q.; Ni, J.; Zhang, D. K.; Sun, J.; Zhao, Y.; Geng, X. H. Textured Surface Boron-Doped ZnO Transparent Conductive Oxides on Polyethylene Terephthalate Substrates for Si-Based Thin Film Solar Cells. *Thin Solid Films* **2011**, *520* (4), 1263–1267. https://doi.org/10.1016/j.tsf.2011.04.199.

Chapter 4 n-Type transparent and conductive P-doped ZnO thin films via aerosol assisted chemical vapor deposition

This chapter is adapted from work published in *RSC Advances: "n-Type Conducting P doped ZnO Thin Films via Chemical Vapor Deposition"* [*RSC Adv.,* 2020, **10**, 34527-34533, Copyright the Royal Society of Chemistry 2020. DOI: 10.1039/d0ra05667g]. This work was completed by JL, SS, CC and myself. The main part of the work including thin film deposition, characterizations and analysis were carried out by myself. SS and CC provided many useful ideas, advice and supervision of the project. SS carried out the XPS analysis and JL provided ideas and calculated the unit cell parameters.
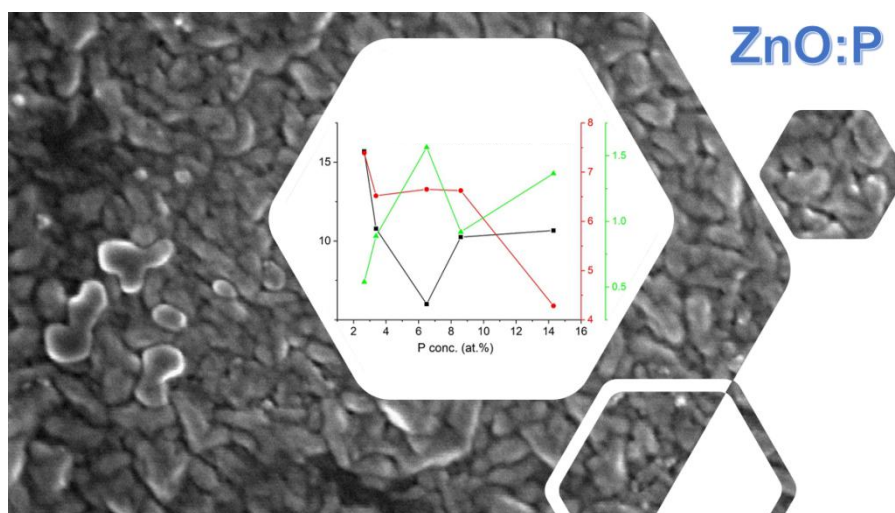
Representative image describing the improved electrical properties of ZnO:P thin films compared with undoped ZnO thin films showing the surface morphology in the background.

4.1 General introduction

In this study, P-doped ZnO thin films were grown on glass substrates via aerosol assisted chemical vapour deposition (AACVD). XPS results indicate the presence of the P^{5+} in the films whilst XRD and Hall effect data suggest that P has successfully doped into the ZnO to form a solid solution. P was able to enhance the n-type conductivity to 6.0×10^{-3} Ω.cm while maintaining visible light transmittance at $\sim$ 75%. The ZnO:P thins films were characterized by X-ray diffraction (XRD) studies that showed only Bragg peaks for the wurtzite ZnO phase. Lattice parameter calculations indicated a general expansion in the ZnO unit cell upon incorporation of the relative larger P(V) ions in place of the Zn(II) ions.

4.2 Experiment methods

4.2.1 Film synthesis

Depositions were carried out under N_2 (BOC Ltd., 99.99% purity) flow. Zinc acetate dihydrate ($Zn(OAc)_2 \cdot 2H_2O$), triethyl phosphate ($[PO(OEt)_3]$ (99%) and methanol (99%)) were purchased from Sigma. Glass substrates were cleaned by scrubbing in detergent, water and then rinsing isopropanol before being dried in a 70 °C oven. $[Zn(OAc)_2 \cdot 2H_2O]$ (0.40 g, 1.82 mmol) in methanol (20 mL) was placed in a glass bubbler. $[PO(OEt)_3]$ (x mol.% based on Zn, x = 0, 0.5, 1.0, 5.0, 7.0 and 10.0) was added in the same bubbler. The solution was atomised through a piezoelectric device (Johnson Matthey liquifog®). The aerosol mist was delivered to the AACVD reaction chamber and passed over the heated substrate (float glass with a SiO_2 barrier layer) using N_2 carrier gas at 1.0 L min^{-1}. Depositions were carried out at 500 °C and lasted until the precursor solution was fully used. After the deposition the substrates were cooled under a flow of N_2. The glass substrate was not removed until the graphite block was cooled to below 50 °C. The films on the substrates were handled and stored in air.

4.2.2 Film characterisation

The characterisations technology including XRD, XPS, SEM/EDS, UV-vis and Hall effect measurements were carried out on all the ZnO based thin films and the details are given in section 3.2.2.

4.3 Results and Discussion

AACVD was used to prepare undoped and P-doped ZnO films in this project from zinc acetate dihydrate [$Zn(OAc)_2 \cdot 2H_2O$] dissolved in methanol with varying amounts of triethylphosphate ($PO(OEt)_3$). The Zn source in this chapter is cheaper than that in the Chapter 3 ([$ZnEt_2$]), although [$Zn(OAc)_2 \cdot 2H_2O$] here cannot provide as much adventitious hydrogen as [$ZnEt_2$],[1–3] the dopant atom P^{5+} has higher valence and can contribute more free electrons than the dopant atom Mo^{4+} in Chapter 3 resulting in the similar level of the lowest resistivities ($\sim 10^{-3}$ Ω.cm) in these two chapters. Depositions were carried out at 500 °C under a N_2 atmosphere with 1.0 L min^{-1} as the N_2 flow rate. All ZnO based films were well adhered to the substrate and passed the Scotch tape test.[4] The bulk concentrations of P dopants in the ZnO films and film thickness were determined through energy dispersive X-ray spectroscopy (EDS) and side on SEM, respectively, as shown in Table 4.1. X-ray diffraction patterns of nominally undoped and P-doped ZnO films are shown in Figure 4.1. Peaks were seen at 31.8, 34.4, 36.3, 47.5, 56.6 and 63.0° and match only the wurtzite phase of ZnO, with no secondary oxide phases visible. The degree of preferred orientation in the polycrystalline samples was qualitatively accessed and showed that all films had a preference for the (002) direction. This is likely a consequence of the (002) plane in the wurtzite structure having the lowest surface energy. Moreover, the amorphous substrate may have also had an effect on the ZnO films causing strain on the unit cell and/or changes in preferred crystallographic orientation.[5]
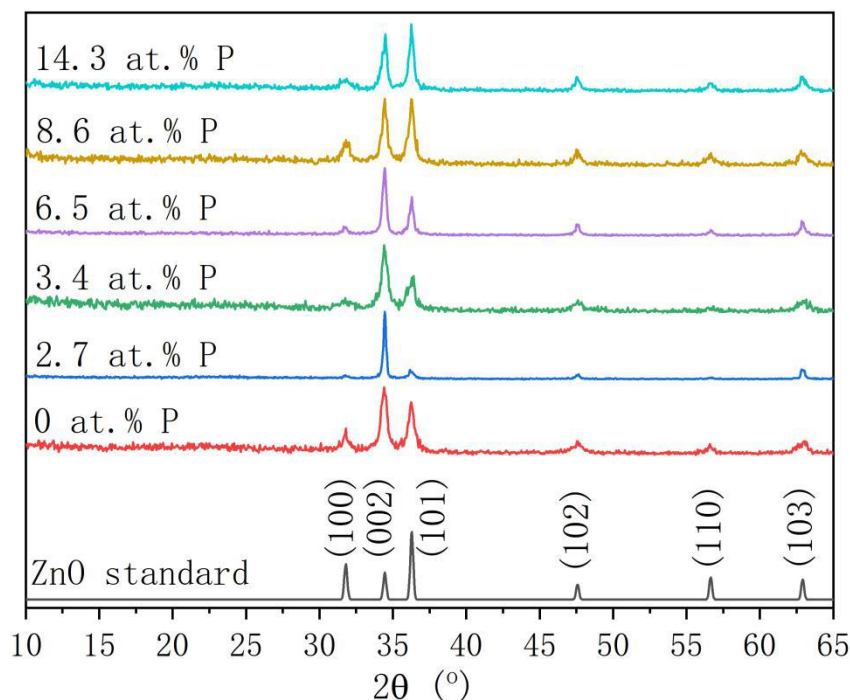
Figure 4.1: XRD patterns of the undoped and P-doped ZnO thin films prepared at 500 ºC through AACVD, show that the wurtzite phase of ZnO has been successfully formed. No secondary phases are visible.

Table 4.1: The results of concentrations of P (at.%) on the ZnO thin films through EDS analysis

Initial Mo concentration / mol.%	Mo concentration / at.%	Film thickness / nm
0	0	730
1.0	2.7(6)	847
0.5	3.4(8)	625
5.0	6.5(0)	605
7.0	8.6(0)	655
10	14.3(0)	780

The surface morphology of the nominally undoped and P-doped ZnO thin films is shown in Figure 4.2. There are many factors that can have an influence on the morphology of AACVD grown ZnO thin films, including precursor, oxidant source, carrier gas, substrate, solvent and substrate temperature. For the undoped ZnO film, the morphology consists of platelet and grains with varying sizes and in random orientations. Upon P doping to 2.7 and 3.4 at.% there were minimal changes in the surface morphology compared to the nominally undoped films. Although at the higher

doping concentrations, in particular for the 6.5 at.% P doped sample, a more platelet like morphology was seen. This is all consistent with the XRD results that showed that although changes in preferred orientation towards the (002) were observed there was minimal change in the ZnO unit cell volume.[6–8]

Table 4.2: The unit cell parameters for the pure and P-doped ZnO thin films prepared through AACVD

P concentration / at.%	Unit cell parameters		
	a / Å	c / Å	Volume / Å^3
0	3.252(3)	5.211(3)	47.71(014)
2.7	3.253(2)	5.202(0)	47.68(009)
3.4	3.243(4)	5.206(2)	47.42(018)
6.5	3.248(2)	5.205(1)	47.57(009)
8.6	3.250(2)	5.210(2)	47.64(010)
14.3	3.251(2)	5.201(2)	47.62(010)

From analysis of the XRD patterns, the unit cell parameters of the ZnO thin films with/without P doping were determined via JADE software, which is shown in Table 4.2. The volume for pure ZnO was 47.71 Å^3, which is larger than the volumes for the P-doped ZnO films. This may result from the ionic radius of P^{5+} being 0.29 Å, which is smaller than that of Zn^{2+} at 0.60 Å. The result of the unit cell volumes can also indicate that P^{5+} has been doped into ZnO lattice. Although the change of unit cell volume may not be liner, the doped ZnO thin films always show smaller unit cell volumes compared to undoped ZnO, which suggests P^{5+} (0.29 Å) is substitute for Zn^{2+} (0.60 Å) but not in interstitial formation in the ZnO lattice.
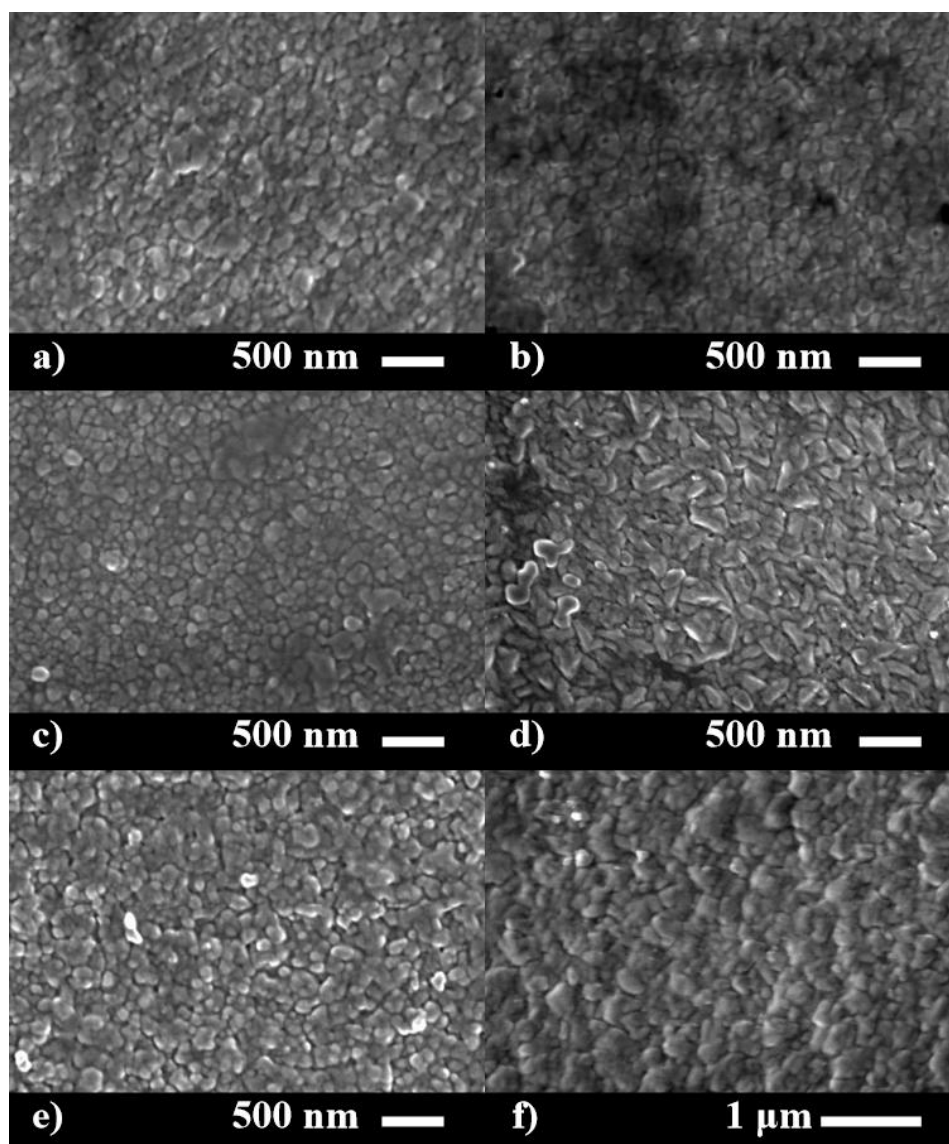
Figure 4.2: SEM images for the morphology of the a) undoped and b) 2.7, c) 3.4, d) 6.5, e) 8.6 and f) 14.3 at.% P doped ZnO films prepared via AACVD.

Figure 4.3 and Table 4.3 shows the X-ray photoelectron spectroscopy (XPS) data and binding energy values determined through peak fitting. for the nominally undoped and P doped films. It was found that the binding energy of Zn $2p_{3/2}$ was ~ 1022.1 eV in all the graphs, indicating that Zn in all the thin films is in the form of Zn^{2+} based on the literature binding energy for ZnO.[9] Furthermore, according to Figure 4.3, the binding energy of P $2p_{3/2}$ was always ~ 133 eV, which indicates the oxidation states of P on the surface of all the films was +5.[6,10,11] For example, the binding energies of P $2p_{3/2}$ for compounds containing phosphorus (+5) including Na_3PSO_3, $Na_4P_2O_7$ and $(C_6H_5)_3PO$ were 133.0 eV,[10] 133.3 eV[10] and 132.7 eV,[10] respectively while that for the

compounds with phosphorus in other oxidation states (P^{3+} or P^{3-}), such as H_3PO_3, $(C_6H_6S)_3P$ and InP, were observed at 134.3 eV,[12] 134.4 eV[10,12] and 128.7 eV,[12] respectively. The peaks seen at ~ 139 eV in the P 2p scan range belongs to the Zn 3s transitions.[6] Hence, no indication of P^{3+} or P^{3-} was found on the surface of the thin films. Moreover, the ZnO:P (14.3 at%) thin film has been measured by XPS depth profiling displayed in Figure 4.4, which suggested P to be surface segregated as opposed to evenly distributing across the depth of the films. Surface segregation of dopants in ZnO is common and has been seen previously in literature with anionic and cationic dopants.[13,14]
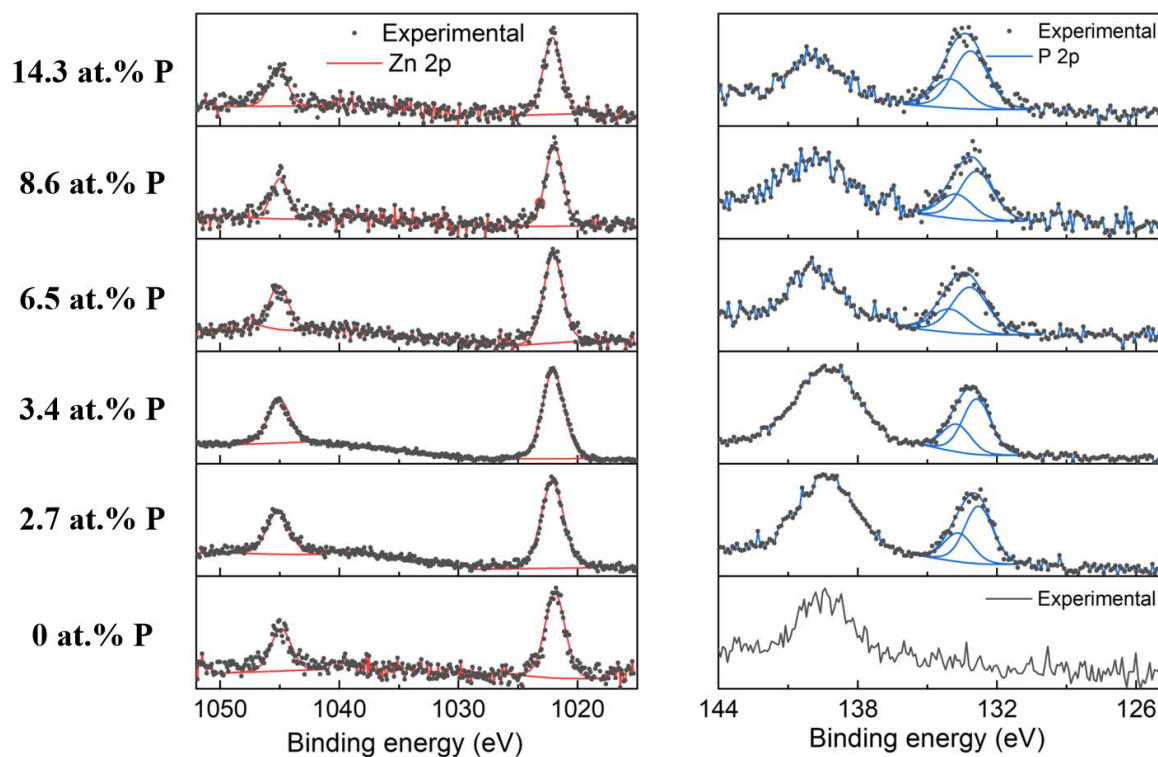
Figure 4.3: Core level XPS analysis showing the P on the surface of the doped ZnO films.
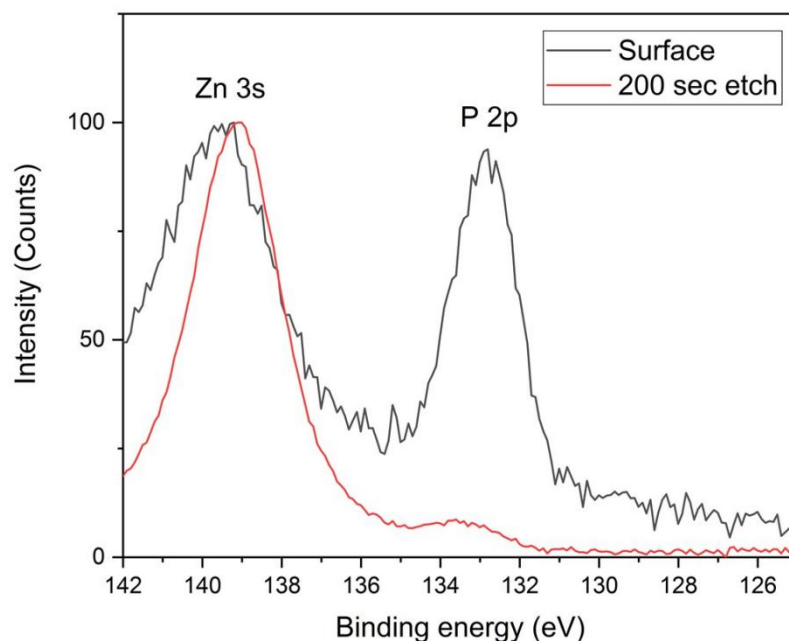
Figure 4.4: Depth profiling of the ZnO:P (14.3 at%) thin film showing P to be highly surface segregated. XPS results show 52% P relative to Zn on the surface and only 2% after 200 seconds (40 nm) of etching. This is likely due to preferential sputtering of of P over Zn as it is lighter and therefore may not be representative of the bulk P concentration.

Table 4.3: The positions of P 2P from XPS analysis for the P-doped ZnO thin films prepared at 450 ºC via AACVD

Dopants P concentrations (at.%)	Positions of P 2P from XPS analysis (eV)	
	$2P_{1/2}$	$2P_{3/2}$
0	-	-
2.7	133.7	132.8
3.4	133.7	132.9
6.5	133.8	133.0
8.6	133.8	132.9
14.3	134.0	133.1

The electrical properties of the pure ZnO and P-doped ZnO thin films were determined through Hall effect measurements and the trends in bulk concentration (n), carrier mobility (µ) and resistivity (ρ) for P doped ZnO films is shown in Figure 4.5.

Hall effect studies confirmed that, as expected, electrons were the majority carriers in the n-type P:ZnO samples. The resistivity of the nominally undoped ZnO film was too high to be measured using the Hall instrument but crude measurements using a two point probe showed the resistance to be in the M Ω range. As mentioned earlier, the substitutional doping of P^{5+} on Zn^{2+} sites can offer up to three electrons for enhanced charge carrier density and conductivity. As such upon the introduction of P, the carrier density increases from 5.3×10^{19} cm^{-1} for 2.7 at.% P to 8.9×10^{19} cm^{-1} for 3.4 at.% P before maximizing at 1.66×10^{20} cm at 6.5 at.% P. This increase in carrier concentration results in a decrease of resistivity to 6.5×10^{-3} Ω.cm.

As P started to dope into the ZnO crystals, one P^{5+} can offer three more electrons than Zn^{2+}, which improved the electron density leading to an obvious decrease of the resistivity for ZnO:P films. When the concentration of P (at.%) kept increasing, the resistivity showed a rising trend, which was suspected to be the result of the self-compensating mechanisms[15] and the solubility limit of P dissolved into ZnO films reached in this period.[16] The carrier mobility showed an overall reduced trend as the atomic% of P increased, which may be caused by the increase of grain boundary scattering and the formation of interstitial defects (scattering centres).[16]

The best resistivity achieved was 6.0×10^{-3} Ω.cm with a bulk concentration of 1.56×10^{20} cm^{-3} and a carrier mobility of 6.65 cm^2 V^{-1} s^{-1} when the concentration of P was 6.5 at.%, which has similar electrical properties from simple AACVD route with low cost, comparing with some other ZnO:P thin films via different synthetic methods. In addition, the bulk concentration seems relatively high and the resistivity is quite low compared with some other cation doped ZnO films[16,17] with similar Zn source and same synthetic route (AACVD), which is thought to be due to the high bulk concentration resulting from the extra electrons given from P^{5+}.

In addition, the Zn source in this study, $[Zn(OAc)_2 \cdot 2H_2O]$, has been widely used in the formation of doped ZnO thin films and some former reports are shown in Table 4.5. In comparison with some other doped ZnO thin films, the resistivity here is also relatively low, which suggest that these areprospective TCO thin films.
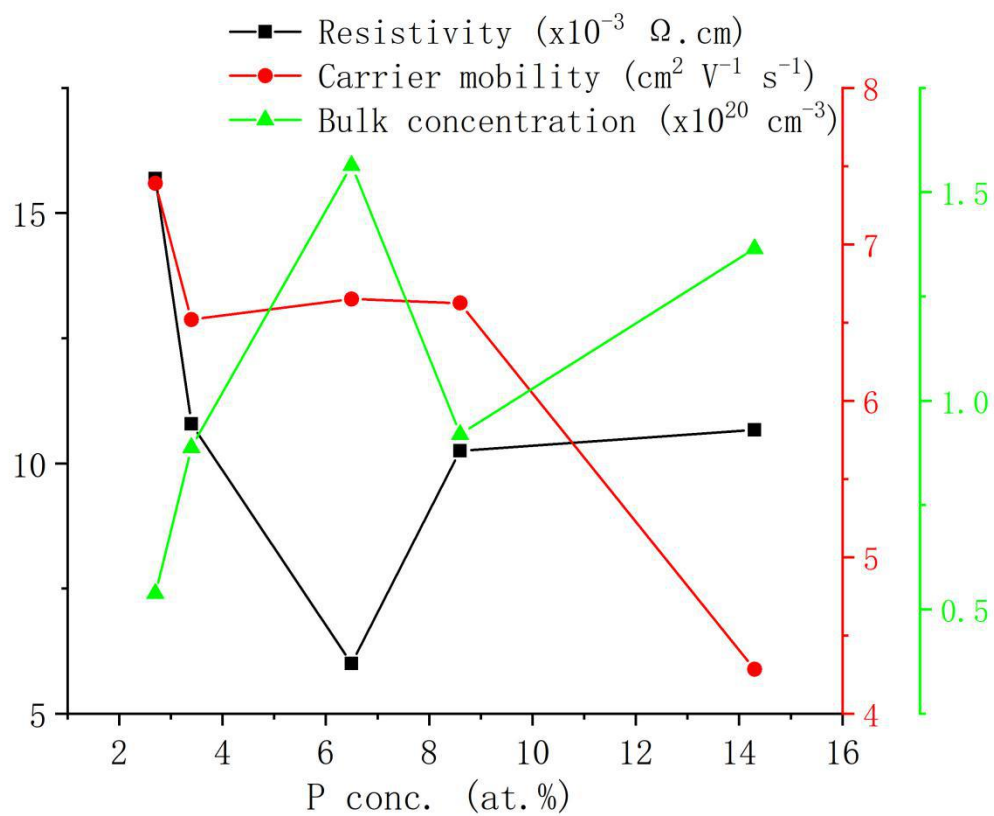
Figure 4.5: The electrical properties of the undoped and P doped ZnO films derived from Hall measurements displaying the trend in carrier concentration, carrier mobility and resistivity.

Table 4.4: Comparison with some other P doped ZnO thin films from different synthetic routes

Zn precursor	Dopant(s)	Dopant conc.	ρ ($\times 10^{-3}$ Ω.cm)	n ($\times 10^{20}$ cm^{-3})	μ (cm^2 V^{-1} s^{-1})	Ref
diethylzinc	P	ALD	3	1.3	8.4	(7)[7]
purity ZnO	P	pulsed laser deposition	10	-	-	(6)[6]
purity ZnO	P	RF magnetron sputtering	~ 5	-	-	(8)[8]
[Zn(OAc)$_2$·2H$_2$O]	P	AACVD	6.0	1.6	6.65	This project[18]

Table 4.5: Comparison with some other doped ZnO thin films through AACVD from the same Zn precursor.

Zn precursor	Dopant(s)	Dopant conc.	ρ ($\times 10^{-3}$ Ω.cm)	n ($\times 10^{20}$ cm^{-3})	μ (cm^2 V^{-1} s^{-1})	Ref
[Zn(OAc)$_2$·2H$_2$O]	Sc	AACVD	1.2	7.2	7.5	(19)[19]
[Zn(OAc)$_2$·2H$_2$O]	Al	AACVD	3.54	1.76	22.92	(20)[20]
[Zn(OAc)$_2$·2H$_2$O]	In	AACVD	72	-	-	(21)[21]
[Zn(OAc)$_2$·2H$_2$O]	Cl	AACVD	42.8	0.176	8.66	(22)[22]
[Zn(OAc)$_2$·2H$_2$O]	Cl	AACVD	2.72 ± 0.04	0.858 ± 0.016	26.74 ± 0.13	(23)[23]
[Zn(OAc)$_2$·2H$_2$O]	In	sol-gel spin-coating	0.61	-	-	(24)[24]
[Zn(OAc)$_2$·2H$_2$O]	Al	sol-gel method	7.08	0.389	-	(25)[25]
[Zn(OAc)$_2$·2H$_2$O]	Al/Sc	sol-gel method	29.41	0.08976	23.65	(26)[26]
[Zn(OAc)$_2$·2H$_2$O]	P	AACVD	6.0	1.6	6.65	This project[18]

The results of the ultraviolet-visible (UV-vis) spectra for the pure ZnO and ZnO:P thin films on glass substrates are shown in Figure 4.6. The UV-vis scans from 2500 nm to 300 nm, and in the region of visible light (400 - 700 nm), the average transmittance of all the films was between 70% and 85%. Moreover, in this region, the transmittance of the P-doped ZnO films was better than the undoped ZnO films, which demonstrates doping P into ZnO thin films can improve the optical properties of ZnO films. In the near infrared area, the transmittance reduces as the bulk concentration increases,[19] which compares well with the results reported in the literature. The band gaps also have been determined through the Tauc method. All the films have band gaps between 3.1 - 3.2 eV shown in Figure 4.7, which are a little below the theoretical value (3.37 eV). Furthermore, when the bulk concentration increases, the band gaps also show a small increase, which is expected.
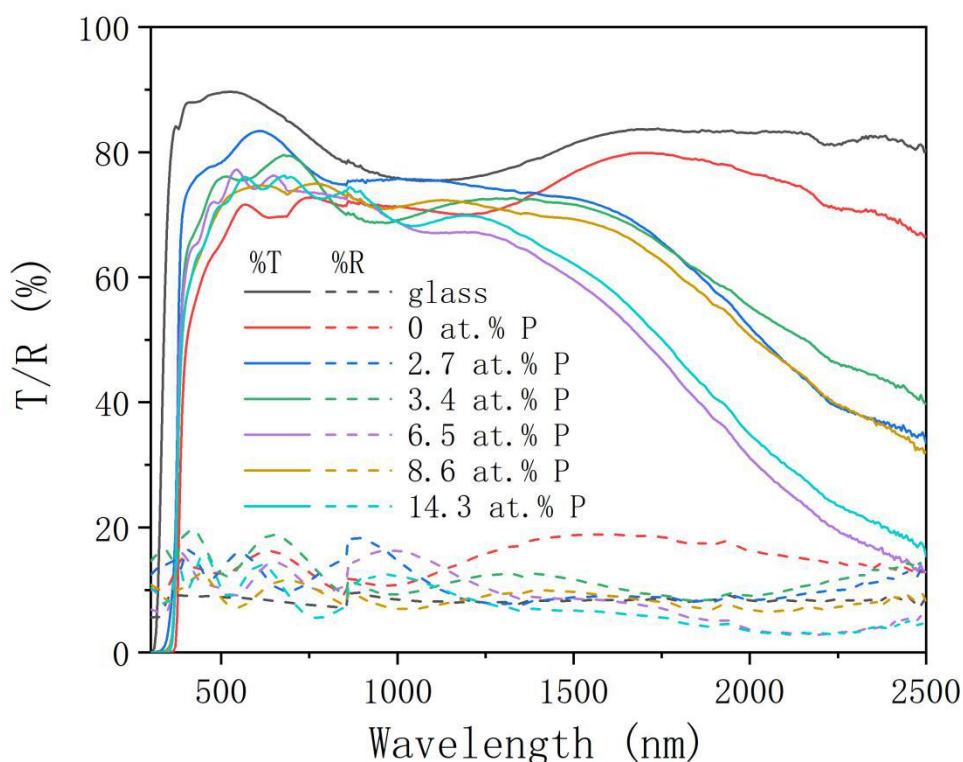
Figure 4.6: The optical data for the undoped and P doped ZnO films on glass substrates showing the UV/vis spectra.
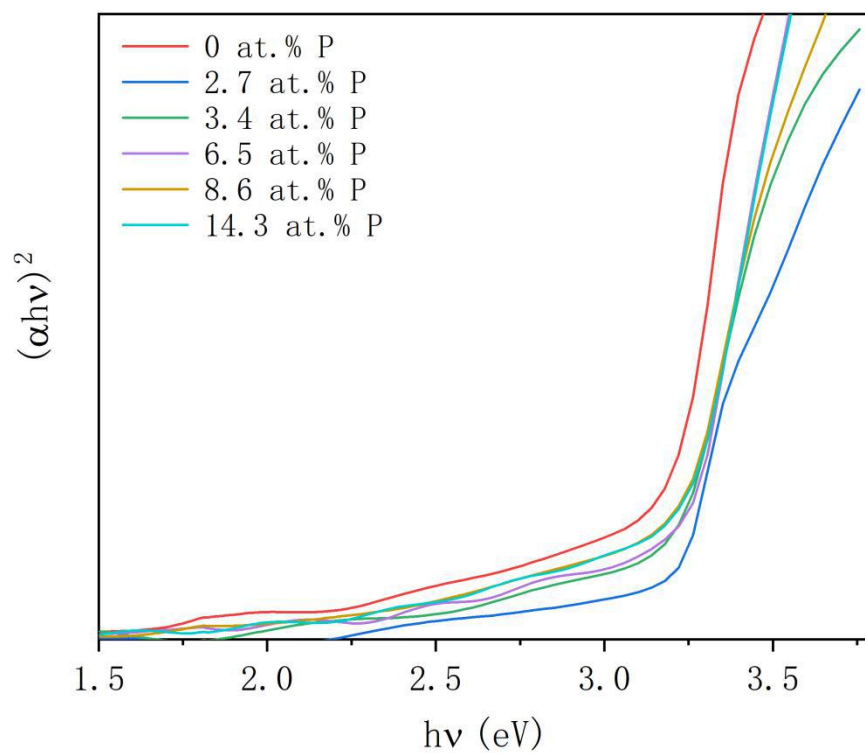
Figure 4.7: The Tauc plot for the undoped and P doped ZnO films on glass substrates calculating from the UV/vis data.

4.4 Conclusion

A series of undoped and P-doped ZnO thin films with different concentrations of P were grown on glass substrates via AACVD. XRD indicated that there was only formation of the ZnO phase without any secondary phases. Based on the XPS analysis, the oxidation states of P and Zn were determined to be +5 and +2 on the surface, respectively. The UV-vis test showed the transmittance of all the films were around 75% in the visible light area and the doped ZnO films displayed higher transmittance than the undoped one. According to the Hall effect measurements, all the ZnO:P thin films had much lower resistivities than the pure ZnO thin films. The lowest resistivity was the ZnO thin film with 6.5 at.% P doping at 6.0×10^{-3} Ω.cm (bulk concentration at 1.56×10^{20} cm^{-3} and carrier mobility at 6.65 cm^2 V^{-1} s^{-1}). This is the first time that P-doped ZnO thin films have been prepared using the AACVD route and relatively low resistivity compared to some other cation doped ZnO thin films was achieved.[16,17] In addition, the cost of the precursors for Zn source and P source are lower than the current ITO and FTO sources as well as the synthetic route in this study (AACVD) being a convenient and cheap one, which represents that preparing P doped ZnO thin films as TCOs materials through AACVD may be considered as a promising method. In contrast with the Mo-doped ZnO thin films, if the precursors of Zn source were both chosen as zinc acetate dihydrate ($Zn(OAc)_2 \cdot 2H_2O$), the P doped ones show much better conductivity than the Mo doped ones, which means P may be a better dopant for ZnO films compared with Mo. This may be the result of increased free electrons given by P^{5+} than Mo^{4+}, which improves the bulk concentration leading to relatively lower resistivity.

4.5 References

(1)   Mccluskey, M. D.; Jokela, S. J. Defects in ZnO. *J. Appl. Phys.* **2009**, *106* (7). https://doi.org/10.1063/1.3216464.

(2)   Janotti, A.; Van De Walle, C. G. Native Point Defects in ZnO. *Phys. Rev. B - Condens. Matter Mater. Phys.* **2007**, *76* (16), 1–22. https://doi.org/10.1103/PhysRevB.76.165202.

(3)   Bhachu, D. S.; Sankar, G.; Parkin, I. P. Aerosol Assisted Chemical Vapor Deposition of Transparent Conductive Zinc Oxide Films. *Chem. Mater.* **2012**, *24* (24), 4704–4710. https://doi.org/10.1021/cm302913b.

(4)   Mittal, K. L. Adhesion Measurement of Thin Films. *Electrocompon. Sci. Technol.* **1976**, *3* (1), 21–42. https://doi.org/10.1155/apec.3.21.

(5)   Ghosh, R.; Basak, D.; Fujihara, S. Effect of Substrate-Induced Strain on the Structural, Electrical, and Optical Properties of Polycrystalline ZnO Thin Films. *J. Appl. Phys.* **2004**, *96* (5), 2689–2692. https://doi.org/10.1063/1.1769598.

(6)   Li, Y.; Liu, Z.; Ren, J. Properties of Phosphorus-Doped Zinc Oxide Films Grown by Pulsed Laser Deposition. *J. Vac. Sci. Technol. A Vacuum, Surfaces, Film.* **2011**, *29* (3), 03A109. https://doi.org/10.1116/1.3554838.

(7)   Yuan, H.; Luo, B.; Campbell, S. A.; Gladfelter, W. L. Atomic Layer Deposition of P-Type Phosphorus-Doped Zinc Oxide Films Using Diethylzinc, Ozone and Trimethylphosphite. *Electrochem. Solid-State Lett.* **2011**, *14* (5), 181–183. https://doi.org/10.1149/1.3537326.

(8)   Kim, Y. Y.; Han, W. S.; Cho, H. K. Determination of Electrical Types in the P-Doped ZnO Thin Films by the Control of Ambient Gas Flow. *Appl. Surf. Sci.* **2010**, *256* (14), 4438–4441. https://doi.org/10.1016/j.apsusc.2010.01.035.

(9)   Nishino, J.; Ohshio, S.; Kamata, K. Preparation of Aluminum-Doped Zinc Oxide Films by a Normal-Pressure CVD Method. *J. Am. Ceram. Soc.* **1992**, *75* (12), 3469–3472. https://doi.org/10.1111/j.1151-2916.1992.tb04452.x.

(10)   Pelavin, M.; Hendrickson, D. N.; Hollander, J. M.; Jolly, W. L. Phosphorus 2p

Electron Binding Energies. Correlation with Extended Hückel Charges. *J. Phys. Chem.* **1970**, *74* (5), 1116–1121. https://doi.org/10.1021/j100700a027.

(11)   Fang, X.; Wang, X.; Pu, S.; Li, J.; Wei, Z.; Fang, F.; Li, S.; Wang, F.; Zhao, D. P-Doped ZnO Nanoparticals Synthesized by Thermal Decomposition. *Integr. Ferroelectr.* **2012**, *137* (1), 143–148. https://doi.org/10.1080/10584587.2012.687324.

(12)   Hoffmann, E.; Korugic-Karasz, L. Interpreting of XPS C1s Binding Energies in Silicon Containing Polymers and Nanoparticles. *Recent Dev. Adv. Mater. Process.* **2006**, *518*, 375–379.

(13)   Xu, H.; Rosa, A. L.; Frauenheim, T.; Zhang, R. Q. N-doped ZnO Nanowires: Surface Segregation, the Effect of Hydrogen Passivation and Applications in Spintronics. *Phys. status solidi* **2010**, *247* (9), 2195–2201.

(14)   Suzuki, T. T.; Adachi, Y.; Saito, N.; Hashiguchi, M.; Sakaguchi, I.; Ohashi, N.; Hishita, S. Surface Segregation of W Doped in ZnO Thin Films. *Surf. Sci.* **2014**, *625*, 1–6.

(15)   Swallow, J. E. N.; Williamson, B. A. D.; Whittles, T. J.; Birkett, M.; Featherstone, T. J.; Peng, N.; Abbott, A.; Farnworth, M.; Cheetham, K. J.; Warren, P.; Scanlon, D. O.; Dhanak, V. R.; Veal, T. D. Self-Compensation in Transparent Conducting F-Doped SnO_2. *Adv. Funct. Mater.* **2018**, *28* (4), 1–10. https://doi.org/10.1002/adfm.201701900.

(16)   Potter, D. B.; Powell, M. J.; Darr, J. A.; Parkin, I. P.; Carmalt, C. J. Transparent Conducting Oxide Thin Films of Si-Doped ZnO Prepared by Aerosol Assisted CVD. *RSC Adv.* **2017**, *7* (18), 10806–10814. https://doi.org/10.1039/c6ra27748a.

(17)   Potter, D. B.; Bhachu, D. S.; Powell, M. J.; Darr, J. A.; Parkin, I. P.; Carmalt, C. J. Al-, Ga-, and In-Doped ZnO Thin Films via Aerosol Assisted CVD for Use as Transparent Conducting Oxides. *Phys. Status Solidi Appl. Mater. Sci.* **2016**, *213* (5), 1346–1352. https://doi.org/10.1002/pssa.201532996.

(18)   Zhao, D.; Li, J.; Sathasivam, S.; Carmalt, C. J. N-Type Conducting P Doped ZnO Thin Films via Chemical Vapor Deposition. *RSC Adv.* **2020**, *10* (57),

34527–34533. https://doi.org/10.1039/d0ra05667g.

(19) Dixon, S. C.; Sathasivam, S.; Williamson, B. A. D.; Scanlon, D. O.; Carmalt, C. J.; Parkin, I. P. Transparent Conducting N-Type ZnO:Sc-Synthesis, Optoelectronic Properties and Theoretical Insight. *J. Mater. Chem. C* **2017**, *5* (30), 7585–7597. https://doi.org/10.1039/c7tc02389h.

(20) Li, J.; Sathasivam, S.; Taylor, A.; Carmalt, C. J.; Parkin, I. P. Single Step Route to Highly Transparent, Conductive and Hazy Aluminium Doped Zinc Oxide Films. *RSC Adv.* **2018**, *8* (74), 42300–42307. https://doi.org/10.1039/c8ra09338e.

(21) Nolan, M. G.; Hamilton, J. A.; O'brien, S.; Bruno, G.; Pereira, L.; Fortunato, E.; Martins, R.; Povey, I. M.; Pemble, M. E. The Characterisation of Aerosol Assisted CVD Conducting, Photocatalytic Indium Doped Zinc Oxide Films. *J. Photochem. Photobiol. A Chem.* **2011**, *219* (1), 10–15.

(22) Jiamprasertboon, A.; Powell, M. J.; Dixon, S. C.; Quesada-Cabrera, R.; Alotaibi, A. M.; Lu, Y.; Zhuang, A.; Sathasivam, S.; Siritanon, T.; Parkin, I. P.; Carmalt, C. J. Photocatalytic and Electrically Conductive Transparent Cl-Doped ZnO Thin Films: Via Aerosol-Assisted Chemical Vapour Deposition. *J. Mater. Chem. A* **2018**, *6* (26), 12682–12692. https://doi.org/10.1039/c8ta01420e.

(23) Jiamprasertboon, A.; Dixon, S. C.; Sathasivam, S.; Powell, M. J.; Lu, Y.; Siritanon, T.; Carmalt, C. J. Low-Cost One-Step Fabrication of Highly Conductive ZnO:Cl Transparent Thin Films with Tunable Photocatalytic Properties via Aerosol-Assisted Chemical Vapor Deposition. *ACS Appl. Electron. Mater.* **2019**, *1* (8), 1408–1417. https://doi.org/10.1021/acsaelm.9b00190.

(24) Bouaine, A.; Bourebia, A.; Guendouz, H.; Riane, Z. Synthesis and Characterization of In Doped ZnO Thin Film as Efficient Transparent Conducting Oxide Candidate. *Optik (Stuttg).* **2018**, *166*, 317–322. https://doi.org/10.1016/j.ijleo.2018.04.017.

(25) Lin, K. moh; Tsai, P. Growth Mechanism and Characterization of ZnO: Al

Multi-Layered Thin Films by Sol-Gel Technique. *Thin Solid Films* **2007**, *515* (24 SPEC. ISS.), 8601–8604. https://doi.org/10.1016/j.tsf.2007.04.012.

(26)   Chen, J.; Chen, D.; He, J.; Zhang, S.; Chen, Z. The Microstructure, Optical, and Electrical Properties of Sol-Gel-Derived Sc-Doped and Al-Sc Co-Doped ZnO Thin Films. *Appl. Surf. Sci.* **2009**, *255* (23), 9413–9419. https://doi.org/10.1016/j.apsusc.2009.07.044.

Chapter 5 Transparent and conducting boron doped ZnO thin Films from two different solvents grown through aerosol assisted chemical vapor deposition

This chapter is adapted from a paper manuscript submitted to *RSC Advances*. [*RSC Adv.,* 2022, **12**, 33049-33055, Copyright the Royal Society of Chemistry 2022. DOI: 10.1039/d2ra05895b]. Donglei Zhao, Sanjayan Sathasivam, Mingyue Wang and Claire J. Carmalt. Transparent and Conducting Boron Doped ZnO Thin Films Grown By Aerosol Assisted Chemical Vapor Deposition.

This work was completed by SS, MW, CC and myself. The main part of the work including thin film deposition, characterizations and analysis were carried out by myself. SS and CC provided many useful ideas, advice and supervision. MW calculated the unit cell parameters.
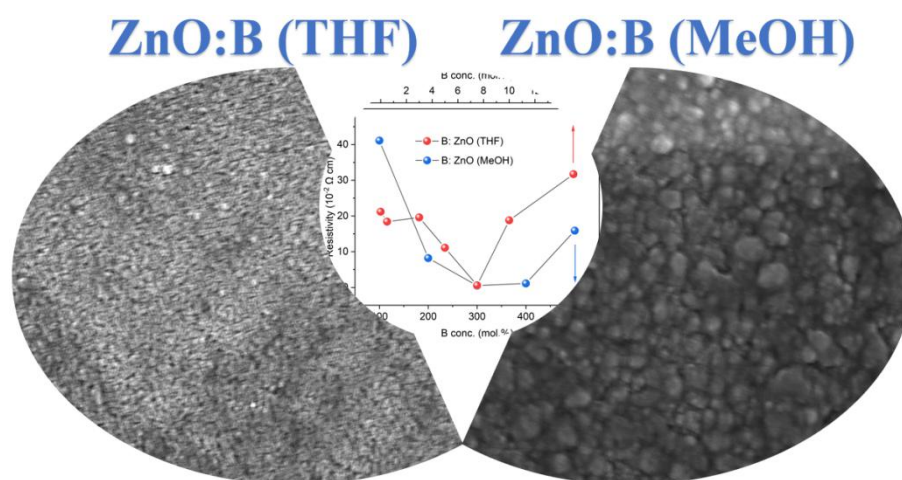
Representative image shows the TCO material B-doped ZnO thin film using THF and MeOH as solvents deposited via AACVD which showed excellent optical and electrical properties and different surface morphology based on solvent influence.

5.1 General introduction

In this investigation, B-doped ZnO thin films were grown on glass substrates from two different solvents, tetrahydrofuran (THF) and methanol (MeOH), via aerosol assisted chemical vapour deposition (AACVD). Due to THF having good miscibility with the B precursor solution (triethylborane in hexane) but poor solubility for the Zn precursors (zinc acetate dihydrate), while MeOH has good solubility for the Zn precursor but low miscibility for the B precursor solution, both THF and MeOH solvents were investigated and the properties of the resulting films compared. All the thin films showed visible light transmittance of ~ 75 - 90% based on the ultraviolet-visible (UV-vis) spectra. From the Hall effect measurement, most B-doped ZnO films had resistivities in the 10^{-2} Ω.cm level, which were lower than the undoped ZnO film. The B-doped ZnO thin films showed lowest resistivities of 5.84×10^{-3} Ω.cm for low concentration B doping at 7.5 mol.% using THF as solvent and 5.10×10^{-3} Ω.cm for high concentration B doping at 300 mol.% using MeOH as solvent, respectively. In general, doping B into the ZnO films improved both the optical and electrical properties. The thin films were analyzed by X-ray diffraction (XRD), scanning electron microscopy (SEM) and X-ray photoelectron spectroscopy (XPS) characterizations.

5.2 Experimental

5.2.1 Film synthesis

Depositions were carried out under N_2 (BOC Ltd., 99.99% purity) flow. Zinc acetate dihydrate ($Zn(OAc)_2 \cdot 2H_2O$), triethylborane (BEt_3) solution (1.0 M in hexanes), acetone (99%), tetrahydrofuran (THF, 99%) and methanol (MeOH, 99%) were purchased from Sigma. Glass substrates were cleaned using detergent, water and isopropanol then dried in a 70 °C oven.

For the ZnO:B thin films from THF solvent, $Zn(OAc)_2 \cdot 2H_2O$ (0.40 g, 1.82 mmol) in THF (20 mL) was placed in a glass bubbler. $[BEt_3]$ (x mol.% based on Zn, x = 0, 0.5, 3, 7.5, 10 and 15) was added to the same bubbler.

For the ZnO:B thin films from MeOH solvent, $Zn(OAc)_2 \cdot 2H_2O$ (0.40 g, 1.82 mmol) in MeOH (20 mL) was placed in a glass bubbler. $[BEt_3]$ (x mol.% based on Zn, x = 0, 5, 7.5, 10, and 15 as low concentration doping and 100, 200, 300, 400 and 500 as high concentration doping) was added to the same bubbler. Several drops of acetone were also added to the bubbler to aid dissolution of the precursors.

All solutions were atomised using a piezoelectric device (Johnson Matthey liquifog®). The aerosol mist was delivered to the AACVD reaction chamber and passed over the heated substrate (float glass with a SiO_2 barrier layer) using N_2 carrier gas at 1.0 L min^{-1}.[1] Depositions were carried out at 475 °C and lasted until the precursor solution was fully used. After the depositions the substrates were cooled under a flow of N_2. The glass substrates were not removed until the graphite block was cooled to below 50 °C. The films on the substrates were handled and stored in air.

5.2.2 Film characterisation

All the samples were characterised through XRD, XPS, SEM/EDS, UV-vis and Hall effect measurements and the details are given in section 3.2.2.

5.3 Results and Discussion

All of the B-doped ZnO thin films were prepared from zinc acetate dihydrate ($Zn(OAc)_2.2H_2O$) as the Zn precursor with/without triethylborane solution (BEt_3, 1.0 M in hexanes) as the B dopants via AACVD. Two solvents, tetrahydrofuran (THF) and methanol (MeOH) were studied due to the differing solubility/immiscibility of the Zn and B precursors in each solvent. For the B-doped ZnO thin films from THF solvent, based on the good miscibility for the B source in THF solvent, and dopants being usually easily enrich to dope via AACVD, relatively low concentrations of B doping were chosen for THF solvent. For the B-doped ZnO thin films from MeOH solvent, due to the B source not having sufficient miscibility in MeOH solvent, the concentrations of B dopants were chosen to be high as well as using the normal doping level. The other deposition conditions were all the same at 475 °C as deposition temperature and 1.0 L min^{-1} as carrier gas N_2 flow rate to reach the optimal substrate coverage, ZnO crystallinity and film thickness. All the ZnO:B thin films adhered to the substrate well and passed the Scotch tape test.[2]

XRD

The X-ray diffraction patterns of undoped and B-doped ZnO (B:ZnO) films using the solvent THF and MeOH are illustrated in Figure 5.1 and 5.2, respectively. The crystal structures of all the thin films from the two different solvents suggest formation of the wurtzite phase of ZnO according to the six characteristic peaks at ~ 31.8, 34.4, 36.3, 47.5, 56.6 and 63.0° without any secondary oxide phases for zinc or boron in the patterns.

The preferred orientation for crystal growth could be investigated qualitatively from XRD patterns in Figure 5.1 and 5.2. The six characteristic peaks correspond to the (100), (002), (101), (102), (110) and (103) planes. Moreover, there are several factors that have effect on the preferred orientation through the CVD route, such as substrates, precursors, dopants, solvents, deposition rates and deposition temperatures.[3,4] For example, the pure ZnO thin film from [$ZnEt_2$] precursor in Chapter 3 showed relatively lack of growth in the (002) plane comparing with that from

[Zn(OAc)$_2$·2H$_2$O] precursor in Chapter 4 and 5, which could find some similar results of preferred orientations for pure ZnO thin films from previous literature.[4–7]

For the ZnO:B thin films from THF in Figure 5.1, the lowest surface energy of the (002) plane of the wurtzite ZnO phase results in the relatively preferred orientation of the plane (002) for all the films. As the concentrations of B dopants increases, it can be found that the degrees of preferred orientation for the plane (101) also increases generally, which may result from the substrate influence.[8] Another possible reason is the dopant induced preferential orientation resulting from changes in the growth kinetics due to ion substitution.[9] The planes (102), (110) and (103) show relative lack of growth based on the substrate influence[8] as well.

For the ZnO:B thin films from MeOH, shown in Figure 5.2, the plane (002) was always the most preferred orientation for all the thin films due to the lowest surface energy mentioned above. The (101) plane showed a small increase as the B dopant concentration increased, although to a smaller extent than observed in Figure 5.1. Resulting from the substrate influence,[8] lack of growth was been found in the planes (102), (110) and (103).

To compare the B:ZnO thin films from the two solvents, THF and MeOH, the preferred growing plane (002) and lack of growth in the planes (102), (110) and (103) was observed in thin films from both solvents. In addition, although the plane (101) increased as the B dopant concentration increased, this was more significant in films grown using THF than from MeOH. Moreover, the plane (101) showed a higher degree of preferred growth than the plane (002) in the ZnO:B (5, 7.5, 10 and 15 mol.%) thin films from THF solvent while the plane (002) still showed the highest preferred growth in the ZnO:B thin films with high concentrations of B doping from MeOH solvent.

Tables 5.1 and 5.2 show the unit cell parameters of undoped and B-doped ZnO thin

films from THF solvent and MeOH solvent, respectively. These were calculated through the JADE software on the basis of the XRD patterns. The volume for pure ZnO from THF solvent was 47.50 $Å^3$ and larger than any of the ZnO:B thin films from THF solvent. As the ionic radii of Zn^{2+} and B^{3+} are 0.60 Å and 0.23 Å, respectively,[10,11] substitutional doping of B into the ZnO crystalline lattice would cause a reduction in unit cell volume. Similarly, the unit cell volume for undoped ZnO from MeOH solvent was 47.51 $Å^3$. The unit cell volumes for the ZnO:B thin films from MeOH were similar to the undoped ZnO until the initial B concentrations were increased to 200 mol.%. This could be due to two reasons 1) that the B is doping in interstitial sites within the ZnO unit cell due to its small size (0.23 Å) or 2) the B is present in the form of a secondary oxide, perhaps as a thin layer on the surface of the film. The evidence for the latter is more compelling as XPS depth profiling studies found boron only on the surface of the samples up to 100 mol%. Another possibility is that for the low concentrations of B precursor along with poor miscibility in the MeOH solvent that the concentrations of B actually doping into the films is negligible or low therefore minimizing the distortion caused to the ZnO lattice. Hence, when the actual concentrations of B doping are low, the doping form may prefer to be interstitial while at higher B dopant concentrations, substitutional may result, as observed for the much higher miscibility of the B source in THF than that in MeOH. Moreover, the electrical properties discussed below indicate that the lowest resistivities were obtained for different B precursor concentrations for THF versus MeOH, with ZnO:B (7.5 mol.%, THF) and ZnO:B (300 mol.%, MeOH), which suggests the substitutional method of B doping may increase the electrical performance of the B-doped ZnO thin films more significantly.
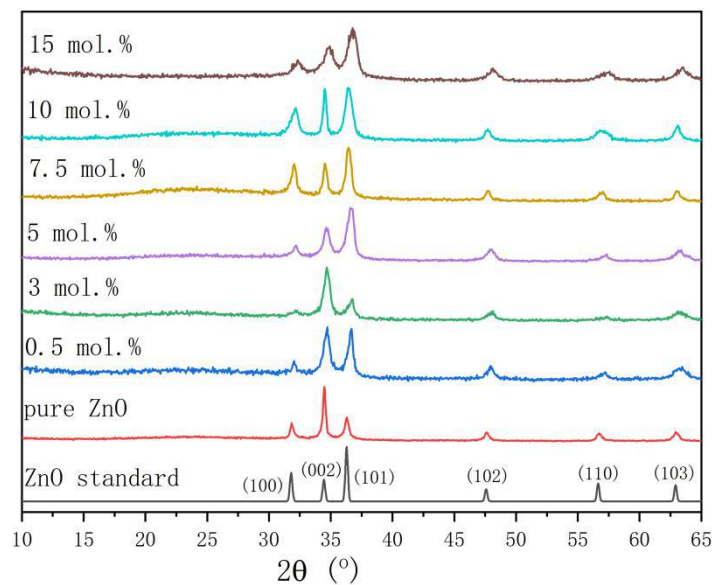
Figure 5.1: XRD patterns showing the undoped and B-doped ZnO films using THF as solvent prepared at 475 ºC to be in the wurzite phase of ZnO. No secondary phases are visible.
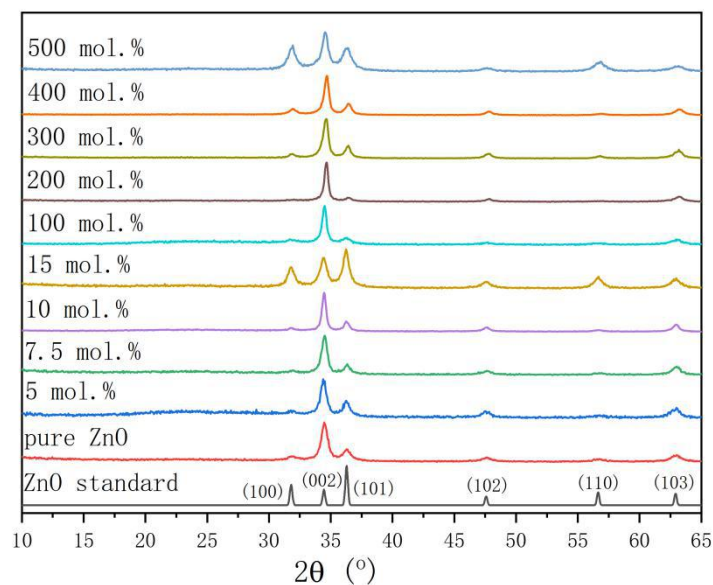
Figure 5.2: XRD patterns showing the undoped and B-doped ZnO films using MeOH as solvent prepared at 475 ºC to be in the wurzite phase of ZnO. No secondary phases are visible.

Table 5.1: The unit cell parameters for the pure ZnO and B-doped ZnO thin films from THF solvent grown via AACVD

Initial B concentrations	Unit cell parameters	

(mol.%)	a / Å	c / Å	Volume / Å^3
0	3.248	5.198	47.50
0.5	3.215	5.174	46.30
3	3.216	5.166	46.28
5	3.210	5.176	46.19
7.5	3.228	5.203	46.94
10	3.226	5.197	46.84
15	3.201	5.170	45.86

Table 5.2: The unit cell parameters for the pure ZnO and B-doped ZnO thin films from MeOH solvent grown via AACVD

Initial B concentrations (mol.%)	Unit cell parameters		
	a / Å	c / Å	Volume / Å^3
0	3.248	5.201	47.51
5	3.246	5.205	47.50
7.5	3.250	5.195	47.51
10	3.249	5.201	47.56
15	3.251	5.207	47.65
100	3.249	5.197	47.51
200	3.240	5.177	47.07
300	3.241	5.179	47.12
400	3.239	5.171	46.99
500	3.243	5.187	47.26

SEM

Figures 5.3, 5.4 and 5.5 describe the surface morphology of the series of undoped and B-doped ZnO thin films from THF, and from MeOH with low concentrations and high concentrations B doping, respectively. The surface morphology of ZnO based

thin films may be influenced by several factors, including precursors, oxidant source, substrate, carrier gas and deposition temperature. Hence, the surface morphology will be discussed and compared for the ZnO:B thin films from THF solvent and MeOH solvent, as above.

For the ZnO thin films with/without B doping from THF solvent, the pure ZnO thin film represents random orientations and grains and platelets of varying sizes, which is similar to the undoped ZnO thin film from MeOH solvent and some other nominally pure ZnO thin films via AACVD.[10] As B was introduced into the films, minimal impact on the morphology was observed for the films grown from THF solutions, however when MeOH was used as the solvent the presence of the B dopant caused a more noticeable change in the surface morphology. Previous reports have described the influence that MeOH can have on the microstructure of thin films deposited via AACVD, and in general aerosols from different solvents can influence the microscopic surface morphology besides their normal transportation effect.[12,13] There is also some difference in sizes after B doping. Some large round grains can be found in the ZnO:B thin films, which were more significant and common in the B-doped ZnO thin films from MeOH solvent (e.g. B-ZnO 500 mol%; MeOH) than from THF solvent. As described above, most of the thin film showed preferential growth on two specific planes, the (002) and (101) planes, as investigated in the XRD patterns.
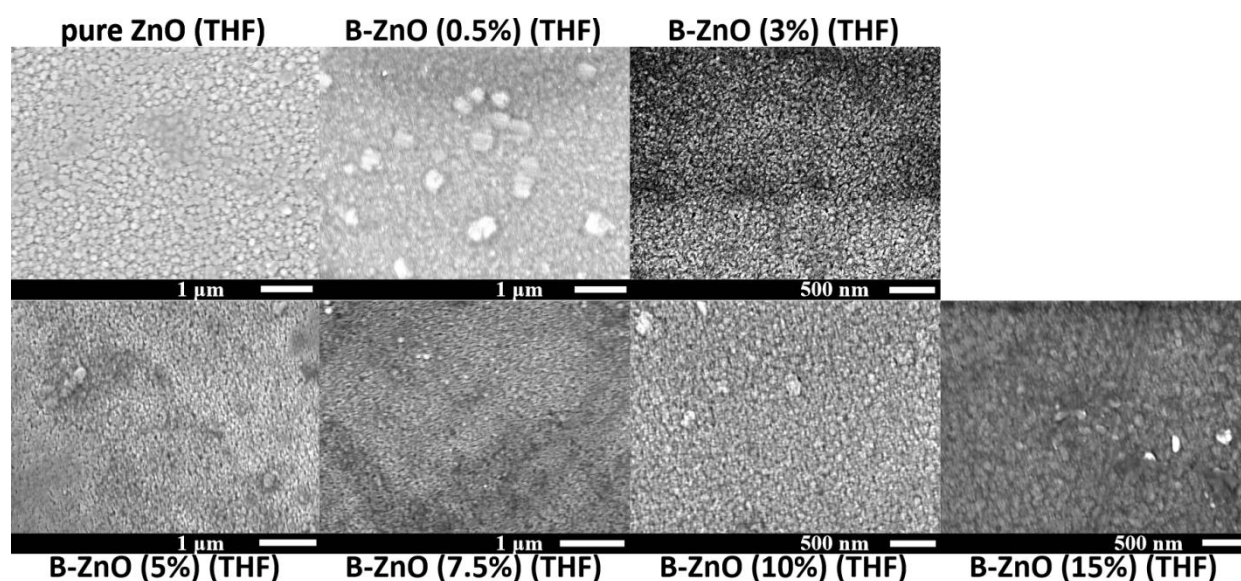
Figure 5.3: SEM images for the morphology of the undoped and 0.5, 3, 5, 7.5, 10 and 15 mol.% ZnO:B thin films using THF as solvent prepared through AACVD.
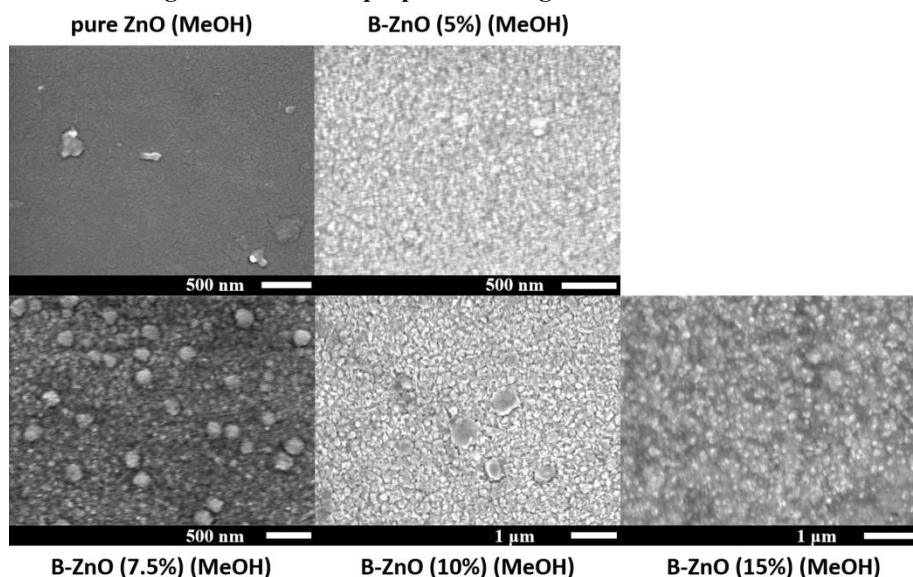
Figure 5.4: SEM images for the morphology of the ZnO thin films with/without low concentrations B doping at 5, 7.5, 10 and 15 mol.% using MeOH as solvent prepared through AACVD.
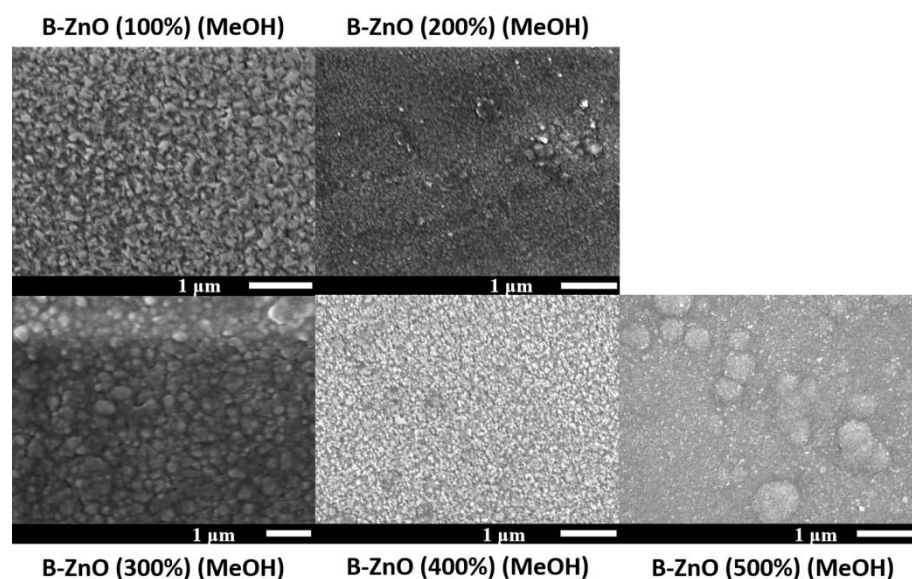
Figure 5.5: SEM images for the morphology of the ZnO thin films with high concentrations B doping at 100, 200, 300, 400 and 500 mol.% using MeOH as solvent prepared through AACVD.

XPS analysis

According to the X-ray photoemission spectroscopy (XPS) analysis, Figures 5.6 and 5.7 describe the oxidation states and elemental compositions on the surface and at ~ 150 nm depth for the ZnO:B thin films from THF solvent, respectively. Figures 5.8 and 5.9 describe the same parameters on the surface and at ~ 150 nm depth for the

ZnO:B thin films from MeOH solvent, respectively. For the Zn 2p analysis, all the thin films shown in these four figures do not have large differences and the binding energy of Zn $2p_{3/2}$ was always ~ 1022.1 eV, which means that Zn^{2+} was formed in all the thin films resulting from the binding energy of ZnO in literature.[14] For the B 1s analysis, the binding energy of B 1s has only a small shift between 191.3 eV and 191.9 eV for all doped thin films both on the surface and depth, which is shown in Tables 5.3 and 5.4. This corresponds to the binding energy for B^{3+} in the literature.[15] However, due to the B source not mixing well with the MeOH solvent, the peaks for the ZnO:B (low concentrations) thin films from MeOH solvent were relatively small and hard to fit compared to those observed for films from THF solvent. Moreover, the B 1s peaks of ZnO:B (5, 7.5, 10 and 15 mol.%) were not found in the depth XPS analysis.

In addition, due to the B element being very light and it cannot be determined through the bulk test method, energy dispersive X-ray spectroscopy (EDS). Therefore, the concentrations of B/Zn in the films were calculated and are shown in Tables 5.3 and 5.4 via XPS analysis. For the thin films from THF solvent, B is surface segregated and therefore high concentrations for the surface result, which may result from the excellent miscibility of the B source in THF and therefore the depth results can be considered to be reliable. In contrast, due to the immiscibility of the B source with MeOH solvent, the B dopants may not dope into the depth well under low concentrations level, which suggests that only the surface concentrations may be reliable. In general, any concentrations from XPS only provide an indication and should be treated with caution particularly since XPS analysis only shows the point concentrations of thin films, which is not as reliable as results for bulk concentrations from EDS test. For example, the ZnO:B (10 mol.%, MeOH) thin film has a higher surface concentration than the ZnO:B (100 mol.%, MeOH) film, which may be caused from the B dopants focus point. In addition, sputtering the films for depth profiling can lead to inaccuracies due to how preferential sputtering of different elements can occur. Therefore, the concentrations of B dopants from XPS analysis here can only provide an imprecise indication of at% in the actual films.
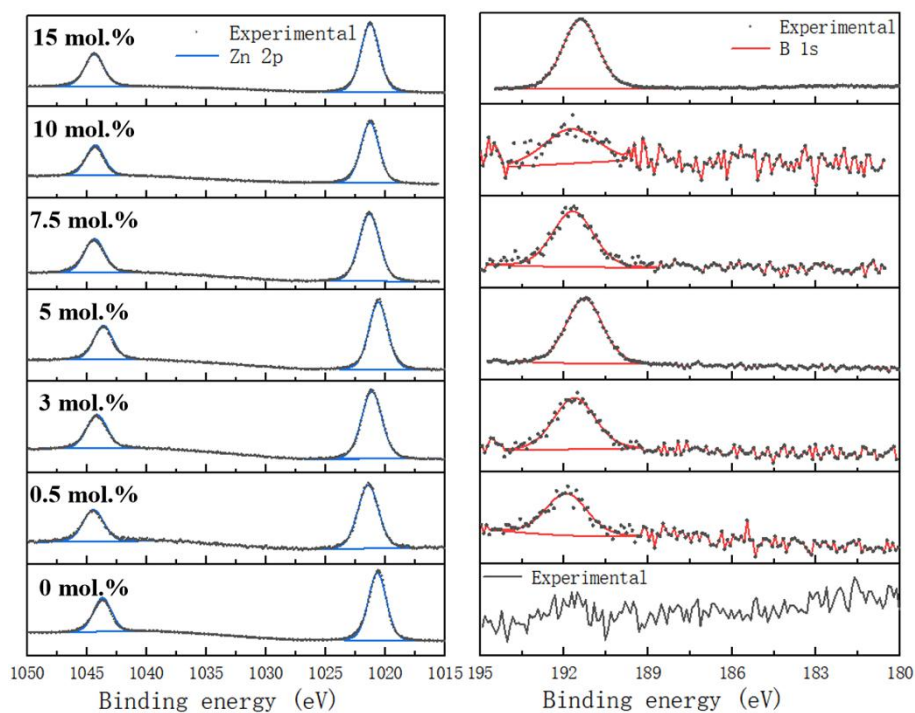
Figure 5.6: Core level XPS analysis showing the surface compositions and oxidation of the undoped and 0.5, 3, 5, 7.5, 10 and 15 mol.% ZnO:B thin films using THF as solvent grown via AACVD.
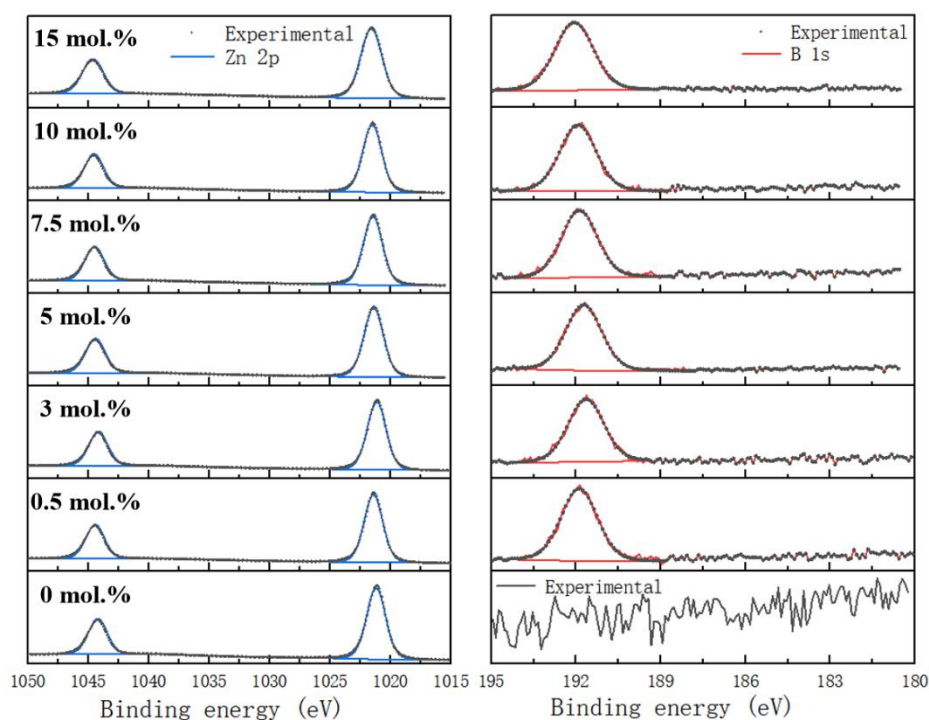
Figure 5.7: Core level XPS analysis showing the compositions and oxidation in ~ 150 nm depth of the undoped and 0.5, 3, 5, 7.5, 10 and 15 mol.% ZnO:B thin films using THF as solvent grown via AACVD.
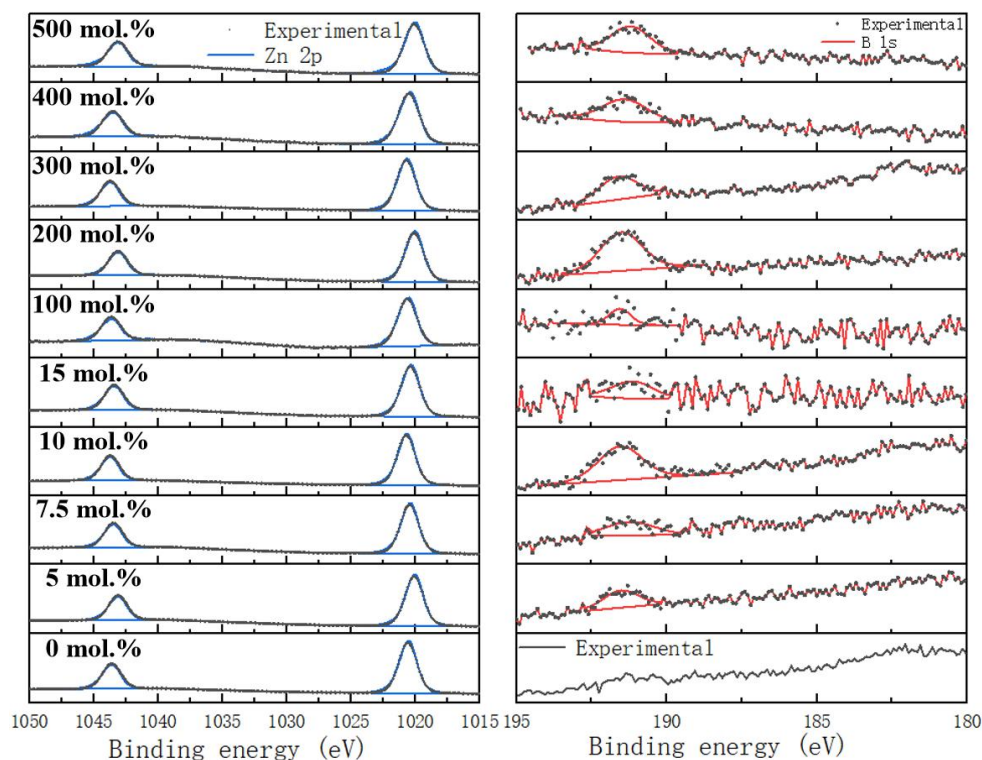
Figure 5.8: Core level XPS analysis showing the surface compositions and oxidation of the undoped and 5, 7.5, 10, 15, 100, 200, 300, 400 and 500 mol.% ZnO:B thin films using MeOH as solvent grown via AACVD.
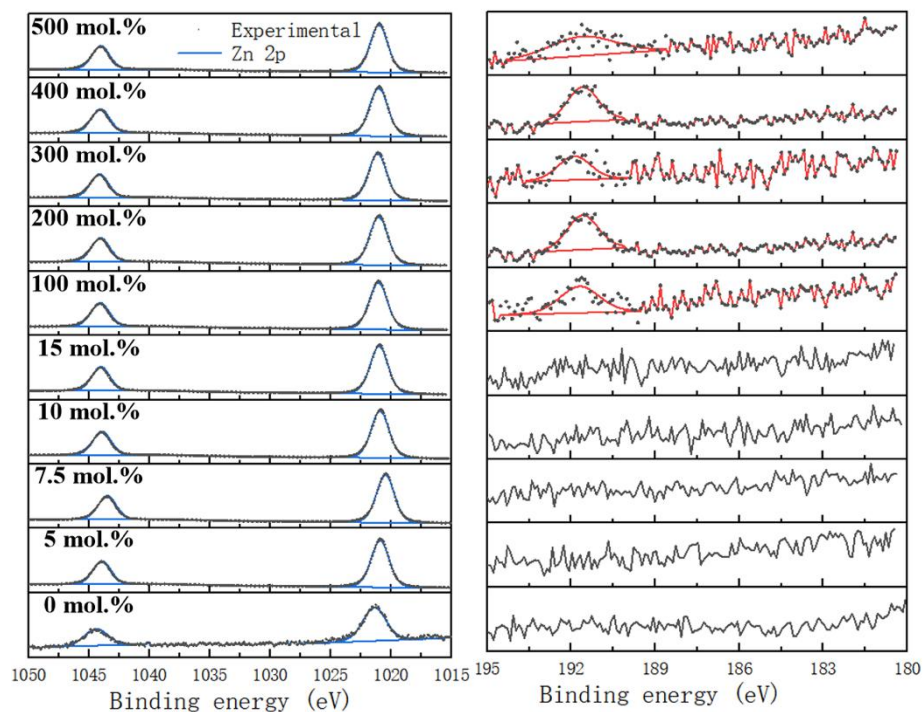
Figure 5.9: Core level XPS analysis showing the compositions and oxidation in ~ 150 nm depth of the undoped and 5, 7.5, 10, 15, 100, 200, 300, 400 and 500 mol.% ZnO:B thin films using MeOH as solvent grown via AACVD.

Table 5.3: The positions and concentrations of B element from XPS analysis for the ZnO:B thin films from THF solvent grown at 475 ºC through AACVD

Initial B concentrations (mol.%)	Positions of B 1s from XPS analysis (eV)		Concentrations of B from XPS analysis (at.%)	
	Surface	Depth (~ 150 nm)	Surface	Depth (~ 150 nm)
0	-	-	-	-
0.5	191.9	191.9	98.7	15.6
3	191.6	191.6	65.1	12.7
5	191.3	191.7	93.3	23.1
7.5	191.7	191.9	76.9	15.2
10	191.8	191.9	21.3	15.6
15	191.3	191.6	42.9	28.3

Table 5.4: The positions and concentrations of B element from XPS analysis for the ZnO:B thin films from MeOH solvent grown at 475 ºC through AACVD

Initial B concentrations (mol.%)	Positions from XPS analysis (at.%)		Concentrations from XPS analysis (at.%)	
	Surface	Depth (~ 150 nm)	Surface	Depth (~ 150 nm)
0	-	-	-	-
5	191.5	-	1.44	-
7.5	191.2	-	1.75	-
10	191.5	-	2.41	-
15	191.1	-	1.64	-
100	191.6	191.7	5.66	1.61
200	191.5	191.6	8.12	2.46
300	191.6	191.9	12.3	1.25
400	191.3	191.6	13.93	3.07
500	191.2	191.6	13.89	2.03

Hall effect measurement

The electrical properties of the ZnO thin films with/without B doping from both THF and MeOH solvents were determined via the Hall effect measurements. The film thickness was calculated optically using UV-Vis spectroscopy in reflectance mode.

The results shown in Table 5.5 and 5.6 in detail as well as the most important electrical properties of the TCO materials, resistivities (ρ), which can evaluate the electrical conductivities of materials quantitatively and also be displayed in Figure 5.10 visually. All the ZnO:B thin films from two different solvents are considered as n-type semiconductors resulting as confirmed by Hall effect measurements. The nominally undoped film deposited using MeOH was too resistive to obtain any values but crude measurements via a two-point probe showed the resistance to be in the M order. For the THF solvent system, the nominally undoped film was measurable but still high at 2.12 x10^{-1} .cm. The differences observed may be due to intrinsic vacancies/dopants such as oxygen vacancies, zinc interstitials or even adventitious hydrogen.[16]

For the B-doped ZnO thin films from THF solvent, from the resistivity trend shown in Figure 5.10, increasing the concentration of B doping results in the resistivity showing a general decrease trend which reaches the lowest resistivity at 5.84×10^{-3} Ω.cm for ZnO:B (7.5 mol.%) thin films. Then, the resistivity increases again to relatively high values at the 15 mol.% B doping. When the B started to dope into ZnO thin films, one B^{3+} can offer one more electron compared to Zn^{2+} to improve the bulk concentrations leading to the decrease of resistivities. However, B^{3+} may not offer as much electrons as some other dopants with high oxidation states, such as P^{5+}, $Mo^{6+/4+}$ and W^{5+},[10,17–20] which means the resistivity may not decrease significantly at the beginning (e.g. 0.5 mol.% and 3 mol.%). Moreover, the lowest resistivity (5.84×10^{-3} Ω.cm) here can be considered similar to other high valence dopants from similar synthetic route, for example, P^{5+} doped ZnO thin film at 6.0×10^{-3} Ω.cm,[10] which may be due to the significant effect of the B dopants to increase the carrier mobility of ZnO thin films.

For the B-doped ZnO thin films from MeOH solvent, in the low doping concentrations, the resistivities were always at a relatively high level even when the initial B concentrations increases, and the lowest resistivity (1.26×10^{-1} Ω.cm) was reached for ZnO:B (10 mol.%) thin film, which suggests that the initial concentrations of the B precursor were not sufficient to provide B doping into the ZnO films and hence higher concentrations were required. However, if the initial B concentrations

were increased to >100 mol.% based on Zn source, a good resistivity trend, as shown in Figure 5.10, was observed with the ZnO:B (300 mol.%) and ZnO:B (400 mol.%) thin films showing low resistivities of 5.10×10^{-3} Ω.cm and 1.12×10^{-2} Ω.cm, respectively, which may result from the improved bulk concentrations. This can also be seen in the near infrared area of the transmittance graph from UV-vis test in Figure 5.12. Furthermore, the ZnO:B (300 mol.%) thin film shows lower resistivity than the ZnO:B (400 mol.%) thin film which may result from the higher carrier mobility. The ZnO:B (400 mol.% and 500 mol.%) thin films are likely to have too high B initial concentrations which resulted in some white hazy areas on the surface of thin films, which may cause a decrease of carrier mobilities.

To compare the electrical properties (resistivity) of the B-doped ZnO thin films from THF solvent and MeOH solvent, ZnO thin films from the dopants-miscible solvent THF have good electrical property at low concentrations while films from dopants-immiscible solvent MeOH required relatively high concentrations to reach low resistivity at 10^{-3} Ω level. The lowest resistivities of the ZnO:B thin films from these two different solvents were similar, 5.84×10^{-3} Ω.cm for thin film with 7.5 mol.% B doping from THF solvent and 5.10×10^{-3} Ω.cm for thin film with 300 mol.% B doping from MeOH solvent, respectively. The resulting low resistivities data for these films was achieved using the abundant B dopants and are comparable to typical TCO material shown in Table 3.5 and Table 4.5, ZnO:Al thin films grown from the same synthesis technology (AACVD) and the same Zn source ([Zn(OAc)$_2$.2H$_2$O]) with resistivities of 3.54×10^{-3} Ω.cm.[21] The results here show lower resistivities than some ZnO thin films also with 3+ dopants such as ZnO:Ga thin film (1.3×10^{-2} Ω.cm)[6] and ZnO:In thin film (1.7×10^{-2} Ω.cm)[6] from a different Zn source {Zn(acac)$_2$] via the same film grown method, AACVD. In addition, ZnO:B thin films have also been investigated as TCO materials from some other synthetic routes displayed in Table 5.7, such as radio frequency (RF) magnetron sputtering[15] and chemical spray pyrolysis[22] and their lowest resistivities were 5.65×10^{-3} Ω.cm and 4.5×10^{-3} Ω.cm, respectively, which are similar to the lowest resistivities in this study although here the scalable and inexpensive synthesis method of AACVD was used.

To compare the electrical properties of ZnO based thin films in Chapter 3,4 and 5, which have been illustrated in Table 5.8, all the doped ZnO thin films demonstrate excellent electrical conductivity comparing with some other typical TCO materials from previous reports, as shown in Table 3.5 and Table 4.5. For the Mo, P and B doped ZnO thin films from Chapter 3, 4 and 5, respectively, the ZnO:Mo thin film reached the lowest resistivities at 2.6×10^{-3} Ω.cm. However, the precursor of this thin film is diethylzinc, which has higher cost than the precursor ([Zn(OAc)$_2$·2H$_2$O]) of ZnO:P and ZnO:B thin films. In addition, the P doped ZnO thin film had only a slightly higher resistivity than that of the B doped one, however the concentrations of P dopants required were at a much lower level (5.0 mol.%) than that of the B dopants (300 mol.%), resulting in lower cost of the P doped ZnO thin films. In general, all the three kinds of doped ZnO thin films investigated in this thesis can be considered as alternative TCO thin films of current widely used ITO materials. If the preference is better conductivity, Mo doped ZnO thin film is the first choice while the P doped ZnO thin film is the first choice if the preference is low cost.

Table 5.5: The film thickness and resistivities of ZnO:B thin films from THF solvent via AACVD

Initial B concentrations (mol.%)	Film thickness (nm)	Resistivities / $\times 10^{-2}$ Ω.cm
0	181	21.2
0.5	151	18.4
3	254	19.6
5	308	11.1
7.5	189	0.584
10	478	18.8
15	448	31.7

Table 5.6: The film thickness and resistivities of ZnO:B films from MeOH solvent via AACVD

Initial B concentrations (mol.%)	Film thickness (nm)	Resistivities / $\times 10^{-2}$ Ω.cm
0	251	very high
5	246	high
7.5	191	257.7
10	245	12.6
15	957	29.6
100	208	41.1
200	188	8.22
300	229	0.510
400	835	1.12
500	524	15.9
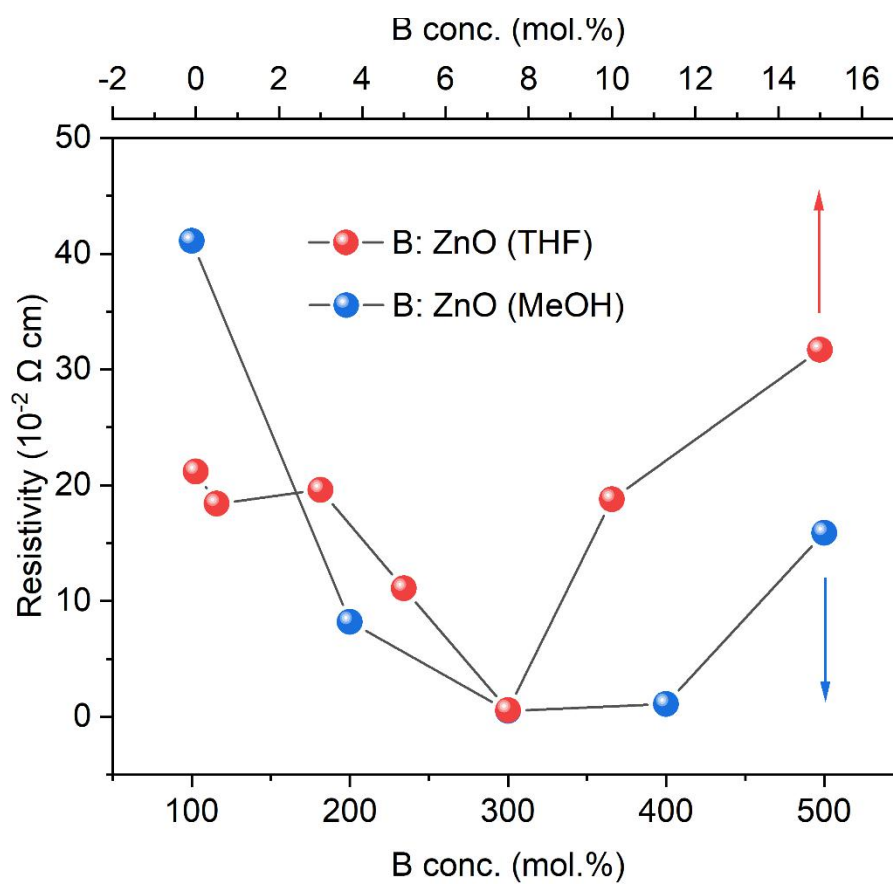
Figure 5.10: The resistivities of the undoped and B doped ZnO films using THF and MeOH as solvents grown through AACVD derived from Hall measurements.

Table 5.7: Comparison with some other B doped ZnO thin films from different synthetic routes

Zn precursor	Dopant(s)	Dopant conc.	ρ ($\times 10^{-3}$ Ω.cm)	n ($\times 10^{20}$ cm^{-3})	μ (cm^2 V^{-1} s^{-1})	Ref
purity ZnO	B	RF magnetron sputtering	5.65	~ 9.6	5.4	(15)[15]
purity ZnO	B	chemical spray pyrolysis[22]	4.5	-	-	(22)[22]
[Zn(OAc)$_2$·2H$_2$O]	B	AACVD	5.1	-	-	This project[23]

Table 5.8: Comparison with the ZnO based n-type TCOs thin films from Chapter 3, 4 and 5

Zn precursor	Dopant(s)	Dopant conc.	ρ ($\times 10^{-3}$ Ω.cm)	n ($\times 10^{20}$ cm^{-3})	μ (cm^2 V^{-1} s^{-1})	Ref
diethylzinc	Mo	AACVD	2.6	2.4	10.2	Chapter 3[24]
[Zn(OAc)$_2$·2H$_2$O]	P	AACVD	6.0	1.6	6.65	Chapter 4[10]
[Zn(OAc)$_2$·2H$_2$O]	B	AACVD	5.1	-	-	Chapter 5[23]

UV-vis test

The results of the optical property, transmittance, have been determined through the ultraviolet-visible (UV-vis) spectra, as shown in Figures 5.11 and Figure 5.12. The scanning range of UV-vis is between 2500 nm and 300 nm and it can be found that all the ZnO:B thin films from both THF solvent and MeOH solvent have obvious transparent properties with transmittance at ~ 75% - 90% in visible light (400 - 700 nm).

For the B-doped ZnO thin films from THF solvent, all the doped thin films were >80% for visible transmittance and have better transmittance than the undoped one, which means doping B into ZnO thin films can improve the optical property in this case. The general tendency of ZnO:B thin films from THF solvent is higher than that from MeOH solvent which illustrates that THF is better for optical transmittance than MeOH for ZnO thin films.

For the B-doped ZnO thin films from MeOH solvent, the visible transmittance were around ~ 75% - 80% for most thin films. The ZnO thin films with low concentrations B doping showed higher transmittance than the undoped ZnO thin films while the high concentrations ones had lower transmittance than undoped ZnO. Moreover, for the film deposited using 400-500 mol.% BEt$_3$ solution concentration, hazier films were seen possibly due to the formation of boron oxides.[21]

In the near infrared area, the ZnO:B thin films from THF solvent only show a small change compared with the undoped ZnO, which suggests that the bulk concentrations may not provide a large improvement[5,10,25] The low resistivities result from the relative high carrier mobility of the ZnO:B thin films from THF solvent. For the ZnO:B thin films from MeOH solvent, the transmittance in the near infrared area for most ZnO:B thin films are lower than the undoped one in the same area, especially for the two lowest resistivities materials, B:ZnO (300% and 400%), which represent higher bulk concentrations based on the plasmon resonance,[5,10,25] and may be the key factor for the improved electrical properties of B-doped ZnO thin films from MeOH solvent, with similar results to other doped ZnO thin films prepared from the same Zn source and solvent via AACVD.[10] In addition, the band gaps can be seen in Figures

5.13 and 5.14, the band gaps of most B-doped ZnO thin films are smaller than the undoped one as with the trend of transmittance in the near infrared area.
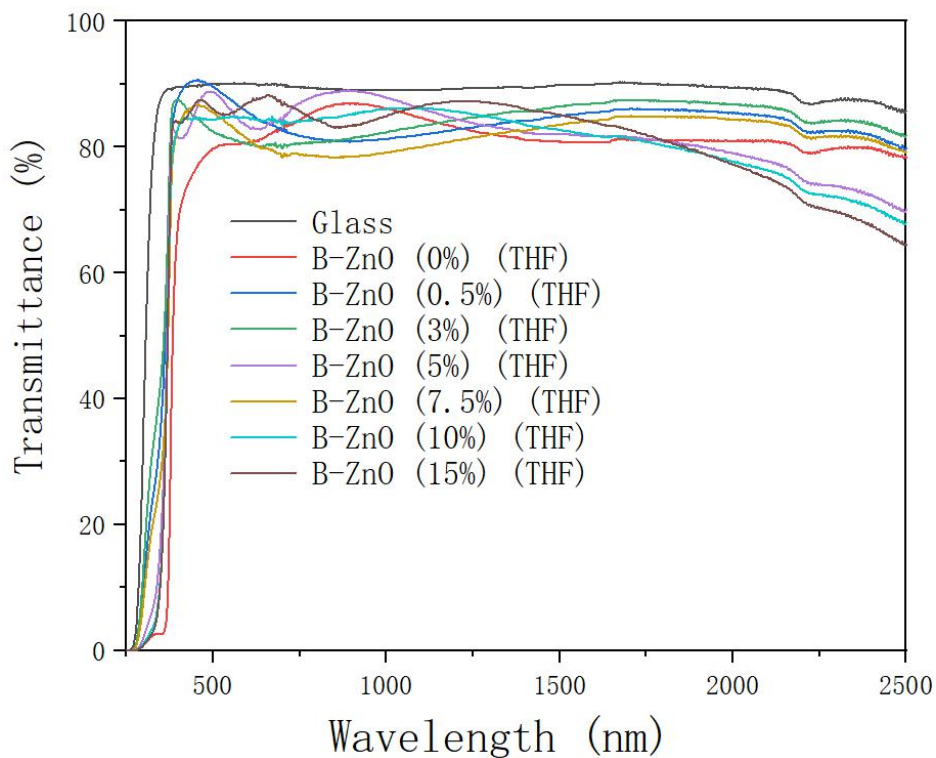
Figure 5.11: The optical data for the undoped and 0.5, 3, 5, 7.5, 10 and 15 mol.% ZnO:B thin films on glass substrates using THF as solvent prepared via AACVD showing the UV/vis spectra.
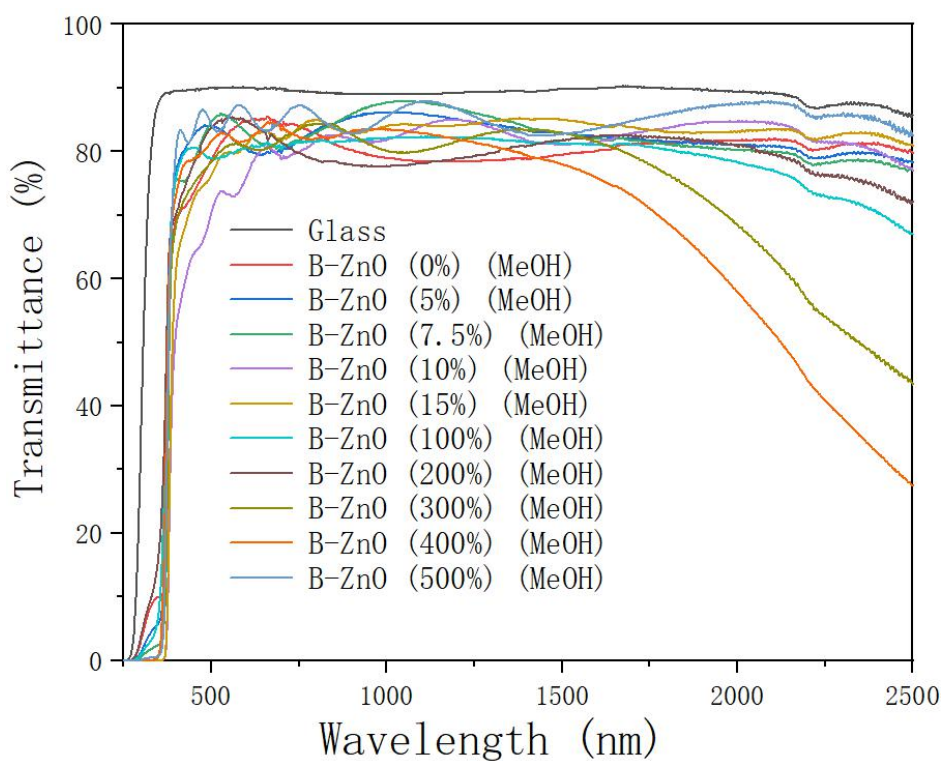
Figure 5.12: The optical data for undoped and 5, 7.5, 10, 15, 100, 200, 300, 400 and 500 mol.% ZnO:B thin films on glass substrates using MeOH as solvent prepared via AACVD showing the UV/vis spectra.
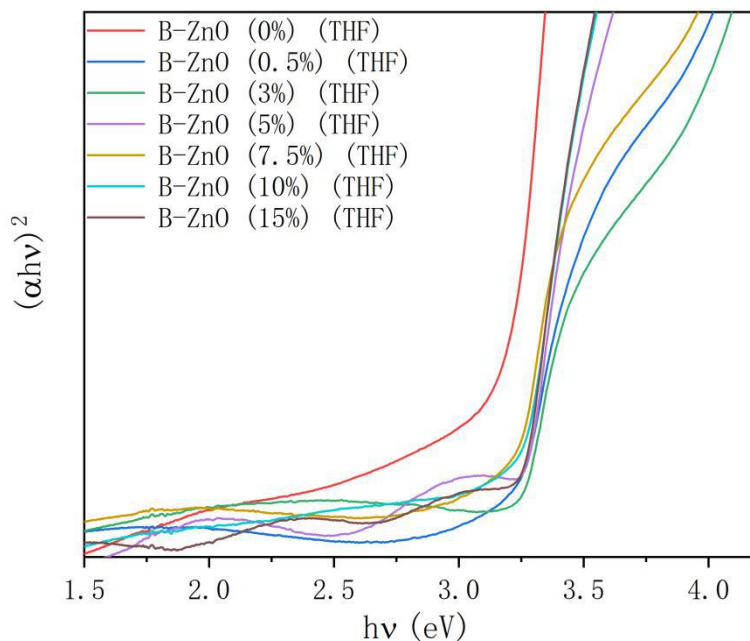
Figure 5.13: The Tauc plot for the pure and 0.5, 3, 5, 7.5, 10 and 15 mol.% ZnO:B films on glass substrates using THF as solvent prepared through AACVD calculating from the UV/vis data.
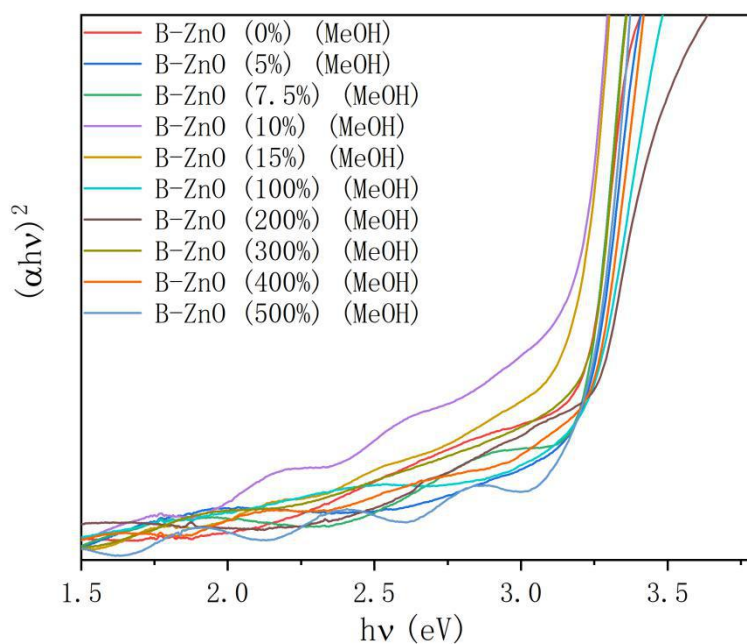
Figure 5.14: The Tauc plot for the pure and 5, 7.5, 10, 15, 100, 200, 300, 400 and 500 mol.%

ZnO:B films on glass substrates using MeOH as solvent prepared through AACVD calculating from the UV/vis data.

5.4 Conclusion

ZnO thin films with different concentrations of B doping deposited via AACVD on glass substrates from two different solvents, THF and MeOH, were prepared, compared and discussed in this investigation. Only the ZnO phase without any secondary phases were observed in the XRD patterns. The XPS analysis indicated that the oxidation states of Zn and B were +2 and +3, respectively, on the surface and at ~ 150 nm depth for all the ZnO:B thin films. For the optical properties, all the thin films were considered as transparent with transmittance at ~ 75% - 90% in the visible light from the UV-vis test and the doped thin films from THF solvent showed higher visible transmittance than that from MeOH solvent generally. For the electrical properties, the lowest resistivities of the doped ZnO thin films from the two different solvents were similar, at 5.84×10^{-3} Ω.cm for ZnO:B (7.5 mol.%) from THF and at 5.10×10^{-3} Ω.cm for ZnO:B (300 mol.%) from MeOH, respectively. Comparing with some other cations doped into ZnO films,[6,10] the resistivities in this study are low and can meet some high oxidation states dopants (P^{5+})[10] and lower than some 3+ oxidation states dopants $(Ga^{3+}$ and $In^{3+})$,[6] which may be due to doping B into ZnO crystals improving the carrier mobilities significantly. In addition, although the ZnO:B (low concentrations) thin films from THF solvent showed better optical properties and similar electrical properties compared with those from MeOH solvent, the ZnO:B (MeOH) thin films also have the advantage that to grow larger areas of thin films, the same amount of Zn precursor based on the much higher solubility of the Zn source in MeOH solvent than that in THF solvent, could be used. Moreover, the film growth technology (AACVD) in this project is a convenient synthetic technology with relative low cost, while the sources of Zn and B are also cheaper than the sources for current ITO and FTO thin films. Hence, B doped ZnO thin films could be considered as a good method for formation of potential TCO materials, as an alternative material to ITO and FTO thin films.

Adapted from: D. Zhao, S. Sathasivam, M. Wang and C. J. Carmalt, *RSC Adv.,* 2022, **12**, 33049

5.5 References

(1)   Wildsmith, T.; Hill, M. S.; Johnson, A. L.; Kingsley, A. J.; Molloy, K. C. Exclusive Formation of SnO by Low Temperature Single-Source AACVD. *Chem. Commun.* **2013**, *49* (78), 8773–8775. https://doi.org/10.1039/c3cc45676e.

(2)   Potter, D. B.; Powell, M. J.; Darr, J. A.; Parkin, I. P.; Carmalt, C. J. Transparent Conducting Oxide Thin Films of Si-Doped ZnO Prepared by Aerosol Assisted CVD. *RSC Adv.* **2017**, *7* (18), 10806–10814. https://doi.org/10.1039/c6ra27748a.

(3)   Ghosh, R.; Basak, D.; Fujihara, S. Effect of Substrate-Induced Strain on the Structural, Electrical, and Optical Properties of Polycrystalline ZnO Thin Films. *J. Appl. Phys.* **2004**, *96* (5), 2689–2692. https://doi.org/10.1063/1.1769598.

(4)   Ponja, S. D.; Sathasivam, S.; Parkin, I. P.; Carmalt, C. J. Transparent Conductive Aluminium and Fluorine Co-Doped Zinc Oxide Films Viaaerosol Assisted Chemical Vapour Deposition. *RSC Adv.* **2014**, *4* (91), 49723–49728. https://doi.org/10.1039/c4ra09997d.

(5)   Dixon, S. C.; Sathasivam, S.; Williamson, B. A. D.; Scanlon, D. O.; Carmalt, C. J.; Parkin, I. P. Transparent Conducting N-Type ZnO:Sc-Synthesis, Optoelectronic Properties and Theoretical Insight. *J. Mater. Chem. C* **2017**, *5* (30), 7585–7597. https://doi.org/10.1039/c7tc02389h.

(6)   Potter, D. B.; Bhachu, D. S.; Powell, M. J.; Darr, J. A.; Parkin, I. P.; Carmalt, C. J. Al-, Ga-, and In-Doped ZnO Thin Films via Aerosol Assisted CVD for Use as Transparent Conducting Oxides. *Phys. Status Solidi Appl. Mater. Sci.* **2016**, *213* (5), 1346–1352. https://doi.org/10.1002/pssa.201532996.

(7)   Jiamprasertboon, A.; Powell, M. J.; Dixon, S. C.; Quesada-Cabrera, R.; Alotaibi, A. M.; Lu, Y.; Zhuang, A.; Sathasivam, S.; Siritanon, T.; Parkin, I. P.; Carmalt, C. J. Photocatalytic and Electrically Conductive Transparent Cl-Doped ZnO Thin Films: Via Aerosol-Assisted Chemical Vapour Deposition. *J. Mater. Chem. A* **2018**, *6* (26), 12682–12692.

https://doi.org/10.1039/c8ta01420e.

(8)   Sathasivam, S.; Williamson, B. A. D.; Althabaiti, S. A.; Obaid, A. Y.; Basahel, S. N.; Mokhtar, M.; Scanlon, D. O.; Carmalt, C. J.; Parkin, I. P. Chemical Vapor Deposition Synthesis and Optical Properties of Nb_2O_5 Thin Films with Hybrid Functional Theoretical Insight into the Band Structure and Band Gaps. *ACS Appl. Mater. Interfaces* **2017**, *9* (21), 18031–18038. https://doi.org/10.1021/acsami.7b00907.

(9)   Sanchez-Perez, C.; Dixon, S. C.; Darr, J. A.; Parkin, I. P.; Carmalt, C. J. Aerosol-Assisted Route to Low-E Transparent Conductive Gallium-Doped Zinc Oxide Coatings from Pre-Organized and Halogen-Free Precursor. *Chem. Sci.* **2020**, *11* (19), 4980–4990. https://doi.org/10.1039/d0sc00502a.

(10)   Zhao, D.; Li, J.; Sathasivam, S.; Carmalt, C. J. N-Type Conducting P Doped ZnO Thin Films via Chemical Vapor Deposition. *RSC Adv.* **2020**, *10* (57), 34527–34533. https://doi.org/10.1039/d0ra05667g.

(11)   Erat, S.; Ozkendir, O. M.; Yildirimcan, S.; Gunaydin, S.; Harfouche, M.; Demir, B.; Braun, A. Study on Crystallographic and Electronic Structure of Micrometre-Scale ZnO and ZnO:B Rods via X-Ray Absorption Fine-Structure Spectroscopy. *J. Synchrotron Radiat.* **2021**, *28*, 448–454. https://doi.org/10.1107/S1600577520015866.

(12)   Hassan, I. A.; Ratnasothy, A.; Bhachu, D. S.; Sathasivam, S.; Carmalt, C. J. The Effect of Solvent on the Morphology of Indium Oxide Deposited by Aerosol-Assisted Chemical Vapour Deposition. *Aust. J. Chem.* **2013**, *66* (10), 1274–1280. https://doi.org/10.1071/CH13226.

(13)   Edusi, C.; Hyett, G.; Sankar, G.; Parkin, I. P. Aerosol-Assisted CVD of Titanium Dioxide Thin Films from Methanolic Solutions of Titanium Tetraisopropoxide; Substrate and Aerosol-Selective Deposition of Rutile or Anatase. *Chem. Vap. Depos.* **2011**, *17* (1–3), 30–36. https://doi.org/10.1002/cvde.201006872.

(14)   Hung-Chun Lai, H.; Basheer, T.; Kuznetsov, V. L.; Egdell, R. G.; Jacobs, R. M. J.; Pepper, M.; Edwards, P. P. Dopant-Induced Bandgap Shift in Al-Doped

ZnO Thin Films Prepared by Spray Pyrolysis. *J. Appl. Phys.* **2012**, *112* (8). https://doi.org/10.1063/1.4759208.

(15)   Wong, L. H.; Lai, Y. S. Characterization of Boron-Doped ZnO Thin Films Prepared by Magnetron Sputtering with (100-x)ZnO-xB$_2$O$_3$ Ceramic Targets. *Thin Solid Films* **2015**, *583* (1), 205–211. https://doi.org/10.1016/j.tsf.2015.04.003.

(16)   Buckeridge, J.; Catlow, C. R. A.; Farrow, M. R.; Logsdail, A. J.; Scanlon, D. O.; Keal, T. W.; Sherwood, P.; Woodley, S. M.; Sokol, A. A.; Walsh, A. Deep vs Shallow Nature of Oxygen Vacancies and Consequent n -Type Carrier Concentrations in Transparent Conducting Oxides. *Phys. Rev. Mater.* **2018**, *2* (5), 56–59. https://doi.org/10.1103/PhysRevMaterials.2.054604.

(17)   Zhao, D.; Sathasivam, S.; Li, J.; Carmalt, C. J. Transparent and Conductive Molybdenum-Doped ZnO Thin Films via Chemical Vapor Deposition. *ACS Appl. Electron. Mater.* **2020**, *2* (1), 120–125. https://doi.org/10.1021/acsaelm.9b00647.

(18)   Wu, C.; Shen, J.; Ma, J.; Wang, S.; Zhang, Z.; Yang, X. Electrical and Optical Properties of Molybdenum-Doped ZnO Transparent Conductive Thin Films Prepared by Dc Reactive Magnetron Sputtering. *Semicond. Sci. Technol.* **2009**, *24* (12). https://doi.org/10.1088/0268-1242/24/12/125012.

(19)   Can, M. M.; Frat, T.; Ismat Shah, S. Magnetoelectrical Properties of W Doped ZnO Thin Films. *J. Magn. Magn. Mater.* **2012**, *324* (23), 4054–4060. https://doi.org/10.1016/j.jmmm.2012.07.014.

(20)   Xiu, X.; Pang, Z.; Lv, M.; Dai, Y.; Ye, L.; Han, S. Transparent Conducting Molybdenum-Doped Zinc Oxide Films Deposited by RF Magnetron Sputtering. *Appl. Surf. Sci.* **2007**, *253* (6), 3345–3348. https://doi.org/10.1016/j.apsusc.2006.07.024.

(21)   Li, J.; Sathasivam, S.; Taylor, A.; Carmalt, C. J.; Parkin, I. P. Single Step Route to Highly Transparent, Conductive and Hazy Aluminium Doped Zinc Oxide Films. *RSC Adv.* **2018**, *8* (74), 42300–42307. https://doi.org/10.1039/c8ra09338e.

(22)   Pawar, B. N.; Cai, G.; Ham, D.; Mane, R. S.; Ganesh, T.; Ghule, A.; Sharma, R.; Jadhava, K. D.; Han, S. H. Preparation of Transparent and Conducting Boron-Doped ZnO Electrode for Its Application in Dye-Sensitized Solar Cells. *Sol. Energy Mater. Sol. Cells* **2009**, *93* (4), 524–527. https://doi.org/10.1016/j.solmat.2008.12.010.

(23)   Zhao, D.; Sathasivam, S.; Wang, M.; Carmalt, C. J. Transparent and Conducting Boron Doped ZnO Thin Films Grown by Aerosol Assisted Chemical Vapor Deposition. *RSC Adv.* **2022**, *12* (51), 33049–33055. https://doi.org/10.1039/d2ra05895b.

(24)   Zhao, D.; Sathasivam, S.; Li, J.; Carmalt, C. J. Transparent and Conductive Molybdenum-Doped ZnO Thin Films via Chemical Vapor Deposition. *ACS Appl. Electron. Mater.* **2020**, *2* (1), 120–125. https://doi.org/10.1021/acsaelm.9b00647.

(25)   Noor, N.; Chew, C. K. T.; Bhachu, D. S.; Waugh, M. R.; Carmalt, C. J.; Parkin, I. P. Influencing FTO Thin Film Growth with Thin Seeding Layers: A Route to Microstructural Modification. *J. Mater. Chem. C , 3 pp. 9359-9368.* **2015**.

Chapter 6 Towards boron phosphide (BP) thin films through aerosol assisted chemical vapor deposition

6.1 General introduction

6.1.1 Background

Boron phosphide (BP) is a semiconductor which can be widely used in the high temperature optoelectronic and electronic areas.[1–3] BP has a relatively narrow band gap at about 2 eV,[1] high melting point and high decomposition temperature (~1130 °C) with impressive chemical resistance and inertness[3] leading to excellent optical, thermal and mechanical properties.[1] BP can show both n-type and p-type propeties,[3,4] which has been considered as a good choice for p-n heterojunctions.[4] The aim in this project was to deposit BP as a p-type TCO in this project.

There have been many researches on BP thin films, for example, the traditional synthetic method for preparing BP requires a high temperature of ~ 1000 °C for the reactions between (1) boron and phosphorus, Zn_3P or PH_3, (2) BCl_3 and PH_3, Zn_3P or AlP, (3) BCl_3 and PCl_3.[4–6] Moreover, the CVD route also has been investigated to prepare $B_{12}P_2$ thin film with similar high temperature at 1100 °C,[7] which still requires relatively extreme conditions. Hence, finding a simpler synthetic route may enable the use of this material in a range of applications. In this project, a convenient synthetic method, AACVD, has been used to grow BP thin films.

6.1.2 Project abstract

In this study, BP thin films with different B/P mol.% ratio were prepared on SiO_2 quartz via the aerosol assisted chemical vapour deposition (AACVD) route, in an attempt to develop a p-type transparent conductive oxide (TCO) material. The B source, P source and solvent were $[BEt_3]$, $[P(NMe_2)_3]$ and hexane, respectively. The whole system was under N_2 gas (1.0 L min^{-1}) during all preparation and deposition steps and a deposition temperature of 550 °C was used. X-ray photoelectron spectroscopy (XPS) analysis of the resulting films suggested the formation of BP. However, although a Schlenk line and oil bubbler were used to avoid the influence of

oxygen, the resulting thin films were found to have significant B and P oxides existing on the surface according to XPS analysis. Based on the X-ray diffraction (XRD) patterns, only peaks for quartz were observed for all of the BP thin films, which suggests the thin films were amorphous materials. The thin films also did not have significant electrical properties resulting from the B and P oxides on the surface, even though BP material was also seen on the surface and in the depth from XPS analysis. Generally, amorphous BP thin films have been prepared and the further plan to improve the electrical properties through doping was not studied due to the existence of the B and P oxides on the surface. Future investigations should attempt to reduce the amount of oxide formation, potentially by the use of alternative precursors or modifications to the AACVD rig and if this could be achieved then doping the BP films would be of great interest in order to achieve the desirable electronic properties.

6.2 Experiment methods

6.2.1 Film synthesis

Depositions were carried out under N_2 (BOC Ltd., 99.99% purity) flow. Triethylborane solution ([BEt$_3$] (1.0 M in hexanes)), tris(dimethylamino)phosphine ([P(NMe$_2$)$_3$] (97%) and hexane (99%)) were purchased from Sigma. The glass substrates are float glass from Pilkington NSG. The quartz substrates are amorphous but some crystallinity arises from the 1000 ^{o}C annealing step They were purchased from Alfa Aesar Quartz Microscope Slides (made from fused quartz). Glass and quartz substrates were cleaned via detergent, water and isopropanol then dried in a 70 ^{o}C oven.

[BEt$_3$] solution (2.6 ml, 2.60 mmol) and [P(NMe$_2$)$_3$] (1.18 ml, 6.50 mmol) were dissolved in hexanes (15 mL) and placed in a glass bubbler. This deposition used quartz as substrate and an oil bubbler at the end of the AACVD reactor to avoid the possible influence of external air. All solutions were atomised through a piezoelectric device (Johnson Matthey liquifog$^®$). The aerosol mist was delivered to the AACVD reaction chamber and passed over the heated substrate (SiO$_2$ quartz substrate on the float glass with a SiO$_2$ barrier layer substrate) using N_2 carrier gas at 1.0 L min^{-1}. Depositions were carried out at 550 ^{o}C and lasted until the precursor solution was fully used. After the depositions the substrates were cooled under a flow of N_2. The glass substrates would not be removed unless that with the graphite block was cooled to below 50 °C. The quartz was annealed at 1000 °C under Ar flow for 1 h in furnace after characterizations and was cooled to below 50 °C. The films on the substrates were handled and stored in air.

6.2.2 Film characterisation

A modified Bruker-Axs D8 diffractometer with parallel beam optics and a PSD

LynxEye silicon strip detector were used for the X-ray diffraction (XRD) test, in which the range 10 - 65° 2θ was scan with a monochromated Cu K$_\alpha$ source operated at 40 kV with 30 mA emission current with 0.5° as incident beam angle and 0.05° at 1 s/step as step frequency. The surface elemental surroundings were investigated via X-ray photoelectron spectroscopy (XPS) by a Thermo Scientific K-alpha photoelectron spectrometer using monochromatic Al$_{k\alpha}$ radiation. Higher resolution scans were recorded for the principal peaks of boron (1s), phosphorus (2p), oxygen (1s) and carbon (1s) at a pass energy of 50 eV, and the data was dealt by CasaXPS software with calibration by adjusting the binding energy of adventitious carbon at 284.5 eV.

6.3 Results and Discussion

In this project, a series of boron phosphide (BP) thin films with different B/P mol. ratio were grown on the SiO_2 quartz substrates via AACVD. The precursors here were two non-oxide materials, [BEt$_3$] and [P(NMe$_2$)$_3$] and the solvent was hexane, which also did not contain oxide element. The deposition temperatures for all thin films were 550 °C while the whole system was under N_2 atmosphere (1.0 L min^{-1} as flow rate) unless the temperatures were under 50 °C. Annealing the films deposited on the quartz substrate was investigated and the films were annealed at 1000 °C after XRD and XPS analysis. Due to the heating limits of the CVD system (~600 °C) the higher temperature annealing had to be carried out as a separate step using a tube furnace. In order to reduce the influence of external oxygen based on the high tendency of both B and P elements to be oxidized, a Schlenk line was used during the preparation process for the precursor solution and an oil bubbler was placed at the end of the AACVD reactor to avoid a backward flow from the outlet of the reactor. However, the B and P oxides were determined through XPS analysis due to such methods still cannot avoid the influence of O_2 completely or the possible rapid oxidation in the air at room temperature, which have a significant effect on the BP thin films in this study. Due to all the BP thin films have nearly the same characterization results and with no e significant electrical properties, one B/P mol.% ratio of the thin film was chosen to show its crystal/amorphous structure from XRD patterns, following annealing and surface/depth element composition and oxide states from XPS analysis as representative of all thin films.

Figure 6.1 displays the X-ray diffraction (XRD) patterns of the BP thin film with/without annealing. The peak at ~ 21.8° resulted from the quartz substrate.[2] No other peaks were observed in the XRD even after the annealing process, suggesting that the BP thin film was highly disordered or amorphous.
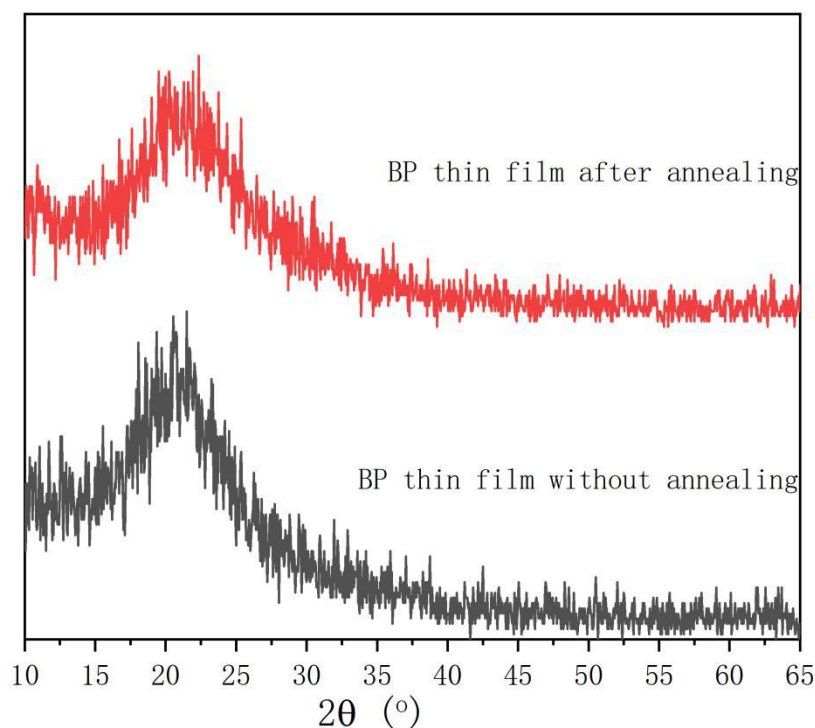
Figure 6.1: XRD patterns of the BP thin films prepared at 550 ºC via AACVD before and after annealing at 1000 ºC under Ar flow for 1 h.

The oxidation states and elemental composition on the surface and in the depth of the BP thin film based from the X-ray photoemission spectroscopy (XPS) are shown in the Table 6.1 and Figure 6.2. For the surface XPS analysis, the binding energy of B 1s was ~188.05 eV and 191.50 eV. The peak at 188.05 eV corresponds to B 1s in BP, while the peak at 191.50 eV matches previous reports for boron oxides.[2,3] The peaks at ~129.91 eV and 130.78 eV correspond to P $2p_{3/2}$ and $2p_{1/2}$ of BP, respectively, while the peaks at ~133.21 eV and 134.08 eV can be considered as P $2p_{3/2}$ and $2p_{1/2}$ of phosphorus oxides, respectively.[2,3,8] For the depth XPS analysis, the B 1s peak corresponding to boron oxides at ~192.21eV was significantly reduced compared to the surface XPS and the other peak at 188.65 eV for BP was the major peak. The peaks at ~130.81 eV and 131.68 eV corresponding to P $2p_{3/2}$ and $2p_{1/2}$ of BP were observed in the depth XPS, however the peaks for phosphorus oxides disappeared. These results suggest that the surface of the BP thin film has some boron oxide and

phosphorus oxide impurities besides the BP film, which may result from oxidation during the deposition process. The majority of the depth of the thin film is BP while only small amounts of phosphorus oxide impurities exists on the surface. In the other words, the BP thin film has been synthesized, however, the surface of this film is very easy to be oxidized.

Although the material BP can be seen on the surface and in the depth based on the XPS analysis, the B and P oxides covered the surface and highly prevented the change of electrical properties. Reliable data from Hall effect measurement was not possible for all the films due to the too high resistivity and the expected p-type properties will not be discussed in this project.

Table 6.1: The positions of B and P elements based on the XPS analysis for the BP thin film grown at 550 ºC through AACVD

Elements	Positions from XPS analysis (eV)	
	Surface	Depth
B (BP)	188.1	188.7
B (Boron oxides)	191.5	192.2
P (BP)	129.9	130.8
	130.8	131.7
P (Phosphorus oxides)	133.2	-
	134.1	-
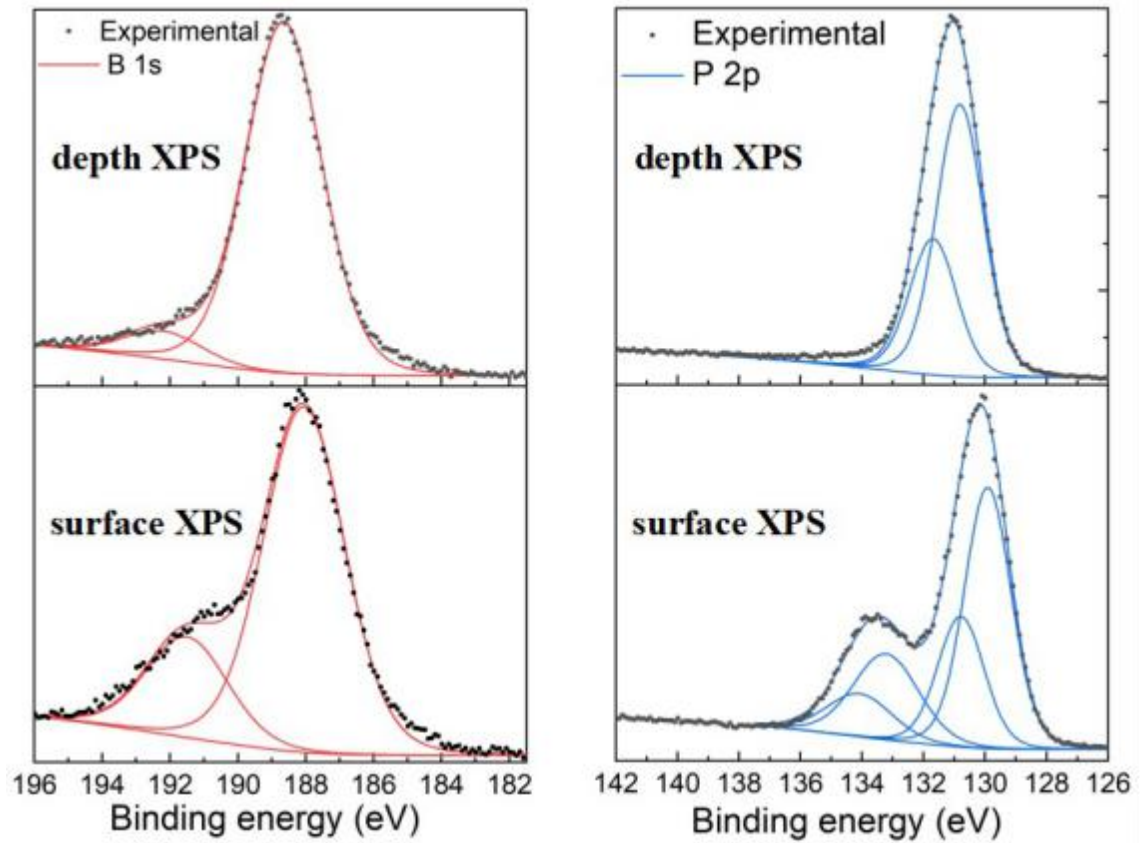
Figure 6.2: Core level XPS test showing the B and P on the surface and in the depth of BP thin film.

6.4 Conclusion

Boron phosphide (BP) thin film on quartz substrate has been prepared through AACVD. There were not any peaks of BP seen in the XRD patterns, which means the thin film was amorphous. According to the surface XPS analysis, the binding energy of all of the BP thin films, boron oxides and phosphorus oxides can be found while only the binding energy of BP with some boron oxide contamination was observed in the depth XPS analysis. Therefore, the amorphous BP thin film has been synthesized successfully whose surface area is easily oxidized. In order to get crystalline BP thin films, further investigations, such as changing the precursors and annealing directly after depositions, may be necessary. However, these experiments could not be progressed and have not been investigated in this study, but they may be worth trying in the future.

6.5 References

(1)   Gu, Y.; Zheng, H.; Guo, F.; Qian, Y.; Yang, Z. A Benzene-Thermal Synthesis of Cubic Boron Phosphide (BP) Ultrafine Powders. *Chem. Lett.* **2002**, No. 7, 724–725. https://doi.org/10.1246/cl.2002.724.

(2)   Zhang, X. W.; Xu, S. Y.; Han, G. R. Boron Nitride Phosphide Thin Films Grown on Quartz Substrate by Hot-Filament and Plasma-Assisted Chemical Vapor Deposition. *Phys. Status Solidi Appl. Res.* **2004**, *201* (13), 2922–2928. https://doi.org/10.1002/pssa.200406845.

(3)   Dalui, S.; Hussain, S.; Varma, S.; Paramanik, D.; Pal, A. K. Boron Phosphide Films Prepared by Co-Evaporation Technique: Synthesis and Characterization. *Thin Solid Films* **2008**, *516* (15), 4958–4965. https://doi.org/10.1016/j.tsf.2007.09.047.

(4)   Kumashiro, Y. Refractory Semiconductor of Boron Phosphide. *J. Mater. Res.* **1990**, *5* (12), 2933–2947. https://doi.org/10.1557/JMR.1990.2933.

(5)   Mizutani, T.; Asano, H.; Tatau Nishinaga; Uchiyama, S. Vapor Etching of Boron Monophosphide by Gaseous Hydrogen Chloride. *Jpn. J. Appl. Phys.* **1977**, *16* (9), 1629–1633. https://doi.org/10.1143/JJAP.16.1629.

(6)   Franetović, V.; Milat, O.; Ivček, D.; Bonefačić, A. Quenching Efficiency of Some Splat-Cooling Devices. *J. Mater. Sci.* **1979**, *14* (2), 498–500. https://doi.org/10.1007/BF00589850.

(7)   Kumashiro, Y.; Yoshizawa, H.; Yokoyama, T. Epitaxial Growth of Rhombohedral Boron Phosphide Single Crystalline Films by Chemical Vapor Deposition. *J. Solid State Chem.* **1997**, *133* (1), 104–112. https://doi.org/https://doi.org/10.1006/jssc.1997.7324.

(8)   Pelavin, M.; Hendrickson, D. N.; Hollander, J. M.; Jolly, W. L. Phosphorus 2p Electron Binding Energies. Correlation with Extended Hückel Charges. *J. Phys. Chem.* **1970**, *74* (5), 1116–1121. https://doi.org/10.1021/j100700a027.

Chapter 7 Catalytic molybdenum sulfides thin films for oxygen evolution reaction through aerosol assisted chemical vapor deposition

This chapter is adapted from a paper manuscript that will be submitted to a journal. Donglei Zhao, Jianwei Li, Siyu Zhao, Sanjayan Sathasivam, Yeshu Tan, Guanjie He, Ivan P. Parkin and Claire J. Carmalt. Phosphorus doped Molybdenum Sulfide Thin Films Grown via Aerosol Assisted Chemical Vapor Deposition for Efficient Oxygen Evolution Reaction.

This work was completed by JL, SZ, SS, YT, GH, IP, CC and myself. The main part of the work thin film depositions, characterizations and analysis were carried out by myself. JL, SZ and CC provided many useful ideas, advice and discussions during the whole process; CC and SS supervised the work. YT offered his help and kind advice for the electrochemical characterizations, GH and IPP have given many useful advice and discussions for the submitted manuscript.
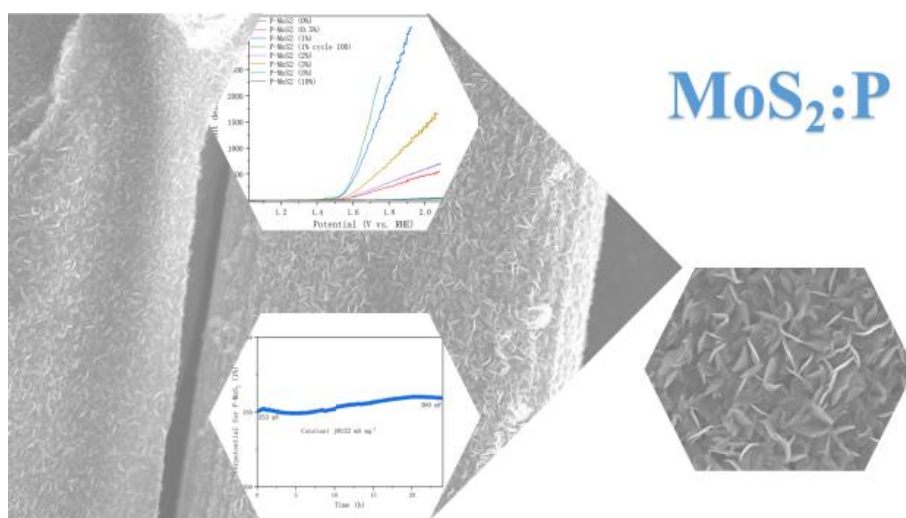
Representative image shows the P-doped MoS₂ thin films grown via AACVD which show excellent OER catalytic properties with long time stability and have typical beautiful microscopic surface morphology like flowers.

7.1 General introduction

7.1.1 Background

The transition metal disulfide material, molybdenum disulfide (MoS₂), is a two dimensional (2D) material with unique layered structures and electronic properties,[1] and relative low free energy for H adsorption,[2–4] which have attracted a lot of attention in the electrocatalytic areas. The crystal structure of the most stable and common 2-H MoS₂ phase is displayed in Figure 7.1.[5] As the catalytic properties of electrocatalysts are influenced by the numbers of exposed active sites and electrical conductivity,[1,6] and only few active sites located at the edge of the MoS₂ layer,[1,2,7–12] the electrocatalytic applications for pure MoS₂ material are limited and requires different methods to improve its electrocatalytic properties. In general, there are two main methods to improve the catalytic performance of MoS₂ materials, which include increasing the numbers of active sites and reducing the internal resistance.[1] For increasing active sites of MoS₂ material, there are several methods, such as preparing ultrathin defective MoS₂ nanosheets, MoS₂ quantum dots, forming porous structure and doping with heteroatoms.[2,11] For example, some reports use cobalt (Co) to dope into MoS₂ material, which can modify the electron density and electronic structure of MoS₂ leading to high electrocatalytic performance.[13] In order to reduce the internal resistance of MoS₂, some investigations introduced substrates with low resistivities including nanoporous carbon, graphene and carbon nanotube,[2] which can also improve the catalytic activity resulting from the lower aggregation[14] and higher conductivity.[15–17] Phosphorus (P) was used as a dopant here, and investigated as a prospective dopant in the water splitting area,[18–24] as a heteroatom dopant and deposited P-doped MoS₂ thin films on hydrophilic carbon paper substrates to obtain high catalytic activity for oxygen evolution reaction (OER).

MoS₂ based materials are known as typical electrocatalysts for HER on the basis of the high chemisorption capability for hydrogen from the Mo-S sites at the edge,[13,25] while usually this material has relatively low catalytic activity for OER.[13,25–27]

Although, there are some MoS_2 based materials that also have good OER catalytic properties reported before,[2,11–13,25–29] the compositions of these materials are more likely to be heterostructures or hybridizing 3D transition metals (such as Fe, Co and Ni) doped ones, which may combine both HER and OER catalytic activity, which suggests that the MoS_2 brings HER activity while the other material brings OER activity. For example, some reports indicated that the catalytic performance of OER was resulting from the 3D transition metal-based components, but not from the MoS_2 material directly.[13,25,30–34] However, in this project, the simply prepared P-doped MoS_2 thin films showed significant electrocatalytic properties only for OER in alkaline medium, which is important to be investigated for MoS_2 based materials in the electrocatalytic water splitting area.
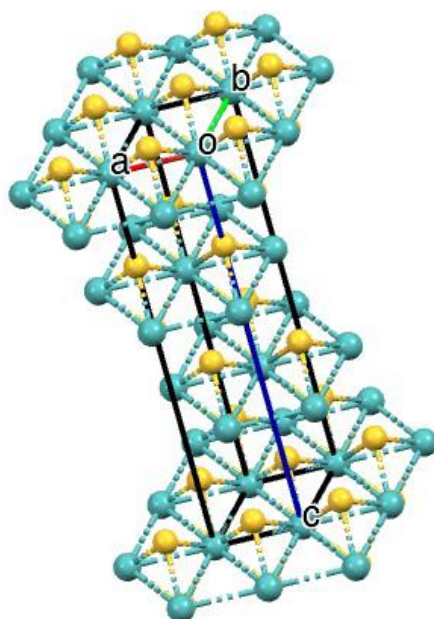
Figure 7.1: Crystal structure of 2-H MoS_2 (ICSD #38401).

7.1.2 Project abstract

In this investigation, a series of MoS_2 thin films with different initial concentrations of P doping, which can be considered as a potential electrocatalyst of oxygen evolution

reaction (OER) used in the water electrolysis for renewable energy source area, were grown on carbon paper substrates through aerosol assisted chemical vapour deposition (AACVD). The carbon paper was chosen as substrate in order to decrease the internal resistance to obtain better catalytic properties. The Mo precursor used was tetrakis(diethyldithiocarbamato) molybdenum(IV) $[Mo(S_2CNEt_2)_4]$, while tris(dimethylamino)phosphine $[P(NMe_2)_3]$ was used as the P precursor. The thin films were synthesized from $[Mo(S_2CNEt_2)_4]$ and various quantities of $[P(NMe_2)_3]$ dissolved in tetrahydrofuran (THF) via the convenient and low cost synthetic route of AACVD under Ar gas at 475 °C for the deposition conditions. The P-doped MoS_2 thin films showed excellent catalytic performance for OER test in alkaline medium (1M KOH). For the MoS_2:P (1 mol.%) thin film, the lowest overpotential was only 319 mV with current density at 10 mA cm^{-2} and 173 mV with current density at 10 mA mg^{-1}, respectively, while the high mass activity of 1000 A g^{-1} at small overpotential of 450 mV. Further investigation of the MoS_2:P (1 mol.%) thin film showed that the catalytic performance increases initially and then remained stable after repeating linear sweep voltammetry (LSV), and the lowest overpotential for the 100 LSV cycle reached 313 mV with current density at 10 mA cm^{-2} and 143 mV with current density at 10 mA mg^{-1}. In addition, the long term stability test showed that the materials did not have significant change of overpotential after a one day chronovoltammetry OER test.

7.2 Experimental

7.2.1 Precursor synthesis

The synthesis of the precursor tetrakis(diethyldithiocarbamato)molybdenum(IV) ($[Mo(S_2CNEt_2)_4]$) was prepared using the method based on previous literature reports.[35,36] The synthesis was carried out under Ar (BOC Ltd., 99.99% purity) flow. The molybdenumhexacarbonyl ($[Mo(CO)_6]$, 98%), tetraethylthiuram disulfide ($[Et_2NCSS_2CSNEt_2]$, $\geq$ 97%) and acetone (99%) were purchased from Sigma. $[Mo(CO)_6]$ (2.0 g, 7.4 mmol) was added into three-necked flask with $[Et_2NCSS_2CSNEt_2]$ (2.3 g, 14.8 mmol) dissolved in acetone (80 ml), then the system was heated to reflux for 2 h under an Ar flow. After reflux, the flask was cooled to the room temperature slowly, and the flask was put in the fridge overnight. After crystallization in the fridge, the solid in the flask was isolated by suction filtration and washed with pentane (3 x 20 mL) to obtain a black microcrystalline solid of $[Mo(S_2CNEt_2)_4]$ (yield 65%).

7.2.2 Film synthesis

Depositions were carried out under an Ar (BOC Ltd., 99.99% purity) flow. The Mo precursor ($[Mo(S_2CNEt_2)_4]$) was prepared as described above, whereas tris(dimethylamino)phosphine ($[P(NMe_2)_3]$, 97%) and tetrahydrofuran (THF, 99.9%) were purchased from Sigma. Hydrophilic carbon paper substrates were placed on the surface of the glass substrates, which were cleaned using detergent, water and isopropanol then dried in a 70 °C oven.

$[Mo(S_2CNEt_2)_4]$ (0.35 g, 0.51 mmol) in THF (30 mL) was placed in a glass bubbler. $[P(NMe_2)_3]$ (x mol.% based on Mo, x = 0, 0.5, 1.0, 2.0, 3.0, 5.0 and 10.0) was added into the same bubbler. The solution was atomised through a piezoelectric device (Johnson Matthey liquifog®). The aerosol mist was delivered to the AACVD reaction chamber, which has been previously described,[37,38] and was passed over the heated

substrate (hydrophilic carbon paper on the float glass with a SiO_2 barrier layer) using Ar carrier gas at 0.6 L min^{-1}. The weight of carbon paper was determined using an analytical balance before and after depositions to confirm the MoS_2 weight on the carbon paper substrate. Depositions were carried out at 475 °C and lasted until the precursor solution was fully used. After the deposition the substrates were cooled under a flow of Ar. The carbon paper and glass substrates were not removed until the graphite block was cooled to below 50 °C. This process was repeated once to make sure that thin films were deposited on both sides of the carbon paper substrates. The P-doped MoS_2 (1 mol.%) thin film was also grown on the glass substrate with one layer of fluorine doped tin oxide (FTO) (FTO glass substrate) under the same deposition conditions as the thin films grown on carbon paper substrates. The films on the substrates were handled and stored in a vacuum drying oven at room temperature without air.

7.2.3 Film characterisation

The X-ray diffraction (XRD) analysis scanning from 10 to 60° (2θ) chose a modified Stoe STADI-P 2-axis diffractometer with parallel beam optics and a Dectris Mythen 1K detector. The scans used a monochromated Cu Kα source operated at 40 kV and its emission current was 40 mA with 0.5° as incident beam angle and 0.05° at 1 s/step as step frequency. The X-ray photoelectron spectroscopy (XPS) analysis was used to determine the surface elemental surroundings by a Thermo Scientific K-alpha photoelectron spectrometer using monochromatic Alkα radiation. Higher resolution scans were recorded for the principal peaks of molybdenum (Mo 3d), phosphorus (P 2p), sulfur (S 2p), oxygen (O 1s) and carbon (C 1s) at a pass energy of 50 eV, and then using the CasaXPS software to deal with the data from the XPS analysis. The binding energy of adventitious carbon was adjusted at 284.5 eV as calibration. The RENISHAW invia Raman spectrometer was used with laser at 514.5 nm and scanned from 2000 nm to 100 nm for materials on carbon paper substrates. The JEOL JSM-6301F Field Emission Scanning Electron Microscopy (SEM) with 10 and 15 keV as

accelerating voltage was used to investigate the surface morphologies of the thin films and carbon paper substrates. All the samples were coated with gold before the analysis to avoid charging. Mass spectrometry was determined through the ASAP-HESI ionisation connected to the Q Exactive Plus mass spectrometer performed in UCL Chemistry Mass Spectrometry Facility using an ASAP probe integrated into the HESI ion source. The Exactive Plus mass spectrometer is used to measure the generated gas phase ions. For measurement conditions, the HESI parameters were the auxiliary gas to 5, the sheath and sweep gases to 0, the auxiliary gas heater to 400°C and typical operating temperatures were between 100°C and 450°C but higher temperatures are needed for some compounds and lower more appropriate for others. The discharge voltage range was 3.5 - 4.0 kV providing the stable background ion signal depending on the structure of analyte. The FT-IR spectrum used Bruker Alpha-T ATR-FTIR Fourier Transform Infrared Spectrometer via scanning from 4000 nm^{-1} to 400 nm^{-1}. The electrochemical performance of the catalytic thin films were tested in one three-electrode cell and the Gamry Interface 1000 potentiostat was used for electrochemical measurements. The counter electrode was graphite rod and the reference electrode was Ag/AgCl (saturated KCl) electrode while the working electrode was prepared by ourselves from the doped MoS_2 thin films on carbon paper. The electrolyte in this system was 1M KOH solution. In the electrochemical measurements from Gamry, the data of linear sweep voltammetry (LSV) was measured at a scan rate of 10 mV s^{-1}. The potentials versus (vs.) Ag/AgCl electrode from LSV were converted into potentials vs. reversible hydrogen electrode (RHE), $E_{RHE} = E_{Ag/AgCl} + 0.197 + 0.059$ x pH. Further investigation of the materials with best catalytic performance in this project, MoS_2:P (1 mol.%) thin film, involved 100 cycles linear sweep voltammetry (LCV) scans. The long-term stability was analyzed by the chronovoltammetry measurement for one day. All of the LSV measurements for the thin films on carbon papers substrates are presented with iR compensation.

7.3 Results and Discussion

In this project, P-doped MoS_2 (0, 0.5, 1, 2, 3, 5 and 10 mol.%) thin films were grown on carbon paper substrates via AACVD. The Mo source $[Mo(S_2CNEt_2)_4]$ ($[MoL_4]$) was used with/without adding dopant amounts of $[P(NMe_2)_3]$ as the P source. The Mo precursor ($[MoL_4]$) was prepared based on the method of former literature[35,36] and was characterized via mass spectrometry (Figure 7.2) and Fourier transform infrared spectroscopy analysis (FT-IR) (Figure 7.3). From the mass spectrum, the peaks for the experimental data in Figure 7.2 (a) and theoretical data ($[C_{20}H_{40}S_8N_4Mo]$) in Figure 7.2 (b) were similar and different peaks relating to isotopes can be seen resulting from the high resolution mass spectrum. In addition, the peaks in the FT-IR spectrum were at $\sim$ 2972 cm^{-1} (w), 2925 cm^{-1} (w), 2867 cm^{-1} (w), 1488 cm^{-1} (m), 1456 cm^{-1} (m), 1425 cm^{-1} (m), 1375 cm^{-1} (m), 1353 cm^{-1} (m), 1300 cm^{-1} (m), 1266 cm^{-1} (m), 1210 cm^{-1} (m), 1143 cm^{-1} (m), 1096 cm^{-1} (m), 1072 cm^{-1} (m) and 1001 cm^{-1} (m), which matches the FT-IR results previously reported in the literature.[35] According to these characterizations, it can be confirmed that the Mo precursor ($[MoL_4]$) has been prepared in this project. All depositions were carried out at 475 °C during film growth, with the system under an Ar atmosphere (0.6 L min^{-1} as flow rate) until it was cooled to below 50 °C once the depositions were complete. Both sides of the carbon paper were deposited with doped MoS_2 thin films to be used as self-standing OER electrodes and all thin films were characterized by X-ray diffraction (XRD), Raman spectroscopy, scanning electron microscopy (SEM) and X-ray photoelectron spectroscopy (XPS) analysis. Moreover, due to some characterization techniques being influenced by the high concentrations of carbon paper substrates, the MoS_2:P (1 mol.%) thin film with the best catalytic performance in this study has been prepared on FTO glass substrate at the same deposition conditions and compared with that on carbon paper substrate after similar characterizations.
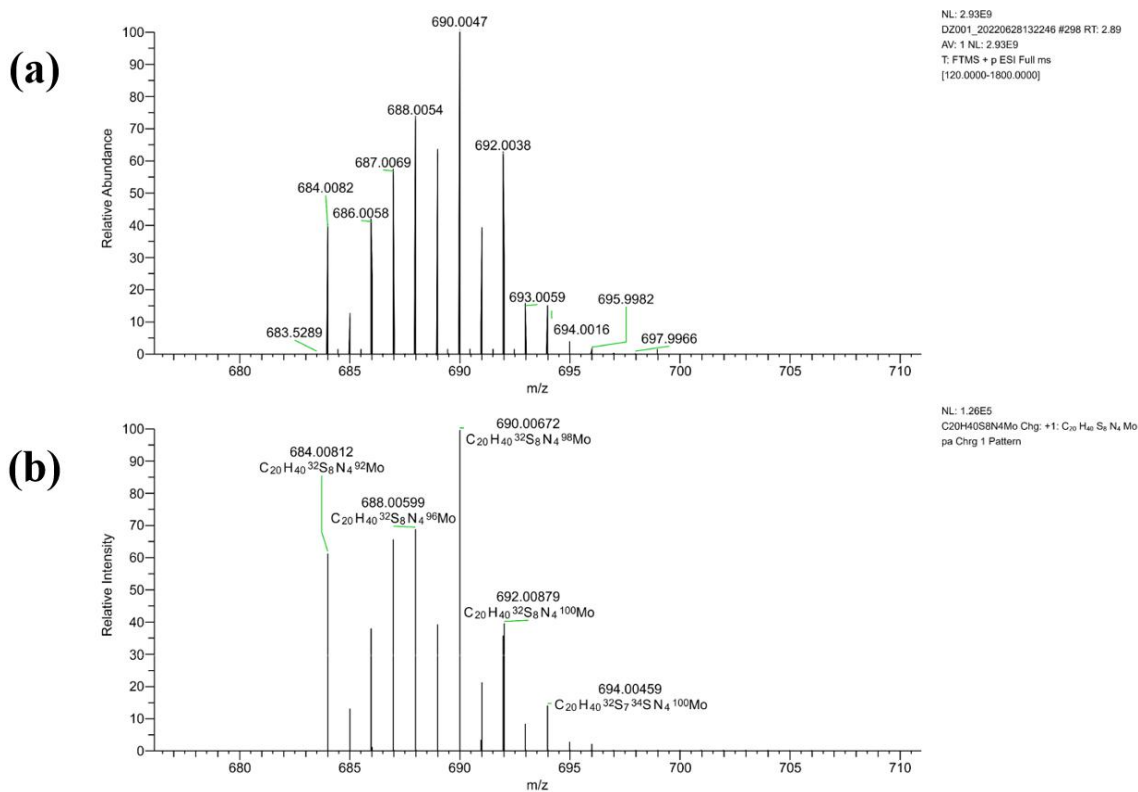
Figure 7.2: Experimental (a) and theoretical (b) Mass spectrum for the Mo precursor [Mo(S₂CNEt₂)₄].
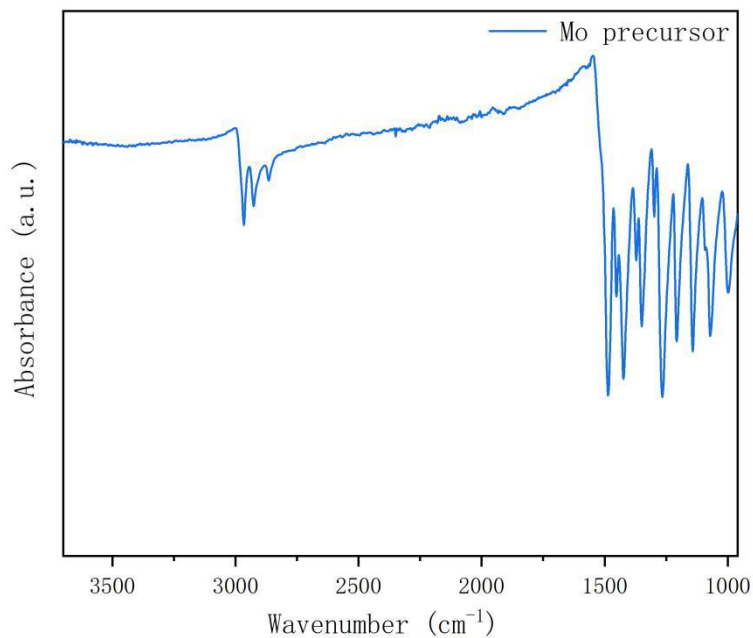

Figure 7.3: FT-IR (solid) spectrum for the Mo precursor [Mo(S₂CNEt₂)₄].

XRD

XRD patterns of the undoped and P-doped MoS_2 thin films on carbon paper are displayed in Figure 7.4. Four main peaks were observed in the XRD patterns for all the MoS_2 thin films with/without dopants. However, all these peaks correspond to the graphite material from the carbon paper substrates and characteristic peaks (e.g. 14.3^o for the plane (002) of MoS_2) for any secondary phases for MoS_2 material were not observed.[1,19,20] From the XRD results it was difficult to see any peaks for the MoS_2:P thin films (although a broad peak at ~33° may correspond to the (100) plane of MoS_2, which was previously indicated to be the most intense peak in the XRD of AACVD deposited MoS_2[39]) due to the strong diffraction peaks from the carbon paper substrate that make any peaks due to MoS_2 undetectable. Evidence for the formation of MoS_2:P thin films was gained from Raman spectroscopy and XPS analysis (*vide infra*).

Moreover, in order to further investigate the MoS_2 thin films after OER test without the effect of carbon paper in XRD, the P-doped MoS_2 (1 mol.%) thin film on normal glass substrate and FTO glass substrate also has been characterized from XRD and is shown in Figure 7.5. However, the characteristic peaks of MoS_2 also cannot be seen here. Besides the peaks for FTO (F doped SnO_2) layer, there are only two small peaks at ~ 33.1^o and 58.7^o, which is similar to that on barrier coated glass substrate. These peaks are not enough to determine one material, and also cannot match any materials with Mo element. Similarly, the MoS_2:P (1 mol.%) thin film after OER test also only has one more peak at ~ 12.7^o, which could not be identified from only one peak. The XRD patterns from MoS_2:P (1 mol.%) thin films on normal glass and FTO glass substrate further suggest the MoS_2:P thin films in this study may be highly disordered or amorphous after justifying the existence of MoS_2:P material.
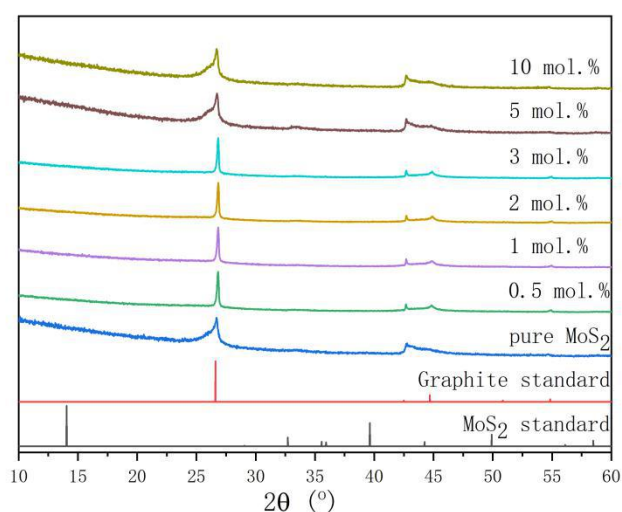
Figure 7.4: XRD patterns showing the undoped and P doped MoS₂ (0.5, 1, 2, 3, 5 and 10 mol.%) films prepared at 475 °C through AACVD on carbon paper substrates.
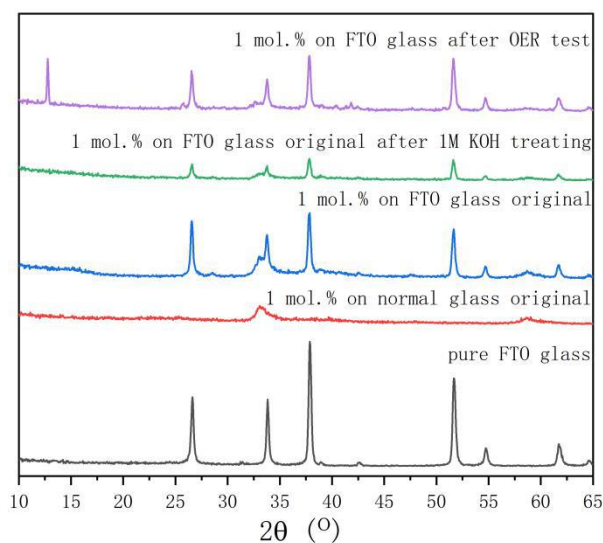
Figure 7.5: XRD patterns showing the pure FTO substrate, the MoS₂:P (1 mol.%) films on FTO and glass. Diffraction patters are also show for the films after 1M KOH treatment and OER tests.

Raman Spectroscopy

Raman spectra of the pure MoS$_2$ and P-doped MoS$_2$ (0.5, 1, 2, 3, 5 and 10 mol.%) thin films as-deposited and after the OER tests are shown in Figure 7.6, which confirms the formation of MoS$_2$ materials. For all the as-deposited MoS$_2$ based thin films, two intense peaks at ~406 cm^{-1} and ~383 cm^{-1} and one broad peak at ~227 cm^{-1}

were observed, which correspond well with the known characteristic peaks for MoS_2 materials in the literature.[35,40] There is a small shift for the peaks at ~406 cm^{-1} of the undoped MoS_2 thin film after P doping. For example, the intense peaks for pure MoS_2 and MoS_2:P (1 mol.%) thin film were at ~406.3 cm^{-1} and ~406.0 cm^{-1}, respectively, which is shown in Figure 7.7. Two small peaks in the high Raman shift area (> 1000 cm^{-1}) correspond to carbon based materials, which result from the carbon paper used as substrates.

The most intense peaks of the MoS_2 and P-doped MoS_2 thin films (Figure 7.6), were observed at ~ 383 cm^{-1} and ~ 406 cm^{-1}, which correspond to the in-plane E^1_{2g} mode and the out-of-plane A_{1g} mode, respectively. The in-plane E^1_{2g} mode indicates vibration of opposite directions between one Mo atom and two S atoms, while the out-of-plane A_{1g} mode indicates vibration in opposite directions for only S atoms.[40–42] The positions of these peaks and distance between them can be used to determine the numbers of layers of MoS_2 thin films approximately.[40–42] Based on previous reports in literature,[41] the positions at 382.7 cm^{-1} (E^1_{2g}) and 405.8 cm^{-1} (A_{1g}) measured by the Raman spectrometer using a laser at 514.5 nm correspond to 3 layers of MoS_2 thin films, which are closest to our Raman results and suggest that the MoS_2:P films in this investigation could be evaluated as 3 layers of MoS_2.

It is worth noting that analysis of the Raman spectrum for the P-doped MoS_2 (1 mol.%) after the OER test, shows peaks only in the high shift area (> 1000 cm^{-1}) corresponding to carbon paper and no peaks for MoS_2, as shown by the green line in Figure 7.6. In order to reduce error here, the uncontacted alkaline solution area for the same piece of carbon paper after OER test also has been characterized and displayed similar peaks with that of the other original MoS_2:P thin films. This suggest that the composition and structure of the material is changed significantly after the OER test, which can also be seen from the XPS analysis and SEM images (*vide infra*). This indicates that a different material with high OER catalytic performance may be formed during the oxygen evolution progress in alkaline environment (1M KOH) and this new material cannot be detected from the Raman spectrum analysis.

The MoS_2:P (1 mol.%) thin film grown on FTO glass substrate has a similar Raman

spectrum, as shown in Figure 7.8. It can be found that the significant characteristic peaks of MoS_2 in low shift area only were seen for the original material and the material after OER test only had high shift area peaks for the carbon based materials from the substrates.

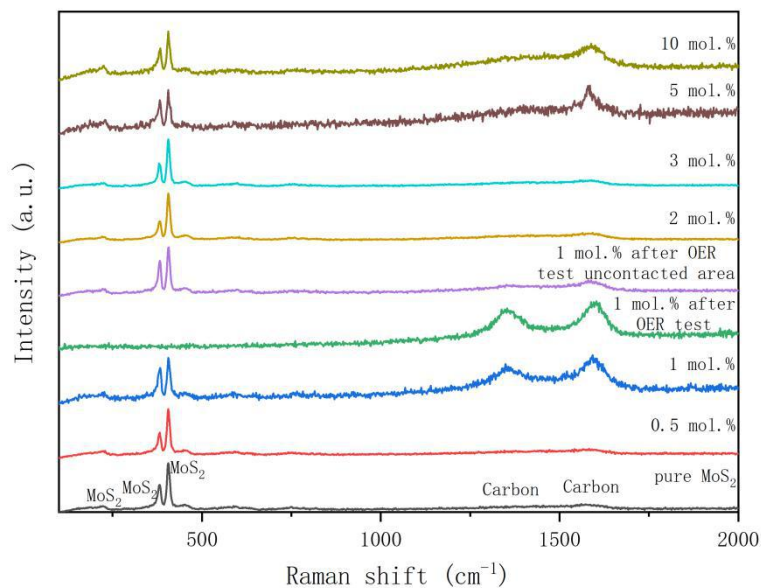**Figure 7.6: Raman spectra of undoped and P-doped MoS₂ (0, 0.5, 1, 2, 3, 5 and 10 mol.%) thin films on carbon paper substrates prior/post OER tests.**
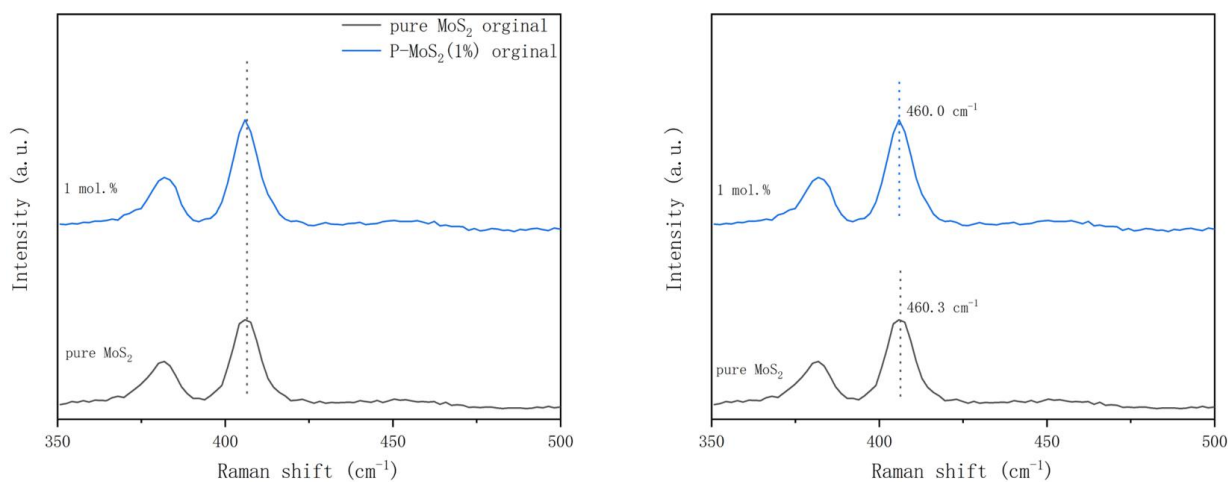
Figure 7.7: Comparisons of the Raman spectra of the undoped MoS₂ and P-doped MoS₂ (1 mol.%) thin films grown at 475 ᵒC through AACVD on carbon paper substrates.
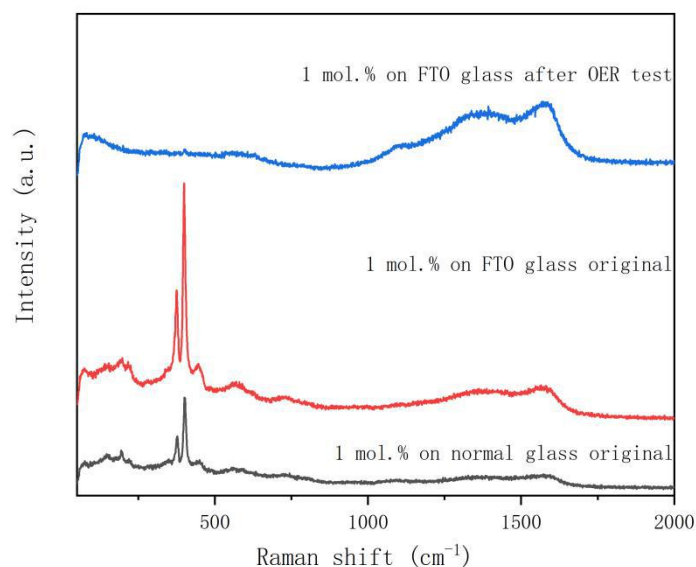
Figure 7.8: Raman spectra of the P doped MoS$_2$ (1 mol.%) thin films on glass/FTO glass substrates prior to and post OER tests for films deposited at 475 ºC via AACVD.

SEM

Figures 7.9 and 7.10 display the surface morphology of the MoS$_2$:P thin films. For the thin films grown via AACVD, several factors including precursors, dopants source, carrier gas, substrate and deposition temperature can influence the final surface morphology. However, for these films the as-deposited undoped and P-doped MoS$_2$ thin films did not show significant differences, as exhibited in Figures 7.9 and 7.10, with all showing plate-like structures randomly orientated. The size of the structures did show a small increase as the concentrations of the P dopants increased. As the ionic radius of Mo^{4+}, S^{2-} and P^{5+} was 0.65 Å, 1.84 Å and 0.29 Å, respectively, it can be assumed that the doping form of P atoms is insertion in the MoS$_2$ surface layer or MoS$_2$ layers between layers, which is different from the substitutional form of doping. The surface morphology shown in Figure 7.11, indicates that there was a significant difference between the as-deposited MoS$_2$:P (1 mol.%) thin film and the film after the OER test. The plate-like grains covering the carbon substrates can be seen in the SEM image of the as-deposited MoS$_2$:P (1 mol.%) thin film, similar to all the other MoS$_2$ thin films in this study. However, for the MoS$_2$:P (1 mol.%) thin film after the OER

measurement, the plate-like grains, typical of MoS_2 morphology, was no longer visible. This illustrates that the morphology of the MoS_2 has changed or a new material has formed, consistent with the XRD results. In addition, it was observed that the particle size increased as the time of the OER test increases, as seen in the SEM image of the MoS_2:P (1 mol.%) thin film after the long term stability test.

The surface morphology for the MoS_2 thin film on FTO glass substrate has significant difference with that on carbon paper substrate based on the substrate influence. It can only be determined that the surface morphology also has been changed after OER test from Figure 7.12.
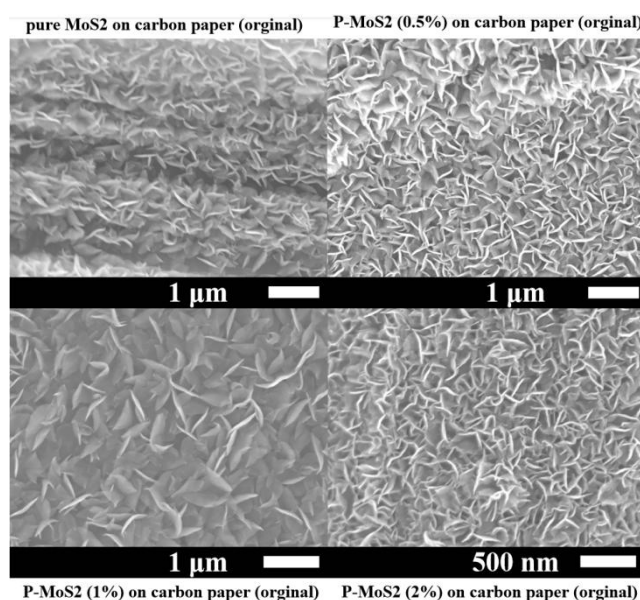
Figure 7.9: SEM images for the morphology of undoped and P-doped MoS_2 (0.5, 1 and 2 mol.%) films prepared at 475 ºC through AACVD on carbon paper substrates.
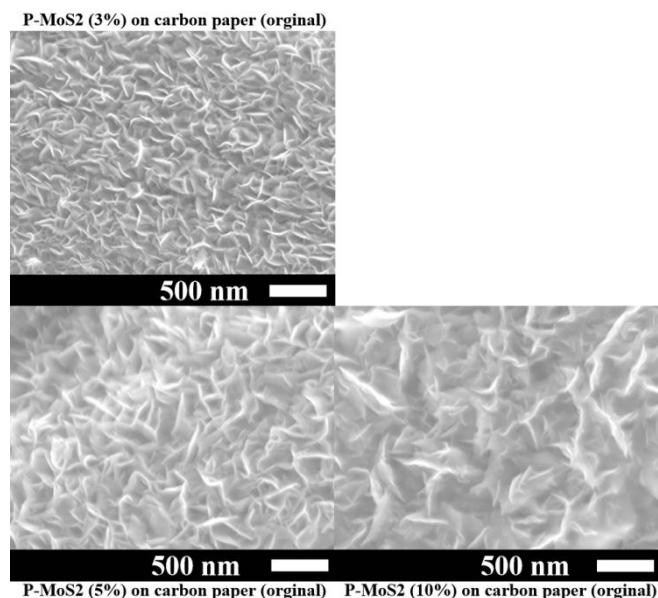
Figure 7.10: SEM images for the morphology of undoped and P-doped MoS₂ (3, 5 and 10 mol.%) films prepared at 475 ºC through AACVD on carbon paper substrates.

Figure 7.11: SEM images for the morphology of the original, after OER test and after one day constant current OER test of the MoS₂:P (1 mol.%) films prepared at 475 ºC through AACVD on carbon paper substrates.
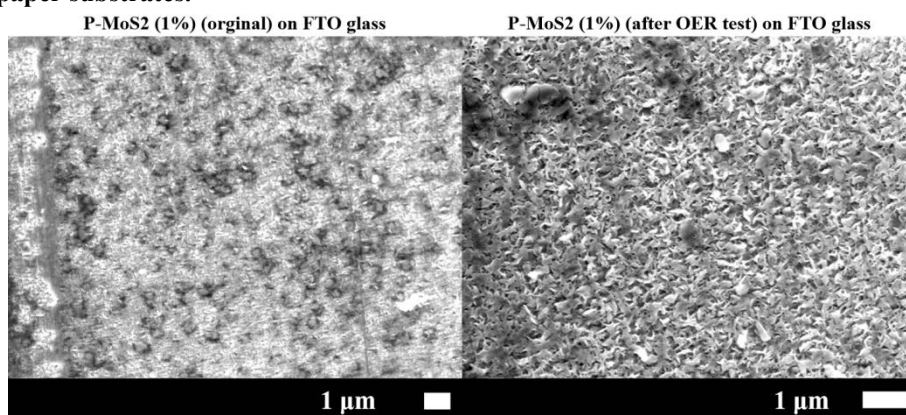
Figure 7.12: SEM images for the morphology of the original and after OER test for the MoS₂:P (1 mol.%) films prepared at 475 ºC through AACVD on FTO glass substrates.

XPS

The composition and oxidation states on the surface of the undoped and P-doped MoS_2 thin films before/after the OER tests on carbon paper substrates, were determined from X-ray photoelectron spectroscopy (XPS), as shown in Figures 7.13 and 7.14. For all of the as-deposited thin films, displayed in Figure 7.13 and in Table 7.1, the binding energy positions of Mo $3d_{5/2}$, S $2P_{3/2}$ and P $2P_{1/2}$ were at ~229.10 eV - 229.25 eV (corresponding to Mo^{4+}),[1,19,20,40,43] ~161.93 eV - 162.06 eV (corresponding to S^{2-})[1,19,20,40] and ~133.97 eV - 134.48 eV (corresponding to P^{5+}),[1,19,20,40,44] respectively, which correspond well with previously reported XPS results of some other P(V) doped MoS_2 thin films.[40] A small peak at ~226 eV - 227 eV corresponds to the binding energy of S 2s.[1,20,40] Some differences were observed in the XPS spectra for the MoS_2:P thin films after the OER tests, as shown in Figure 7.14. Firstly, the peaks corresponding to the P dopants were no longer observed. Then, peaks corresponding to Mo 3d and S 2p have become very complicated and it is hard to fit accurately. For example, the peaks corresponding to Mo 3d may suggest the mixture of Mo^{4+} and Mo^{6+} or even the mixture of Mo^{4+}, Mo^{5+} and Mo^{6+}, which cannot find their fitting areas individually. The changes would correspond to the changes observed in the other characterization techniques. As mentioned above, surface reconstruction of the catalyst will take place after the OER tests, according to the Raman and SEM measurements, which may correspond to the shifted peaks for Mo 3d and S 2p from the XPS analysis. In general, it is not possible to be determine accurately through current common characterization methods in our department including XRD, Raman spectroscopy, SEM and XPS analysis.

The MoS_2:P (1 mol.%) thin film on FTO glass substrate, shown in Figure 7.15, did not provide any further insight. This was due to the MoS_2:P thin film on FTO glass not showing any significant catalytic properties and OER could not be carried out, hence the peaks for Mo^{6+} were not observed, while S^{6+} could be seen and although the P dopants were not detected after OER test, as seen previously for carbon substrates.
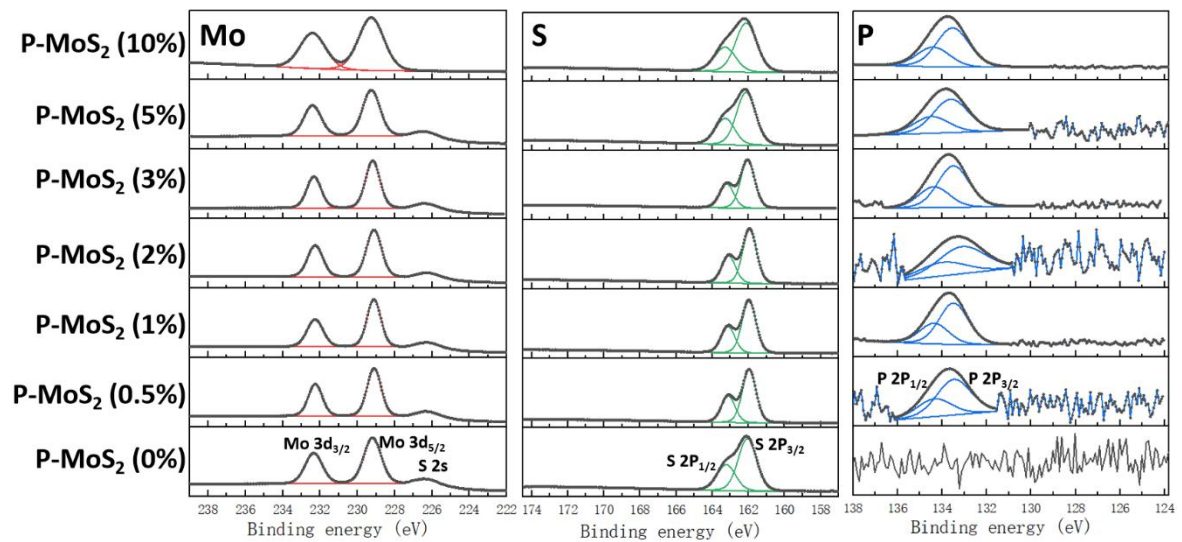
Figure 7.13: Core level XPS analysis showing the surface compositions and oxidation of the undoped and P doped MoS₂ (0.5, 1, 2, 3, 5 and 10 mol.%) films prepared at 475 ºC via AACVD on carbon paper substrates.
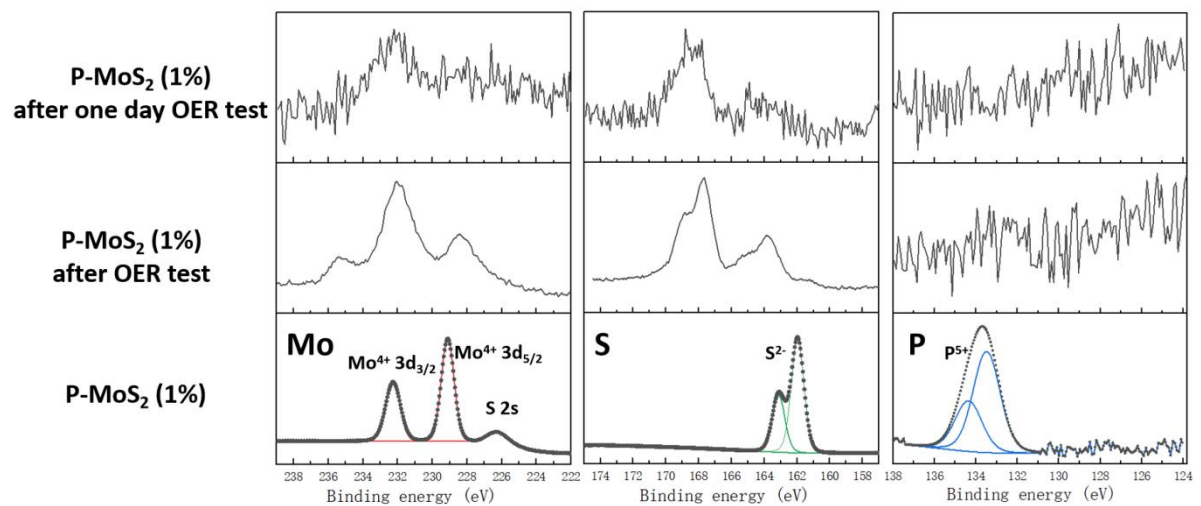
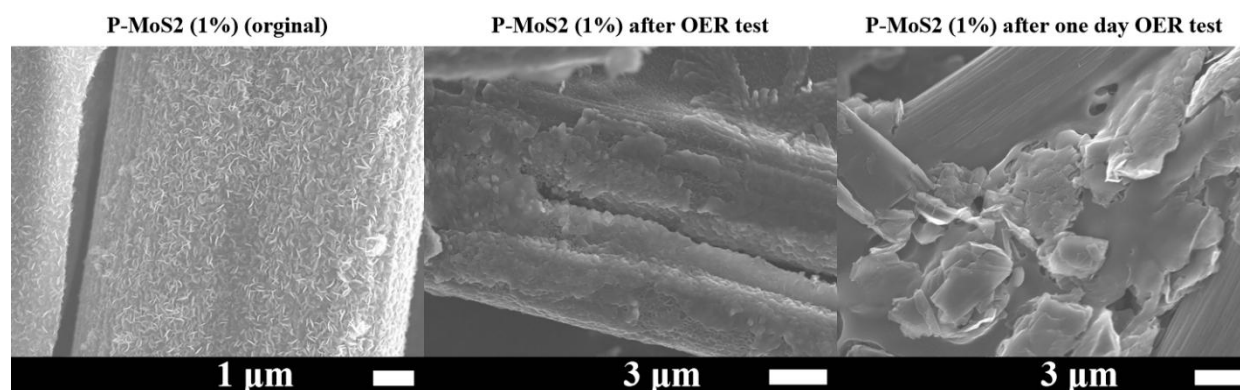**Figure 7.14: Core level XPS analysis showing the surface compositions and oxidation original, after OER test and after one day constant current OER test of the MoS2:P (1 mol.%) films prepared at 475 oC via AACVD on carbon paper substrates.**
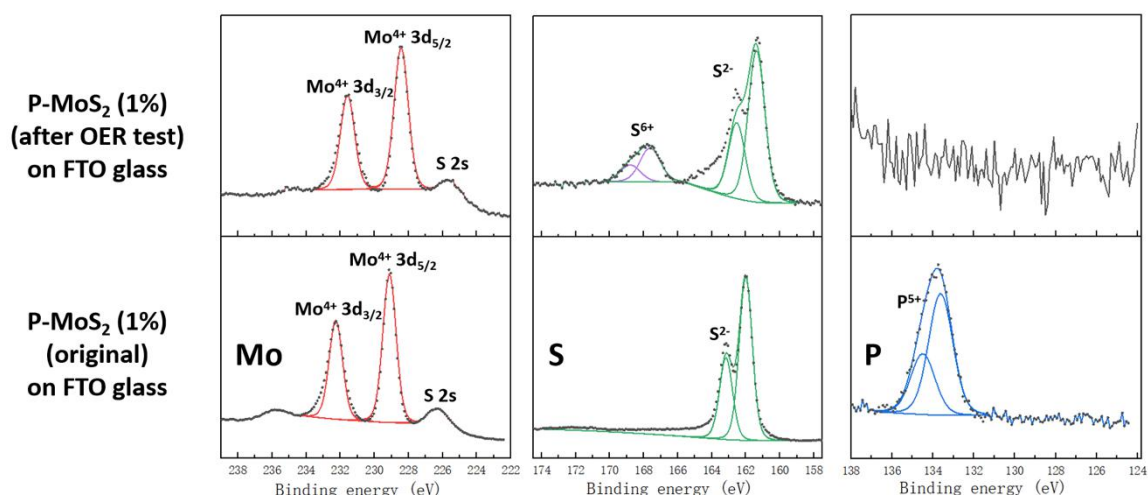
Figure 7.15: Core level XPS analysis showing the surface compositions and oxidation of the original and after OER test for the MoS$_2$:P (1 mol.%) films prepared at 475 ºC via AACVD on FTO glass substrates.

Table 7.1: The positions of Mo 3d, S 2p and P 2p from XPS analysis for the MoS$_2$:P thin films grown at 475 ºC through AACVD

Initial P concentrations (mol.%)	Positions of Mo 3d from XPS analysis (eV)		Positions of S 2p from XPS analysis (eV)		Positions of P 2p from XPS analysis (eV)	
	3d$_{3/2}$	3d$_{5/2}$	2P$_{1/2}$	2P$_{3/2}$	2P$_{1/2}$	2P$_{3/2}$
0	232.3	229.2	163.2	162.1	-	-
0.5	232.3	229.1	163.1	162.0	134.3	133.5
1	232.3	229.1	163.1	162.0	134.4	133.5
2	232.3	229.1	163.1	161.9	134.0	133.1
3	232.3	229.2	163.2	162.0	134.4	133.5
5	232.4	229.3	163.3	162.1	134.5	133.6
10	232.4	229.3	163.3	162.1	134.4	133.5

Table 7.2: The concentrations of Mo, S and P on surface from XPS analysis for the MoS$_2$:P thin films grown at 475 ºC through AACVD

Initial P concentrations (mol.%)	Concentrations of Mo from XPS analysis (%)		Concentrations of S from XPS analysis (%)	Concentrations of P from XPS analysis (%)	
	Mo^{6+}	Mo^{4+}	P^{5+}	S^{6+}	S^{2-}
0	-	100	-	-	260
0.5	-	100	1.80	-	251
1	-	100	10.2	-	248
2	-	100	1.60	-	225
3	-	100	7.58	-	250
5	-	100	5.66	-	264
10	-	100	79.2	-	257
15	-	100	9.27	-	270

OER Electrocatalytic Performance

The catalytic performance for oxygen evolution in 1M KOH of all the MoS_2:P thin films was determined in this investigation, as detailed in Table 7.3 and visually in Figures 7.16 - 7.21. The carbon paper with the MoS_2:P thin film was cut into a 1 cm × 1 cm piece and used as the working electrode. Due to the materials used being of low mass on the substrates, the results of the electrocatalytic properties with both units of mA cm^{-2} and mA mg^{-1} are discussed and compared. In Figure 7.16 and Figure 7.19, the polarization curves of the undoped and P-doped MoS_2 (0.5, 1, 2, 3, 5 and 10 mol.%) thin films can be observed. The undoped MoS_2 and the P-doped MoS_2 films with higher concentrations of P dopants showed little catalytic properties in the OER test, whereas the low concentration MoS_2:P thin films represent excellent catalytic performance with low overpotentials. The MoS_2:P (1 mol.%) thin film showed the best electrocatalytic performance with the lowest overpotentials at 319 mV for current density at 10 mA cm^{-2} and 173 mV for current density at 10 mA mg^{-1}, respectively. The overpotential in this project can meet the current standard comparing with the mentioned excellent noble metal oxides catalysts IrO_2 at ~ 325 mV.[30] Moreover, the overpotential here has been compared some other MoS_2 based materials and P dopants materials shown in Tables 7.4 and 7.5. Although the OER catalytic activities of these MoS_2 based materials are resulting from other phases but not from MoS_2

materials, the results in this project can display significant OER catalytic properties at similar level. In addition, the MoS_2:P (1 mol.%) thin film here has relative high mass activity of 1000 A g^{-1} at small overpotential of 450 mV. For example, the former investigation reported that the γ-CoOOH nanosheets had high mass activity of 66.6 A g^{-1} at OER overpotential of 300 mV in 1M KOH,[45] which was lower than our mass activity at ~ 75 A g^{-1} with 300 mV overpotential in 1M KOH. In addition, the synthetic technology in this investigation was AACVD, which is advantageous with relatively convenient progress and low cost.

The repeating linear sweep voltammetry (LSV) and long time chronovoltammetry test were used to further investigate the best catalytic MoS_2:P (1 mol.%) thin film. The electrocatalytic performance of the MoS_2:P (1 mol.%) thin film increases at first when the LSV cycles start to repeat, and after ~70 cycles, the overpotentials remained stable at one relative lower level compared with the original samples. For example, the overpotential of the MoS_2:P (1 mol.%) thin film at cycle 100 reached 313 mV for current density at 10 mA cm^{-2} and 143 mV for current density at 10 mA mg^{-1}, separately, which is lower that of the original thin films. In addition, if the sample was taken out of the 1M KOH solution and placed in the vacuum chamber without air for one day, the catalytic properties were significant in the next day OER test, shown in Figures 7.17 and 7.20. However, if the sample was washed with DI water after 100 LSV cycles of OER tests (the sample were also placed in the vacuum chamber without air for one day), the catalytic properties returned to a similar level as the original samples.

To find out the reason for this change, these samples were analyzed via XRD and it can be seen that there were several additional peaks for the thin films after 100 LSV cycles without DI water washing, as displayed in Figure 7.22. The new peaks all corresponded to the compound K_2CO_3, which may cover the surface of the material and reduce the catalytic performance to some extent. Moreover, as the P dopants were not observed after one OER test from XPS analysis, and the similar overpotentials between the original samples and the samples after 100 LSV cycles, DI water washing and placing for one day, it is therefore likely that the P dopant aids the higher OER

catalytic performance during the OER progress and may not be involved in the oxygen evolution progress. This formation process continues when the LSV cycles repeat resulting in an increase of the electrocatalytic performance, until it reaches the new material transformation limit.

Table 7.3: The electrocatalytic performance of undoped and P doped MoS$_2$ films on carbon paper substrates through AACVD used as different electrodes for oxygen evolution in 1M KOH

Initial P concentrations (mol.%)	Carrier (mg/cm^2)	Overpotential for 10 mA/cm^2 (mV)	Overpotential for 10 mA/mg (mV)	Overpotential for 100 mA/mg (mV)	Overpotential for 1 A/mg (mV)
0	0.096	1021	530	-	-
0.5	0.25	342	270	415	-
1 (original)	0.076	319	173	310	450
1 (cycle 100)	0.076	313	143	303	418
2	0.18	354	292	392	-
3	0.066	373	245	351	-
5	0.3	1015	701	-	-
10	0.2	961	689	-	-

The chronovoltammetry test has been carried on for one whole day to consider the long time stability test of the P-doped MoS$_2$ (1 mol.%) thin film. From Figures 7.18 and 7.21, it can be seen that the overpotential has only a small increase from 353 to 360 mV after the long time test, which illustrates the good stability of the MoS$_2$:P thin films. This small increase may be due to the slightly decreased actual contact area between the working electrode and alkaline medium during the long time OER test, which results from the electrolyte consumption. Due to the overpotential of MoS$_2$:P (1 mol.%) thin film in the chronovoltammetry being a little higher than that in the LSV cycles, the formation of new catalytic material may be easier to carry on during the scanning process from low potential to high potential rather than during the constant current progress.

Figure 7.16: The polarization curves used mA cm^{-2} as unit of the undoped and P doped MoS$_2$ (0.5, 1, 2, 3, 5 and 10 mol.%) thin films and on carbon paper substrates via AACVD for oxygen evolution in 1M KOH.

Figure 7.17: The polarization curves used mA cm^{-2} as unit of the MoS$_2$:P (1 mol.%) thin film, that was original, the 100 LSV cycle, after 100 LSV cycles with placing for one day and after 100 LSV cycles and placing for one day with DI water washing on carbon paper substrates via AACVD for oxygen evolution in 1M KOH.
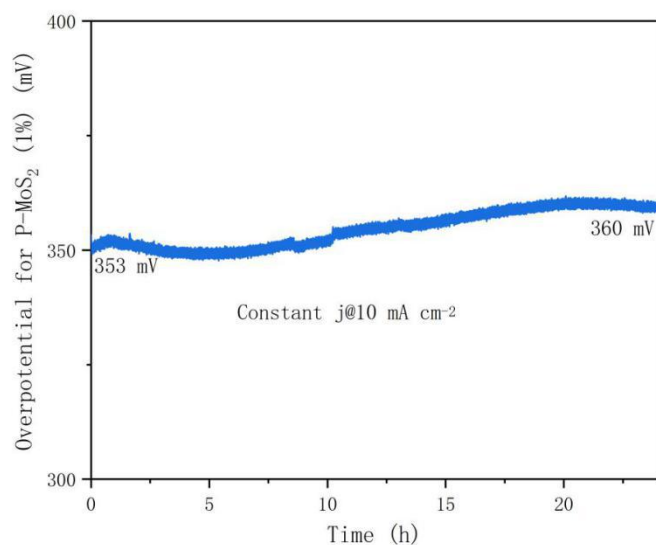
Figure 7.18: The polarization curves used mA cm^{-2} as unit of the long term stability test at one constant current density of 10 mA cm^{-2} for the MoS$_2$:P (1 mol.%) thin film on carbon paper substrates through AACVD for oxygen evolution in 1M KOH.
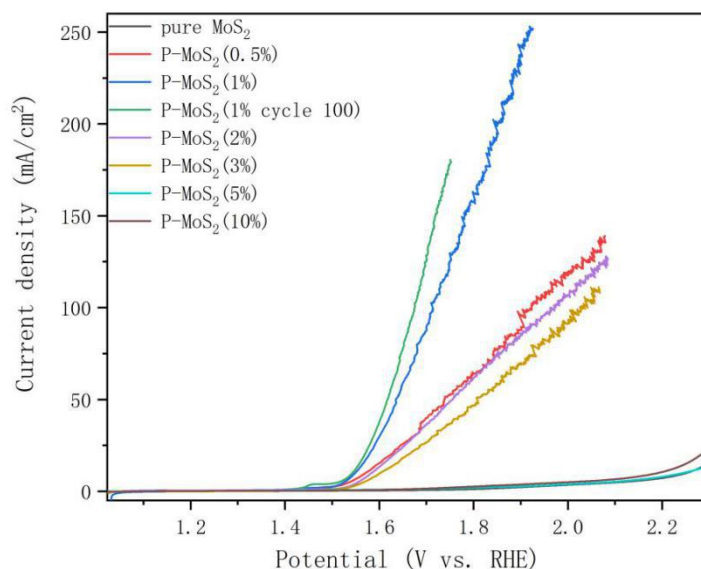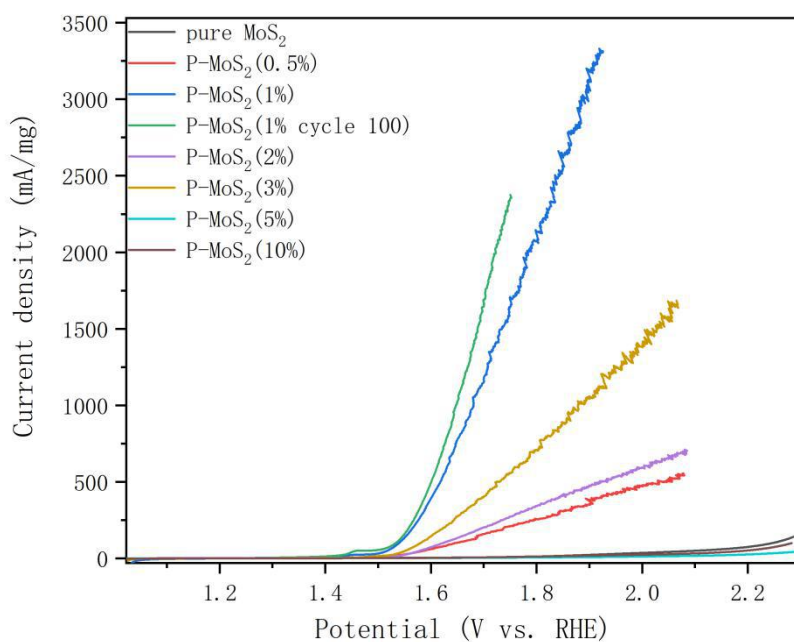

Figure 7.19: The polarization curves used mA mg^{-1} as unit of the undoped and P doped MoS$_2$ (0.5, 1, 2, 3, 5 and 10 mol.%) thin films and on carbon paper substrates via AACVD for oxygen evolution in 1M KOH.
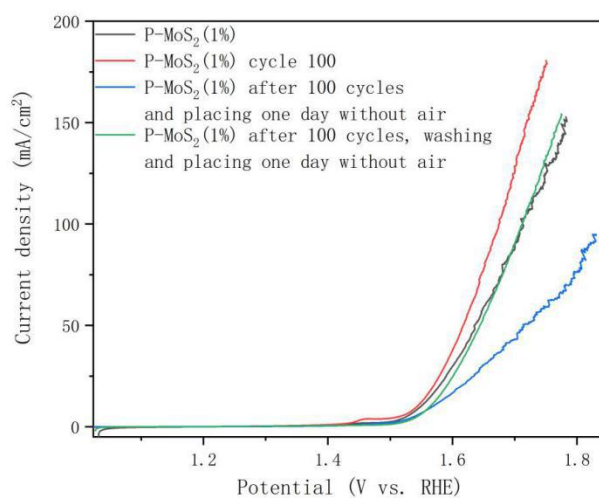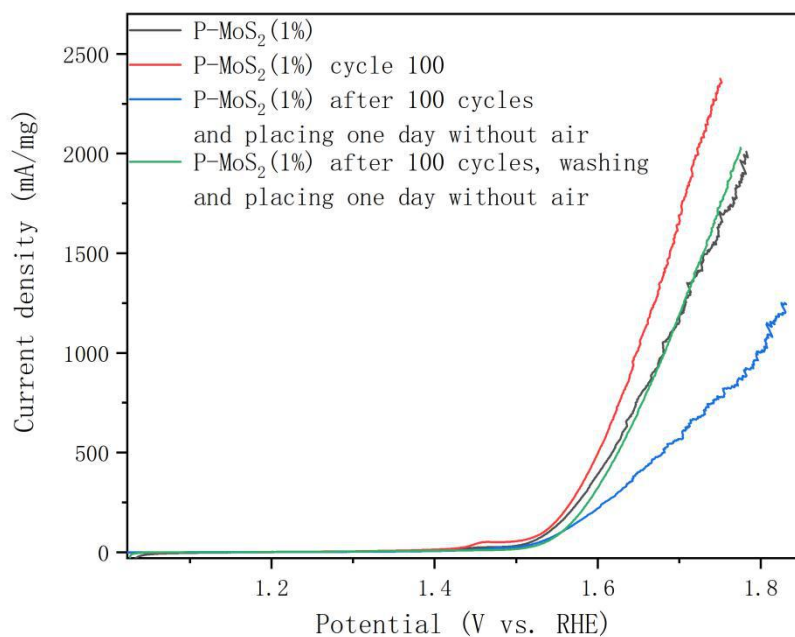
Figure 7.20: The polarization curves used mA mg^{-1} as unit of the MoS$_2$:P (1 mol.%) thin film, that was original, the 100 LSV cycle, after 100 LSV cycles with placing for one day and after 100 LSV cycles and placing for one day with DI water washing on carbon paper substrates via AACVD for oxygen evolution in 1M KOH.
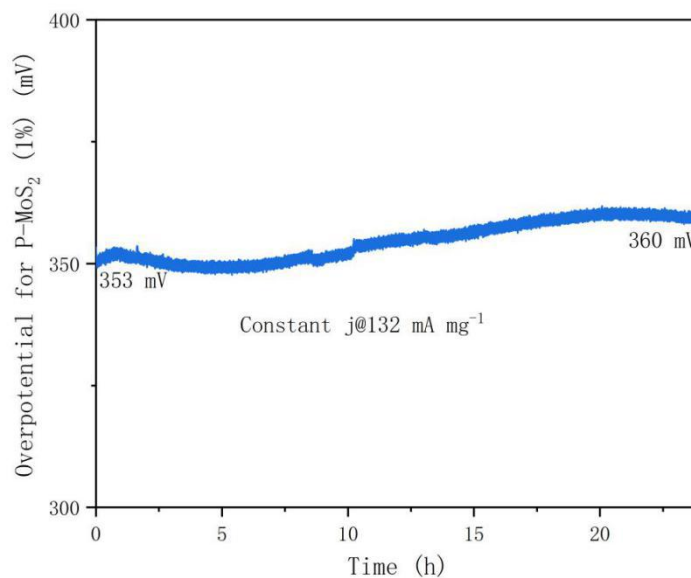
Figure 7.21: The polarization curves used mA mg^{-1} as unit of the long term stability test at one constant current density of 132 mA mg^{-1} for the MoS$_2$:P (1 mol.%) thin film on carbon paper substrates through AACVD for oxygen evolution in 1M KOH.
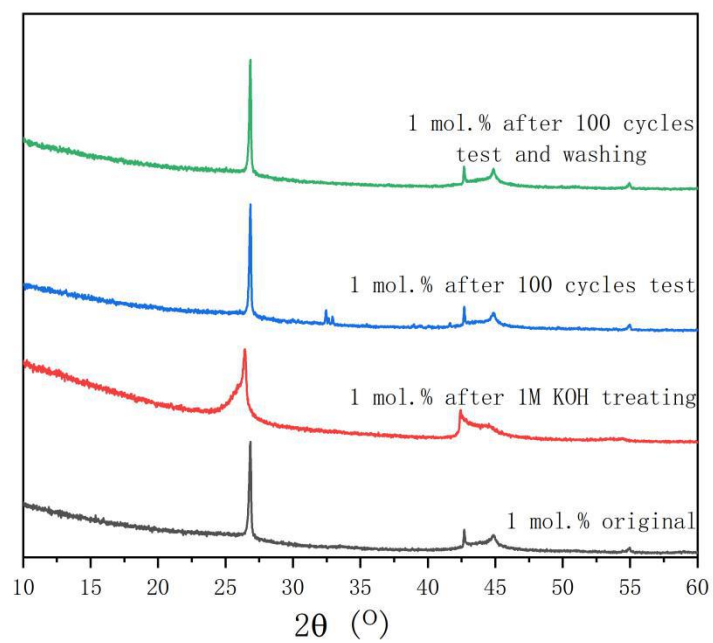
Figure 7.22: XRD patterns showing the original, after 1M KOH treating, after 100 LSV cycles and after 100 LSV cycles with DI water washing of the MoS$_2$:P (1 mol.%) films prepared at 475 ^{o}C through AACVD on carbon paper substrates.

Table 7.4: The overpotentials at 10 mA/cm² of MoS₂ based materials for OER in 1M KOH

| Materials	Overpotential at 10 mA/cm² (mV)	Ref
P-MoS₂	319	This work
P-MoS₂	316	[46]
MoS₂-Co₉S₈-NC	230	[18]
Co-MoS₂	260	[13]
Co₃O₄/MoS₂	230	[28]
Co-MoS₂	347	[2]
MoS₂/Ni₃S₂	218	[25]
CoS-Co(OH)₂@aMoS₂₊ₓ/NF	380	[30]
MoS₂-Ni₃S₂ HNRs/NF	249	[31]
Ni-Co-MoS₂	235	[32]
Co₃O₄@MoS₂	269	[33]

Table 7.5: The overpotentials at 10 mA/cm² of materials with P dopants for OER in 1M KOH

Materials	Overpotential at 10 mA/cm² (mV)	Ref
P-MoS₂	319	This work
P-MoS₂	316	[46]
SrCo₀.₉₅P₀.₀₅O₃₋δ	480	[23]
P,N-graphene	527	[21]
P-CuCo₂O₄	290	[22]

7.4 Conclusion

The MoS_2 thin films with different concentrations of P doping were grown on carbon paper substrates via AACVD and relatively high catalytic performance for OER test in 1M KOH was observed. The XRD patterns only show the phase of graphite and illustrate that all the MoS_2 thin films were largely amorphous. The presence of MoS_2 was determined via Raman spectroscopy and XPS analysis. Based on Raman spectroscopy, significant characteristic peaks of MoS_2 were found and the positions of the peaks indicated that the MoS_2 thin films were likely to correspond to 3 layer materials according to former literature.[41] The oxidation states of Mo, S and P were +4, -2 and +5 for all the P-doped MoS_2 thin films from XPS analysis. The SEM images showed that the undoped MoS_2 thin films had similar plate-like grains as surface morphology. In the OER electrocatalytic measurements, the MoS_2:P (1 mol.%) thin film showed the best catalytic properties with overpotentials at 319 mV for current density at 10 mA cm^{-2} and 173 mV for current density at 10 mA mg^{-1}, respectively. Moreover, the P-doped MoS_2 thin film had a relative high mass activity of 1000 A g^{-1} at small overpotential of 450 mV. In the further study, the catalytic performance increases when repeating LSV cycle, for example, the cycle 100 has lower overpotentials at 313 mV for current density at 10 mA cm^{-2}, 143 mV for current density at 10 mA mg^{-1} and high current density to over 1 A mg^{-1} before the end of LSV measurement. For the long time stability test, the overpotentials of the MoS_2:P (1 mol.%) thin film also did not change much after one day chronovoltammetry OER test. Moreover, the thin film synthetic route in this project is AACVD which is a convenient preparation technology with relative low cost, which suggests the Pdoped MoS_2 thin films can be considered as one prospective electrocatalyst of oxygen evolution in the renewable energy source area.

7.5 References

(1) Ou, G.; Fan, P.; Ke, X.; Xu, Y.; Huang, K.; Wei, H.; Yu, W.; Zhang, H.; Zhong, M.; Wu, H.; Li, Y. Defective Molybdenum Sulfide Quantum Dots as Highly Active Hydrogen Evolution Electrocatalysts. *Nano Res.* **2018**, *11* (2), 751–761. https://doi.org/10.1007/s12274-017-1684-2.

(2) Ma, J.; Cai, A.; Guan, X.; Li, K.; Peng, W.; Fan, X.; Zhang, G.; Zhang, F.; Li, Y. Preparation of Ultrathin Molybdenum Disulfide Dispersed on Graphene via Cobalt Doping: A Bifunctional Catalyst for Hydrogen and Oxygen Evolution Reaction. *Int. J. Hydrogen Energy* **2020**, *45* (16), 9583–9591. https://doi.org/10.1016/j.ijhydene.2020.01.176.

(3) Shi, Y.; Zhou, Y.; Yang, D. R.; Xu, W. X.; Wang, C.; Wang, F. Bin; Xu, J. J.; Xia, X. H.; Chen, H. Y. Energy Level Engineering of MoS_2 by Transition-Metal Doping for Accelerating Hydrogen Evolution Reaction. *J. Am. Chem. Soc.* **2017**, *139* (43), 15479–15485. https://doi.org/10.1021/jacs.7b08881.

(4) Qiao, S.; Zhao, J.; Zhang, B.; Liu, C.; Li, Z.; Hu, S.; Li, Q. Micrometer–Scale Biomass Carbon Tube Matrix Auxiliary MoS_2 Heterojunction for Electrocatalytic Hydrogen Evolution. *Int. J. Hydrogen Energy* **2019**, *44* (60), 32019–32029. https://doi.org/10.1016/j.ijhydene.2019.10.117.

(5) Peters, T. Tonmineralogische Untersuchungen an Einem Keuper-Lias-Profil Im Schweizer Jura (Frick). *Schweizerische Mineral. und Petrogr. Mitteilungen* **1964**, *44*, 1–30.

(6) Lin, R.; Kang, L.; Zhao, T.; Feng, J.; Celorrio, V.; Zhang, G.; Cibin, G.; Kucernak, A.; Brett, D. J. L.; Corà, F.; Parkin, I. P.; He, G. Identification and Manipulation of Dynamic Active Site Deficiency-Induced Competing Reactions in Electrocatalytic Oxidation Processes. *Energy Environ. Sci.* **2022**, *15*. https://doi.org/10.1039/d1ee03522c.

(7) Hinnemann, B.; Moses, P. G.; Bonde, J.; Jørgensen, K. P.; Nielsen, J. H.; Horch, S.; Chorkendorff, I.; Nørskov, J. K. Biomimetic Hydrogen Evolution: MoS_2 Nanoparticles as Catalyst for Hydrogen Evolution. *J. Am. Chem. Soc.*

2005, *127* (15), 5308–5309. https://doi.org/10.1021/ja0504690.

(8)   Jaramillo, T. F.; Jørgensen, K. P.; Bonde, J.; Nielsen, J. H.; Horch, S.; Chorkendorff, I. Identification of Active Edge Sites for Electrochemical H_2 Evolution from MoS_2 Nanocatalysts. *Science (80-.)*. **2007**, *317* (5834), 100–102. https://doi.org/10.1126/science.1141483.

(9)   Hansen, L. P.; Ramasse, Q. M.; Kisielowski, C.; Brorson, M.; Johnson, E.; Topsøe, H.; Helveg, S. Atomic-Scale Edge Structures on Industrial-Style MoS_2 Nanocatalysts. *Angew. Chem. - Int. Ed.* **2011**, *50* (43), 10153–10156. https://doi.org/10.1002/anie.201103745.

(10)   Zhang, H.; Zhou, W.; Dong, J.; Lu, X. F.; Lou, X. W. (David). Intramolecular Electronic Coupling in Porous Iron Cobalt (Oxy)Phosphide Nanoboxes Enhances the Electrocatalytic Activity for Oxygen Evolution. *Energy Environ. Sci.* **2019**, *12* (11), 3348–3355. https://doi.org/10.1039/c9ee02787d.

(11)   Ma, Q.; Qiao, H.; Huang, Z.; Liu, F.; Duan, C.; Zhou, Y.; Liao, G.; Qi, X. Photo-Assisted Electrocatalysis of Black Phosphorus Quantum Dots/Molybdenum Disulfide Heterostructure for Oxygen Evolution Reaction. *Appl. Surf. Sci.* **2021**, *562* (May), 1–7. https://doi.org/10.1016/j.apsusc.2021.150213.

(12)   Zhai, Z.; Li, C.; Wu, H. C.; Zhang, L.; Tang, N.; Wang, W.; Gong, J. Dimensional Construction and Morphological Tuning of Heterogeneous MoS_2/NiS Electrocatalysts for Efficient Overall Water Splitting. *J. Mater. Chem. A* **2018**, *6* (21), 9833–9838. https://doi.org/10.1039/c8ta03304h.

(13)   Xiong, Q.; Wang, Y.; Liu, P. F.; Zheng, L. R.; Wang, G.; Yang, H. G.; Wong, P. K.; Zhang, H.; Zhao, H. Cobalt Covalent Doping in MoS_2 to Induce Bifunctionality of Overall Water Splitting. *Adv. Mater.* **2018**, *30* (29). https://doi.org/10.1002/adma.201801450.

(14)   Dong, Y.; Jiang, H.; Deng, Z.; Hu, Y.; Li, C. Synthesis and Assembly of Three-Dimensional MoS_2/RGO Nanovesicles for High-Performance Lithium Storage. *Chem. Eng. J.* **2018**, *350* (May), 1066–1072. https://doi.org/10.1016/j.cej.2018.06.044.

(15)   Wang, B.; Xia, Y.; Wang, G.; Zhou, Y.; Wang, H. Core Shell MoS₂/C
        Nanospheres Embedded in Foam-like Carbon Sheets Composite with an
        Interconnected Macroporous Structure as Stable and High-Capacity Anodes for
        Sodium Ion Batteries. *Chem. Eng. J.* **2017**, *309*, 417–425.
        https://doi.org/10.1016/j.cej.2016.10.073.

(16)   Pan, Z.; Pan, N.; Chen, L.; He, J.; Zhang, M. Flower-like MOF-Derived Co–N-
        Doped Carbon Composite with Remarkable Activity and Durability for
        Electrochemical Hydrogen Evolution Reaction. *Int. J. Hydrogen Energy* **2019**,
        44 (57), 30075–30083. https://doi.org/10.1016/j.ijhydene.2019.09.117.

(17)   Guo, Y.; Gan, L.; Shang, C.; Wang, E.; Wang, J. A Cake-Style
        CoS₂@MoS₂/RGO Hybrid Catalyst for Efficient Hydrogen Evolution. *Adv.
        Funct. Mater.* **2017**, *27* (5). https://doi.org/10.1002/adfm.201602699.

(18)   Huang, N.; Yan, S.; Zhang, M.; Ding, Y.; Yang, L.; Sun, P.; Sun, X. A MoS₂-
        Co₉S₈-NC Heterostructure as an Efficient Bifunctional Electrocatalyst towards
        Hydrogen and Oxygen Evolution Reaction. *Electrochim. Acta* **2019**, *327*.
        https://doi.org/10.1016/j.electacta.2019.134942.

(19)   Huang, H.; Feng, X.; Du, C.; Song, W. High-Quality Phosphorus-Doped MoS₂
        Ultrathin Nanosheets with Amenable ORR Catalytic Activity. *Chem. Commun.*
        2015, *51* (37), 7903–7906. https://doi.org/10.1039/c5cc01841b.

(20)   Ray, C.; Lee, S. C.; Sankar, K. V.; Jin, B.; Lee, J.; Park, J. H.; Jun, S. C.
        Amorphous Phosphorus-Incorporated Cobalt Molybdenum Sulfide on Carbon
        Cloth: An Efficient and Stable Electrocatalyst for Enhanced Overall Water
        Splitting over Entire PH Values. *ACS Appl. Mater. Interfaces* **2017**, *9* (43),
        37739–37749. https://doi.org/10.1021/acsami.7b11192.

(21)   Chai, G. L.; Qiu, K.; Qiao, M.; Titirici, M. M.; Shang, C.; Guo, Z. Active Sites
        Engineering Leads to Exceptional ORR and OER Bifunctionality in P,N Co-
        Doped Graphene Frameworks. *Energy Environ. Sci.* **2017**, *10* (5), 1186–1195.
        https://doi.org/10.1039/c6ee03446b.

(22)   Guo, Z.; Pang, Y.; Xie, H.; He, G.; Parkin, I. P.; Chai, G. L. Phosphorus-Doped
        CuCo₂O₄ Oxide with Partial Amorphous Phase as a Robust Electrocatalyst for

the Oxygen Evolution Reaction. *ChemElectroChem* **2021**, *8* (1), 135–141. https://doi.org/10.1002/celc.202001312.

(23)   Zhu, Y.; Zhou, W.; Sunarso, J.; Zhong, Y.; Shao, Z. Phosphorus-Doped Perovskite Oxide as Highly Efficient Water Oxidation Electrocatalyst in Alkaline Solution. *Adv. Funct. Mater.* **2016**, *26* (32), 5862–5872. https://doi.org/10.1002/adfm.201601902.

(24)   Tan, Y.; Feng, J.; Kang, L.; Liu, L.; Zhao, F.; Zhao, S.; Brett, D. J. L.; Shearing, P. R.; He, G.; Parkin, I. P. Hybrid Ni_2P / CoP Nanosheets as Efficient and Robust Electrocatalysts for Domestic Wastewater Splitting . *Energy Environ. Mater.* **2022**, 0–2. https://doi.org/10.1002/eem2.12398.

(25)   Zhang, J.; Wang, T.; Pohl, D.; Rellinghaus, B.; Dong, R.; Liu, S.; Zhuang, X.; Feng, X. Interface Engineering of MoS_2/Ni_3S_2 Heterostructures for Highly Enhanced Electrochemical Overall-Water-Splitting Activity. *Angew. Chem. - Int. Ed.* **2016**, *55* (23), 6702–6707. https://doi.org/10.1002/anie.201602237.

(26)   Morales-Guio, C. G.; Hu, X. Amorphous Molybdenum Sulfides as Hydrogen Evolution Catalysts. *Acc. Chem. Res.* **2014**, *47* (8), 2671–2681. https://doi.org/10.1021/ar5002022.

(27)   Lu, Q.; Yu, Y.; Ma, Q.; Chen, B.; Zhang, H. 2D Transition-Metal-Dichalcogenide-Nanosheet-Based Composites for Photocatalytic and Electrocatalytic Hydrogen Evolution Reactions. *Adv. Mater.* **2016**, *28* (10), 1917–1933. https://doi.org/10.1002/adma.201503270.

(28)   Muthurasu, A.; Maruthapandian, V.; Yong, H. Applied Catalysis B : Environmental Metal-Organic Framework Derived Co_3O_4 / MoS_2 Heterostructure for Efficient Bifunctional Electrocatalysts for Oxygen Evolution Reaction and Hydrogen Evolution Reaction. **2019**, *248* (January), 202–210.

(29)   Wang, J.; Huang, J.; Zhao, S.; Parkin, I. P.; Tian, Z.; Lai, F.; Liu, T.; He, G. Mo/Fe Bimetallic Pyrophosphates Derived from Prussian Blue Analogues for Rapid Electrocatalytic Oxygen Evolution. *Green Energy Environ.* **2022**. https://doi.org/10.1016/j.gee.2022.02.014.

(30)   Yoon, T.; Kim, K. S. One-Step Synthesis of CoS-Doped β-Co(OH)$_2$@Amorphous MoS$_{2+x}$ Hybrid Catalyst Grown on Nickel Foam for High-Performance Electrochemical Overall Water Splitting. *Adv. Funct. Mater.* **2016**, *26* (41), 7386–7393. https://doi.org/10.1002/adfm.201602236.

(31)   Yang, Y.; Zhang, K.; Lin, H.; Li, X.; Chan, H. C.; Yang, L.; Gao, Q. MoS$_2$-Ni$_3$S$_2$ Heteronanorods as Efficient and Stable Bifunctional Electrocatalysts for Overall Water Splitting. *ACS Catal.* **2017**, *7* (4), 2357–2366. https://doi.org/10.1021/acscatal.6b03192.

(32)   Li, H.; Chen, S.; Jia, X.; Xu, B.; Lin, H.; Yang, H.; Song, L.; Wang, X. Amorphous Nickel-Cobalt Complexes Hybridized with 1T-Phase Molybdenum Disulfide via Hydrazine-Induced Phase Transformation for Water Splitting. *Nat. Commun.* **2017**, *8* (May), 1–11. https://doi.org/10.1038/ncomms15377.

(33)   Liu, J.; Wang, J.; Zhang, B.; Ruan, Y.; Wan, H.; Ji, X.; Xu, K.; Zha, D.; Miao, L.; Jiang, J. Mutually Beneficial Co$_3$O$_4$@MoS$_2$ Heterostructures as a Highly Efficient Bifunctional Catalyst for Electrochemical Overall Water Splitting. *J. Mater. Chem. A* **2018**, *6* (5), 2067–2072. https://doi.org/10.1039/c7ta10048e.

(34)   Islam, M. S.; Kim, M.; Jin, X.; Oh, S. M.; Lee, N. S.; Kim, H.; Hwang, S. J. Bifunctional 2D Superlattice Electrocatalysts of Layered Double Hydroxide-Transition Metal Dichalcogenide Active for Overall Water Splitting. *ACS Energy Lett.* **2018**, *3* (4), 952–960. https://doi.org/10.1021/acsenergylett.8b00134.

(35)   Lewis, D. J.; Tedstone, A. A.; Zhong, X. L.; Lewis, E. A.; Rooney, A.; Savjani, N.; Brent, J. R.; Haigh, S. J.; Burke, M. G.; Muryn, C. A.; Raftery, J. M.; Warrens, C.; West, K.; Gaemers, S.; O'Brien, P. Thin Films of Molybdenum Disulfide Doped with Chromium by Aerosol-Assisted Chemical Vapor Deposition (AACVD). *Chem. Mater.* **2015**, *27* (4), 1367–1374. https://doi.org/10.1021/cm504532w.

(36)   Decoster, M.; Conan, F.; Guerchais, J. E.; Le Mest, Y.; Sala Pala, J.; Jeffery, J. C.; Faulques, E.; Leblanc, A.; Molinie, P. Radical Cation-Radical Anion Salts: Molybdenum Complexes Containing the [TCNQ]•- or [TCNE]•- Radical

Anions. X-Ray Crystal Structure of [Mo(Et₂NCS₂)₄](TCNQ). *Polyhedron* **1995**, *14* (13–14), 1741–1750. https://doi.org/10.1016/0277-5387(94)00487-Y.

(37)   Dixon, S. C.; Sathasivam, S.; Williamson, B. A. D.; Scanlon, D. O.; Carmalt, C. J.; Parkin, I. P. Transparent Conducting N-Type ZnO:Sc-Synthesis, Optoelectronic Properties and Theoretical Insight. *J. Mater. Chem. C* **2017**, *5* (30), 7585–7597. https://doi.org/10.1039/c7tc02389h.

(38)   Dixon, S. C.; Manzi, J. A.; Powell, M. J.; Carmalt, C. J.; Parkin, I. P. Reflective Silver Thin Film Electrodes from Commercial Silver(i) Triflate via Aerosol-Assisted Chemical Vapor Deposition. *ACS Appl. Nano Mater.* **2018**, *1* (7), 3724–3732. https://doi.org/10.1021/acsanm.8b00949.

(39)   Adeogun, A.; Afzaal, M.; O'Brien, P. Studies of Molybdenum Disulfide Nanostructures Prepared by AACVD Using Single-Source Precursors. *Chem. Vap. Depos.* **2006**, *12* (10), 597–599. https://doi.org/10.1002/cvde.200504203.

(40)   Lee, J. S.; Park, C. S.; Kim, T. Y.; Kim, Y. S.; Kim, E. K. Characteristics of P-Type Conduction in P-Doped MoS₂ by Phosphorous Pentoxide during Chemical Vapor Deposition. *Nanomaterials* **2019**, *9* (9). https://doi.org/10.3390/nano9091278.

(41)   Li, H.; Zhang, Q.; Yap, C. C. R.; Tay, B. K.; Edwin, T. H. T.; Olivier, A.; Baillargeat, D. From Bulk to Monolayer MoS₂: Evolution of Raman Scattering. *Adv. Funct. Mater.* **2012**, *22* (7), 1385–1390. https://doi.org/10.1002/adfm.201102111.

(42)   Lee, C.; Yan, H.; Brus, L. E.; Heinz, T. F.; Hone, J.; Ryu, S. Anomalous Lattice Vibrations of Single- and Few-Layer MoS₂. *ACS Nano* **2010**, *4* (5), 2695–2700. https://doi.org/10.1021/nn1003937.

(43)   Zhao, D.; Sathasivam, S.; Li, J.; Carmalt, C. J. Transparent and Conductive Molybdenum-Doped ZnO Thin Films via Chemical Vapor Deposition. *ACS Appl. Electron. Mater.* **2020**, *2* (1), 120–125. https://doi.org/10.1021/acsaelm.9b00647.

(44)   Zhao, D.; Li, J.; Sathasivam, S.; Carmalt, C. J. N-Type Conducting P Doped ZnO Thin Films via Chemical Vapor Deposition. *RSC Adv.* **2020**, *10* (57),

34527–34533. https://doi.org/10.1039/d0ra05667g.

(45)   Huang, J.; Chen, J.; Yao, T.; He, J.; Jiang, S.; Sun, Z.; Liu, Q.; Cheng, W.; Hu,
F.; Jiang, Y.; Pan, Z.; Wei, S. CoOOH Nanosheets with High Mass Activity for
Water Oxidation. *Angew. Chem. - Int. Ed.* **2015**, *54* (30), 8722–8727.
https://doi.org/10.1002/anie.201502836.

(46)   Xue, H.; Meng, A.; Chen, C.; Xue, H.; Li, Z.; Wang, C. Phosphorus-Doped
MoS_2 with Sulfur Vacancy Defects for Enhanced Electrochemical Water
Splitting. *Sci. China Mater.* **2022**, *65* (3), 712–720.
https://doi.org/10.1007/s40843-021-1774-9.

Chapter 8 Conclusion

8.1 Conclusion and outlook

This thesis has focused on the study of 1) transparent conducting oxide thin films based on ZnO and 2) the MoS_2 thin films and their application as OER catalysts.

In Chapter 1, a general introduction and background of this PhD project have been established. Different types of functional thin films, including TCOs materials (n-type, p-type and p-n heterojunctions) and electrocatalytic materials for HER and OER, have been discussed in this chapter.

In Chapter 2, film synthesis routes and characterisation methods have been introduced and discussed in detail. CVD and AACVD were focused on as the main film grown technology while some other technologies such as PLD, ALD, sol–gel method, spin coating and sputtering coating were also mentioned. For characterisation methods, several technologies including XRD, XPS, SEM, EDS, Raman spectroscopy, Mass spectrometry, FT-IR, Hall effect measurement and UV-vis spectroscopy, which have been used in the next chapters, were introduced in this chapter briefly.

In Chapter 3, 4 and 5, ZnO based thin films used as n-type TCOs materials were investigated. Three different dopant regimes were studied, namely Mo, P and B. For the Mo:ZnO, Mo was detected in both the 4+ and 6+ oxidation state via XPS studies. The Mo^{6+} was attributed to surface oxide species with Mo^{4+} present in the Zn sites in the wurtzite unit cell. EDS analysis revealed that the Mo concentration ranged from 0 to 1.6 at.% in the bulk. It was found that the addition of Mo to ZnO resulted in a reduction in resistivity, with the lowest value of 2.6 x 10^{-3} Ω.cm obtained for the 0.6 at.% Mo sample. This resistivity was slightly lower than the best results found in the literature through RF magnetron sputtering and reactive magnetron sputtering that obtained values of 9.2 x 10^{-4} Ω.cm and 7.9 x 10^{-4} Ω.cm. Optically, the AACVD grown Mo:ZnO films had visible light transmittance of ~80%, again comparable to literature reports.

In Chapter 4, P-doped ZnO thin films via the AACVD route was studied. XPS revealed that P was in the 5+ oxidation state and therefore when doped substitutionally it was able to reduce the resistivity of ZnO to 6.0×10^{-3} Ω.cm for the ZnO:P (6.5 at.%) whilst maintaining good visible light transmittance at (~75%). The optoelectronic results obtained for the AACVD P:ZnO films were superior to literature reports for films produced by PVD methods such as pulsed laser deposition with resistivity values of 1×10^{-2} Ω.cm.

In Chapter 5, two different solvents, THF and MeOH, were used to deposit B-doped ZnO thin films through AACVD owing to the differing solubility of BEt_3 and $ZnEt_2$ precursors. Using THF as the solvent, the ZnO:B (7.5 mol.%) thin film had the lowest resistivity at 5.84×10^{-3} Ω.cm, whereas with MeOH as the solvent the ZnO:B (300 mol.%) thin film showed the lowest resistivity at 5.10×10^{-3} Ω.cm. All the thin films from these two different solvents showed transmittance at ~ 75 - 90% in the visible area. These optoelectronic results were comparable to literature examples of B:ZnO films grown via chemical spray (4.5×10^{-3} Ω.cm) and RF magnetron sputtering (5.65×10^{-3} Ω.cm) techniques.

For these three ZnO based systems studied, the optoelectronic properties were sufficiently improved upon doping. The resistivities achieved were similar across all films but the lowest value was obtained using Mo as the dopant.

In Chapter 6, BP thin films were grown on glass substrates through AACVD for potential use as p-type TCOs materials. However, due to the significant influence of external oxygen, although the presence of BP could be determined from XPS analysis, the final product contained boron and phosphorus oxides on the surface, displayed no electrical properties and could not be considered as useful p-type TCOs materials. Due to this result, further doping investigations have not been continued.

In Chapter 7, MoS$_2$ thin films with P doping were prepared on carbon paper substrates via AACVD and used as efficient electrocatalysts for OER process in the water splitting area. The MoS$_2$:P (1 mol.%) thin film can catalytically accelerate the OER process in alkaline medium (1M KOH), with lowest overpotential at only 319 mV with current density at 10 mA cm^{-2} and 173 mV with current density at 10 mA mg^{-1}, respectively, while the high mass activity of 1000 A g^{-1} at small overpotential of 450 mV. Moreover, the electrocatalytic material, P-doped MoS$_2$ (1 mol.%) thin film, had long term stability after the one day chronovoltammetry OER test.

In general, based on the AACVD technology, different functional thin films, including n-type and p-type TCOs materials and electrocatalyst material for OER, which can be considered as promoting alternative materials with high performance and low cost leading to possible contributions for these materials in the commercial market, were prepared, characterized and discussed in this thesis. Moreover, the doping method has been used and studied in most chapters and this method can improve properties of thin films via AACVD simply and significantly to a certain extent. In further work, AACVD can still be used to grow functional thin films used in many areas generally, such as p-n heterojunctions containing both n-type and p-type TCOs materials and some other transition metal-based materials for water splitting, e.g. NiS$_x$, CoS$_x$ and FeS$_x$ based thin films. In addition, the summary of key results and possible further investigations is listed in Table 8.1.

Table 8.1: Summary of key results and possible further investigations.

Chapter	Key results	Further investigations
3	- 2.6×10^{-3} Ω.cm as lowest resistivity - ~ 80% as visible transmittance - appropriately dopants (0.6 at.% Mo) improve thin films performance significantly	- try alternative precursors - try different kinds and concentrations of dopants - try some co-doped thin films
4	- 6.0×10^{-3} Ω.cm as lowest resistivity - ~ 75% as visible transmittance - appropriately dopants (6.5 at.% P) improve thin films performance significantly	- try to investigated some other conditions such as depositions temperatures and flow rates to further improve the electrical and optical properties of the ZnO based thin films here
5	- 5.10×10^{-3} Ω.cm as lowest resistivity - ~ 75 - 90% as visible transmittance - appropriately dopants (300 mol.% B) improve thin films performance significantly	- try to prepare p-n heterojunctions
6	- amorphous BP thin films determined - B and P oxides on the surface hard to remove	- try different alternative precursors such as $^tBuPH_2$ and BEt_3 - try different annealing methods - try appropriate dopants after preparing pure BP thin films - try to prepare p-n heterojunctions
7	- lowest overpotential at 319 mV for 10 mA cm^{-2} - lowest overpotential at 173 mV for 10 mA mg^{-1} - high mass activity of 1000 A g^{-1} at small overpotential of 450 mV - long term stability test of one day shows enough stability for catalytic materials - appropriately dopants (1.0 mol.% P) improve thin films performance significantly	- try alternative precursors and dopants for depositions - try to find out exact catalytic mechanism of P-MoS$_2$ thin films - try to investigate different transition metal based materials with different dopants for catalysis

8.2 Publication list

Publication related to the thesis:

(1) **Zhao, D.**; Sathasivam, S.; Li, J.; Carmalt, C. J. Transparent and Conductive Molybdenum-Doped ZnO Thin Films via Chemical Vapor Deposition. *ACS Appl. Electron. Mater.* **2020**, *2* (1), 120–125. https://doi.org/10.1021/acsaelm.9b00647.

(2) **Zhao, D.**; Li, J.; Sathasivam, S.; Carmalt, C. J. n-Type Conducting P Doped ZnO Thin Films via chemical Vapor Deposition. *RSC Adv.* **2020**, *10* (57), 34527–34533. https://doi.org/10.1039/d0ra05667g.

(3) **Donglei Zhao**, Sanjayan Sathasivam, Mingyue Wang and Claire J. Carmalt. Transparent and Conducting Boron Doped ZnO Thin Films Grown by Aerosol Assisted Chemical Vapor Deposition. *RSC Adv.* **2022**, *12* (51), 33049–33055. https://doi.org/10.1039/d2ra05895b.

Manuscript in preparation for submission related to the thesis:

(4) **Donglei Zhao**, Jianwei Li, Siyu Zhao, Sanjayan Sathasivam, Yeshu Tan, Guanjie He, Ivan P. Parkin and Claire J. Carmalt. Phosphorus doped Molybdenum Sulfide Thin Films Grown via Aerosol Assisted Chemical Vapor Deposition for Efficient Oxygen Evolution Reaction.

(5) **Donglei Zhao**, Sanjayan Sathasivam and Claire J. Carmalt. ZnO thin films used in the transparent conducting oxides and photocatalyts areas.

(6) **Donglei Zhao**, Sanjayan Sathasivam and Claire J. Carmalt. n/p-type transparent conducting oxides materials and p-n heterojunctions.